

Journal of
Mechanics of
Materials and Structures

Volume 3, N^o 8

October 2008

 mathematical sciences publishers

JOURNAL OF MECHANICS OF MATERIALS AND STRUCTURES

<http://www.jomms.org>

EDITOR-IN-CHIEF Charles R. Steele
ASSOCIATE EDITOR Marie-Louise Steele
Division of Mechanics and Computation
Stanford University
Stanford, CA 94305
USA

BOARD OF EDITORS

D. BIGONI University of Trento, Italy
H. D. BUI École Polytechnique, France
J. P. CARTER University of Sydney, Australia
R. M. CHRISTENSEN Stanford University, U.S.A.
G. M. L. GLADWELL University of Waterloo, Canada
D. H. HODGES Georgia Institute of Technology, U.S.A.
J. HUTCHINSON Harvard University, U.S.A.
C. HWU National Cheng Kung University, R.O. China
IWONA JASIUK University of Illinois at Urbana-Champaign
B. L. KARIHALOO University of Wales, U.K.
Y. Y. KIM Seoul National University, Republic of Korea
Z. MROZ Academy of Science, Poland
D. PAMPLONA Universidade Católica do Rio de Janeiro, Brazil
M. B. RUBIN Technion, Haifa, Israel
Y. SHINDO Tohoku University, Japan
A. N. SHUPIKOV Ukrainian Academy of Sciences, Ukraine
T. TARNAI University Budapest, Hungary
F. Y. M. WAN University of California, Irvine, U.S.A.
P. WRIGGERS Universität Hannover, Germany
W. YANG Tsinghua University, P.R. China
F. ZIEGLER Technische Universität Wien, Austria

PRODUCTION


PAULO NEY DE SOUZA Production Manager
SHEILA NEWBERY Senior Production Editor
SILVIO LEVY Scientific Editor

See inside back cover or <http://www.jomms.org> for submission guidelines.

Regular subscription rate: \$500 a year.

Subscriptions, requests for back issues, and changes of address should be sent to Mathematical Sciences Publishers, 798 Evans Hall, Department of Mathematics, University of California, Berkeley, CA 94720-3840.

©Copyright 2009. Journal of Mechanics of Materials and Structures. All rights reserved.

 mathematical sciences publishers

A STUDY OF PENALTY FORMULATIONS USED IN THE NUMERICAL APPROXIMATION OF A RADIALY SYMMETRIC ELASTICITY PROBLEM

ADAIR R. AGUIAR, ROGER L. FOSDICK AND JESÚS A. G. SÁNCHEZ

We consider a class of two-dimensional problems in classical linear elasticity for which material overlapping occurs in the absence of singularities. Of course, material overlapping is not physically realistic, and one possible way to prevent it uses a constrained minimization theory. In this theory, a minimization problem consists of minimizing the total potential energy of a linear elastic body subject to the constraint that the deformation field must be locally invertible. Here, we use an interior and an exterior penalty formulation of the minimization problem together with both a standard finite element method and classical nonlinear programming techniques to compute the minimizers. We compare both formulations by solving a plane problem numerically in the context of the constrained minimization theory. The problem has a closed-form solution, which is used to validate the numerical results. This solution is regular everywhere, including the boundary. In particular, we show numerical results which indicate that, for a fixed finite element mesh, the sequences of numerical solutions obtained with both the interior and the exterior penalty formulations converge to the same limit function as the penalization is enforced. This limit function yields an approximate deformation field to the plane problem that is locally invertible at all points in the domain. As the mesh is refined, this field converges to the exact solution of the plane problem.

1. Introduction

There are problems in the classical linear theory of elasticity whose closed form solutions, while satisfying the governing equations of equilibrium together with well-posed boundary conditions, allow material overlapping to occur. Typically, problems of this kind involve some sort of singularity, and strains exceeding a level acceptable from the point of view of a linear theory occur around the singular points [Aguiar and Fosdick 2001; Aguiar 2006]. But this is not always the case, as we shall show in this work.

We consider a two-dimensional problem in classical linear elasticity for which material overlapping occurs in the absence of singularities. The problem concerns the equilibrium of a circular homogeneous and anisotropic pipe, which is fixed at its inner surface, radially compressed along its outer surface by a uniformly distributed normal pressure, and subjected to an axial force acting on its flat ends. The requirement that the displacement field be radially symmetric with respect to the center of the pipe allows the derivation of a closed-form solution that predicts overlapping of material at the inner surface of the linear elastic pipe when the radial compressive force becomes larger than a critical load, which is small.

One possible way to prevent the anomalous behavior of self-intersection is proposed by Fosdick and Royer-Carfagni [2001]. It combines the linear theory with the constraint of local injectivity through a

Keywords: anisotropic elasticity, constrained minimization, penalty method, finite element method.

Lagrange multiplier technique. These authors investigate the problem of minimizing the total potential energy \mathcal{E} of classical linear elasticity on an admissible set \mathcal{A}_ε of vector-valued functions \mathbf{v} that satisfy the injectivity constraint $\det(\mathbf{1} + \nabla \mathbf{v}) \geq \varepsilon > 0$ for a sufficiently small $\varepsilon \in \mathbb{R}$. In particular, they show the existence of a solution for the constrained minimization problem in two dimensions. The constrained problem is, however, highly nonlinear and, in general, needs to be solved numerically.

Obeidat et al. [2001] and Aguiar [2006] present finite element approaches to solve this class of constrained problems. In the former, a carefully designed algorithm is required to keep track of all subdomains of the reference configuration where the injectivity constraint is violated.

The approach in [Aguiar 2006] is based on an *interior penalty formulation*, which consists of replacing \mathcal{E} by a penalized functional $\mathcal{E}_\gamma = \mathcal{E} + \mathcal{Q}/\gamma$, where γ is an arbitrary positive number and \mathcal{Q} is a penalty functional defined on the constraint set \mathcal{A}_ε . The penalty functional is nonnegative on \mathcal{A}_ε , satisfies $\mathcal{Q}[\mathbf{v}] \rightarrow \infty$ as \mathbf{v} approaches the boundary of \mathcal{A}_ε , and is designed so that minimizers of $\mathcal{E}_\gamma[\cdot]$ lie in the interior of the constraint set \mathcal{A}_ε ; hence the term *interior penalty method*. Thus, the penalty formulation of the constrained problem consists of finding $\mathbf{u}_\gamma \in \mathcal{A}_\varepsilon$ that minimizes the penalized functional \mathcal{E}_γ over the constraint set \mathcal{A}_ε .

In this work, we consider an *exterior penalty formulation*, which consists of replacing \mathcal{E} by a penalized functional $\mathcal{E}_\delta = \mathcal{E} + \mathcal{P}/\delta$, where δ is an arbitrary positive number and \mathcal{P} is a penalty functional defined on the whole set \mathcal{A} . The penalty functional is nonnegative on \mathcal{A} and vanishes on \mathcal{A}_ε . Thus, the penalty formulation of the constrained problem consists of finding $\mathbf{u}_\delta \in \mathcal{A}$ that minimizes the penalized functional \mathcal{E}_δ over the set \mathcal{A} . This method has the advantage of yielding an unconstrained minimization problem. In general, the minimizers of $\mathcal{E}_\delta[\cdot]$ lie in the exterior of the constraint set \mathcal{A}_ε ; hence the term *exterior penalty method*. In this work, however, numerical results shown in Section 5 indicate that the minimizers of \mathcal{E}_δ for the class of problems considered in Section 3 lie in the interior of \mathcal{A}_ε for sufficiently small δ . It is not known whether this is to be generally expected.

In Section 2 we apply both penalty formulations on the class of constrained minimization problems considered by Fosdick and Royer-Carfagni [2001]. In Section 3 we present some exact results concerning the compressed pipe problem in the context of both the unconstrained and the constrained theories. For this, we assume that the problem is radially symmetric, which yields a one-dimensional problem for the determination of the radial displacement in the pipe. In Section 4 we use the finite element method to obtain discrete problems from the interior and exterior penalty formulations of the constrained pipe problem and discuss briefly a solution strategy presented by Aguiar [2006]. The resulting numerical scheme is simple to implement, and can be applied in the numerical solution of problems in any dimension. In particular, we apply the numerical scheme in the approximate solution of the one-dimensional problem with the injectivity constraint. Fosdick et al. [2008] use the numerical strategy of Aguiar [2006] to solve the pipe problem in the full two-dimensional setting. For certain values of the shear modulus of the material, their numerical solution is very different from the solution of the one-dimensional problem. This shows that, depending on the elastic parameters, the constrained minimization problem may have more than one solution. In this work, we investigate the one-dimensional problem, because our primary goal is to compare both penalty formulations. Thus, in Section 5 we compare the numerical results obtained from the solutions of the discrete problems using the interior and the exterior penalty methods with the analytical results obtained from the closed-form solution of the constrained minimization problem considered in Section 3. In Section 6 we present some concluding remarks.

2. The penalty functional formulation

Let $\mathcal{B} \subset \mathbb{R}^2$ be the undistorted natural reference configuration of a body. Points $\mathbf{x} \in \mathcal{B}$ are mapped to points $\mathbf{y} = \mathbf{f}(\mathbf{x}) \equiv \mathbf{x} + \mathbf{u}(\mathbf{x}) \in \mathbb{R}^2$, where $\mathbf{u}(\mathbf{x})$ is the displacement of \mathbf{x} . The boundary $\partial\mathcal{B}$ of \mathcal{B} is composed of two nonintersecting parts, $\partial_1\mathcal{B}$ and $\partial_2\mathcal{B}$, $\partial_1\mathcal{B} \cup \partial_2\mathcal{B} = \partial\mathcal{B}$, $\partial_1\mathcal{B} \cap \partial_2\mathcal{B} = \emptyset$, such that $\mathbf{u}(\mathbf{x}) = \mathbf{0}$ for $\mathbf{x} \in \partial_1\mathcal{B}$ and such that a dead load traction field $\bar{\mathbf{t}}(\mathbf{x})$ is prescribed for $\mathbf{x} \in \partial_2\mathcal{B}$. In addition, a body force $\mathbf{b}(\mathbf{x})$ per unit volume of \mathcal{B} acts on points $\mathbf{x} \in \mathcal{B}$.

We consider the problem of minimum potential energy

$$\min_{\mathbf{v} \in \mathcal{A}_\varepsilon} \mathcal{E}[\mathbf{v}], \quad \mathcal{E}[\mathbf{v}] \equiv \frac{1}{2} a[\mathbf{v}, \mathbf{v}] - f[\mathbf{v}], \tag{1}$$

where

$$a[\mathbf{v}, \mathbf{v}] \equiv \int_{\mathcal{B}} \mathbb{C}[\mathbf{E}] \cdot \mathbf{E} dx, \quad f[\mathbf{v}] \equiv \int_{\mathcal{B}} \mathbf{b} \cdot \mathbf{v} dx + \int_{\partial_2\mathcal{B}} \bar{\mathbf{t}} \cdot \mathbf{v} dx, \tag{2}$$

and $\mathbf{E} \equiv [\nabla\mathbf{v} + (\nabla\mathbf{v})^T]/2$ is the infinitesimal strain tensor field. The functional $\mathcal{E}[\cdot]$ is the total potential energy of classical linear theory of elasticity. Furthermore,

$$\mathcal{A}_\varepsilon \equiv \{ \mathbf{v} : W^{1,2}(\mathcal{B}) \rightarrow \mathbb{R}^2 \mid \det(\mathbf{1} + \nabla\mathbf{v}) \geq \varepsilon > 0, \mathbf{v} = \mathbf{0} \text{ almost everywhere on } \partial_1\mathcal{B} \}, \tag{3}$$

is the class of admissible displacement fields and $\mathbb{C} = \mathbb{C}(\mathbf{x})$ is the elasticity tensor, assumed to be positive definite and totally symmetric. We suppose that $\varepsilon > 0$ in (3) is sufficiently small.

Fosdick and Royer-Carfagni [2001] fully characterize the solutions of the minimization problem (1)–(3). In particular, they show that there exists a solution to this problem and they derive first variation conditions for a minimizer $\mathbf{u} \in \mathcal{A}_\varepsilon$ of $\mathcal{E}[\cdot]$. More specifically, they let

$$\mathcal{A} \equiv \{ \mathbf{v} : W^{1,2}(\mathcal{B}) \rightarrow \mathbb{R}^2 \mid \mathbf{v} = \mathbf{0} \text{ almost everywhere on } \partial_1\mathcal{B} \}, \tag{4}$$

and obtain the first variation of $\mathcal{E}[\cdot]$ at \mathbf{u} in the form

$$\langle D\mathcal{E}[\mathbf{u}], \mathbf{v} \rangle \equiv a[\mathbf{u}, \mathbf{v}] - f[\mathbf{v}], \quad \forall \mathbf{v} \in \mathcal{A},$$

where $a[\cdot, \cdot]$ and $f[\cdot]$ are defined in (2). It is then shown that there exists a scalar Lagrange multiplier field $\lambda : \mathcal{L}^2(\mathcal{B}) \rightarrow \mathbb{R}$ such that the first variation has the equivalent representation

$$\langle D\mathcal{E}[\mathbf{u}], \mathbf{v} \rangle = \int_{\mathcal{B}} \lambda \operatorname{cof} \nabla\mathbf{f} \cdot \nabla\mathbf{v} dx,$$

for all $\mathbf{v} \in \mathcal{A}$, where $\operatorname{cof} \nabla\mathbf{f}$ is the cofactor of the deformation gradient and we recall from above that $\mathbf{f}(\mathbf{x}) = \mathbf{x} + \mathbf{u}(\mathbf{x})$. Then, defining

$$\mathcal{B}_> \equiv \operatorname{int}[\{ \mathbf{x} \in \mathcal{B} : \det \nabla\mathbf{f} > \varepsilon \}], \quad \mathcal{B}_= \equiv \operatorname{int}[\{ \mathbf{x} \in \mathcal{B} : \det \nabla\mathbf{f} = \varepsilon \}], \tag{5}$$

where $\operatorname{int}[\cdot]$ denotes the interior of a set, the necessary first variation conditions for the existence of a minimizer were shown to be given by:

- The Euler–Lagrange equations

$$\operatorname{Div} \mathbf{T} + \mathbf{b} = \mathbf{0} \quad \text{in } \mathcal{B}_>, \quad \operatorname{Div}(\mathbf{T} - \varepsilon\lambda(\nabla\mathbf{f})^{-T}) + \mathbf{b} = \mathbf{0}, \quad \lambda \geq 0, \quad \text{in } \mathcal{B}_=, \tag{6}$$

together with the boundary conditions

$$\mathbf{T}\mathbf{n} = \bar{\mathbf{t}} \quad \text{on } \partial\mathcal{B}_> \cap \partial_2\mathcal{B}, \quad (\mathbf{T} - \varepsilon\lambda(\nabla\mathbf{f})^{-T})\mathbf{n} = \bar{\mathbf{t}}, \quad \text{on } \partial\mathcal{B}_= \cap \partial_2\mathcal{B}, \quad (7)$$

where $\mathbf{T} = \mathbb{C}[\mathbf{E}]$ is the constitutive stress tensor and \mathbf{n} is the outer unit normal to $\partial_2\mathcal{B}$.

- Jump conditions across $\Sigma \equiv \bar{\mathcal{B}}_> \cap \bar{\mathcal{B}}_=$, which is assumed to be sufficiently smooth,

$$(\mathbf{T} - \varepsilon\lambda(\nabla\mathbf{f})^{-T})\Big|_{\Sigma \cap \bar{\mathcal{B}}_=} \mathbf{n} = \mathbf{T}\Big|_{\Sigma \cap \bar{\mathcal{B}}_>} \mathbf{n}, \quad (8)$$

where \mathbf{n} is a unit normal to Σ and where $\Sigma \cap \bar{\mathcal{B}}_=$ and $\Sigma \cap \bar{\mathcal{B}}_>$ mean that the evaluations are understood as limits to the dividing interface Σ from within $\mathcal{B}_=$ and $\mathcal{B}_>$, respectively.

The expression $\mathbf{T} - \varepsilon\lambda(\nabla\mathbf{f})^{-T}$ is regarded as the total stress in $\mathcal{B}_=$, with λ representing the *constraint stress*.

An *interior penalty functional formulation* of the minimization problem (1)–(3) consists of replacing the energy functional (1)b by a penalized potential energy functional $\mathcal{E}_\gamma : \mathcal{A}_\varepsilon \rightarrow \bar{\mathbb{R}}$, $\bar{\mathbb{R}} \equiv \mathbb{R} \cup \{\infty\}$, of the form

$$\mathcal{E}_\gamma[\mathbf{u}] = \mathcal{E}[\mathbf{u}] + \frac{1}{\gamma} \mathcal{Q}[\mathbf{u}], \quad (9)$$

where $\gamma > 0$ is a penalty parameter and $\mathcal{Q} : \mathcal{A}_\varepsilon \rightarrow \bar{\mathbb{R}}$ is an *interior penalty functional*, also called a *barrier functional*. The penalty functional is designed so that minimizers of $\mathcal{E}_\gamma[\cdot]$ lie in the interior of the constraint set \mathcal{A}_ε . Thus, the addition of $(1/\gamma)\mathcal{Q}$ has the effect of establishing a barrier on the boundary of the constraint set \mathcal{A}_ε that prevents a search procedure for a minimizer from leaving the set \mathcal{A}_ε . In this work, we consider the barrier functional defined by

$$\mathcal{Q}[\mathbf{v}] = \int_{\mathcal{B}} \frac{1}{\det(\mathbf{I} + \nabla\mathbf{v}) - \varepsilon} \, d\mathbf{x}, \quad \forall \mathbf{v} \in \mathcal{A}_\varepsilon. \quad (10)$$

Observe from (10) that \mathcal{Q} is nonnegative on \mathcal{A}_ε and satisfies $\mathcal{Q}[\mathbf{v}] \rightarrow \infty$ as \mathbf{v} approaches the boundary of \mathcal{A}_ε .

We then wish to find an admissible displacement field $\mathbf{u}_\gamma \in \mathcal{A}_\varepsilon$ that minimizes the penalized potential $\mathcal{E}_\gamma[\cdot]$, that is,

$$\min_{\mathbf{v} \in \mathcal{A}_\varepsilon} \mathcal{E}_\gamma[\mathbf{v}], \quad (11)$$

where $\mathcal{E}_\gamma[\mathbf{v}]$ is given by the expressions (9), (1)b, (2), and (10). This is a constrained problem, and indeed the functional to be minimized is somewhat more complicated than the original energy functional (1)b. The advantage of considering this problem, however, is that we can use numerical procedures commonly employed in the numerical approximation of solutions of unconstrained problems.

On the other hand, an *exterior penalty functional formulation* of the minimization problem (1)–(3) consists of replacing the energy functional (1)b by a penalized potential energy functional $\mathcal{E}_\delta : \mathcal{A} \rightarrow \mathbb{R}$ of the form

$$\mathcal{E}_\delta[\mathbf{u}] = \mathcal{E}[\mathbf{u}] + \frac{1}{\delta} \mathcal{P}[\mathbf{u}], \quad (12)$$

where $\delta > 0$ is a penalty parameter and $\mathcal{P} : \mathcal{A} \rightarrow \mathbb{R}$ is a *penalty functional*, which is nonnegative in \mathcal{A} and is designed so that $\mathcal{P}[\mathbf{v}]$ increases with the distance from \mathbf{v} to the constraint set \mathcal{A}_ε . In this work, we

consider

$$\mathcal{P}[\mathbf{v}] = \frac{1}{2} \int_B \left[\max(0, -p(\mathbf{v})) \right]^2 d\mathbf{x}, \quad \forall \mathbf{v} \in \mathcal{A}, \tag{13}$$

where $\max(0, -p) \equiv (-p + |p|)/2$ and

$$p(\mathbf{v}) = \det(\mathbf{1} + \nabla \mathbf{v}) - \varepsilon. \tag{14}$$

Clearly, $\mathcal{P}[\mathbf{v}] = 0$ if the injectivity constraint is satisfied; otherwise, $\mathcal{P}[\mathbf{v}] > 0$. In Section 4 we see that the choice (13) for \mathcal{P} leads to a discrete version of the penalized energy functional \mathcal{E}_δ that is continuous and differentiable everywhere.

We then wish to find an admissible displacement field $\mathbf{u}_\delta \in \mathcal{A}$ that minimizes the penalized potential $\mathcal{E}_\delta[\cdot]$, that is,

$$\min_{\mathbf{v} \in \mathcal{A}} \mathcal{E}_\delta[\mathbf{v}], \tag{15}$$

where $\mathcal{E}_\delta[\mathbf{v}]$ is given by (12), (1)b, (2), (13), and (14). This is an unconstrained problem, which has the advantage of yielding discrete minimization problems that can be solved by classical unconstrained optimization techniques.

In Section 4 we use both penalty formulations presented above to construct a numerical scheme that is used in Section 5 for the solution of the constrained plane problem presented in Section 3.2.

3. The pipe problem

In this section we present the solution of a plane problem, which will serve as a model problem in our computations, in the context of both the classical linear theory, Section 3.1, and the constrained minimization theory, Section 3.2.

3.1. The unconstrained pipe problem. In classical linear elasticity, the *pipe problem* concerns the equilibrium of a homogeneous and aeolotropic plate of uniform thickness whose cross section is bounded by two concentric circles, that is, a pipe whose length is the thickness of the plate with an inner radius ρ_i and an outer radius ρ_e . The pipe is radially compressed along its external contour by a uniformly distributed normal pressure p and is subjected to a normal force Q acting on its flat ends. In isotropic elasticity, $Q = 0$ characterizes a state of generalized plane stress parallel to the flat ends of a thin plate. In general, however, this is not the case, that is, we may have $Q = 0$ and still have nonzero normal stresses acting on the flat ends that cannot be disregarded. We comment more on this below.

In a cylindrical coordinate system (ρ, θ, ζ) , we employ the contracted notation σ_α , $\alpha = 1, 2, \dots, 6$, for the stress components, where $\sigma_1 = \sigma_{\rho\rho}$, $\sigma_2 = \sigma_{\theta\theta}$, $\sigma_3 = \sigma_{\zeta\zeta}$, $\sigma_4 = \sigma_{\theta\zeta}$, $\sigma_5 = \sigma_{\zeta\rho}$, $\sigma_6 = \sigma_{\rho\theta}$. An analogous notation is also employed for the strain components, that is, $\epsilon_1 = \epsilon_{\rho\rho}$, $\epsilon_2 = \epsilon_{\theta\theta}$, $\epsilon_3 = \epsilon_{\zeta\zeta}$, $\epsilon_4 = 2\epsilon_{\theta\zeta}$, $\epsilon_5 = 2\epsilon_{\zeta\rho}$, $\epsilon_6 = 2\epsilon_{\rho\theta}$. These components are related to each other by the linear constitutive relations

$$\sigma_\alpha = c_{\alpha\beta} \epsilon_\beta, \tag{16}$$

where $c_{\alpha\beta}$ are the elastic constants for a cylindrically aeolotropic material. The corresponding 6×6 matrix, $[c_{\alpha\beta}]$, is symmetric and positive definite. In this work, we consider that $c_{\alpha\beta} = 0$ for $\alpha \leq 3$, $\beta > 3$ and for $\beta > \alpha > 3$. Following Christensen [1994], we call the corresponding material *cylindrically orthotropic*.

We assume that the stress components are radially symmetric with respect to the center of the pipe, so that $\sigma_\alpha = \sigma_\alpha(\rho)$. In the absence of body force, the equilibrium equations for the pipe problem require that $\sigma_5 = \sigma_6 = 0$ and yield the equation

$$\frac{\partial \sigma_1}{\partial \rho} + \frac{(\sigma_1 - \sigma_2)}{\rho} = 0.$$

This equation is identically satisfied by the introduction of a stress function $\phi : \mathbb{R} \rightarrow \mathbb{R}$ that is related to the stress components $\sigma_i, i = 1, 2$, through the expressions

$$\sigma_1 = \frac{\phi'(\rho)}{\rho}, \quad \sigma_2 = \phi''(\rho), \tag{17}$$

where $(\cdot)' \equiv d(\cdot)/d\rho$.

On the other hand, we can invert the constitutive relations (16) to obtain the strain-stress relations

$$\epsilon_\alpha = s_{\alpha\beta}\sigma_\beta, \tag{18}$$

where $s_{\alpha\beta}$ are the elastic compliances of the cylindrically aeolotropic material. Since $\sigma_5 = \sigma_6 = 0$, we have that $\epsilon_5 = \epsilon_6 = 0$ for a cylindrically orthotropic material. Also, it follows from both (17) and (18) that $\epsilon_\alpha = \epsilon_\alpha(\rho), \alpha = 1, 2$. The compatibility conditions for the pipe problem are then satisfied if

$$\frac{\partial(\rho\epsilon_2)}{\partial \rho} - \epsilon_1 = 0, \tag{19}$$

ϵ_3 is constant, and $\epsilon_4 = 0$.

To solve the differential equation (19), first, we use the strain-stress relations (18) to obtain

$$\sigma_3 = \frac{1}{s_{33}}(-s_{31}\sigma_1 - s_{32}\sigma_2 + \epsilon_3). \tag{20}$$

We then substitute (17) and (20) into (18) to find that

$$\epsilon_\alpha = \frac{1}{s_{33}} \left(s_{\alpha 313} \frac{\phi'(\rho)}{\rho} + s_{\alpha 323} \phi''(\rho) + s_{\alpha 3} \epsilon_3 \right), \quad \alpha = 1, 2, \tag{21}$$

where

$$s_{\alpha 3\beta 3} \equiv s_{\alpha\beta}s_{33} - s_{3\alpha}s_{3\beta}, \quad \alpha, \beta = 1, 2, \tag{22}$$

is the determinant of a minor submatrix of the matrix $\hat{S} \equiv [s_{\delta\gamma}]$ for $\delta, \gamma = 1, 2, 3$. Substituting (21) into (19), we find that

$$\frac{d}{d\rho}(\rho\phi''(\rho)) - \kappa^2 \frac{\phi'(\rho)}{\rho} = \left(\frac{s_{13} - s_{23}}{s_{2323}} \right) \epsilon_3, \quad \kappa \equiv \sqrt{\frac{s_{1313}}{s_{2323}}}, \tag{23}$$

where we have used the fact that $s_{\alpha 3\alpha 3}$, no sum on α , is positive since it is the determinant of a principal submatrix of \hat{S} .

$$c_{11} = \frac{s_{2323}}{\det \hat{S}}, \quad c_{22} = \frac{s_{1313}}{\det \hat{S}}, \quad c_{12} = -\frac{s_{1323}}{\det \hat{S}}. \tag{24}$$

Observe from (23)b together with (24) that κ is also given by

$$\kappa = \sqrt{\frac{c_{22}}{c_{11}}}. \tag{25}$$

The general solution of the differential equation (23) is given by

$$\phi(\rho) = \frac{\alpha^+}{1+\kappa} \rho^{(1+\kappa)} + \frac{\alpha^-}{1-\kappa} \rho^{(1-\kappa)} + \frac{\tilde{\epsilon}_3}{2} \rho^2 + \hat{\phi}, \quad \tilde{\epsilon}_3 \equiv \left(\frac{s_{13} - s_{23}}{s_{2323} - s_{1313}} \right) \epsilon_3, \tag{26}$$

where $\hat{\phi}$ is a constant of integration. Using (26), we obtain from both (17) and (20) that

$$\begin{aligned} \sigma_1 &= \alpha^+ \rho^{(-1+\kappa)} + \alpha^- \rho^{-(1+\kappa)} + \tilde{\epsilon}_3, \\ \sigma_2 &= \kappa \alpha^+ \rho^{(-1+\kappa)} - \kappa \alpha^- \rho^{-(1+\kappa)} + \tilde{\epsilon}_3, \\ \sigma_3 &= -\frac{s_{13} + \kappa s_{23}}{s_{33}} \alpha^+ \rho^{(-1+\kappa)} - \frac{s_{13} - \kappa s_{23}}{s_{33}} \alpha^- \rho^{-(1+\kappa)} + \left(\frac{s_{22} - s_{11}}{s_{2323} - s_{1313}} \right) \epsilon_3. \end{aligned} \tag{27}$$

Notice from (27)c that σ_{33} depends on ρ , a fact observed by Tings [1999], and, in general, cannot be disregarded, as was done by Lekhnitskii [1968, Page 52], even when the pipe has small axial length, that is, it is *disk-like*. This means that no generalized plane stress parallel to the flat ends of the pipe is possible for a radially symmetric distribution of stress in a cylindrically orthotropic body. We can, however, integrate (27)c over a flat end of the pipe and obtain Q , the resultant force on that end. As observed by Tings [1999], we can allow free extension of the pipe in the axial direction in the sense that $Q = 0$, which yields an expression for the determination of the constant ϵ_3 .

The plane stress analysis carried out by Lekhnitskii [1968], which disregards σ_3 , is still valid for particular classes of cylindrically aeolotropic materials, which include the isotropic materials and materials for which $s_{13} = s_{23} = 0$. In this last case, observe from (27)c together with (22) that we must have $\epsilon_3 = 0$.

Now, recalling that the strains depend only on ρ and disregarding rigid body displacements, we have that the displacement field \mathbf{u} is of the form $\mathbf{u} = u(\rho)\mathbf{e}_\rho + \epsilon_3\mathbf{e}_z$, where $(\mathbf{e}_\rho, \mathbf{e}_\theta, \mathbf{e}_z)$ is an orthonormal basis for the cylindrical coordinate system. It then follows from the linear strain-displacement relations

$$\epsilon_1 = u'(\rho), \quad \epsilon_2 = \frac{u(\rho)}{\rho}, \tag{28}$$

together with (21) and (27), that

$$u(\rho) = \hat{\alpha}^+ \rho^\kappa + \hat{\alpha}^- \rho^{-\kappa} + \hat{\epsilon}_3 \rho, \tag{29}$$

where

$$\begin{aligned} \hat{\alpha}^+ &\equiv \left(\frac{s_{2313} + \kappa s_{2323}}{s_{33}} \right) \alpha^+, & \hat{\alpha}^- &\equiv \left(\frac{s_{2313} - \kappa s_{2323}}{s_{33}} \right) \alpha^-, \\ \hat{\epsilon}_3 &\equiv \left[\frac{(s_{2313} + s_{2323})s_{13} - (s_{2313} + s_{1313})s_{23}}{(s_{2323} - s_{1313})s_{33}} \right] \epsilon_3. \end{aligned} \tag{30}$$

Of major interest in this work is the sign of the Jacobian determinant of the deformation field $\mathbf{f} \equiv \mathbf{x} + \mathbf{u}$, given by

$$J \equiv \det \nabla \mathbf{f} = (1 + \epsilon_1)(1 + \epsilon_2)(1 + \epsilon_3). \tag{31}$$

Because ϵ_3 is constant and small compared to unity, it is of no major consequence to consider only the case $\epsilon_3 = 0$ in this work, which is equivalent to assuming that the pipe is in a state of *plane strain* parallel to its flat ends.

By imposing the condition of zero displacement on the inner radius, $u(\rho_i) = 0$, and the pressure condition on the outer radius, $\sigma_{\rho\rho}(\rho_e) = -p$, we find that

$$\alpha^+ = (s_{2313} - \kappa s_{2323})\rho_i^{-\kappa} \rho_e p / \hat{\alpha}, \quad \alpha^- = -(s_{2313} + \kappa s_{2323})\rho_i^\kappa \rho_e p / \hat{\alpha}, \quad (32)$$

where

$$\hat{\alpha} \equiv (s_{2313} + \kappa s_{2323})\left(\frac{\rho_i}{\rho_e}\right)^\kappa - (s_{2313} - \kappa s_{2323})\left(\frac{\rho_i}{\rho_e}\right)^{-\kappa}. \quad (33)$$

Observe from both expressions (22) and (23)b that $s_{2313}^2 - \kappa^2 s_{2323}^2 = s_{2313}^2 - s_{1313}s_{2323} = -s_{33} \det \hat{S} < 0$. We then have both $\kappa s_{2323} - s_{2313} > 0$ and $\kappa s_{2323} + s_{2313} > 0$, and it follows from (33) that $\hat{\alpha} > 0$.

Substituting (30)a, (32), (33), and (24) into (29), we obtain

$$u(\rho) = -\frac{\rho_i}{2\kappa} \left[\left(\frac{\rho}{\rho_i}\right)^\kappa - \left(\frac{\rho}{\rho_i}\right)^{-\kappa} \right] \frac{\hat{p}}{p_1}, \quad \hat{p} \equiv \frac{p}{c_{11}}, \quad \rho_i < \rho < \rho_e, \quad (34)$$

where

$$p_1 = \frac{\rho_i}{2\kappa\rho_e} \left[(\kappa - \mu_\theta)\left(\frac{\rho_i}{\rho_e}\right)^\kappa + (\kappa + \mu_\theta)\left(\frac{\rho_i}{\rho_e}\right)^{-\kappa} \right] > 0, \quad \mu_\theta \equiv \frac{c_{12}}{c_{11}}. \quad (35)$$

In the limit, as $\rho_i \rightarrow 0$, we obtain from (34) together with (35) the Lekhnitskii classical solution for the *disk problem*, which is given by

$$u_0(\rho) \equiv -\left(\frac{\rho}{\rho_e}\right)^\kappa \rho_e q, \quad q \equiv \frac{p}{\sqrt{c_{11}c_{22}} + c_{12}}, \quad 0 < \rho < \rho_e, \quad (36)$$

The expression (36) is presented by Fosdick and Royer-Carfagni [2001, Equation 1.18] in a slightly different notation.

The disk problem is also considered by Tarn [2002] as a special case of a class of generalized plane problems. The author is mainly concerned with the issue of stress singularity at the center of the disk that results from (27) when $0 < \kappa < 1$. He attributes this singular behavior to a conflicting definition of anisotropy at $\rho = 0$. To resolve this, he considers plane problems involving two concentric cylinders of different elastic materials. The outer cylinder is cylindrically anisotropic and the inner solid cylinder is transversely isotropic. Even though the stress fields obtained from the solutions of these problems are not singular at the center of the resulting compound cylinder, it is observed by Fosdick et al. [2008] that self-intersection is still an issue in his work.

Here, we return to the case $\rho_i > 0$, which corresponds to a compound cylinder with a rigid core, and perform a detailed analysis of the solution (34). For this, we take the derivative of (34) with respect to ρ and obtain

$$u'(\rho) = -\frac{1}{2} \left[\left(\frac{\rho}{\rho_i}\right)^{\kappa-1} + \left(\frac{\rho}{\rho_i}\right)^{-(\kappa+1)} \right] \frac{\hat{p}}{p_1}, \quad (37)$$

which is negative in the interval (ρ_i, ρ_e) . Another derivative of (34) shows that $u''(\rho) > 0$ for $0 < \kappa < 1$, which means that u is a convex function of ρ and that u' is a monotonically increasing function of ρ with its minimum at $\rho = \rho_i$. Thus, a critical value of \hat{p} that yields $J = 0$ at $\rho = \rho_i$ in (31) and (28)a is obtained from $u'(\rho_i) = -1$ in (37) and is given by $\hat{p} = p_1$, where p_1 is defined by (35)a. For larger

values of $\hat{\rho}$, $J = 0$ for a unique radius greater than ρ_i . Clearly, we may have p_1 , and hence $\hat{\rho}$, as small as we wish by decreasing the value of ρ_i and still have bounded stresses and strains everywhere. In this work, we are only concerned with $0 < \kappa < 1$.

Similarly, we can show that $u(\rho)/\rho$ is convex at $\rho = \rho_i$. We can also show that $u(\rho)/\rho$ has a unique minimum at a point with radius $\hat{\rho} > \rho_i$ for $0 < \kappa < 1$. This minimum reaches the value -1 , which corresponds to $J = 0$ from (31) together with (28)b, for $\hat{\rho} = p_2$, where

$$p_2 = (1 - \kappa) \left(\frac{1 + \kappa}{1 - \kappa} \right)^{(1+\kappa)/2\kappa} p_1. \tag{38}$$

This critical value of $\hat{\rho}$ is greater than p_1 for $0 < \kappa < 1$. In fact, observe from Figure 1 that $p_2 > 2p_1$.

To avoid crushing of the outer surface into the inner surface of the pipe, the displacement $u(\rho_e)$ must be such that $-u(\rho_e)/\rho_e < 1 - \rho_i/\rho_e$, which, because of (34), imposes the restriction

$$\hat{\rho} < p_c \equiv \frac{2(1 - \eta)\eta^{\kappa-1}}{1 - \eta^{2\kappa}} p_1, \quad \eta \equiv \rho_i/\rho_e. \tag{39}$$

Since $p_c \gg p_1$ for both $\rho_i \ll \rho_e$ and $\kappa < 1$, we conclude from above that local injectivity is lost for nonzero values of $\hat{\rho}$ that are small compared to the critical value p_c for which global injectivity is lost.

Using (31) with $\epsilon_3 = 0$ and (28), (34), and (37), we obtain the expression

$$J = \left\{ 1 - \frac{1}{2} \left[\left(\frac{\rho}{\rho_i} \right)^{\kappa-1} + \left(\frac{\rho}{\rho_i} \right)^{-(\kappa+1)} \right] \frac{\hat{\rho}}{p_1} \right\} \left\{ 1 - \frac{1}{2\kappa} \left[\left(\frac{\rho}{\rho_i} \right)^{\kappa-1} - \left(\frac{\rho}{\rho_i} \right)^{-(\kappa+1)} \right] \frac{\hat{\rho}}{p_1} \right\}. \tag{40}$$

We then see from (40) together with the previous discussion on the critical values for $\hat{\rho}$ that, as $\hat{\rho}$ increases from zero, J is positive in $[\rho_i, \rho_e]$ for $\hat{\rho} < p_1$. For $p_1 \leq \hat{\rho} \leq p_2$, J is nonpositive in $[\rho_i, \rho_1]$, where $u'(\rho_1) = -1$. In particular, $J = 0$ at $\rho = \rho_1$. If $\hat{\rho} = p_2$, we also have that $J = 0$ at $\rho = \hat{\rho}$, where we recall from above that $\hat{\rho}$ is the radius at which $u(\rho)/\rho$ attains its minimum. For $p_2 < \hat{\rho} < p_c$, $u(\hat{\rho})/\hat{\rho} < -1$ and we have two roots ρ_A and ρ_B , with $\rho_A < \rho_B$, for the algebraic equation $u(\rho)/\rho = -1$. Since $u(\rho_e)/\rho_e > -1 + \rho_i/\rho_e$, both roots belong to the interval (ρ_i, ρ_e) and are such that $u(\rho)/\rho \leq -1$ in the interval $[\rho_A, \rho_B]$. Outside this interval, $u(\rho)/\rho > -1$. Thus, we have $J = 0$ at $\rho = \rho_1, \rho_A$, and ρ_B . In Section 5 we show a numerical example for which $\rho_i < \rho_A < \rho_1 < \rho_B < \rho_e$. In this case, J oscillates;

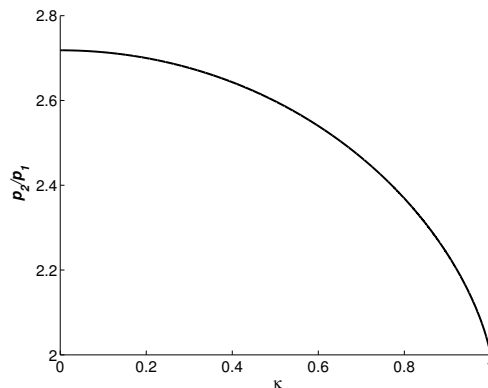


Figure 1. The ratio p_2/p_1 versus κ .

it is negative between ρ_i and ρ_A , positive between ρ_A and ρ_1 , negative again between ρ_1 and ρ_B , and positive again between ρ_B and ρ_e .

In the case of $\rho_i = 0$, $\rho_1 = (\kappa q)^{1/(1-\kappa)}\rho_e$ and $u(\rho)/\rho$ has only one root given by $\rho_2 = q^{1/(1-\kappa)}\rho_e$, where q is defined by the expression (36)b. Here, $J < 0$ inside the annular region defined by

$$0 < \kappa q < \left(\frac{\rho}{\rho_e}\right)^{1-\kappa} < q.$$

Outside the annular region, that is, for small and large values of $(\rho/\rho_e)^{1-\kappa}$, we have $J > 0$. This feature was first noted by Fosdick and Royer-Carfagni [2001].

Thus, for $0 < \kappa < 1$, the classical solution has no physical meaning and therefore should be rejected as a viable solution. The anomalous behavior of material overlapping provides, however, motivation to use a pseudolinear theory which respects the constraint that admissible deformations be at least locally invertible, that is, that $\det \nabla \mathbf{f} > 0$.

3.2. The constrained pipe problem. The solution of the unconstrained pipe problem in Section 3.1 predicts material overlapping for $\kappa \in (0, 1)$. In this section, we consider that $\kappa \in (0, 1)$ and use the first variation conditions (6)–(8) to find a minimizer of (1)–(3) for the constrained pipe problem.

Fosdick and Royer-Carfagni [2001] solve the radially symmetric disk problem of Lekhnitskii outlined in Section 3.1 for the material parameter $\kappa \in (0, 1)$ within the constrained minimization theory outlined in Section 2. They consider only a radially symmetric type solution and our analysis below follows their approach. Recently, Fosdick et al. [2008] have considered the full two-dimensional disk problem and have presented numerical results which show that this symmetry does not persist for all values of the elastic constant c_{66} in (16). Because the constrained theory is nonlinear, there are values of c_{66} for which bifurcation from radial symmetry to nonradial symmetry takes place.

The sets $\mathcal{B}_=$ and $\mathcal{B}_>$ of (5), where the constraint of local injectivity is active ($\det \nabla \mathbf{f} = \varepsilon$) and nonactive ($\det \nabla \mathbf{f} > \varepsilon$), respectively, will be determined explicitly as $\mathcal{B}_= = \{\mathbf{x} = \rho \mathbf{e}_\rho \in \mathcal{B} : \rho_i \leq \rho < \rho_a\}$, $\mathcal{B}_> = \{\mathbf{x} = \rho \mathbf{e}_\rho \in \mathcal{B} : \rho_a < \rho < \rho_e\}$, for some $\rho_a \in [\rho_i, \rho_e]$.

Assuming that the displacement field must be radially symmetric with respect to the center of the pipe in a state of plane strain, that is, $\mathbf{u} = u(\rho)\mathbf{e}_\rho$, we observe that (6)–(8) have the following forms:

- The Euler–Lagrange equations:

$$\begin{aligned} u'' + \frac{u'}{\rho} - \kappa^2 \frac{u}{\rho^2} - \left(1 + \frac{u}{\rho}\right) \frac{d\hat{\lambda}}{d\rho} &= 0, & \hat{\lambda} \geq 0, & \text{for } \rho \in (\rho_i, \rho_a), \\ u'' + \frac{u'}{\rho} - \kappa^2 \frac{u}{\rho^2} &= 0 & & \text{for } \rho \in (\rho_a, \rho_e), \end{aligned} \tag{41}$$

where $\hat{\lambda} \equiv \lambda/c_{11}$.

- The displacement and traction conditions:

$$u(\rho_i) = 0, \quad u'(\rho_e) + \mu_\theta \frac{u(\rho_e)}{\rho_e} = -\hat{p}, \tag{42}$$

where \hat{p} is defined by (34)b and μ_θ is defined by (35)b.

- The continuity and jump conditions across $\rho = \rho_a$:

$$\begin{aligned} u(\rho_a^+) &= u(\rho_a^-), \\ u'(\rho_a^+) &= u'(\rho_a^-) - \left[1 + \frac{u(\rho_a^-)}{\rho_a}\right] \hat{\lambda}(\rho_a^-), \end{aligned} \quad (43)$$

where $\rho_a^\pm \equiv \lim_{\tau \rightarrow 0}(\rho_a \pm \tau)$ for $\tau > 0$. The condition (43)b is obtained from

$$\sigma_{\rho\rho}(\rho_a^+) = \sigma_{\rho\rho}(\rho_a^-) - \left[1 + \frac{u(\rho_a^-)}{\rho_a}\right] \hat{\lambda}(\rho_a^-),$$

together with (16), (28), and (43)a. Observe from (43)b that the jump in u' is zero at $\rho = \rho_a$ provided that $\hat{\lambda}(\rho_a^-) = 0$. We show below that this is indeed the case.

The imposition of the injectivity constraint $\det(\mathbf{1} + \nabla \mathbf{u}) = \varepsilon > 0$ in (ρ_i, ρ_a) yields the problem of finding $u : (\rho_i, \rho_a) \rightarrow \mathbb{R}$ that satisfies

$$\frac{1}{2\rho} \frac{d}{d\rho}(\rho + u)^2 = \varepsilon \quad \text{in } (\rho_i, \rho_a), \quad u(\rho_i) = 0.$$

The solution of this problem is

$$u(\rho) = g(\rho) - \rho, \quad g(\rho) = \sqrt{(\rho^2 - \rho_i^2)\varepsilon + \rho_i^2}, \quad \text{for } \rho \in (\rho_i, \rho_a). \quad (44)$$

Substituting the expression (44) into the first Euler–Lagrange equation (41)a, we obtain a first-order differential equation for $\hat{\lambda}$. The solution of this equation is given by

$$\hat{\lambda}(\rho) = -\frac{(1-\varepsilon)\rho_i^2}{2} \left[\frac{1}{g(\rho)^2} - \frac{1}{g(\tilde{\rho})^2} \right] + \log\left(\frac{g(\rho)}{g(\tilde{\rho})}\right) - \kappa^2 \log\left(\frac{\rho}{\tilde{\rho}}\right) - \frac{(1-\kappa^2)}{\sqrt{\varepsilon}} \log\left(\frac{\sqrt{\varepsilon}\rho + g(\rho)}{\sqrt{\varepsilon}\tilde{\rho} + g(\tilde{\rho})}\right), \quad (45)$$

where $g(\rho)$ is given by (44)b and $\tilde{\rho} \in \mathbb{R}$ is to be determined consistent with $\hat{\lambda}(\tilde{\rho}) \geq 0$. We show in the [Appendix](#) that $u'(\rho_a^+) = u'(\rho_a^-)$ and that $\tilde{\rho} = \rho_a$.

The general solution of the second Euler–Lagrange equation (41)b is of the form

$$u(\rho) = \beta^+ \rho^\kappa + \beta^- \rho^{-\kappa}, \quad (46)$$

where both constants β^+ and β^- are determined from the continuity and jump conditions (43). These constants are given by

$$\beta^+ = \frac{\rho_a^{-\kappa+1}}{2\kappa} \left[-(1+\kappa) + \kappa \frac{g(\rho_a)}{\rho_a} + \frac{\varepsilon\rho_a}{g(\rho_a)} \right], \quad \beta^- = \frac{\rho_a^{\kappa+1}}{2\kappa} \left[1 - \kappa + \kappa \frac{g(\rho_a)}{\rho_a} - \frac{\varepsilon\rho_a}{g(\rho_a)} \right]. \quad (47)$$

We still need to find ρ_a in (47). For this, we substitute (46) and (47) into the traction condition (42)b and obtain the algebraic equation

$$0 = r(\zeta) \equiv s(\zeta; \kappa) + s(\zeta; -\kappa) + \hat{\rho}, \quad \zeta \equiv \frac{\rho_a}{\rho_e}, \quad (48)$$

where

$$s(\zeta; \kappa) \equiv \left(\frac{\kappa + \mu\theta}{2\kappa} \right) \zeta^{1-\kappa} \left[-(1+\kappa) + \frac{\kappa \hat{g}(\zeta)}{\zeta} + \frac{\varepsilon\zeta}{\hat{g}(\zeta)} \right], \quad (49)$$

is a function of ζ parameterized by κ and

$$\hat{g}(\zeta) \equiv \sqrt{\varepsilon\zeta^2 + (1 - \varepsilon)\zeta_i^2}, \quad \zeta_i \equiv \frac{\rho_i}{\rho_e}. \tag{50}$$

First, notice from the expressions (48)–(50) that $r(\zeta_i) = \hat{p} - (1 - \varepsilon)p_1$, where p_1 is given by (35)a. Notice also that $r(1) = \hat{p} - p_0$, where

$$p_0 \equiv 1 + \mu_\theta - \left[\frac{\varepsilon + \mu_\theta \hat{g}(1)^2}{\hat{g}(1)} \right] > p_1, \tag{51}$$

since both ζ_i and $\varepsilon > 0$ are small. Taking the derivative of r , we obtain

$$r'(\zeta) = - \left[\frac{(\kappa + \mu_\theta)\zeta^{-\kappa} + (\kappa - \mu_\theta)\zeta^\kappa}{2\kappa} \right] \left\{ 1 - \kappa^2 + \frac{\kappa^2 \hat{g}(\zeta)}{\zeta} - \frac{\varepsilon\zeta}{\hat{g}(\zeta)} \left[2 - \varepsilon \left(\frac{\zeta}{\hat{g}(\zeta)} \right)^2 \right] \right\}, \quad \zeta \in (\zeta_i, 1),$$

which is negative, because $\kappa + \mu_\theta > 0$, $\kappa - \mu_\theta > 0$, and $\varepsilon > 0$ is small. Thus, if $r(\zeta_i) < 0$, then $r(\zeta) = 0$ has no roots, which is consistent with results obtained in Section 3.1, according to which $\hat{p} - p_1 < 0$ implies no self-intersection. If, on the other hand, both $r(\zeta_i) \geq 0$ and $\hat{p} \leq p_0$, then there exists a unique $\zeta \in [0, 1]$ that satisfies $r(\zeta) = 0$. In particular, if $\hat{p} = (1 - \varepsilon)p_1$, then $\zeta = \zeta_i$ and if $\hat{p} = p_0$, then $\zeta = 1$. Furthermore, if $\hat{p} > p_0$, no $\zeta \in [0, 1]$ exists that satisfies $r(\zeta) = 0$. In this case, $\rho_a = \rho_e$, which means that the constraint is active in the whole pipe.

In the limit, as $\rho_i \rightarrow 0$ in (44)b, we obtain the solution of the *constrained disk problem* considered by Fosdick and Royer-Carfagni [2001], which is given by

$$u(\rho) = \begin{cases} -(1 - \sqrt{\varepsilon})\rho & \text{for } \rho \in (0, \rho_a), \\ -\frac{(1 - \sqrt{\varepsilon})\rho_a}{2\kappa} \left[(1 + \kappa) \left(\frac{\rho}{\rho_a} \right)^\kappa - (1 - \kappa) \left(\frac{\rho}{\rho_a} \right)^{-\kappa} \right] & \text{for } \rho \in (\rho_a, \rho_e). \end{cases} \tag{52}$$

The radius ρ_a in (52) is determined from an algebraic equation obtained from (48)–(50) when $\rho_i = 0$. Fosdick and Royer-Carfagni [2001] show that there exists a unique root for this equation for any positive value of $p \leq (1 - \sqrt{\varepsilon})(c_{11} + c_{12})$. If $p > (1 - \sqrt{\varepsilon})(c_{11} + c_{12})$, the algebraic equation has no root and $\rho_a = \rho_e$. Thus, for any $p > 0$, we have a disk-like region of radius $\rho_a > 0$ where the constraint $J \equiv \det(\mathbf{1} + \nabla \mathbf{u}) = \varepsilon$ is satisfied.

In the pipe problem, for which $\rho_i > 0$, we must have $p \geq (1 - \varepsilon)p_1$ for the constraint $J = \varepsilon$ to be satisfied in a region bounded by the radii ρ_i and ρ_a . Observe from (35) that p_1 is small for small values of ρ_i . Also, recall from (51) that $p_0 > p_1$. In Section 5 we consider $(1 - \varepsilon)c_{11}p_1 < p < c_{11}p_0$ and find numerically a root $\rho_a \in (\rho_i, \rho_e)$ for the algebraic equation (48). Notice that for small $\varepsilon > 0$ and small $\zeta_i > 0$, it follows from (51) together with both (35)b and (50) that $c_{11}p_0$ is approximately equal to $c_{11} + (1 - \zeta_i)c_{12}$, which is of the same order of magnitude as $(1 - \sqrt{\varepsilon})(c_{11} + c_{12})$, as referenced in the previous paragraph.

Using (46) together with $\mathbf{f}(\rho) = [\rho + u(\rho)]\mathbf{e}_\rho$, we can easily obtain an expression for $\det \nabla \mathbf{f}(\rho)$, which is positive everywhere in $[\rho_i, \rho_e]$. Thus, the solution (46) together with (47) describe the deformation of the pipe, which is both locally and globally injective.

4. The discrete formulation

We wish to construct an approximate solution to both penalty minimization problems (11) and (15) for given penalty parameters γ and δ , respectively. For this, it is necessary to consider a finite element formulation based on the introduction of discrete minimization problems over a finite-dimensional space $\mathcal{A}_h \subset \mathcal{A}$, where the subscript h denotes a characteristic length of the finite element and \mathcal{A} is given by (4). These problems can be solved using an unconstrained minimization method with a line search technique.

Holding h fixed and increasing γ in the interior penalty formulation, the strategy is to first generate a sequence of solutions parameterized by γ for the discrete problems that converges to an approximate solution \mathbf{u}_h^i of the minimization problem (1)–(3), as $\gamma \rightarrow \infty$. The aim is then to refine the finite element mesh by decreasing h and repeat the process above. In so doing, we shall generate a sequence of solutions \mathbf{u}_h^i parameterized by h which converges to the solution \mathbf{u} of the original minimization problem (1)–(3).

A similar strategy is used to generate a convergent sequence of solutions \mathbf{u}_h^e for the exterior penalty formulation. Here, \mathbf{u}_h^e is the limit function of a sequence of solutions parameterized by δ as δ tends to zero. In Section 5 we show numerical results which indicate that $\mathbf{u}_h^i = \mathbf{u}_h^e$ for a given h .

The strategies outlined above are general and apply to problems in any dimension. Here, however, we consider the two-dimensional model problem described in Section 3 with the imposition of the injectivity constraint $\det(\mathbf{1} + \nabla \mathbf{v}) \geq \varepsilon > 0$, where $\mathbf{v} \in \mathcal{A}$. In fact, since the fully linear theory in Section 3.1 is radially symmetric, we shall consider only the one-dimensional radially symmetric numerical solution here. Because the constrained theory is nonlinear, radial symmetry need not be the sole possibility as is shown in the work of Fosdick et al. [2008]. Here, we let $\mathbf{v} = v\mathbf{e}_\rho$, where v is a scalar function defined on the interval $(0, \rho_e)$.

Since the energy potential $\mathcal{E}[\cdot]$ is given by (1)b and (2), we can write

$$\mathcal{E}[v\mathbf{e}_\rho] = \pi c_{11} \left\{ \int_{\rho_i}^{\rho_e} \left[(v')^2 \rho + \frac{(\kappa v)^2}{\rho} \right] d\rho + \mu_\theta v(\rho_e)^2 \right\} + 2\pi p v(\rho_e) \rho_e, \tag{53}$$

for the model problem described in Section 3, where κ and μ_θ are given by, respectively, (25) and (35)b. Since $\det(\mathbf{1} + \nabla(v\mathbf{e}_\rho)) = (1 + v')(1 + v/\rho)$, the inverse barrier functional, defined by (10), becomes

$$\mathcal{Q}[v\mathbf{e}_\rho] = 2\pi \int_{\rho_i}^{\rho_e} \frac{\rho}{(1 + v')(1 + v/\rho) - \varepsilon} d\rho, \tag{54}$$

and the exterior penalty functional, defined by (13) and (14), becomes

$$\mathcal{P}[v\mathbf{e}_\rho] = \frac{\pi}{4} \int_{\rho_i}^{\rho_e} \left[-(1 + v')(1 + v/\rho) + \varepsilon + |(1 + v')(1 + v/\rho) - \varepsilon| \right]^2 \rho d\rho. \tag{55}$$

The penalized potential $\mathcal{E}_\gamma[\cdot]$ for the interior formulation is then obtained from (9), (53), and (54), while the penalized potential $\mathcal{E}_\delta[\cdot]$ for the exterior formulation is obtained from (12), (53), and (55). In both cases, because of the assumption of radial symmetry, the discrete formulations are one-dimensional.

Now, let $\rho_i \equiv \rho_0 < \rho_1 < \rho_2 < \dots < \rho_n \equiv \rho_e$ be a partition of the interval $\mathcal{I} \equiv (\rho_i, \rho_e)$ into subintervals $\mathcal{I}_j = (\rho_{j-1}, \rho_j)$ of length $\Delta\rho_j = \rho_j - \rho_{j-1}$, $j = 1, 2, \dots, n$. Let also \mathcal{A}_h be the set of functions $v\mathbf{e}_\rho$ such that v is linear over each subinterval \mathcal{I}_j , $v \in C^0(\mathcal{I})$, and $v(\rho_i) = 0$. Clearly, $\mathcal{A}_h \subset \mathcal{A}$, where \mathcal{A} is given by (4).

Next, introduce the piecewise linear basis functions $\phi_j \mathbf{e}_\rho \in \mathcal{A}_h, j = 1, 2, \dots, n$, defined by

$$\phi_j(\rho_k) = \delta_{kj}, k, j = 1, 2, \dots, n.$$

Then, a function $v_h \mathbf{e}_\rho \in \mathcal{A}_h$ has the representation

$$v_h(\rho) = \mathbf{s} \cdot \mathbf{g}(\rho), \quad \rho \in \mathcal{I}, \tag{56}$$

which is the inner product between the vector $\mathbf{s} \equiv (\eta_1, \eta_2, \dots, \eta_n) \in \mathbb{R}^n$ and the n -dimensional vector-valued function $\mathbf{g} \equiv (\phi_1, \phi_2, \dots, \phi_n)$ defined over the interval \mathcal{I} . The coefficients η_i are given by

$$\eta_k = v_h(\rho_k). \tag{57}$$

Substituting v_h into (53)–(55), we obtain

$$\mathcal{E}_h(\mathbf{s}) \equiv \frac{\mathcal{E}[(\mathbf{s} \cdot \mathbf{g}) \mathbf{e}_\rho]}{2\pi p \rho_e} = \frac{c_{11}}{2p \rho_e} \left\{ \int_{\rho_i}^{\rho_e} \left[(\mathbf{s} \cdot \mathbf{g}')^2 \rho + \frac{(\kappa \mathbf{s} \cdot \mathbf{g})^2}{\rho} \right] d\rho + \mu_\theta [\mathbf{s} \cdot \mathbf{g}(\rho_e)]^2 \right\} + \mathbf{s} \cdot \mathbf{g}(\rho_e), \tag{58}$$

$$\mathcal{Q}_h(\mathbf{s}) \equiv \frac{\mathcal{Q}[(\mathbf{s} \cdot \mathbf{g}) \mathbf{e}_\rho]}{2\pi p \rho_e} = \int_{\rho_i}^{\rho_e} \frac{\rho}{[(1 + \mathbf{s} \cdot \mathbf{g}')(1 + \mathbf{s} \cdot \mathbf{g}/\rho) - \varepsilon]} d\rho, \tag{59}$$

$$\mathcal{P}_h(\mathbf{s}) \equiv \frac{\mathcal{P}[(\mathbf{s} \cdot \mathbf{g}) \mathbf{e}_\rho]}{2\pi p \rho_e} = \frac{1}{8} \int_{\rho_i}^{\rho_e} \left[-(1 + \mathbf{s} \cdot \mathbf{g}')(1 + \mathbf{s} \cdot \mathbf{g}/\rho) + \varepsilon + |(1 + \mathbf{s} \cdot \mathbf{g}')(1 + \mathbf{s} \cdot \mathbf{g}/\rho) - \varepsilon| \right]^2 \rho d\rho, \tag{60}$$

respectively. Observe from (56)–(60) that $\mathcal{E}_h, \mathcal{Q}_h$, and \mathcal{P}_h are scalar functions of an n -dimensional vector of coefficients $\eta_k, k = 1, 2, \dots, n$. Also, \mathcal{P}_h is a continuous function of \mathbf{s} with continuous first derivative.

The discrete versions of the penalized potentials $\mathcal{E}_\gamma[\cdot]$ and $\mathcal{E}_\delta[\cdot]$ are then defined by

$$\mathcal{F}_\gamma(\mathbf{s}) \equiv \mathcal{E}_h(\mathbf{s}) + \frac{1}{\gamma} \mathcal{Q}_h(\mathbf{s}), \quad \mathcal{F}_\delta(\mathbf{s}) \equiv \mathcal{E}_h(\mathbf{s}) + \frac{1}{\delta} \mathcal{P}_h(\mathbf{s}), \tag{61}$$

respectively, for a fixed h . In (61), both penalty parameters γ and δ have been redefined so that their new values are their old values multiplied by $p \rho_e$. The discrete version of the minimization problem (11), applied to the constrained pipe problem of Section 3.2, consists of finding an n -dimensional vector $\mathbf{r}_\gamma \equiv \{\chi_{\gamma 1}, \chi_{\gamma 2}, \dots, \chi_{\gamma n}\}$ that minimizes the scalar function \mathcal{F}_γ , given by (61)a, over all vectors \mathbf{s} in \mathbb{R}^n that satisfy the injectivity constraint

$$\det(\mathbf{1} + \nabla((\mathbf{s} \cdot \mathbf{g}) \mathbf{e}_\rho)) - \epsilon = (1 + \mathbf{s} \cdot \mathbf{g}')(1 + \mathbf{s} \cdot \mathbf{g}/\rho)^2 - \epsilon \geq 0, \quad 0 \leq \rho \leq \rho_e. \tag{62}$$

A nodal value of the constraint (62) is evaluated at the midpoint of the subinterval immediately to the left of the node under consideration. For the discrete version of the minimization problem (15), we search for $\mathbf{r}_\delta \equiv \{\chi_{\delta 1}, \chi_{\delta 2}, \dots, \chi_{\delta n}\}$ that minimizes the scalar function \mathcal{F}_δ , given by (61)b, over all vectors \mathbf{s} in \mathbb{R}^n . Notice from these statements that the discrete version of (11) is a constrained minimization problem while the discrete version of (15) is an unconstrained minimization problem.

The discrete minimization problems stated above are solved iteratively using a standard unconstrained second-order minimization method with a line search technique. The method is based on an *iterative descent algorithm* presented in [Aguiar 2006], which is used here to search for an approximate solution

of the minimization problem

$$\min_{\mathbf{s} \in \mathbb{R}^n} \mathcal{F}_\gamma(\mathbf{s}) \quad \text{subject to the restriction (62),} \quad (63)$$

where \mathcal{F}_γ is given by the expression (61) together with (58) and (59).

Starting from an initial guess $\mathbf{s}_0 \in \mathbb{R}^n$, which corresponds to the undistorted natural state of the body, we generate a sequence of approximate solutions $\mathbf{s}_k \in \mathbb{R}^n$, $k = 0, 1, 2, \dots$, denoted by $\{\mathbf{s}_k\}$, using the recursive formula

$$\mathbf{s}_{k+1} = \mathbf{s}_k + \alpha_k \mathbf{d}_k, \quad (64)$$

where α_k is a scalar minimizing \mathcal{F}_γ in a given direction of search \mathbf{d}_k . Procedures to obtain both α_k and \mathbf{d}_k are described below.

The scalar α_k is a solution of the (unidirectional) minimization problem

$$\min_{\alpha \in \mathbb{R}} \mathcal{H}(\alpha) \equiv \min_{\alpha \in \mathbb{R}} \mathcal{F}_\gamma(\mathbf{s}_k + \alpha \mathbf{d}_k),$$

which is highly nonlinear and is solved iteratively using a standard Newton–Raphson technique. The technique is based on the assumption that we can approximate $\mathcal{H}(\alpha)$ by a quadratic function obtained from the sum of the first three terms of a Taylor series expansion of $\mathcal{H}(\alpha)$ about the minimizer α_k . We assume that $\alpha^{(0)} = 0$ is a good initial guess for α_k . By minimizing the quadratic function, we generate the estimate $\alpha^{(1)}$, which is taken as the next guess for α_k . By repeating this process, we arrive at the recursive formula

$$\alpha^{(i+1)} = \alpha^{(i)} - \frac{\mathcal{H}'(\alpha^{(i)})}{\mathcal{H}''(\alpha^{(i)})}, \quad \alpha^{(0)} = 0, \quad i = 0, 1, \dots \quad (65)$$

We then generate the sequence $\{\alpha^{(i+1)}\}$, $i = 0, 1, \dots$, which is expected to converge to α_k as the number of elements in the sequence tends to infinity [Aguilar 2006].

For each $\alpha^{(i+1)}$ calculated from (65), we check the signs of the nodal values of the discrete injectivity constraint, given by (62), to make sure that they are all positive for $\mathbf{s} = \mathbf{s}_k + \alpha^{(i+1)} \mathbf{d}_k$. This is the only place in the whole numerical scheme where we check for constraint violations.

To determine a direction of search \mathbf{d}_k in (64), we consider that, in a vicinity of \mathbf{s}_k , the scalar function \mathcal{F}_γ can be approximated by the quadratic form

$$\mathcal{F}_\gamma(\mathbf{s}) \approx \mathcal{Q}_n(\mathbf{s}) \equiv \mathcal{F}_\gamma(\mathbf{s}_k) + \nabla_{\mathbf{s}} \mathcal{F}_\gamma(\mathbf{s}_k) \cdot (\mathbf{s} - \mathbf{s}_k) + \frac{1}{2} (\mathbf{s} - \mathbf{s}_k) \cdot \nabla_{\mathbf{s}}^2 \mathcal{F}_\gamma(\mathbf{s}_k) (\mathbf{s} - \mathbf{s}_k),$$

where $\nabla_{\mathbf{s}} \mathcal{F}_\gamma \equiv (\partial \mathcal{F}_\gamma / \partial \eta_1, \partial \mathcal{F}_\gamma / \partial \eta_2, \dots, \partial \mathcal{F}_\gamma / \partial \eta_n)$ is the gradient of \mathcal{F}_γ and $\nabla_{\mathbf{s}}^2 \mathcal{F}_\gamma$ is the Hessian of \mathcal{F}_γ . By solving the equation $\nabla_{\mathbf{s}} \mathcal{Q}_n(\mathbf{s}) = 0$, which is a necessary condition for the existence of a minimizer $\hat{\mathbf{s}}$ of the quadratic form \mathcal{Q}_n , we obtain

$$\mathbf{d}_k \equiv \hat{\mathbf{s}} - \mathbf{s}_k = - [\nabla_{\mathbf{s}}^2 \mathcal{F}_\gamma(\mathbf{s}_k)]^{-1} \nabla_{\mathbf{s}} \mathcal{F}_\gamma(\mathbf{s}_k), \quad k = 0, 1, \dots$$

The sequence of limit points $\{\mathbf{s}_k\}$ generated by (64) converges to the solution $\mathbf{r}_\gamma \in \mathbb{R}^n$ of the discrete minimization problem (63).

Next, we increase the penalty parameter γ and repeat the whole minimization process outlined above. Now, however, we start the new minimization process taking for \mathbf{s}_0 the limit point \mathbf{r}_γ of the previous minimization process. The initial direction of search \mathbf{d}_0 is the direction of steepest descent evaluated at

the new point \mathbf{s}_0 . Using this procedure for a fixed h , we generate a sequence $\{\mathbf{r}_\gamma\}$ that converges to a limit point $\mathbf{r}_h \in \mathbb{R}^n$ as $\gamma \rightarrow \infty$. We use \mathbf{r}_h together with the representation (56) to construct the function $\mathbf{u}_h = (\mathbf{r}_h \cdot \mathbf{g})\mathbf{e}_\rho$. This function is an approximation of the solution \mathbf{u} of the original problem (1)–(3) for a fixed h . Letting $h \rightarrow 0$, we generate a sequence $\{\mathbf{u}_h\}$ that converges to \mathbf{u} .

The algorithm for the minimization problem $\min_{\mathbf{s} \in \mathbb{R}^n} \mathcal{F}_\delta(\mathbf{s})$, where \mathcal{F}_δ is given by (61)b together with (58) and (60), is similar to the algorithm described above. Here, however, we let $\delta \rightarrow 0$ in order to generate a sequence $\{\mathbf{r}_\delta\}$ that converges to the limit point $\mathbf{r}_h \in \mathbb{R}^n$. Also, we do not need to check the signs of the nodal values of the discrete injectivity constraint, given by (62), since the minimization is performed over all $\mathbf{s} \in \mathbb{R}^n$.

5. Numerical results

We apply the numerical method presented in Section 4 to solve numerically the constrained pipe problem described in Section 3.2. We have normalized all lengths by setting the radius of the pipe $\rho_e = 1$. Furthermore, in dimensionless units, the inner radius of the pipe is $\rho_i = 0.001$, the elastic constants are $c_{11} = 10^5$, $c_{22} = 10^3$, and $c_{12} = 10^3$, and the applied load on the boundary of the pipe is $p = 500$. With these geometric and material parameters, we find from (25), (34)b, (35)a, b, (38), and (39) that $\kappa = 0.1 < 1$, $\hat{p} = 0.005$, $p_1 \cong 0.00132$, $\mu_\theta = 0.01$, $p_2 \cong 0.00359$, and $p_c \cong 1.76913$, respectively. Recall from Section 3 that p_1 is the value of \hat{p} below which $1 + u'(\rho)$ is positive and no self-intersection occurs, p_2 is the value of \hat{p} above which we have two roots for the algebraic equation $1 + u(\rho)/\rho = 0$, and p_c is an upper bound for \hat{p} . Then, the roots of the algebraic equations $1 + u'(\rho) = 0$ and $1 + u(\rho)/\rho = 0$, where u is the unconstrained solution given by the expression (34) together with (35), are given by $\rho_1 \cong 0.00381$, $\rho_A \cong 0.00148$, and $\rho_B \cong 0.00784$. Also, we take $\varepsilon = 0.1$ for the lower bound of the injectivity constraint¹. The radius of the core subregion $\mathcal{B}_=$ where the constraint is active is calculated from (48) together with (49), yielding $\rho_a \cong 0.00554$, and the value of \hat{p} above which $\det(\mathbf{1} + \nabla \mathbf{u}) = \varepsilon$ in $[\rho_i, \rho_e]$ is calculated from (51), yielding $p_0 = 0.69061$.

In Figure 2 we show two graphs for the determinant of the deformation gradient $J \equiv \det(\mathbf{1} + \nabla \mathbf{u})$ calculated from the exact solutions of both the constrained pipe problem, represented by the solid line, and the unconstrained pipe problem, represented by the dashed line. The graph on the left side refers to the entire interval, whereas the graph on the right side refers to a neighborhood of the inner surface of the pipe. Observe from the graph on the left that, away from the inner surface, both curves are close to each other and from the graph on the right that J , obtained from the unconstrained solution, vanishes at the radii ρ_A , ρ_1 , and ρ_B , whereas J , obtained from the constrained solution, is constant in $[\rho_i, \rho_a]$, increasing thereafter.

The numerical solutions were obtained with nonuniform partitions of the interval $(0, \rho_e)$ in such a way that the coarsest partition has 300 elements in $(0, 0.07\rho_e)$, 100 elements in $(0.07\rho_e, 0.46\rho_e)$, and 80 elements in $(0.46\rho_e, \rho_e)$ ², totaling 480 elements. The other partitions are obtained from the coarse partition by multiplying the number of elements of this partition by integer powers of 2. Thus, the most

¹ These geometric and material parameters are used by Fosdick and Royer-Carfagni [2001] in their analytical study of the compressed disk problem.

² The nonuniform mesh of 480 elements is similar to the mesh used by Obeidat et al. [2001] in their computational study of the compressed disk problem.

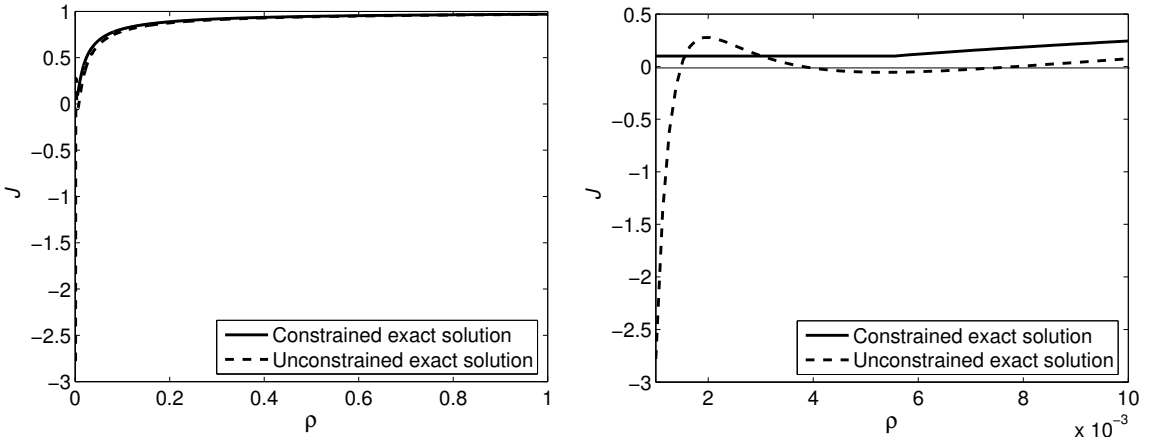


Figure 2. Determinant of the deformation gradient $J \equiv \det(\mathbf{1} + \nabla \mathbf{u})$ versus radius ρ for both the constrained and unconstrained pipe problems.

refined mesh has $2^4 \times 480$ elements, totaling 7680 elements. In what follows, the characteristic length h is the length of the largest interval and n is the total number of elements. Also, we increase the penalty parameter γ in (61)a by powers of 10, that is, we consider $\gamma = 10, 10^2, \dots$, and we decrease the penalty parameter δ in (61)b by negative powers of 10, meaning we consider $\delta = 10^{-1}, 10^{-2}, \dots$.

In Figure 3 we show two graphs with both the exact analytical solution, given by (46) and (47) and represented by the solid line, and the numerical solutions, obtained with the nonuniform mesh of 7680 elements and represented by the dash-dotted lines. The graph on the left side was obtained with the interior penalty formulation using increasing values of γ and the graph on the right side was obtained with the exterior penalty formulation using decreasing values of δ . We see from both graphs that the sequences of numerical solutions converge to limit functions that cannot be distinguished from the analytical solution.

In Figure 4 we show curves for the base 10 logarithm of the Euclidean norm of the error e between the exact solution $\mathbf{u} = u\mathbf{e}_\rho$, given by (46) together with (47), and the numerical solution $\mathbf{u}_h = (\mathbf{r}_h \cdot \mathbf{g})\mathbf{e}_\rho$,

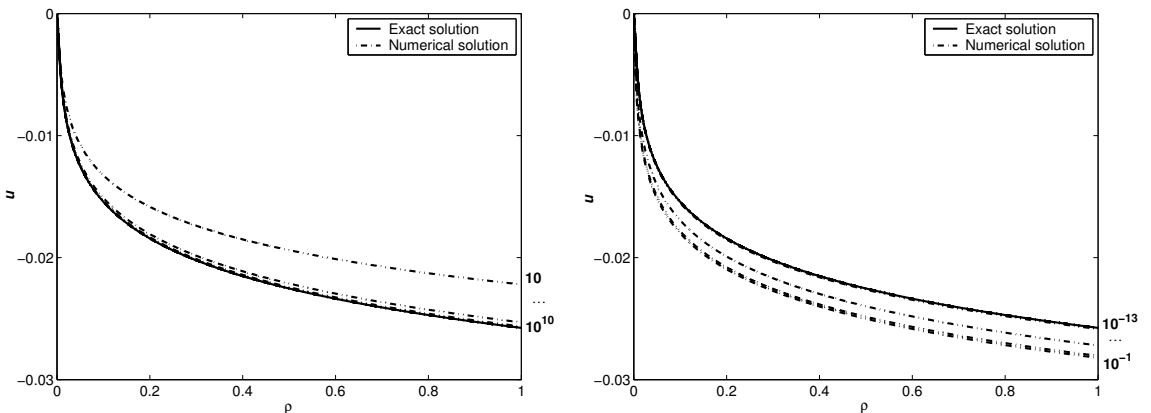


Figure 3. Radial displacement u versus radius ρ for the constrained pipe problem with $n = 7680$. Left: $\gamma = 10, \dots, 10^{10}$. Right: $\delta = 10^{-1}, \dots, 10^{-13}$.

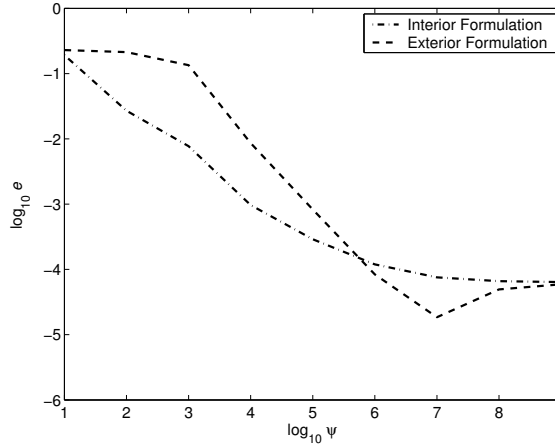


Figure 4. Base 10 logarithm of the error $e \equiv \|\mathbf{r} - \mathbf{r}_h\|_2$ versus base 10 logarithm of the penalty parameter ψ , where ψ is either γ or $1/\delta$.

obtained from the most refined mesh of 7680 elements. This error is plotted against the base 10 logarithm of the penalty parameter ψ , which is equal to γ for the interior penalty formulation (dash-dotted line) and is equal to $1/\delta$ for the exterior penalty formulation (dashed line). Observe from the dash-dotted line that $\log_{10} e$ decreases monotonically with increasing values of γ and tends to an asymptotic value as γ becomes large. A different behavior is observed for the dashed line. Here, $\log_{10} e$ is almost constant for small and large values of $1/\delta$ and decreases rapidly in an interval of intermediate values of $1/\delta$. For small $1/\delta$, the penalty part in (61) is not enforced and the numerical solution is a good approximation of the solution for the unconstrained pipe problem of Section 3.1. Thus, for small $1/\delta$, e is the approximate error between the unconstrained and constrained solutions.

In both curves shown in Figure 4 we see that the errors tend to asymptotic values as both γ and $1/\delta$ tend to infinity. In Figure 5 we consider different discretizations and show curves for the base 10 logarithm of the Euclidean error $\|\mathbf{r}_b - \mathbf{r}_h\|_2$ between the best numerical solution $u_b \equiv \mathbf{r}_b \cdot \mathbf{g}$, obtained with large values of either γ or $1/\delta$ for each discretization, and the numerical solution $u_h = \mathbf{r}_h \cdot \mathbf{g}$. This error is plotted against both the base 10 logarithm of the parameter γ in the graph on the left side and the base 10 logarithm of the parameter $1/\delta$ in the graph on the right side.

Observing the graph on the left side of Figure 5, we see that $\|\mathbf{r}_b - \mathbf{r}_h\|_2$ decreases monotonically with increasing values of γ and that all the curves are similar to each other. In particular, notice that all these curves are almost straight lines for large values of γ . Performing a linear regression on the curve corresponding to 7680 elements, represented by the dash-dotted line, we find that the angular coefficient is approximately equal to -0.73717 , which corresponds to a convergence ratio³ of $10^{-0.73717} \cong 0.18$. Similar analysis can be performed on the curves shown in the graph on the right side of Figure 5. Observe from this graph that all the curves are almost straight lines for $1/\delta \geq 10^6$. For these values of δ , the angular coefficient obtained from a linear regression analysis of the curve corresponding to 7680 elements is approximately equal to -0.52206 , which corresponds to a convergence ratio of $10^{-0.52206} \cong 0.30$.

³Consider the ratio between two consecutive values of a sequence of real numbers. If this ratio tends to a constant value as the number of terms in the sequence tends to infinity, then the ratio is called the convergence ratio of the sequence.

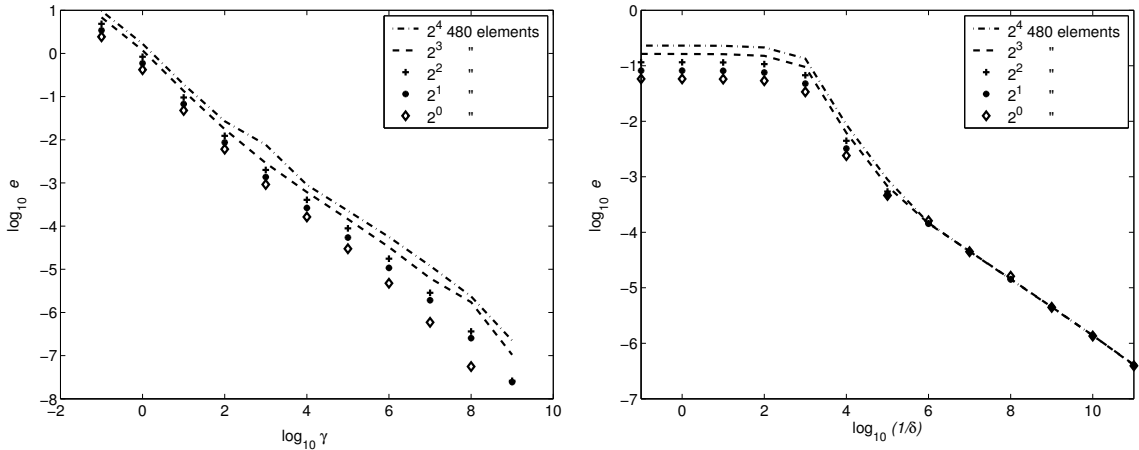


Figure 5. Base 10 logarithm of the Euclidean error $e = \|\mathbf{r}_b - \mathbf{r}_h\|_2$ versus base 10 logarithm of the parameter a) γ (left), b) $1/\delta$ (right).

We see from the this that, for sufficiently large n , the sequence of numerical solutions parameterized by γ converges faster to a limit function than the sequence of numerical solutions parameterized by δ . Also, this convergence is more uniform for the sequence of solutions parameterized by γ than it is for the sequence of solutions parameterized by δ . In particular, notice that this last sequence yields a convergence ratio close to one for small values of $1/\delta$. To quantify this, we performed a linear regression analysis on the curve corresponding to 7680 elements for $1/\delta < 10$ and found that the angular coefficient is approximately equal to -0.01045 , which corresponds to a convergence ratio of $10^{-0.01045} \cong 0.98$.

Next, we chose the largest value of γ in the interior penalty formulation for each discretization and obtained the numerical solutions represented by the dash-dotted lines in Figure 6. Observe from the graph

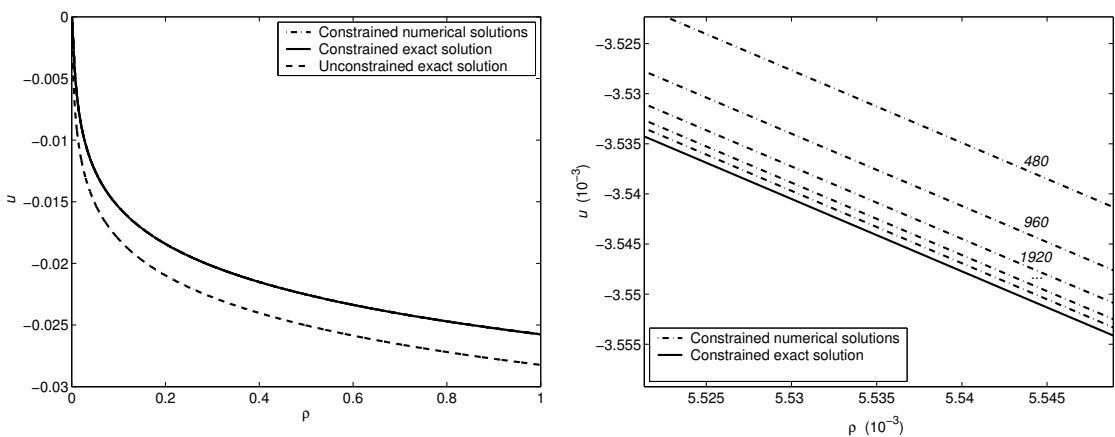


Figure 6. Radial displacement u versus radius ρ for the constrained pipe problem for either large γ or small δ and for an increasing number of elements. Left: Interval (ρ_i, ρ_e) . Right: Magnified view showing the distinction between the numerical solutions and the exact solution.

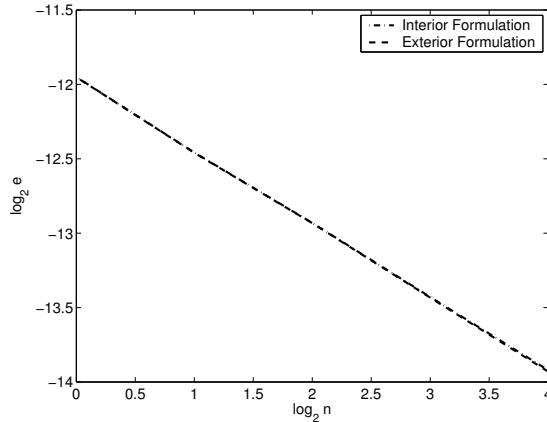


Figure 7. Base 2 logarithm of the Euclidean error e versus base 2 logarithm of the number of elements n for either large γ or small δ . Both curves are indistinguishable at this scale.

on the left side of this figure that the numerical solutions are not distinguishable from the constrained exact solution, given by (46) together with (47) and represented by the solid line. We also show in this graph the unconstrained exact solution, which is given by (34) and (35) and is represented by the dashed line. By comparing this line with the solid line, we conclude that the imposition of the injective constraint has the effect of stiffening the material. Similar conclusions are reached by Aguiar [2006] and Fosdick and Royer-Carfagni [2001] in their treatment of radially symmetric constrained problems.

The graph in Figure 6, right, corresponds to a zoom in a neighborhood of $\rho = \rho_a$. Here, we can see that the sequence of numerical solutions obtained with increasing n converges to the constrained exact solution. At this scale, it is not possible to see the dashed line corresponding to the unconstrained exact solution. Identical curves were obtained using the exterior penalty formulation with a fixed small δ .

In Figure 7 we show curves for the base 2 logarithm of Euclidean norm of the error between the exact solution $\mathbf{u} = u\mathbf{e}_\rho$, given by (46) and (47), and the numerical solution $\mathbf{u}_h = (\mathbf{r}_h \cdot \mathbf{g})\mathbf{e}_\rho$ versus the base 2 logarithm of the number of elements n . The dash-dotted line corresponds to the numerical solution obtained with the interior formulation and the dashed line corresponds to the numerical solution obtained with the exterior formulation. Observe from the figure that both curves are on the top of each other and are almost straight lines. Observe also that the error decreases with the increasing number of elements. Performing a linear regression on these curves, we found that the angular coefficients are approximately equal to -0.49316 , which corresponds to a convergence ratio of $2^{-0.49316} \cong 0.7105$.

In Figure 8 we show the determinant of the deformation gradient $J \equiv \det(\mathbf{1} + \nabla \mathbf{u})$ calculated from both the exact solution of the constrained pipe problem, represented by the solid line, and the corresponding numerical approximations. These approximations, which are represented in the figure by different line styles, were obtained using both the interior penalty formulation with large γ and the nonuniform meshes. The graph on the left in Figure 8 refers to the entire interval, whereas the graph on the right refers to a neighborhood of the inner surface of the pipe which contains the active region, that is, for $\rho \in (\rho_i, \rho_a)$. Observe from the graph on the left the very good agreement between the analytical and the numerical results and from the graph on the right that the numerical approximations of J converge to the analytical

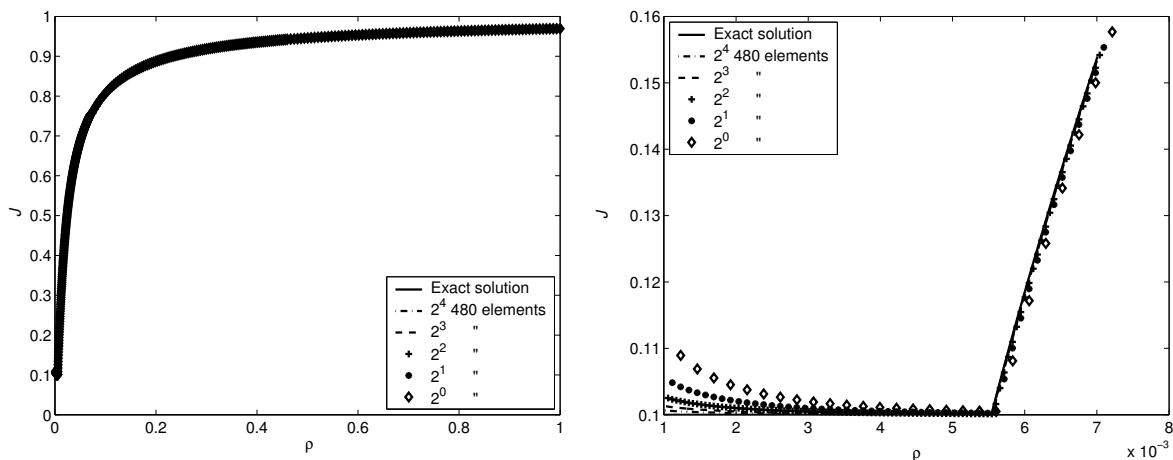


Figure 8. Determinant of the deformation gradient $J \equiv \det(\mathbf{1} + \nabla \mathbf{u})$ versus radius ρ for the constrained pipe problem using large γ .

solution as the mesh is refined. In particular, observe from this last graph that the numerical scheme captures well the sharp change in J at $\rho = \rho_a$. Identical curves were obtained using the exterior penalty formulation.

In [Figure 9](#) we show the determinant of the deformation gradient $J \equiv \det(\mathbf{1} + \nabla \mathbf{u})$ calculated from both the exact solution of the constrained pipe problem, represented by the solid line, and its numerical approximations, represented by the dash-dotted line, for the most refined mesh of 7680 elements. The graphs on the left and the right sides of [Figure 9](#) refer to the approximations obtained with, respectively, the interior and the exterior penalty formulations. Observe from both graphs that J_h converges to a limit function as the penalty parameter is enforced in each case, that is, as $\gamma \rightarrow \infty$ on the left graph and as $\delta \rightarrow 0$ on the right graph. Recall from the analysis of [Figure 8](#) that both limit functions are identical, are represented by the dash-dotted line in the graph on the right of that figure, and approximate the analytical solution $J = \varepsilon$ (recall, $\varepsilon = 0.1$) in the interval (ρ_i, ρ_a) .

Observe from the graph on the right side of [Figure 9](#) that, in the interval (ρ_i, ρ_a) , the approximations u_h of the minimizer u lie in the exterior of the set \mathcal{A}_ε for large δ since, in this case, $J_h < \varepsilon$. Nevertheless, contrary to what one might expect, as $\delta \rightarrow 0$, the sequence of approximations $\{u_h\}$ converges to a limit function that belongs to the constrained set \mathcal{A}_ε .

6. Conclusion

In this work we investigate the problem of equilibrium of a circular homogeneous and cylindrically orthotropic pipe that is fixed at its inner surface, is radially compressed along its outer surface, and is subjected to an axial force on its flat ends. In the classical linear theory, the solution to this problem is smooth everywhere, including the boundary of the pipe, and predicts self-intersection in a neighborhood of the inner surface for a sufficiently large, but reasonable, compressive radial pressure. Of course, this behavior has no physical meaning. By using a minimization theory that enforces the injectivity condition $J \geq \varepsilon > 0$, where J is defined in the expression (31) and ε is small, we obtain a radially symmetric solution

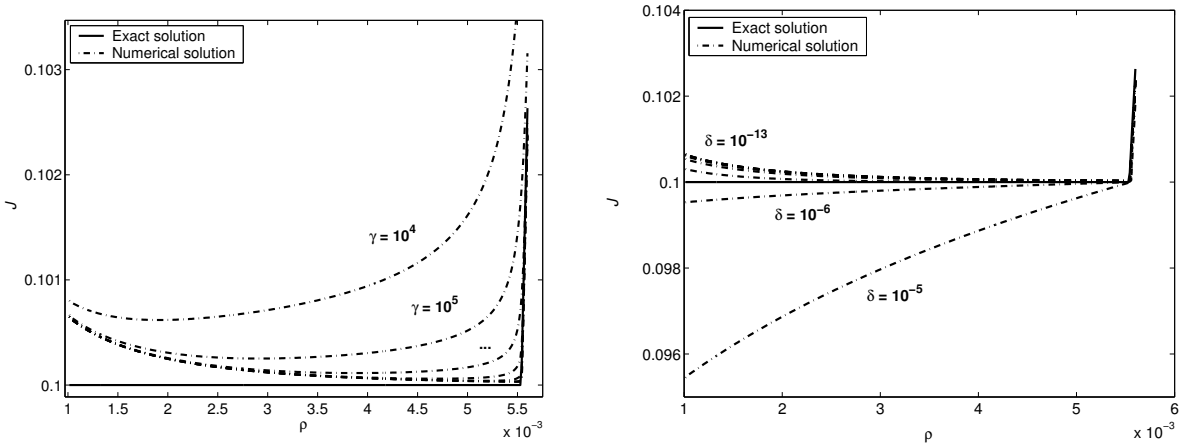


Figure 9. Determinant of the deformation gradient $J \equiv \det(\mathbf{1} + \nabla \mathbf{u})$ versus radius ρ for the constrained pipe problem using $n = 7680$. Interior (left) and exterior (right) penalty formulations.

to the corresponding constrained minimization problem that satisfies this injectivity condition, as shown in Figure 2, that does not predict the anomalous self-intersecting behavior anywhere in the pipe, and that yields a stiffer material response.

The advantage of investigating radially symmetric one-dimensional problems is that, in general, their solutions are known in the context of both unconstrained and constrained minimization theories of quadratic functionals [Fosdick and Royer-Carfagni 2001; Aguiar 2006]. A disadvantage of this investigative approach is that not all possible solutions of the corresponding full two-dimensional problems can be obtained in the context of the constrained theory (see, for instance, the numerical treatment of a full two-dimensional problem by Fosdick et al. [2008]).

We then use both an interior and an exterior penalty formulation of the constrained minimization problem together with a standard finite element method and classical nonlinear programming techniques to find approximate solutions to this constrained problem. We show numerical results obtained from discrete versions of both formulations that are in very good agreement with analytical results presented in Section 3.2. We highlight below the main findings from the analysis of these results.

- (1) For a given finite element mesh, the sequences of numerical results obtained with both penalty formulations converge to the same limit function as the penalization is enforced (see Figures 6 and 7). These sequences are, however, very different from each other (see Figure 3) and converge at different rates (see Figures 4 and 5).
- (2) For a given finite element mesh, the results shown in Figure 5 indicate that the interior penalty formulation yields a sequence of numerical solutions that converges faster and more uniformly to a limit function than the sequence obtained from the exterior penalty formulation.
- (3) For a given finite element mesh, a sequence of numerical solutions u_ψ , where either $\psi = \gamma$ for the interior penalty formulation or $\psi = 1/\delta$ for the exterior penalty formulation, yields a convergent sequence of $J_\psi = \det(\mathbf{1} + \nabla \mathbf{u}_\psi)$ that satisfies $J_\psi \geq \varepsilon$ everywhere in the pipe as $\psi \rightarrow \infty$ (see Figure 8).

- (4) The interior formulation yields, expectedly, $J_\gamma \geq \varepsilon$ for every $\gamma > 0$ (see [Figure 9](#) on the left) and the exterior formulation yields $J_{1/\delta} < \varepsilon$ in $(0, \rho_a)$ for large δ and $J_{1/\delta} \geq \varepsilon$ in $(0, \rho_a)$ for small δ (see [Figure 9](#) on the right). This last result was not expected, because, in general, the exterior formulation yields a sequence of penalized solutions that converges to the solution of the problem from the exterior of the constrained set. Here, however, the sequence is converging from the interior of the set as $1/\delta \rightarrow \infty$.

In summary, both penalty methods are viable methods of analysis for the class of constrained minimization problems considered in [Section 2](#), lead to simple numerical schemes that yield very accurate approximate solutions to the corresponding constrained problems, and can be used to solve more complex problems. The main advantage of the exterior penalty method is that the corresponding minimization problem is unconstrained. Also, the exterior penalty functional chosen in this work, given by the expression [\(13\)](#), leads to a penalty function \mathcal{F}_δ , given by [\(61\)b](#) together with [\(58\)](#) and [\(60\)](#), that is differentiable everywhere. On the other hand, the main findings highlighted above suggest that, given a finite element mesh, the interior penalty method yields a sequence of numerical solutions that converges faster and more uniformly to a limit function than the sequence obtained from the exterior penalty method. In addition, the numerical solutions obtained with the interior penalty method are kinematically admissible for any penalty parameter.

This work is part of an ongoing research effort to determine the best strategy to tackle general higher dimensional singular problems in elasticity for which the corresponding solution may exhibit self-intersection in the vicinity of corners and crack tips. The results obtained in this work suggest that the best strategy might be a combination of both penalty formulations. One might use the interior penalty formulation to generate a numerical solution that is a good approximation to the solution of the constrained problem and then use this numerical solution as the initial guess in the search of the constrained solution with the exterior penalty formulation.

Appendix

Here, we resolve the technical issue that arose in the solution [\(45\)](#) for the Lagrange multiplier function $\hat{\lambda}(\rho)$.

Proposition. To be consistent with $\hat{\lambda}(\rho) \geq 0$ in (ρ_i, ρ_a) , the jump of u' across $\rho = \rho_a$ must be zero and $\tilde{\rho} = \rho_a$.

Proof. We consider a procedure that is analogous to the procedure used by [\[Fosdick and Royer-Carfagni 2001\]](#) in the analysis of a model problem that is a particular case of our problem when $\rho_i = 0$.

First, we rewrite the expression [\(45\)](#) as

$$\hat{\lambda}(\rho) = -\frac{\rho_i^2(\tilde{\rho}^2 - \rho^2)(1 - \varepsilon)\varepsilon}{2[g(\rho)g(\tilde{\rho})]^2} + \log\left(\frac{h(\rho)}{h(\tilde{\rho})}\right), \quad \rho \in (\rho_i, \rho_a), \tag{A.1}$$

where

$$h(\rho) = \frac{g(\rho)}{\rho^{\kappa^2}[\sqrt{\varepsilon}\rho + g(\rho)]^\alpha}, \quad \alpha \equiv \frac{(1 - \kappa^2)}{\sqrt{\varepsilon}}. \tag{A.2}$$

Next, we substitute the expressions (44), (A.1), and (A.2) in the jump condition (43)b to obtain

$$\log\left(\frac{h(\rho_a)}{h(\tilde{\rho})}\right) = -\frac{\rho_a}{g(\rho_a)} \left| [u'(\rho_a)] \right| + \frac{\rho_i^2(\tilde{\rho}^2 - \rho_a^2)(1 - \varepsilon)\varepsilon}{2[g(\rho_a)g(\tilde{\rho})]^2}, \tag{A.3}$$

where $|[u'(\rho_a)]| \equiv u'(\rho_a^+) - u'(\rho_a^-)$ is the jump of u' across $\rho = \rho_a$.

Noting that $\log(h(\rho)/h(\tilde{\rho})) = \log(h(\rho)/h(\rho_a)) + \log(h(\rho_a)/h(\tilde{\rho}))$ and using (A.3) in (A.1), we can rewrite $\hat{\lambda}$ as

$$\hat{\lambda}(\rho) = -\frac{\rho_i^2(\rho_a^2 - \rho^2)(1 - \varepsilon)\varepsilon}{2[g(\rho)g(\rho_a)]^2} + \log\left(\frac{h(\rho)}{h(\rho_a)}\right) - \frac{\rho_a}{g(\rho_a^-)} \left| [u'(\rho_a)] \right|. \tag{A.4}$$

Since $\hat{\lambda}(\rho_a) \geq 0$, we see from (A.4) that $|[u'(\rho_a)]| \leq 0$, which implies that

$$u'(\rho_a^+) \leq u'(\rho_a^-). \tag{A.5}$$

On the other hand, the condition $\det \nabla \mathbf{f} \geq \varepsilon$ in (ρ_a, ρ_e) together with the expressions (31), (28), and $\varepsilon_3 = 0$, yields $(1 + u'(\rho_a^+))(1 + u(\rho_a^+)/\rho_a) \geq \varepsilon$. Also, $(1 + u'(\rho))(1 + u(\rho)/\rho) = \varepsilon$ for $\rho \in (\rho_i, \rho_a)$. Since $u(\rho_a^+) = u(\rho_a^-)$ from the jump condition (43)a, we then find that

$$u'(\rho_a^+) \geq u'(\rho_a^-). \tag{A.6}$$

Thus, it follows from both (A.5) and (A.6) that $|[u'(\rho_a)]| = 0$. □

Acknowledgements. The author wishes to acknowledge Fundação de Amparo à Pesquisa do Estado de São Paulo (FAPESP), proc. # 2007/03753-9, and the University of Minnesota Supercomputing Institute (UMSI) for their support of this research.

References

[Aguiar 2006] A. R. Aguiar, “Local and global injective solution of the rotationally symmetric sphere problem”, *J. Elasticity* **84**:2 (2006), 99–129.

[Aguiar and Fosdick 2001] A. R. Aguiar and R. L. Fosdick, “Self-intersection in elasticity”, *Int. J. Solids Struct.* **38**:28–29 (2001), 4797–4823.

[Christensen 1994] R. M. Christensen, “Properties of carbon fibers”, *J. Mech. Phys. Solids* **42**:4 (1994), 681–695.

[Fosdick and Royer-Carfagni 2001] R. L. Fosdick and G. Royer-Carfagni, “The constraint of local injectivity in linear elasticity theory”, *Proc. R. Soc. Lond. A* **457**:2013 (2001), 2167–2187.

[Fosdick et al. 2008] R. L. Fosdick, F. Freddi, and G. Royer-Carfagni, “Bifurcation instability in linear elasticity with the constraint of local injectivity”, *J. Elasticity* **90**:1 (2008), 99–126.

[Lekhnitskii 1968] S. G. Lekhnitskii, *Anisotropic plates*, Gordon and Breach, New York, 1968.

[Obeidat et al. 2001] K. Obeidat, H. Stolarski, R. Fosdick, and G. Royer-Carfagni, “Numerical analysis of elastic problems with injectivity constraints”, in *Solids, structures and coupled problems in engineering: 2nd European Conference on Computational Mechanics (ECCM-2001); proceedings* (Cracow, 2001), Politechnika Krakowska, Cracow, 2001. On CD.

[Tarn 2002] J.-Q. Tarn, “Stress singularity in an elastic cylinder of cylindrically anisotropic materials”, *J. Elasticity* **69**:1–3 (2002), 1–13.

[Tings 1999] T. C. T. Tings, “New solutions to pressuring, shearing, torsion, and extension of a cylindrically anisotropic elastic circular tube or bar”, *Proc. R. Soc. Lond. A* **455**:1989 (1999), 3527–3542.

Received 21 Jan 2008. Revised 15 May 2008. Accepted 6 Aug 2008.

ADAIR R. AGUIAR: aguilarar@sc.usp.br

*Department of Structural Engineering, São Carlos School of Engineering, University of São Paulo, Av. Trabalhador
São-carlense, 400, 13566-590 São Carlos, SP, Brazil*

<http://www.set.eesc.usp.br/public/pessoas/professor.php?id=2>

ROGER L. FOSDICK: fosdick@aem.umn.edu

*Aerospace Engineering and Mechanics, University of Minnesota, 107 Akerman Hall, 110 Union St. SE, Minneapolis, MN
55455-0153, United States*

<http://www.aem.umn.edu/people/faculty/bio/fosdick.shtml>

JESÚS A. G. SÁNCHEZ: jesusg@sc.usp.br

*Department of Structural Engineering, São Carlos School of Engineering, University of São Paulo, Av. Trabalhador
São-carlense, 400, 13566-590 São Carlos, SP, Brazil*

NUMERICAL AND EXPERIMENTAL STUDIES OF DEEP INDENTATION ON SINGLE CRYSTALS

YONG X. GAN, XI CHEN AND MANHONG ZHAO

Indentation tests with large penetration depths have been used to study the plastic deformation behavior of materials. In this work, finite element simulations of wedge indentation into face-centered cubic single crystals were performed. Numerical solutions to the stresses and shear strains within the single crystals indented with a relatively large penetration depth were obtained. The crystal lattice rotation map of the indented crystals was also shown. Indentation experiments were conducted on copper crystals and the results were used to validate the numerical predictions. Comparison of the numerical solutions to the crystal lattice rotation with the experimentally measured lattice rotation map was made. The main features of the crystal lattice in-plane rotation map from the finite element simulations are also found on the map developed from the electron backscatter diffraction measurements. Both simulations and experimental measurements reveal the same dislocation structures as evidenced by the slip sectors underneath the wedge indentation zone.

1. Introduction

Indentation is useful for obtaining load-displacement data and the data may be used for mechanical property evaluation [Beghini et al. 2006], post-yielding analysis [Habbab et al. 2006], and materials rheology study [Bigot et al. 2005]. Vlassak and Nix [1994] measured the elastic properties of anisotropic materials such as copper and brass under indentation. The indentation size effect was studied to reveal the variation of measured properties with the applied loading levels. Based on the indentation studies on titanium and aluminum, it is found that the contact surface area between the specimens and the indenter causes the variation of microhardness [Iost and Bigot 1996]. In the work performed by Gerberich et al. [2002], the indentation size effect is correlated to the ratio of the energy of newly created surface and the plastic strain energy dissipation. The ratio of contact surface area to plastic volume remains constant if the indentation depth is within several hundred nanometers. Another phenomena related to shallow indentation, the surface step effect, was found [Zimmerman et al. 2001], meaning that the load needed to nucleate dislocations decreases significantly when indenting close to a surface step.

From indentation tests, important information about dislocation activities within materials can be obtained. For example, Kysar et al. [2007] used indentation data to calculate the geometrically necessary dislocation density. The condition for dislocation pile-up under a conical nanoindenter is determined by Zaafarani et al. [2008]. Bhattacharya and Nix [1991] showed how to determine the shapes of plastic zones under indenters. They also clarified the effects of shear modulus, bulk modulus and indenter angle on the hardness of hard and soft materials. Laursen and Simo [1992] provided an approach to

Keywords: finite element simulation, indentation, plastic deformation, copper crystal, stress field, shear strain, electron backscatter diffraction, crystal lattice rotation, slip, dislocation structure.

computing the hardness, contact stiffness, effective composite modulus, and surface profile under load and thus the amount of pileup (or sink-in) around the indenter in the fully loaded configuration, as well as the variation of the actual contact area during indenter withdrawal, can be predicted. Marx and Balke [1997] identified the influence of material properties on the unloading response. Bolshakov and Pharr [1998] showed how to use indentation load-displacement data to identify when pileup occurs. The work performed by Giannakopoulos et al. [1994] evaluated the hardness formulae for materials under Vickers indentation tests.

Studies of spherical indentation into a half-space have been performed for a long time, as shown in the works performed by Follansbee and Sinclair [1984], Sinclair et al. [1985], and Hill et al. [1989], which provide important information about hardness, contact pressure distributions, and the transition from the initial elastic regime to the fully plastic contact regime. Cylindrical indentation induced deformation in face-centered cubic (FCC) metal single crystals was examined in our earlier work [Gan et al. 2007]. For sharp indentation tests using conical, pyramidal, or wedge indenters, the behavior of tested materials may not be deduced directly. So, numerical simulations were used [Pelletier 2006] to predict the deformation of the indented region. For example, Qu et al. [2006] used finite elements (FE) to simulate the mechanism-based strain gradient plasticity in an indented iridium specimen. Indentation with small or moderate penetration depth has been studied for evaluating the elastic-plastic properties of materials such as thin films [Zhao et al. 2006; 2007]. Deep penetrating indentation tests may be used to study the plastic deformation behavior of materials. At the micron length scale, materials often exhibit heterogeneous behavior as shown by Rashid et al. [1992] via the slip of copper single crystals at different loading rates. Havner and Yu [2005] analyzed the finite double slip behavior in FCC crystals. The number and orientation of active slip systems are dependent and may vary during an indentation test [Bouvier and Needleman 2006]. Constitutive modeling of materials at different finite deformation states was performed [Naghdabadi et al. 2005]. A deformation gradient based kinematic hardening model was reported [Wallin and Ristinmaa 2005]. Lattice orientation effects on plastic deformation and damage evolution in FCC single crystals were also studied [Potirniche et al. 2006].

The work on simulations of indentation into single crystals spans atomic discrete simulations [Miller et al. 2004], nanoscale plasticity simulations [Horstemeyer et al. 2001], mesoscale investigation [Yoshino et al. 2001], micromechanics based FE analysis [Premachandran and Horii 1994], and quasicontinuum analysis [Tadmor et al. 1996]. For example, the simulation at atomic scale levels using molecular dynamics methodologies was presented by Miller et al. [2004]. Atomistic simulations of elastic deformation and dislocation nucleation during nanoindentation were performed by Lilleodden et al. [2003]. Horstemeyer et al. [2001] investigated the structure-property relations for plasticity at different length scales through simulations using embedded atom potentials. Three dimensional finite element simulations of dislocation nucleation under indentation were investigated based on the analysis of nanoscale contact of single crystal copper by a cylindrical indenter [Zhu et al. 2004], and by a conical indenter [Wang et al. 2004]. Based on three dimensional FE analysis, the complex equilibrium crack front of indentation into thin film coated on a thick silicon crystal substrate was identified [Xia et al. 2004], and the indent-induced plastic zone in FCC crystals was defined [Fivel et al. 1998]. Simulation of the strain gradient effects on a microscopic strain field was also performed [Shu and Barlow 2000]. Quasicontinuum analysis [Tadmor et al. 1996] allows us to obtain simultaneous solutions for continuum and atomistic length scales. However, the computation (either atomistic or multiscale) is very expensive and not applicable to

large length scales. It cannot simulate very deep indents. Therefore, FE simulations of indentation into single crystals were used to predict the plastic properties of single crystals, for example, Al, Ni, and Pb [Xu and Rowcliffe 2002], and MgO [Yoshioka 1991; Xu and Rowcliffe 2002]. However, there is very little work on validating the numerical solutions using experimental results.

In this work, we simulated the wedge indentation in copper single crystals with special orientations. Comparison of the finite element solutions with experimental results was made. The paper is organized as follows. First, the numerical simulations based on finite deformation theory of single crystal plasticity will be presented. Implementation of finite element simulations will be delineated. Second, indentation test procedures will be given and the lattice rotation measurement will be briefly described. Then, stress, shear strain, and in-plane lattice rotation solutions from the FE simulations will be given. Subsequently, the indentation experimental results will be presented. Following that, comparison of the numerical solutions and the experimentally measured lattice rotation results will be carried out to validate the finite element solutions. The novelty of this work is in testing the numerical predictions through experimental results.

2. Finite element simulation

The finite element analysis was performed using the commercial software ABAQUS. A user-material subroutine for single crystal plasticity was used in implementation of the simulations for copper single crystals. The subroutine is based on the framework of kinematical theory for the mechanics of single crystals [Turkmen et al. 2004]. For the finite deformation of single crystals,

$$\hat{\mathbf{D}} + \hat{\mathbf{\Omega}} = \hat{\mathbf{F}}\hat{\mathbf{F}}^{-1}, \quad \mathbf{D}^{\mathbf{P}} + \mathbf{\Omega}^{\mathbf{P}} = \sum_{k=1}^n \dot{\gamma}^{(k)} \hat{\mathbf{s}}^{(k)} \otimes \hat{\mathbf{m}}^{(k)},$$

where \mathbf{F} is the deformation gradient, \mathbf{D} stands for the symmetric stretching tensor and $\mathbf{\Omega}$ is the spin tensor, which can be decomposed into elastic parts ($\hat{\cdot}$) and plastic parts ($\cdot^{\mathbf{P}}$). The superscript k denotes the k -th slip system, $\dot{\gamma}^{(k)}$ is the shear strain rate, n is the total number of the active slip systems, $\hat{\mathbf{s}}^{(k)}$ and $\hat{\mathbf{m}}^{(k)}$ are unit vectors along the slip direction and normal to the slip plane in the reference configuration, respectively.

The constitutive relation for single crystals under finite deformation is $\hat{\hat{\sigma}} + \sigma(I : \hat{\mathbf{D}}) = \mathbf{L} : \hat{\mathbf{D}}$, where L is the tensor of elastic moduli and $\hat{\hat{\sigma}}$ is the corotational stress rate on axes that rotate with the crystal lattice. $\hat{\hat{\sigma}}$ can be expressed as $\hat{\hat{\sigma}} = \tilde{\sigma} + (\mathbf{\Omega} - \hat{\mathbf{\Omega}})\sigma - \sigma(\mathbf{\Omega} - \hat{\mathbf{\Omega}})$, where $\tilde{\sigma}$ is the corotational stress rate on axes rotating with the material, which is $\tilde{\sigma} = \dot{\sigma} - \mathbf{\Omega}\sigma + \sigma\mathbf{\Omega}$. The Schmid stress and the rate of Schmid stress are given as

$$\tau^{(k)} = \hat{\mathbf{m}}^{(k)} \frac{\rho_0}{\rho} \sigma \hat{\mathbf{s}}^{(k)}, \quad \dot{\tau}^{(k)} = \hat{\mathbf{m}}^{(k)} \left[\hat{\hat{\sigma}} + \sigma(I : \hat{\mathbf{D}}) + \sigma \hat{\mathbf{D}} - \hat{\mathbf{D}}\sigma \right] \hat{\mathbf{s}}^{(k)},$$

where ρ_0 and ρ are the mass density in the reference and current states, respectively. $\tau^{(k)}$ is the resolved shear stress onto the k -th slip system.

To find $\dot{\gamma}^{(k)}$ we used a rate-dependent relation for single crystals as proposed by Hutchinson [1976]:

$$\dot{\gamma}^{(k)} = \dot{\gamma}_0 \operatorname{sgn}[\tau^{(k)}] \left| \frac{\tau^{(k)}}{g^{(k)}} \right|^m,$$

where $\dot{\gamma}_0$ is the reference strain rate, $\tau^{(k)}$ is the applied resolved shear stress, m is the rate sensitivity exponent, and $g^{(k)}$ is related to the critical resolved shear stress of the k -th slip system.

The evolution of strength is related to the strain rate, $\dot{\gamma}$, and the slip hardening moduli h_{kl} by

$$\dot{g}^{(k)} = \sum_{l=1}^n h_{kl} \dot{\gamma}^{(l)}.$$

The hardening moduli are found in different forms depending on the model used [Kysar 2001]. In the Bassani–Wu hardening model, h_{kl} takes the form

$$h_{kk} = \left\{ (h_0 - h_\infty) \cosh^{-2} \left[\left| \frac{(h_0 - h_\infty) \gamma^{(k)}}{\tau_\infty - \tau_0} \right| + h_\infty \right] + h_\infty \right\} G(\gamma^{(l)}),$$

$$h_{kl} = q h_{kk}, \quad (k \neq l)$$

where h_0 is the initial value of hardening modulus, and h_∞ is the saturated value of hardening modulus. τ_0 is the initial value of $g^{(k)}$. τ_∞ is the stress at which hardening moduli reach h_∞ . G is a function related to cross-hardening that occurs between slip systems.

In order to formulate the finite element program, the increment of shear strain is formulated as

$$\Delta \gamma^{(k)} - (1 - \Theta) \Delta t \dot{\gamma}^{(k)} - \Theta \Delta t \dot{\gamma}^{(k)} f^{(k)} \frac{\tau_t^{(k)} + \Delta \tau_t^{(k)}}{g_t^{(k)} + \Delta g^{(k)}} = 0,$$

where Θ is the interpolation parameter which takes a value between 0 and 1, $f^{(k)}$ is a dimensionless function which reveals the dependence of strain rate on the stress, and $\Delta \tau^{(k)}$ and $\Delta g^{(k)}$ are the increments of resolved shear stress and current strength in the k -th slip system within the time increment Δt , respectively.

The increments of resolved shear stress, $\Delta \tau^{(k)}$, depend on the strain increments $\Delta \epsilon_{ij}$ and the stress as

$$\Delta \tau^{(k)} = \left[\tilde{E}_{ijab} \mu_{ab}^{(k)} + \omega_{ia}^{(k)} \sigma_{ja} + \omega_{ja}^{(k)} \sigma_{ia} \right] \left[\Delta \epsilon_{ij} - \sum_{k=1}^n \mu_{ij}^{(k)} \Delta \gamma^{(k)} \right],$$

where \tilde{E}_{ijab} are the elastic moduli. $\mu_{ij}^{(k)}$ is the Schmid factor, and $\omega_{ij}^{(k)}$ is a tensor related to the spin tensor Ω and $\hat{\Omega}$, which are

$$\mu_{ij}^{(k)} = \frac{1}{2} [\hat{s}_i^{(k)} \hat{m}_j^{(k)} + \hat{s}_j^{(k)} \hat{m}_i^{(k)}], \quad \omega_{ij}^{(k)} = \frac{1}{2} [\hat{s}_i^{(k)} \hat{m}_j^{(k)} - \hat{s}_j^{(k)} \hat{m}_i^{(k)}], \quad \Omega_{ij}^{(k)} - \hat{\Omega}_{ij}^{(k)} = \sum_{k=1}^n \omega_{ij}^{(k)} \dot{\gamma}^{(k)}.$$

Therefore, for given strain increments, the increments of shear strain can be determined. Then, the stress increments, $\Delta \sigma_{ij}$, can also be solved by

$$\Delta \sigma_{ij} = \tilde{E}_{ijab} \Delta \epsilon_{ab} - \sigma_{ij} \Delta \epsilon_{aa} - \sum_{k=1}^n \left[\tilde{E}_{ijab} \mu_{ab}^{(k)} + \omega_{ia}^{(k)} \sigma_{ja} + \omega_{ja}^{(k)} \sigma_{ia} \right] \Delta \gamma^{(k)}.$$

In addition, the explicit forms of the increments of lattice rotation are found to be [Asaro 1983]

$$\Delta \hat{s}_i^{(k)} = \left\{ \Delta \epsilon_{ij} + \Omega_{ij} \Delta t - \sum_{k=1}^n [\mu_{ij}^{(k)} + \omega_{ij}^{(k)}] \Delta \gamma^{(k)} \right\} \hat{s}_j^{(k)},$$

$$\Delta \hat{m}_i^{(k)} = - \left\{ \Delta \epsilon_{ji} + \Omega_{ji} \Delta t - \sum_{k=1}^n [\mu_{ji}^{(k)} + \omega_{ji}^{(k)}] \Delta \gamma^{(k)} \right\} \hat{m}_j^{(k)}.$$

The convergence of the finite element simulations is assured by choosing a relatively small time incremental step size in the users' subroutines.

In this work, the numerical computation generates errors on the order of Δt^2 , where Δt is the step size used in simulation. The indentation contact, loading, and unloading were set under displacement control to achieve better convergence properties than in the case of under load control. The critical shear stress, τ , for the copper single crystals was assumed to be 61 MPa. This is based on the experimental results. We did compression tests (along the [001] direction) on three copper crystal samples with the dimensions $5 \times 5 \times 10$ mm to find the yield point. The average load at the yield point was used to calculate the shear strength by multiplying the Schmid factor related to this crystallographic orientation. The element used in the simulation is a plane strain reduced integration, hybrid element (CPE4RH). The mesh is schematically shown in Figure 1. The crystal in a quadrant and the 90° wedge indenter are put together in the drawing. Figure 1a is the global view of the indenter and the half single crystal with the mesh. Figure 1b shows the finer mesh close to the tip of the indenter. There are three mesh sizes. The first 12,880 elements in the region closed to the indenter tip have the mesh size $1.5 \times .5 \mu\text{m}$. The 16,100 elements away from the indenter tip have the mesh size of $3 \times 1.5 \mu\text{m}$. The rest of 19,320 elements far away from the indenter have varied mesh sizes. The mesh size changes from $1.5 \times 3 \mu\text{m}$ to $4 \times 3 \mu\text{m}$. It must be pointed out that some variables may be chosen dimensionless in the simulations. For example, the mesh and indentation depth could be set as dimensionless by normalizing these parameters by the indenter size. However, since the indenter is assumed as analytically rigid, the yield strength of the indenter in this case approaches

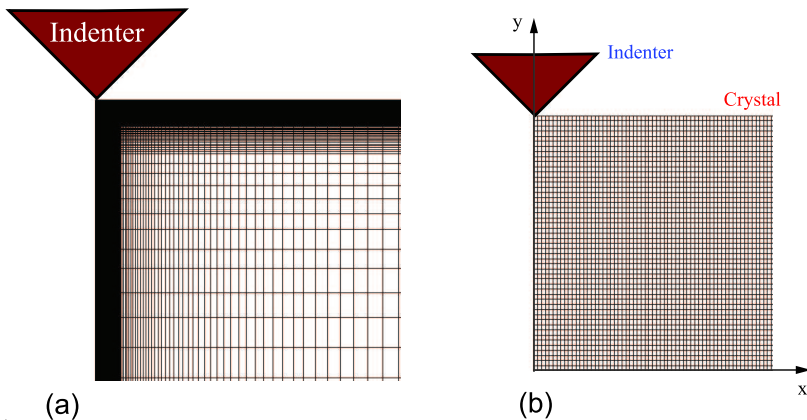


Figure 1. Mesh for the finite element simulation of wedge indentation: (a) global view of the mesh and the wedge indenter and (b) mesh close to the wedge indenter tip and the boundaries of the crystal, the dark region in (a).

infinity. This might cause convergence problems if we would normalize the yield strength of the crystal specimen by the yield strength of the indenter. The shear strength of copper crystal, 61 MPa, is used in the simulation. This unit is equivalent to $\mu\text{N}/\text{mm}^2$. Consequently, the mesh size of the crystal and the indenter penetration depth are also carrying the unit of μm . Numerical tests of mesh convergence were carried out to ensure that the presented results were independent of further mesh refinement. Excessive mesh distortion was not observed during simulation and thus remeshing was not used.

The wedge indenter is defined as analytically rigid and the contact between the indenter and the crystal is frictionless. In the finite element analysis, lattice rotation and stresses were solved incrementally by ABAQUS. The constitutive properties are chosen as elastic-ideally plastic because the load increases almost linearly with the indentation penetration depth as will be shown in Figure 7b. From this behavior and taking into account that the indentation contact area is increasing linearly, we concluded that the nominal strength of the copper single keeps almost the same. Therefore the material is very close to an elastic-ideally plastic state under the indentation conditions. The power-law rate-dependent relationship proposed by Hutchinson [1976] and delineated by Connolly and McHugh [1999], Peirce et al. [1983], and Savage et al. [2004], was applied in the simulation. Since elastic-ideally plastic properties are used in this simulation, the function related to critical resolved shear stress of the k -th slip system is taken as a constant. The reference strain rate was 10^{-3} s^{-1} , and the rate sensitivity exponent was 50.0. The stress at which hardening moduli are saturated was 109.5 MPa. The ratio of latent over self hardening moduli of various sets of slip systems was 1. During the simulation, the minimum iteration step used was 1×10^{-9} and the maximum step was 5×10^{-5} and 20000 increments were performed in the loading and unloading simulations. The computation was implemented on a computer with CPU frequency of 2.88 GHz and the CPU time of 43200 s.

3. Experimental methods

Wedge indentation tests were performed on copper single crystal specimens. Three specimens were used in the tests. All the results were based on the average of the data obtained from the three specimens. The wedge indenter used in this study had an apex angle of 90° . The indenter was made of tungsten carbide bonded by a ferrous alloy. The indentation direction is along the $[00\bar{1}]$ crystallographic orientation of the copper single crystals. During indentation tests, the load and displacement data were recorded. After the indentation, the midsection of the single crystal specimens with plane strain deformation conditions was exposed through cutting. This exposed plane corresponds to the crystallographic plane of (110). After being cut, the copper single crystal specimens were put into a compacted fixture and the indented surface was filled with a polymer to protect the indented surface from mechanical damage during subsequent processes.

The surfaces of the crystals were mechanically polished following the procedures as follows. Sandpaper (grit 600) was used to grind the surface under minimum pressure along one direction until any deep scratches from the previous cutting process were invisible. Water was used as lubricant and coolant for preventing the polishing surface from becoming overheated. The purpose of this polishing procedure is to remove the possible deep deformation layer from the previous grinding processes. The grinding/polishing along one direction can prevent rounded corner formation along the edges of the polished surface. The polish direction was changed by 90° to the same grit 600 sand paper, with even less pressure applied

until the scratches from the previous polishing procedure were invisible. Water was applied continuously. The purpose of this polishing procedure is to remove the possible residual stress layer generated from previous polishing. The specimen was washed with tap water to prevent any coarse abrasive going into the next polishing procedure. The procedure was repeated using 1200 grit sandpaper. Fine polishing was performed using diamond compound with diameter of $6\ \mu\text{m}$. The specimens were then washed in soapy water. Having been polished mechanically, the copper single crystals were cleaned. The cleaned copper crystals were surface activated in a 10% HCl solution followed by rinsing in deionized water. After that, the surface of (110) of the single copper crystals were electrochemically polished in an 85% orthophosphoric acidic solution.

Scanning electron microscopic (SEM) examination and electron backscatter diffraction (EBSD) data acquisition were carried out on a scanning electron microscope. Figure 2a is an SEM image showing the indented single crystal. For EBSD measurement, a polycrystalline copper block was put on the right-hand side of the copper single crystal specimen for subtracting background signals, and a piece of silicon single crystal with the surface normal of [001] orientation was aligned on the left-hand side of the copper single crystal at the same level with the same tilt angle of 70° . The Si single crystal was used for detector orientation calibration and for projection parameter calibration. Figure 2b schematically shows the relative positions of the polycrystal, the single crystal Cu specimen, and the Si single crystal. The EBSD measurement was carried out on the middle section of the specimen at a tilt angle of 70° . Following the calibration, surface mapping was performed at an acceleration voltage of 20 kV. The EBSD mapping data were saved for subsequent analysis.

4. Results and discussion

In this section, both simulation and experimental results of wedge indentation into copper single crystals will be presented. The finite element simulation results, including the stress solutions, shear strain solutions, and lattice rotation map, will be given first. Then, the experimental data will be given. The finite element solutions will be compared with the experimental results.

4.1. Finite element solutions. The finite element simulation results will be presented in the following three parts. First, numerical solutions for stresses will be shown. Second, the numerical solutions to

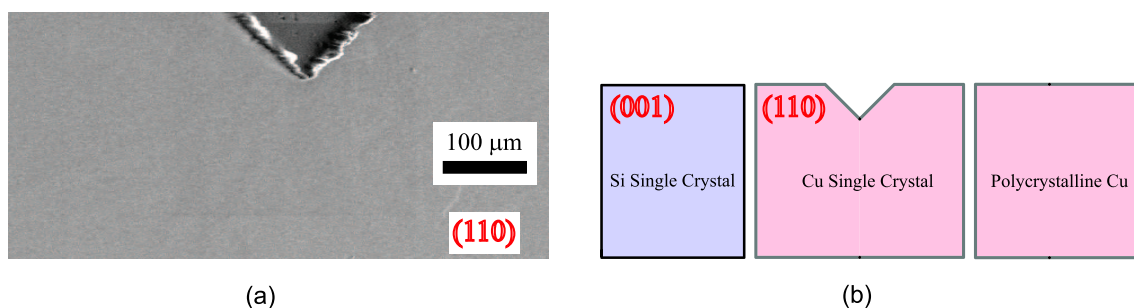


Figure 2. SEM image of the indented specimen and configuration for EBSD measurement: (a) SEM image of the indented specimen and (b) specimen alignment for the EBSD data acquisition.

shear strains associated with the slip of different slip systems will be shown. Then, the solution for the in-plane crystal lattice rotation will be given.

The finite element solutions for the normalized in-plane stress components of σ_{11}/τ , σ_{12}/τ , and σ_{22}/τ for the wedge indented copper crystal are shown in Figure 3a–c. From the results shown in both Figure 3a and c, we can see that underneath the indenter tip, the region within the copper single crystal was severely compressed because both σ_{11}/τ and σ_{22}/τ are negative. Farther away from the indentation tip, the region shows position value of σ_{11}/τ and σ_{22}/τ . The shear stress σ_{12}/τ , as shown in Figure 3b, reveals a highly heterogenous and anisotropic behavior related to the indentation. The rapid change in shear stress is found in the areas both underneath the indenter tip and far below the indenter/single crystal contact region.

In order to define the shear strain on each activated slip system, a schematic drawing to show the physical orientations of all the most favorable slip systems associated with the special crystallographic orientation of the copper crystal under indentation is given in Figure 4. The numerical results of plastic shear strain on these slip systems, $\gamma^{(n)}$, were obtained. n is an integer with the values of 1, 2, and 3. The results of shear strains for different slip systems are output as solution dependent variables (SDVs).

Figure 5 shows the solutions for the plastic strain in the copper single crystal associated with the wedge indentation. Figure 5a–c illustrate the shear strain from each individual slip system as sketched in Figure 4. The plastic strain from all the three slip systems is given in Figure 5d. It is noted that $\gamma^{(1)}$ refers to the shear strain due to the dislocation motion of slip system (1), $\gamma^{(2)}$ stands for the shear strain due to the dislocation motion of slip system (2), $\gamma^{(3)}$ is the shear strain due to the dislocation motion of slip

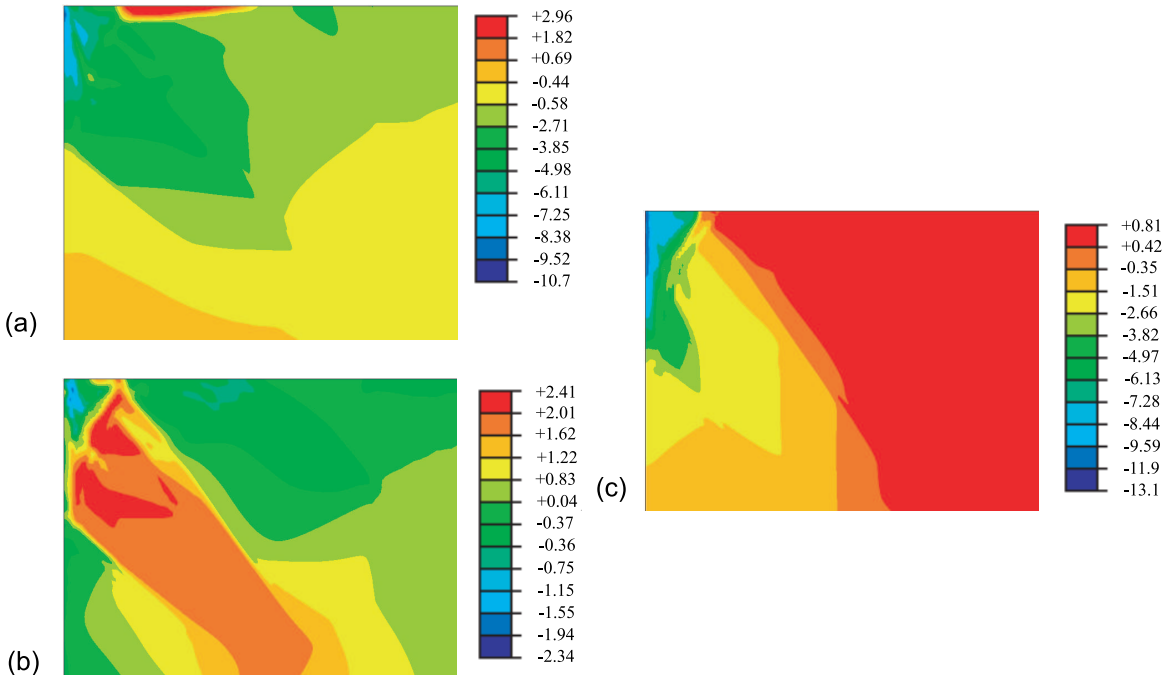


Figure 3. Numerical solutions to the stress components: (a) σ_{11}/τ , (b) σ_{12}/τ , and (c) σ_{22}/τ .

system (3), and γ refers to the total shear strain due to the dislocation motion of all the three slip systems. It can be seen from Figure 5a that $\gamma^{(1)}$, the shear strain due to the dislocation motion of slip system (1), takes significantly higher values on the right side of the indented region. However, the $\gamma^{(2)}$ and $\gamma^{(3)}$ as shown in Figure 5b and c, respectively, are considerably low in this region, where $\gamma^{(2)}$ represents the shear strain from slip system (2) and $\gamma^{(3)}$ stands for the shear strain from slip system (3). Thus, the numerical simulation predicts that the primary slip system in this region is slip system (1). As will be shown in Section 4.2, the EBSD experimental data about the in-plane lattice rotation define different regions where the dislocation motion of each of the three slip systems dominates the plastic deformation in a specific slip sector. For example, in the right hand side region adjacent to the extension line of the indenter tip, the dislocation motion is mainly due to the activation of slip system (1). Therefore, it is shown that the numerical predictions compare well with the experimental results. The results shown in Figure 5a–c also provide the information about the size of the plastic zone. It is found that the plastic zone is not just limited to the region underneath the indenter tip. Rather, it propagates into the crystal at least twice as far as the indentation penetration depth.

Figure 6 is the in-plane crystal lattice rotation map obtained from the finite element simulation. The unit of the lattice rotation angle is degree, which is calculated from the specific SDVs in the ABAQUS finite element simulation program. Comparison with the experimental results shown in Section 4.2.2 will be made later. The unit of lattice rotation as shown in Figure 6 is degree. The main features of the in-plane rotation from the simulation are as follows: In the lower left part of Figure 6, a region with negative lattice rotation can be found. This is due to the active dislocation movement of slip system (1). The existence of such a negative lattice rotation region can be validated by the experimental results as will be illustrated in Section 4.2.

The righthand side region adjacent to the lattice negative rotation region is a zero rotation region, which corresponds to the active dislocation movement of slip system (2). In the rightmost part of Figure 6, there is a positive lattice rotation region, which is caused by the active dislocation movement of slip system (3). All these features are comparable to the experimental results as will be shown in Section 4.2.

4.2. Experimental results.

4.2.1. Load displacement relation. Figure 7a is the loading profile recorded by the data acquisition unit connected to the materials testing system. As can be seen from Figure 7a, the loading and unloading processes were performed by applying a triangle waveform. It is noted that the loading level is normalized by the width of the single crystal such that the unit of the loading is N/mm. The load-displacement relation corresponding to the loading and unloading behavior of the copper single crystal under the wedge indentation is shown in Figure 7b from which two stages of deformation can be seen. The first stage is the elastic-plastic deformation associated with loading. This stage lasts until the load reaches the peak point A as shown in Figure 7b. The total deformation (penetration depth) is about 0.4 mm. The second stage shows elastic unloading and a large hysteresis area under the load displacement curve, as shown in Figure 7b, reveals that the plastic deformation is the dominant mechanism during the indentation process. The second stage finishes once the load drops to point B in Figure 7b. It can be seen that the elastic part of deformation is about 0.03 mm, which can be calculated from the difference in displacement between points A and B on the plot. During the loading process, with the increasing of the loading time, the indentation penetration depth increases almost linearly as shown in Figure 7c. This reveals that the

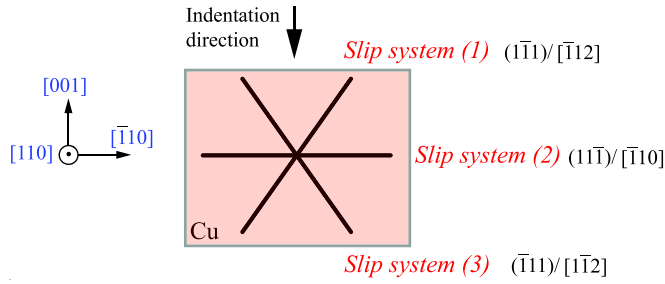


Figure 4. Configuration of the three slip systems.

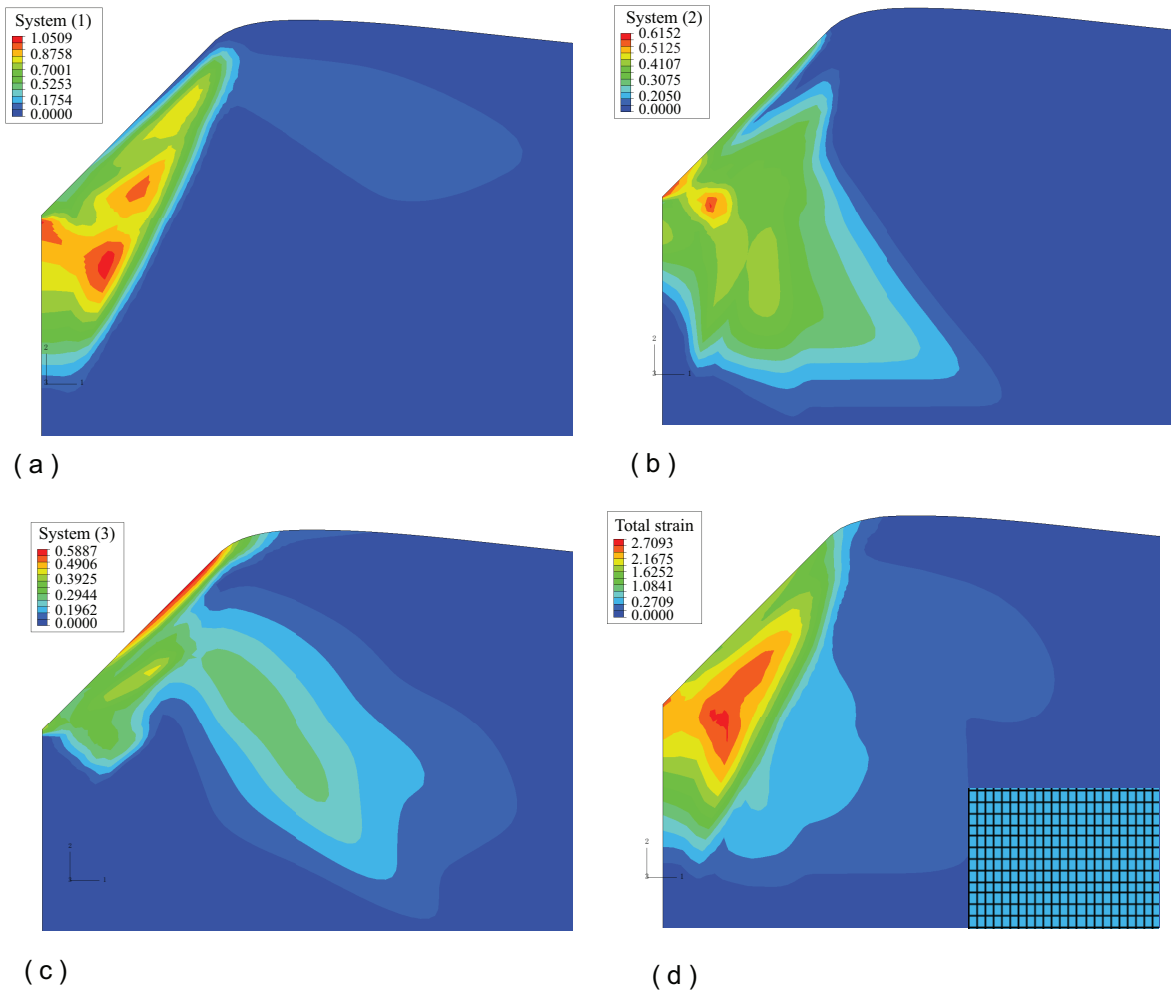


Figure 5. Numerical solutions to the shear strains under wedge indentation (deformed state): (a) shear strain of slip system (1), $\gamma^{(1)}$, (b) shear strain of slip system (2), $\gamma^{(2)}$, (c) shear strain of slip system (3), $\gamma^{(3)}$, and (d) the total shear strain, γ . The lower right corner shows the mesh with dimensions $1.5 \times 1.5 \mu\text{m}$.

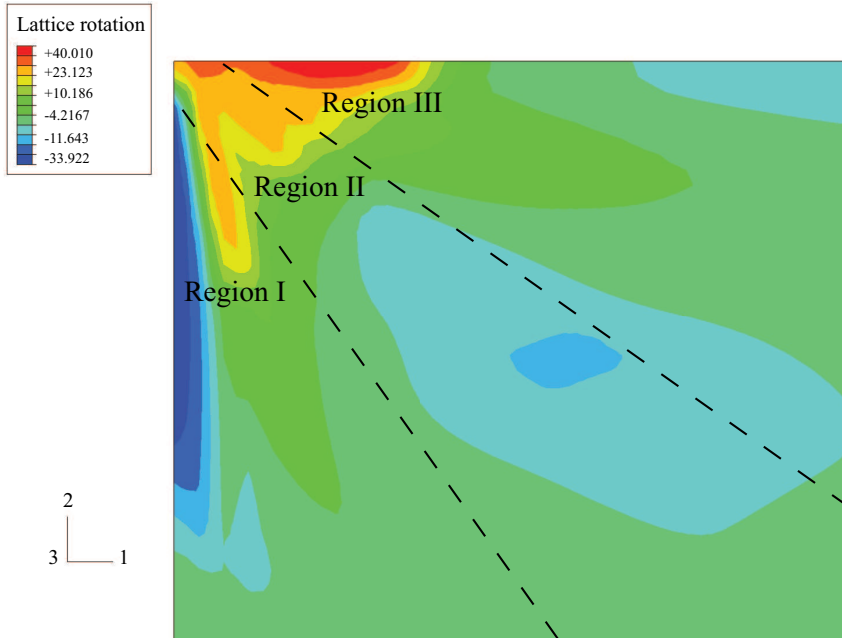


Figure 6. Numerical solution to the in-plane crystal lattice rotation showing three distinct regions. The unit of rotation is degree.

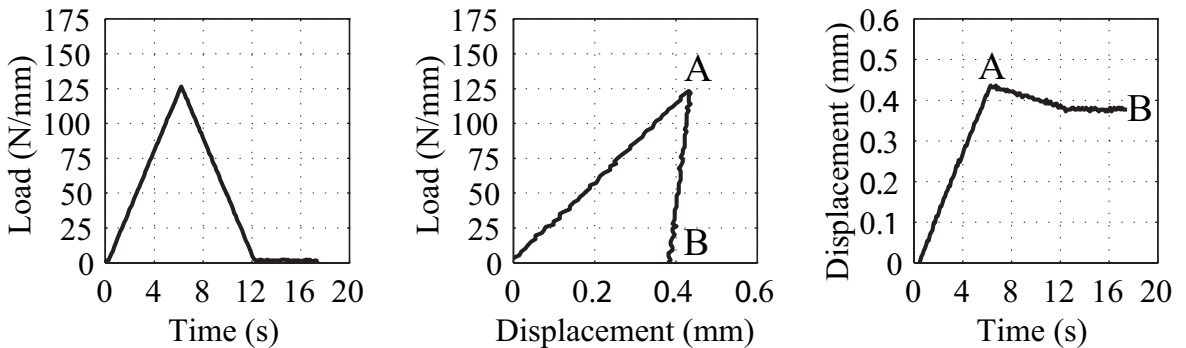


Figure 7. Load-displacement response during wedge indentation. Left: the triangle waveform showing force control mode. Middle: load-displacement relation. Right: displacement versus time.

averaged behavior of the copper single crystal is close to ideally plastic in the first deformation stage since the load carrying area increases linearly with the increasing of indenter penetration depth.

4.2.2. Lattice rotation map of indented copper single crystal. A schematic of the indented region and the EBSD mapped area for data analysis are illustrated in Figure 8a. In Figure 8b, a contour plot showing the in-plane lattice rotation associated with the wedge indentation is given. It is found from Figure 8b that different regions with distinct lattice rotation features exist underneath the indented region. The change of crystal lattice rotation is in the range from about 20° to -20° . The highest value is about 35° , and

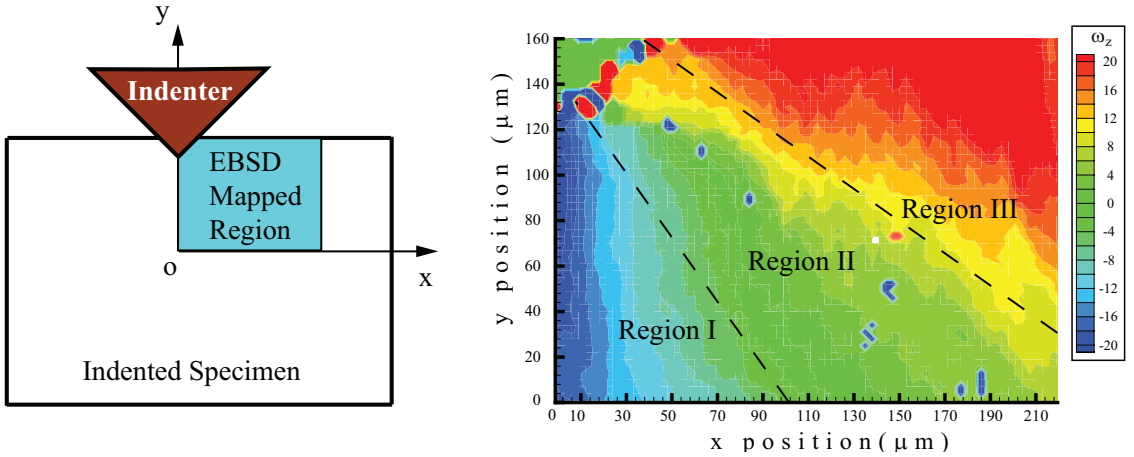


Figure 8. EBSD measured in-plane lattice rotation of a copper single crystal under wedge indentation. Left: sketch of the mapped region. Right: lattice rotation contour plot. The unit of in-plane rotation angle, ω_z , is the degree.

the lowest value is -37° . Such scattering values are from the local damage of the specimen. Chemical adsorption in some areas also results in scattering of the measuring results.

It is interesting to examine the evolution of plastic deformation features through the thickness of the indented specimen. Generally, the lattice rotation data taken from a section away from the midplane will show out-of-plane rotation because there is plastic flow along the through thickness direction, that is, the axis of indentation. To demonstrate this, we performed optical examination on the side surface of the indented specimen. Figure 9 is the optical image of the side surface. A sketch of the indenter is also included in the picture to show the relative size of the indented region. Plastic deformation in the forms of shear lines and rings can be observed. Since this surface was not polished, the three slip zones are clearly shown at different levels. The extrusion stages due to the out-of-plane lattice rotation is especially found in Region II of Figure 8b. It is predicted that the magnitude of the out-of-plane lattice rotation is related to the thickness of the specimens. Obviously, systematic experimental studies are needed for generating a series of lattice rotation maps from the locations along the indenter axis, which is one of the important aspects in our future work.

4.3. Comparison of numerical solutions and experimental results. As compared with the results shown in Figure 6 (numerical solutions), it can be seen that the in-plane crystal lattice rotation map of Figure 8b can also be divided into three distinct regions in a quadrant. The one with negative lattice rotation is due to the active dislocation motion of slip system (1), as shown in Figure 4. The zero lattice rotation region is corresponding to the active dislocation movement of slip system (2). The positive lattice rotation region is due to the active dislocation movement of slip system (3) as also shown in Figure 4. Thus, the salient features of the in-plane lattice rotation as determined by EBSD experiments are comparable to the results as predicted by the finite element simulations shown in Figure 6. It is noted that there is some difference in lattice rotation quantity between the results shown in Figure 6 and Figure 8b. In the qualitative sense,

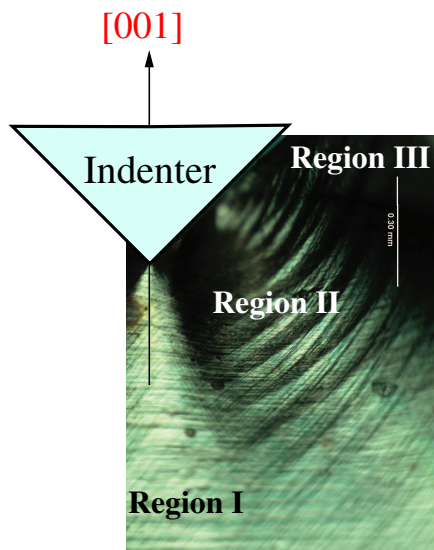


Figure 9. Optical micrograph showing plastic deformation in the form of extrusion stages due to the out-of-plane lattice rotation.

it is still reasonable to say that the numerical solutions agree with the experimental results. Therefore, the simulations can be validated by the indentation experiments.

The measured texture component map is also compared with the prediction from the plasticity theory and the finite element simulation results. In **Figure 10**, the $[110]$ texture component along the x -axis is shown. The dark color stands for 100% of materials being oriented along the $\langle 110 \rangle$ crystallographic direction. The brighter and yellow colored areas are those regions with misorientation. The orientation of the materials in these regions shifts away from the $[110]$ direction. The maximum shift was found to be 35° (this is not marked in **Figure 10** because texture component maps generated by the software have

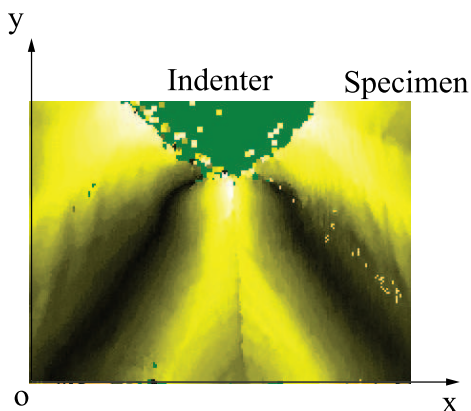


Figure 10. Texture component of indented copper single crystal ($[110]$ texture along x -direction) showing the plastic spin predicted by the single crystal plasticity theory and the finite element simulation.

no contour legends). Comparing the features shown in [Figure 10](#) with those obtained through numerical simulations (see [Figure 6](#)), it is found that a zero-lattice rotation region (Region II) located in the the same area. It must be pointed out that single crystal plasticity theory also predicts the existence of a zero-lattice rotation region associated with the dislocation activities associated with slip system (2), the complex slip system. Regions I and III are separated by this zero-lattice rotation region, as shown in [Figure 6](#), the numerical results.

The numerical simulations as described in this study have a relatively low cost as compared with the experiments. Despite its simplicity, some of the most essential features of wedge indentation, including lattice rotation, can be well captured by the model. We note that in most indentation experiments, especially the sharp indentation tests, a nominally constant plastic strain impression is generated which does not allow the behavior of tested materials to be measured directly. For that matter, construction of equivalent stress fields, strain, and lattice rotation responses of materials with finite element simulations is necessary and could reveal important indentation mechanisms. The importance of numerical simulations becomes more evident through their qualitative agreement with experiment. Further improvements on the simulation method to obtain more accurate results and better quantitative agreements with experiment remain our future work. One of the possible directions is to modify the single crystal plasticity constitutive model. We also expect to simulate different crystals and use different shapes of indenter tip.

It must be pointed out that the preliminary work presented here is based on the special orientation of the crystal, meaning the [001] crystallographic orientation. The results obtained here are useful for dealing with the polycrystal cases, since an arbitrarily selected orientation of a crystal (designated as $[hkl]$) can always be mapped into other orientations by a series of rotation transformations. Thus, a general grain can be treated through transformations such that its orientation matches the [001] case. Accordingly, the modification on the materials subroutine for simulations is needed, and the output variables such as stresses and strains can be obtained by tensorial transformations. For multiple grains, a statistic model may be necessary to accommodate the interactions of different grains and the effect of the grain boundaries. Such a complex case remains to be the topic for future study.

5. Conclusions

Based on the experimental studies and finite element simulations of wedge indentation into face-centered cubic (FCC) copper single crystals, the following conclusions are made:

- (1) Finite element simulations of the wedge indentation into the copper crystal have provided stress, shear strain, and in-plane lattice rotation solutions. The results reveal highly heterogeneous plastic deformation behavior of the single crystals under wedge indentation with deep penetration depth.
- (2) The load-displacement relation of the single crystal under wedge indentation shows a plastic deformation dominated behavior. The load increases almost linearly with the indentation penetration depth. Taking into account that the indentation contact area also increases linearly, the elastic ideally plastic behavior of the crystal can be deduced.
- (3) The crystal lattice rotation measurements show three distinct regions in a quadrant, revealing three slip zones. These results show the existence of different single slip sectors in the region within the single crystal underneath the indenter tip as predicted by the single crystal plasticity theory and the finite element simulations.

- (4) The numerical solutions also predict the occurring of dislocation movement along different effective slip systems activated by the wedge indentation. Therefore, the finite element solutions to both the plastic shear strain and lattice rotation are qualitatively validated by the electron backscatter diffraction (EBSD) experimental results. The plastic spin is also verified by the texture component measurement.

Acknowledgments. This work was supported in part by University of Toledo Research Awards and Fellowship (URAF) Programs. We appreciate the reviewers for their valuable suggestions on modification of the paper.

References

- [Asaro 1983] R. J. Asaro, “[Micromechanics of crystals and polycrystals](#)”, *Adv. Appl. Mech.* **23** (1983), 1–115.
- [Beghini et al. 2006] M. Beghini, L. Bertini, and V. Fontanari, “[Evaluation of the stress-strain curve of metallic materials by spherical indentation](#)”, *Int. J. Solids Struct.* **43**:7–8 (2006), 2441–2459.
- [Bhattacharya and Nix 1991] A. K. Bhattacharya and W. D. Nix, “[Finite element analysis of cone indentation](#)”, *Int. J. Solids Struct.* **27**:8 (1991), 1047–1058.
- [Bigot et al. 2005] R. Bigot, V. Favier, and C. Rouff, “[Characterisation of semi-solid material mechanical behaviour by indentation test](#)”, *J. Mater. Process. Technol.* **160**:1 (2005), 43–53.
- [Bolshakov and Pharr 1998] A. Bolshakov and G. M. Pharr, “[Influences of pile-up on the measurement of mechanical properties by load and depth sensing indentation techniques](#)”, *J. Mater. Res.* **13**:4 (1998), 1049–1058.
- [Bouvier and Needleman 2006] S. Bouvier and A. Needleman, “[Effect of the number and orientation of active slip systems on plane strain single crystal indentation](#)”, *Model. Simul. Mater. Sci. Eng.* **14** (2006), 1105–1125.
- [Connolly and McHugh 1999] P. Connolly and P. E. McHugh, “[Fracture modelling of WC-Co hardmetals using crystal plasticity theory and the Gurson model](#)”, *Fatigue Fract. Eng. Mater. Struct.* **22**:1 (1999), 77–86.
- [Fivel et al. 1998] M. C. Fivel, C. F. Robertson, G. R. Canova, and L. Boulanger, “[Three-dimensional modeling of indentation-induced plastic zone at a mesoscale](#)”, *Acta Mater.* **46**:17 (1998), 6183–6194.
- [Follansbee and Sinclair 1984] P. S. Follansbee and G. B. Sinclair, “[Quasi-static normal indentation of an elasto-plastic half-space by a rigid sphere, I: Analysis](#)”, *Int. J. Solids Struct.* **20**:1 (1984), 81–89.
- [Gan et al. 2007] Y. X. Gan, Y. Saito, and X. Chen, “[Cylindrical indentation induced deformation in face-centered cubic metal single crystals](#)”, *J. Mech. Mater. Struct.* **2**:3 (2007), 557–572.
- [Gerberich et al. 2002] W. W. Gerberich, N. I. Tymiak, J. C. Grunlan, M. F. Horstemeyer, and M. I. Baskes, “[Interpretations of indentation size effects](#)”, *J. Appl. Mech. (ASME)* **69**:4 (2002), 433–442.
- [Giannakopoulos et al. 1994] A. E. Giannakopoulos, P.-L. Larson, and R. Vestergaard, “[Analysis of Vickers indentation](#)”, *Int. J. Solids Struct.* **31**:19 (1994), 2679–2708.
- [Habbab et al. 2006] H. Habbab, B. G. Mellor, and S. Syngellakis, “[Post-yield characterisation of metals with significant pile-up through spherical indentations](#)”, *Acta Mater.* **54**:7 (2006), 1965–1973.
- [Havner and Yu 2005] K. S. Havner and P. Yu, “[Kinematic, stress, and hardening analysis in finite double slip](#)”, *Int. J. Plast.* **21**:1 (2005), 83–99.
- [Hill et al. 1989] R. Hill, B. Storakers, and A. B. Zdunek, “[A theoretical study of the Brinell hardness test](#)”, *Proc. R. Soc. Lond. A* **423**:1865 (1989), 301–330.
- [Horstemeyer et al. 2001] M. F. Horstemeyer, M. I. Baskes, and S. J. Plimpton, “[Computational nanoscale plasticity simulations using embedded atom potentials](#)”, *Theor. Appl. Fract. Mech.* **37**:1–3 (2001), 49–98.
- [Hutchinson 1976] J. W. Hutchinson, “[Bounds and self-consistent estimates for creep of polycrystalline materials](#)”, *Proc. R. Soc. Lond. A* **348**:1652 (1976), 101–127.
- [Iost and Bigot 1996] A. Iost and R. Bigot, “[Indentation size effect: reality or artefact?](#)”, *J. Mater. Sci.* **31**:13 (1996), 3573–3577.

- [Kysar 2001] J. W. Kysar, “Continuum simulations of directional dependence of crack growth along a copper/sapphire bicrystal interface, I: Experiments and crystal plasticity background”, *J. Mech. Phys. Solids* **49**:5 (2001), 1099–1128.
- [Kysar et al. 2007] J. W. Kysar, Y. X. Gan, T. L. Morse, X. Chen, and M. E. Jones, “High strain gradient plasticity associated with wedge indentation into face-centered cubic single crystals: geometrically necessary dislocation densities”, *J. Mech. Phys. Solids* **55**:7 (2007), 1554–1573.
- [Laursen and Simo 1992] T. A. Laursen and J. C. Simo, “A study of the mechanics of microindentation using finite elements”, *J. Mater. Res.* **7**:3 (1992), 618–626.
- [Lilleodden et al. 2003] E. T. Lilleodden, J. A. Zimmerman, S. M. Foiles, and W. D. Nix, “Atomistic simulations of elastic deformation and dislocation nucleation during nanoindentation”, *J. Mech. Phys. Solids* **51**:5 (2003), 901–920.
- [Marx and Balke 1997] V. Marx and H. Balke, “A critical investigation of the unloading behavior of sharp indentation”, *Acta Mater.* **45**:9 (1997), 3791–3800.
- [Miller et al. 2004] R. E. Miller, L. E. Shilkrot, and W. A. Curtin, “A coupled atomistics and discrete dislocation plasticity simulation of nanoindentation into single crystal thin films”, *Acta Mater.* **52**:2 (2004), 271–284.
- [Naghdbadi et al. 2005] R. Naghdabadi, M. Yeganeh, and A. R. Saidi, “Application of corotational rates of the logarithmic strain in constitutive modeling of hardening materials at finite deformations”, *Int. J. Plast.* **21**:8 (2005), 1546–1567.
- [Peirce et al. 1983] D. Peirce, R. J. Asaro, and A. Needleman, “Material rate dependence and localized deformation in crystalline solids”, *Acta Metall.* **31**:12 (1983), 1951–1976.
- [Pelletier 2006] H. Pelletier, “Predictive model to estimate the stress-strain curves of bulk metals using nanoindentation”, *Tribol. Int.* **39**:7 (2006), 593–606.
- [Potirniche et al. 2006] G. P. Potirniche, J. L. Hearndon, M. F. Horstemeyer, and X. W. Ling, “Lattice orientation effects on void growth and coalescence in fcc single crystals”, *Int. J. Plast.* **22**:5 (2006), 921–942.
- [Premachandran and Horii 1994] R. Premachandran and H. Horii, “A micromechanics-based constitutive model of polycrystalline ice and FEM analysis for prediction of ice forces”, *Cold Regions Sci. Tech.* **23**:1 (1994), 19–39.
- [Qu et al. 2006] S. Qu, Y. Huang, G. M. Pharr, and K. C. Hwang, “The indentation size effect in the spherical indentation of iridium: a study via the conventional theory of mechanism-based strain gradient plasticity”, *Int. J. Plast.* **22**:7 (2006), 1265–1286.
- [Rashid et al. 1992] M. M. Rashid, G. T. Gray, III, and S. Nemat-Nasser, “Heterogeneous deformations in copper single crystals at high and low strain rates”, *Philos. Mag. A* **65**:3 (1992), 707–735.
- [Savage et al. 2004] P. Savage, B. P. O. Donnell, P. E. McHugh, B. P. Murphy, and D. F. Quinn, “Coronary stent strut size dependent stress-strain response investigated using micromechanical finite element models”, *Ann. Biomed. Eng.* **32**:2 (2004), 202–211.
- [Shu and Barlow 2000] J. Y. Shu and C. Y. Barlow, “Strain gradient effects on microscopic strain field in a metal matrix composite”, *Int. J. Plast.* **16**:5 (2000), 563–591.
- [Sinclair et al. 1985] G. B. Sinclair, P. S. Follansbee, and K. L. Johnson, “Quasi-static normal indentation of an elasto-plastic half-space by a rigid sphere, II: Results”, *Int. J. Solids Struct.* **21**:8 (1985), 865–888.
- [Tadmor et al. 1996] E. B. Tadmor, M. Ortiz, and R. Phillips, “Quasicontinuum analysis of defects in solids”, *Philos. Mag. A* **73**:6 (1996), 1529–1563.
- [Turkmen et al. 2004] H. S. Turkmen, M. P. Miller, P. R. Dawson, and J. C. Moosbrugger, “A slip-based model for strength evolution during cyclic loading”, *J. Eng. Mater. Technol. (ASME)* **126**:4 (2004), 329–338.
- [Vlassak and Nix 1994] J. J. Vlassak and W. D. Nix, “Measuring the elastic properties of anisotropic materials by means of indentation experiments”, *J. Mech. Phys. Solids* **42**:8 (1994), 1223–1245.
- [Wallin and Ristinmaa 2005] M. Wallin and M. Ristinmaa, “Deformation gradient based kinematic hardening model”, *Int. J. Plast.* **21**:10 (2005), 2025–2050.
- [Wang et al. 2004] Y. Wang, D. Raabe, C. Klüber, and F. Roters, “Orientation dependence of nanoindentation pile-up patterns and of nanoindentation microtextures in copper single crystals”, *Acta Mater.* **52**:8 (2004), 2229–2238.
- [Xia et al. 2004] Z. H. Xia, W. A. Curtin, and B. W. Sheldon, “A new method to evaluate the fracture toughness of thin films”, *Acta Mater.* **52**:12 (2004), 3507–3517.

- [Xu and Rowcliffe 2002] Z.-H. Xu and D. Rowcliffe, “Method to determine the plastic properties of bulk materials by nanoindentation”, *Philos. Mag. A* **82**:10 (2002), 1893–1901.
- [Yoshino et al. 2001] M. Yoshino, T. Aoki, N. Chandrasekaran, T. Shirakashi, and R. Komanduri, “Finite element simulation of plane strain plastic-elastic indentation on single-crystal silicon”, *Int. J. Mech. Sci.* **43**:2 (2001), 313–333.
- [Yoshioka 1991] M. Yoshioka, “Numerical analysis of slip behavior in the indented MgO single crystal”, *Int. J. Jpn. Soc. Precis. Eng.* **25** (1991), 175–180.
- [Zaafarani et al. 2008] N. Zaafarani, D. Raabe, F. Roters, and S. Zaeferrer, “On the origin of deformation-induced rotation patterns below nanoindenters”, *Acta Mater.* **56**:1 (2008), 31–42.
- [Zhao et al. 2006] M. Zhao, X. Chen, N. Ogasawara, A. C. Razvan, N. Chiba, D. Lee, and Y. X. Gan, “New sharp indentation method of measuring the elastic-plastic properties of compliant and soft materials using the substrate effect”, *J. Mater. Res.* **21**:12 (2006), 3134–3151.
- [Zhao et al. 2007] M. Zhao, X. Chen, Y. Xiang, J. J. Vlassak, D. Lee, N. Ogasawara, N. Chiba, and Y. X. Gan, “Measuring elastoplastic properties of thin films on an elastic substrate using sharp indentation”, *Acta Mater.* **55**:18 (2007), 6260–6274.
- [Zhu et al. 2004] T. Zhu, J. Li, K. J. Van Vliet, S. Ogata, S. Yip, and S. Suresh, “Predictive modeling of nanoindentation-induced homogeneous dislocation nucleation in copper”, *J. Mech. Phys. Solids* **52**:3 (2004), 691–724.
- [Zimmerman et al. 2001] J. A. Zimmerman, C. L. Kelchner, P. A. Klein, J. C. Hamilton, and S. M. Foiles, “Surface step effects on nanoindentation”, *Phys. Rev. Lett.* **87**:16 (2001), #165507.

Received 5 Feb 2008. Revised 8 May 2008. Accepted 10 Oct 2008.

YONG X. GAN: yong.gan@utoledo.edu

Department of Mechanical, Industrial and Manufacturing Engineering, University of Toledo, 2801 West Bancroft Street, Toledo, OH 43606, United States

XI CHEN: Department of Civil Engineering and Engineering Mechanics, Fu Foundation School of Engineering and Applied Science, Columbia University, 500 West 120th Street, New York, NY 10027, United States

MANHONG ZHAO: Department of Civil Engineering and Engineering Mechanics, Fu Foundation School of Engineering and Applied Science, Columbia University, 500 West 120th Street, New York, NY 10027, United States

PREFRACTURE ZONE MODELING FOR AN ELECTRICALLY IMPERMEABLE INTERFACE CRACK IN A PIEZOELECTRIC BIMATERIAL COMPOUND

VLADIMIR B. GOVORUKHA AND MARC KAMLAH

This work is concerned with the analytical characterization of the electromechanical nonlinear effects in the fields surrounding the tip of an interface crack located between two piezoelectric materials. It is assumed that a prefracture zone arises along a line segment in front of the crack tip. The prefracture zone is modeled by electrical displacement reaching a saturation limit and constant stress distribution. This reduces the problem to a linear interface crack analysis leading to a Hilbert problem, which is solved exactly. The prefracture zone length and the stress magnitude in this zone are found from algebraic and transcendental equations. The latter are derived from the requirement of stresses and electrical displacement to be finite at the end of prefracture zone towards the undamaged ligament. Numerical results for certain material combinations and remote loadings are presented and analyzed. In addition, energy release rate and crack opening displacements are introduced, which offers the possibility of formulating a fracture criterion based on the crack opening displacements.

1. Introduction

Piezoelectric materials have found wide technological applications as transducers, sensors and actuators due to their inherent electromechanically coupled behavior. However, piezoelectric materials are brittle and susceptible to fracture. Various defects, such as grain boundaries, flaws and pores, impurities and inclusions, etc, exist in piezoelectric materials. The defects cause geometric, electric and mechanical discontinuities and thus induce strong stress and electric field concentrations, which may induce crack initiation and crack growth, eventually causing fracture and failure. Structural reliability concerns of electromechanical devices call for a better understanding of the mechanisms of piezoelectric fracture.

Important results about fracture in piezoelectric solids based on linear electroelasticity have been derived by Parton [1976], Pak [1992], Sosa [1992], Suo et al. [1992], Dunn [1994], and many others. However, analysis based on linear electroelasticity cannot explain some discrepancies between theory and experiment [Park and Sun 1995]. Hence, various nonlinear models have been suggested. Narita and Shindo [2001] considered a mechanical yield strip model for a piezoelectric crack under a low stress level. In order to derive a fracture criterion suitable for piezoelectrics, Gao et al. [1997] generalized the essential ideas of Dugdale [1960] and proposed a strip saturation model of electrical yielding by assuming that the electrical polarization is saturated in a line segment in front of the crack tip. Based on general linear constitutive equations, the analysis of the strip saturation model was conducted and extended by Ru [1999], Wang [2000] and Li [2003]. McMeeking [2001] gave comprehensive and suggestive comments on the strip saturation model. Beom and Atluri [2003] proposed a nonlinear domain switching model for a ferroelectric material which has a circular zone of perfect saturation near the crack tip. A strip

Keywords: piezoelectric material, nonlinear fracture mechanics, interface crack, prefracture zone.

dielectric breakdown model was introduced by [Zhang and Gao \[2004\]](#) for an electrically impermeable crack of semi-infinite length. [Zhang \[2004\]](#) further discussed this model for a crack of finite length.

All of the works mentioned deal with nonlinear crack models for cracks in homogeneous piezoelectric materials. For interface cracks between piezoelectric bimetals, the situation is more complicated since the field equations are complex and fracture behavior of piezoelectric compounds is far from obvious. Most theoretical studies regarding interface cracks in piezoelectric compounds were performed within the framework of the classical interface crack model (Williams, 1959). This model usually leads to an oscillating singularity at the crack tip and to physically unrealistic overlapping of the crack faces. To eliminate this phenomenon, a contact zone model for a crack between two isotropic materials was suggested by [Comninou \[1977\]](#). It was developed further for interface cracks in piezoelectric bimetals by [Qin and Mai \[1999\]](#), [Herrmann and Loboda \[2000\]](#) and [Govorukha et al. \[2006\]](#). Another way of removing crack tip singularities and modeling fracture processes for interface cracks was introduced by [Needleman \[1990\]](#), [Tvergaard and Hutchinson \[1996\]](#) and [Tvergaard \[2001\]](#) by means of a cohesive zone model. An analysis of the plastic zone for an interface crack was performed by [Huang \[1992\]](#), [Wang and Shen \[1993\]](#) and [Pickthall et al. \[2002\]](#). Plastic strips or prefraction zones in front of interface crack tips were analyzed by [Kaminsky et al. \[1999\]](#) and [Bakirov and Gol'dshtein \[2004\]](#) for the case of isotropic bimetals, while [Loboda et al. \[2007\]](#) studied a permeable interface crack between two piezoelectric materials.

In this paper, we want to model the situation where two piezoelectric materials are bonded by a thin ductile interlayer. Since neither infinite strains nor infinite potential gradients can be sustained at the atomic level, both mechanical and electrical nonlinearity of the interlayer are taken into account. [Shen et al. \[2000\]](#) considered simultaneous mechanical and electrical yielding for a mode III interface crack. However, to the authors knowledge no modeling of electrical and mechanical yielding at the same time for an in-plane interface crack in a piezoelectric bimetal has been done until now. In this paper, such modeling is proposed and an interface crack with mechanical and electrical yield zones is examined.

2. General solution of the basic equations

The constitutive and equilibrium equations for a linear piezoelectric material in the absence of body forces and free charges can be represented in the form [\[Pak 1992\]](#)

$$\Pi_{iJ} = E_{iJKl} V_{K,l}, \quad \Pi_{iJ,i} = 0, \tag{1}$$

where

$$V_K = \begin{cases} u_k, & K = 1, 2, 3, \\ \varphi, & K = 4, \end{cases} \quad \Pi_{iJ} = \begin{cases} \sigma_{ij}, & i, J = 1, 2, 3, \\ D_i, & i = 1, 2, 3, J = 4, \end{cases} \quad E_{iJKl} = \begin{cases} c_{ijkl}, & J, K = 1, 2, 3, \\ e_{lij}, & J = 1, 2, 3, K = 4, \\ e_{ikl}, & K = 1, 2, 3, J = 4, \\ -\varepsilon_{il}, & J = K = 4. \end{cases} \tag{2}$$

Here, u_k , φ , σ_{ij} and D_i are the elastic displacements, electric potential, stresses and electric displacements, respectively, while c_{ijkl} , e_{ijk} and ε_{ij} are the elastic, piezoelectric and dielectric constants. Lowercase subscripts in (1)–(2) and afterwards range from 1 to 3, capital subscripts range from 1 to 4 and Einstein’s summation convention is used in (1).

For two-dimensional deformations, where the vector $\mathbf{V} = [u_1, u_2, u_3, \varphi]^T$ depends on x_1 and x_3 only (the superscript T denoting the transpose), a general solution of (1) can be obtained, following [Pak 1992], by writing

$$\mathbf{V} = \mathbf{a} f(z), \tag{3}$$

where f is an arbitrary function of $z = x_1 + px_3$, and $\mathbf{a} = [a_1, a_2, a_3, a_4]^T$ is an eigenvector and p an eigenvalue. They can be determined by inserting (3) into (1)₁, and then into (1)₂, which yields

$$[\mathbf{Q} + p(\mathbf{R} + \mathbf{R}^T) + p^2\mathbf{T}] \mathbf{a} = 0, \tag{4}$$

where \mathbf{Q} , \mathbf{R} and \mathbf{T} are 4×4 real matrices whose components are defined by $Q_{JK} = E_{1JK1}$, $R_{JK} = E_{1JK3}$, $T_{JK} = E_{3JK3}$.

Since Equation (4) has no real eigenvalues [Suo et al. 1992], we write an eigenvalue of (4) with positive imaginary parts as p_α and the associated eigenvectors of (4) as \mathbf{a}_α , the subscript α here and afterwards ranging from 1 to 4. The general solution of (1) can then be represented as

$$\mathbf{V} = \mathbf{A} f(z) + \bar{\mathbf{A}} \bar{f}(\bar{z}), \tag{5}$$

where $\mathbf{A} = [\mathbf{a}_1, \mathbf{a}_2, \mathbf{a}_3, \mathbf{a}_4]^T$ is a matrix of eigenvectors, $\mathbf{f}(z) = [f_1(z_1), f_2(z_2), f_3(z_3), f_4(z_4)]^T$ with $z_\alpha = x_1 + p_\alpha x_3$ is an arbitrary vector function, and the bar stands for complex conjugation.

By using (1)₁, the vector $\mathbf{t} = [\sigma_{13}, \sigma_{23}, \sigma_{33}, D_3]^T$ can be represented in the form

$$\mathbf{t} = \mathbf{B} \mathbf{f}'(z) + \bar{\mathbf{B}} \bar{\mathbf{f}}'(\bar{z}), \tag{6}$$

where the 4×4 matrix \mathbf{B} is defined by $B_{J\alpha} = (E_{3JK1} + p_\alpha E_{3JK3})A_{k\alpha}$ (not summed over α) and $\mathbf{f}'(z) = [f'_1(z_1), f'_2(z_2), f'_3(z_3), f'_4(z_4)]$.

Consider a bimaterial composed of two different piezoelectric semi-infinite spaces $x_3 > 0$ and $x_3 < 0$, as sketched in Figure 1. The material properties are defined by matrices $E_{iJKl}^{(1)}$ and $E_{iJKl}^{(2)}$. We assume that the vector \mathbf{t} is continuous across the whole bimaterial interface $x_3 = 0$. Furthermore, in the undamaged ligament L of the interface, both parts of the bimaterial are mechanically and electrically fixed to each other, in ideal contact. In summary, the boundary conditions at the interface are

$$\mathbf{t}^{(1)}(x_1, 0) = \mathbf{t}^{(2)}(x_1, 0) \quad \text{for } x_1 \in (-\infty, \infty),$$

$$\mathbf{V}^{(1)}(x_1, 0) = \mathbf{V}^{(2)}(x_1, 0) \quad \text{for } x_1 \in L.$$

In this case according to (5)–(6) the solution of equations (1) can be written for each domain in the form

$$\mathbf{V}^{(m)}(x_1, x_3) = \mathbf{A}^{(m)} \mathbf{f}^{(m)}(z) + \bar{\mathbf{A}}^{(m)} \bar{\mathbf{f}}^{(m)}(\bar{z}),$$

$$\mathbf{t}^{(m)}(x_1, x_3) = \mathbf{B}^{(m)} \mathbf{f}'^{(m)}(z) + \bar{\mathbf{B}}^{(m)} \bar{\mathbf{f}}'^{(m)}(\bar{z}),$$

Here $m = 1$ stands for $x_3 > 0$ and $m = 2$ for $x_3 < 0$; the vector functions $\mathbf{f}^{(1)}(z)$ and $\mathbf{f}^{(2)}(z)$ are analytic in the upper ($x_3 > 0$) and lower ($x_3 < 0$) half-planes, respectively.

An analysis similar to that of Herrmann and Loboda [2000] leads to the expressions

$$\llbracket \mathbf{V}'(x_1, 0) \rrbracket = \mathbf{D} \mathbf{f}'^{(1)}(x_1) + \bar{\mathbf{D}} \bar{\mathbf{f}}'^{(1)}(x_1),$$

$$\mathbf{t}(x_1, 0) = \mathbf{B}^{(1)} \mathbf{f}'^{(1)}(x_1) + \bar{\mathbf{B}}^{(1)} \bar{\mathbf{f}}'^{(1)}(x_1),$$

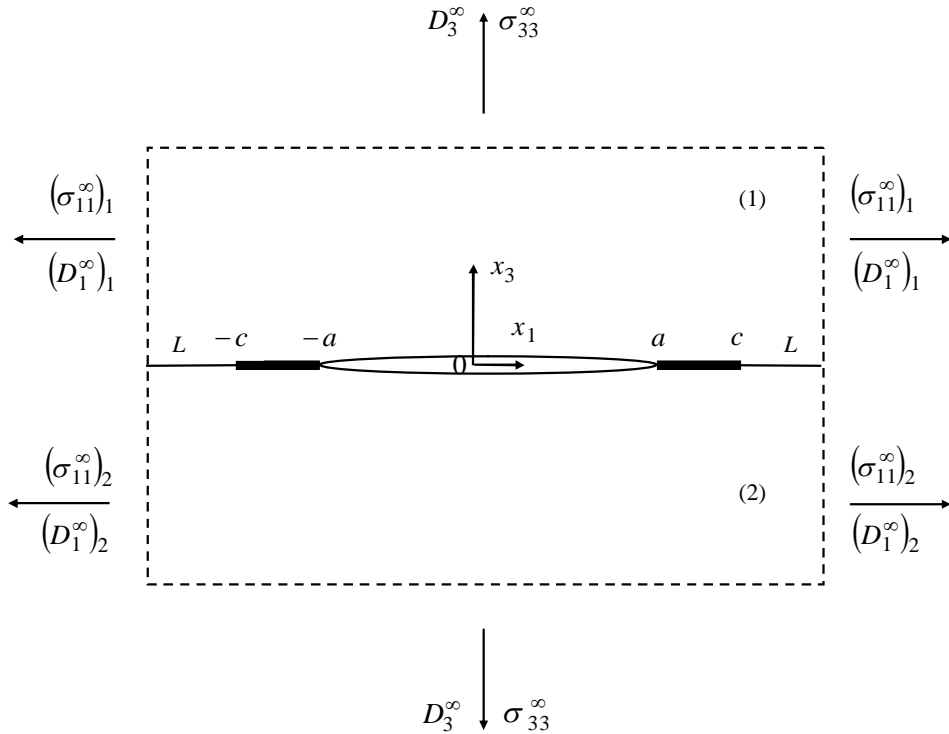


Figure 1. Prefracture zones ahead of the crack tips in a piezoelectric bimaterial compound

where $D = A^{(1)} - \bar{A}^{(2)}(\bar{B}^2)^{-1}B^{(1)}$. Here and afterwards, the double square brackets $[[\cdot]]$ denote the jump of the corresponding function over the material interface, i.e., $[[V'(x_1, 0)]] = V'^{(1)}(x_1, 0) - V'^{(2)}(x_1, 0)$.

Introducing the vector function

$$W(z) = \begin{cases} Df^{(1)}(z) & \text{for } x_3 > 0, \\ -\bar{D}\bar{f}^{(1)}(z) & \text{for } x_3 < 0, \end{cases}$$

one obtains

$$[[V'(x_1, 0)]] = W^+(x_1) - W^-(x_1), \tag{7}$$

$$t(x_1, 0) = GW^+(x_1) - \bar{G}W^-(x_1), \tag{8}$$

where $G = B^{(1)}D^{-1}$, $W^+(x_1) = W(x_1 + i0)$, $W^-(x_1) = W(x_1 - i0)$. It follows from (7) that the vector function $W(z)$ is analytical in the whole (x_1, x_3) -plane, including the bonded parts of the material interface.

In the following, our attention is focused on piezoelectric materials of the symmetry class 6mm poled in direction x_3 , which have an essential practical significance. In this case for loads which are independent of the coordinate x_2 we can look for fields in the (x_1, x_3) -plane, where the displacement u_2 contained as second component in vector function V decouples from the components (u_1, u_3, φ) . Due to this, u_2 can simply be determined after having solved the remaining problem for (u_1, u_3, φ) , and therefore our

attention will be focused on the plane problem for components (u_1, u_3, φ) . For this case, the bimaterial matrix \mathbf{G} without its second row and column has the form [Herrmann and Loboda 2000]

$$\mathbf{G} = \begin{bmatrix} G_{11} & G_{13} & G_{14} \\ G_{31} & G_{33} & G_{34} \\ G_{41} & G_{43} & G_{44} \end{bmatrix} = \begin{bmatrix} ig_{11} & g_{13} & g_{14} \\ g_{31} & ig_{33} & ig_{34} \\ g_{41} & ig_{43} & ig_{44} \end{bmatrix}, \quad (9)$$

where all the g_{ij} are real.

Consider in addition an arbitrary row matrix $\mathbf{S} = [S_1, S_3, S_4]$ and a product $\mathbf{S}t(x_1, 0)$ which by using (8) with \mathbf{G} defined by (9) can be written as

$$\mathbf{S}t(x_1, 0) = \mathbf{S}\mathbf{G}\mathbf{W}^+(x_1) - \mathbf{S}\bar{\mathbf{G}}\mathbf{W}^-(x_1). \quad (10)$$

Introducing the function

$$F(z) = \mathbf{H}\mathbf{W}(z)$$

with $\mathbf{H} = \mathbf{S}\mathbf{G}$ and assuming

$$\mathbf{S}\bar{\mathbf{G}} = -\gamma \mathbf{S}\mathbf{G},$$

where γ is a constant, equation (10) can be written as

$$\mathbf{S}t(x_1, 0) = F^+(x_1) + \gamma F^-(x_1).$$

Here, γ and \mathbf{S}^T are an eigenvalue and an eigenvector of the system

$$(\gamma \mathbf{G}^T + \bar{\mathbf{G}}^T)\mathbf{S}^T = 0. \quad (11)$$

By the use of (9), the roots of the equation $\det(\gamma \mathbf{G}^T + \bar{\mathbf{G}}^T) = 0$ can be represented in the form

$$\gamma_1 = \frac{1 + \delta}{1 - \delta}, \quad \gamma_3 = \frac{1}{\gamma_1}, \quad \gamma_4 = 1, \quad \text{where } \delta^2 = \frac{g_{14}^2 g_{33} + g_{13}^2 g_{44} - 2g_{13} g_{14} g_{34}}{g_{11}(g_{33} g_{44} - g_{34}^2)}.$$

Numerical analysis shows that for a group of compound piezoelectric materials the inequality

$$\delta^2 > 0 \quad (12)$$

holds, while for another group this inequality is not valid. This has been mentioned in [Suo et al. 1992]. In the following, attention is paid to piezoelectric materials satisfying inequality (12). In this case, the eigenvector $\mathbf{S}_j = [S_{j1}, S_{j3}, S_{j4}]$ associated with an eigenvalue γ_j ($j = 1, 3, 4$) can be found from system (11). If one assumes S_{j3} to be real, then S_{j1} is imaginary and S_{j4} is real. Then, the components of the corresponding vectors $\mathbf{H}_j = [H_{j1}, H_{j3}, H_{j4}]$ have the following properties: H_{j1} is real while H_{j3} and H_{j4} are imaginary.

Thus, according to the conclusions above concerning the properties of \mathbf{S}_j and \mathbf{H}_j , and choosing $S_{j3} = 1$, one can write

$$\sigma_{33}(x_1, 0) + m_{j4} D_3(x_1, 0) + im_{j1} \sigma_{13}(x_1, 0) = F_j^+(x_1) + \gamma_j F_j^-(x_1), \quad (13)$$

where

$$F_j(z) = n_{j1} W_1(z) + in_{j3} W_3 + in_{j4} W_4, \quad (14)$$

and $m_{j4} = S_{j4}$, $m_{j1} = -iS_{j1}$, $n_{j1} = H_{j1}$, $n_{j3} = -iH_{j3}$, $n_{j4} = -iH_{j4}$. Here m_{jl} , n_{jl} ($j, l = 1, 3, 4$) are real values. It is clear from (14) that the functions $F_j(z)$ are analytic in the whole (x_1, x_3) -plane, including the bonded parts of the material interface.

For piezoelectric ceramics of the symmetry class 6mm with poling direction x_3 , the relations $m_{41} = 0$, $n_{41} = 0$, $m_{14} = m_{34}$, $m_{11} = -m_{31}$ and $\gamma_3 = 1/\gamma_1$ hold [Herrmann and Loboda 2000]. Using them, we can obtain the solution of the problems (13)–(14) for $j = 3$ from the solution of this problem for $j = 1$. Therefore, only the equations

$$\begin{aligned} \sigma_{33}(x_1, 0) + m_{14}D_3(x_1, 0) + im_{11}\sigma_{13}(x_1, 0) &= F_1^+(x_1) + \gamma_1 F_1^-(x_1), \\ \sigma_{33}(x_1, 0) + m_{44}D_3(x_1, 0) &= F_4^+(x_1) + F_4^-(x_1), \end{aligned} \quad (15)$$

will be considered below.

Equations (7) and (14) lead to the expressions

$$n_{11}[[u'_1(x_1, 0)]] + in_{13}[[u'_3(x_1, 0)]] + in_{14}[[\varphi'(x_1, 0)]] = F_1^+(x_1) - F_1^-(x_1), \quad (16)$$

$$in_{43}[[u'_3(x_1, 0)]] + in_{44}[[\varphi'(x_1, 0)]] = F_4^+(x_1) - F_4^-(x_1) \quad (17)$$

for the derivatives of the displacement and electrical potential jumps.

3. Formulation of the problem

Consider two piezoelectric half-spaces $x_3 > 0$ and $x_3 < 0$ having both the symmetry class 6mm with poling direction x_3 . It is assumed that the half-spaces are adhered to each other by means of an interlayer of very small thickness. The loading at infinity is given by $\sigma_{33}^{(m)} = \sigma_{33}^\infty$, $\sigma_{11}^{(m)} = (\sigma_{11}^\infty)_m$, $D_3^{(m)} = D_3^\infty$ and $D_1^{(m)} = (D_1^\infty)_m$ ($m = 1$ stands for the upper domain, and $m = 2$ for the lower one). Moreover, stresses $(\sigma_{11}^\infty)_m$ and electrical displacement $(D_1^\infty)_m$ are chosen to satisfy continuity conditions at the interface. Assuming the load to be independent of coordinate x_2 , the plane strain problem in the (x_1, x_3) -plane can be considered and the relations from the previous section can be used. It is assumed that a crack $(-a, a)$ is situated in the interlayer (Figure 1). The interlayer thickness is assumed to be small compared to the crack length. Therefore, the exact location of the crack in thickness direction, may it be either between the interlayer and one of the piezoelectric materials or inside the interlayer is not resolved in detail in this work. Rather, the interlayer thickness will not be completely taken into consideration. However, the material properties of the interlayer and its influence upon the fracture process will be accounted for.

As mentioned, a linear piezoelectric constitutive model leads to an oscillating singularity in stresses and in electrical displacement at interface crack tips. To avoid these singularities, electromechanical prefracture zones $[-c, -a]$ and $[a, c]$ are introduced in front of the crack tips. We believe that consideration of such zones of electrical saturation zone and mechanical yielding zone might offer a perspective to understand the currently observed discrepancies between theory and experiments. In general, the electrical saturation zone and the mechanical yielding zone would be of different length. However, a complete nonlinear analysis including such electromechanical zones of different length for the discussion of fracture in piezoelectric bimaterial compounds will encounter considerable mathematical difficulties. In stead, as a first step towards understanding the effects of electromechanical nonlinearity, we propose here to consider a strip saturation model where the zones of electrical and mechanical yielding are of the

same length. In this zone, electric displacement is limited by some given saturation value, i.e., $D_3 = D_s$, while the stresses in this zones are constant and unknown: $\sigma_{33} = \sigma_0, \sigma_{13} = \tau_0$.

In view of this, the interface conditions can be represented in the form

$$\llbracket \mathbf{V}(x_1, 0) \rrbracket = 0, \llbracket t(x_1, 0) \rrbracket = 0 \quad \text{for } x_1 \notin (-c, c), \tag{18}$$

$$\sigma_{33}(x_1, 0) \equiv q_1(x_1) = \begin{cases} \sigma_0, & -c \leq x_1 \leq -a, \\ 0, & -a < x_1 < a, \\ \sigma_0, & \leq x_1 \leq c, \end{cases} \tag{19}$$

$$\sigma_{13}(x_1, 0) \equiv q_2(x_1) = \begin{cases} -\tau_0, & -c \leq x_1 \leq -a \\ 0, & -a < x_1 < a \\ \tau_0, & \leq x_1 \leq c, \end{cases} \tag{20}$$

$$D_3(x_1, 0) \equiv q_3(x_1) = \begin{cases} D_s, & -c \leq x_1 \leq -a \\ 0, & -a < x_1 < a, \\ D_s, & \leq x_1 \leq c. \end{cases} \tag{21}$$

Here, due to continuity, the saturation limit D_s is equal the smaller one of the two materials. The length c of this prefracture zone has to be determined from the above mentioned conditions.

In this way, we have formulated a problem of linear fracture mechanics for a crack $(-c, c)$ between two half-spaces with unknown stress components σ_0, τ_0 and unknown position of the point c .

4. Solution of the problem

Taking into account that $F_j^+(x_1) = F_j^-(x_1)$ ($j = 1, 4$) for $|x_1| > c$, one can write by means of (15) and the prescribed remote electromechanical loads at infinity the conditions

$$F_1(z)|_{z \rightarrow \infty} = \frac{1}{1 + \gamma_1} (\sigma_{33}^\infty + m_{14} D_3^\infty), \quad F_4(z)|_{z \rightarrow \infty} = \frac{1}{2} (\sigma_{33}^\infty + m_{44} D_3^\infty) \tag{22}$$

for the functions $F_j(z)$.

Using equations (15) and imposing the interface conditions (19)–(21), we obtain for $|x_1| < c$

$$F_1^+(x_1) + \gamma_1 F_1^-(x_1) = p_1(x_1), \quad F_4^+(x_1) + F_4^-(x_1) = p_4(x_1), \tag{23}$$

where $p_1(x_1) = q_1(x_1) + m_{14} q_3(x_1) + im_{11} q_2(x_1)$, $p_4(x_1) = q_1(x_1) + m_{44} q_3(x_1)$.

By satisfying conditions at infinity (22), the solution of the problems (23) can be written in the form [Muskhelishvili 1953]

$$F_1(z) = \frac{1}{2\pi i(1 + \gamma_1)Y_1(z)} \left\{ 2\pi i(\sigma_{33}^\infty + m_{14}D_3^\infty)(z - 2ci\varepsilon_1) + (1 + \gamma_1) \int_{-c}^c \frac{Y_1^+(t)p_1(t) dt}{t - z} \right\}, \tag{24}$$

$$F_4(z) = \frac{1}{2\pi iY_4(z)} \left\{ \pi zi(\sigma_{33}^\infty + m_{44}D_3^\infty) + \int_{-c}^c \frac{Y_4^+(t)p_4(t) dt}{t - z} \right\},$$

where $Y_1(z) = (z + c)^{0.5-i\varepsilon_1}(z - c)^{0.5+i\varepsilon_1}$, $Y_4(z) = \sqrt{z^2 - c^2}$, $\varepsilon_1 = (\ln \gamma_1)/(2\pi)$.

By introducing the new functions

$$\begin{aligned} \Phi_{11}(z) &= \frac{1}{2\pi i} \int_{-c}^{-a} \frac{Y_1^+(t) dt}{t-z}, & \Phi_{12}(z) &= \frac{1}{2\pi i} \int_a^c \frac{Y_1^+(t) dt}{t-z}, \\ \Phi_{41}(z) &= \frac{1}{2\pi i} \int_{-c}^{-a} \frac{Y_4^+(t) dt}{t-z}, & \Phi_{42}(z) &= \frac{1}{2\pi i} \int_a^c \frac{Y_4^+(t) dt}{t-z}, \end{aligned}$$

we reduce the equations (24) to the form

$$F_1(z) = \frac{1}{(1+\gamma_1)Y_1(z)} \left\{ (\sigma_{33}^\infty + m_{14}D_3^\infty)(z - 2ci\varepsilon_1) + (1+\gamma_1)(\sigma_0 + m_{14}D_s - im_{11}\tau_0)\Phi_{11}(z) + (1+\gamma_1)(\sigma_0 + m_{14}D_s + im_{11}\tau_0)\Phi_{12}(z) \right\} \quad (25)$$

and

$$F_4(z) = \frac{1}{2Y_4(z)} \left\{ z(\sigma_{33}^\infty + m_{44}D_3^\infty) + 2(\sigma_0 + m_{44}D_s)(\Phi_{41}(z) + \Phi_{42}(z)) \right\}. \quad (26)$$

Taking into account that $\Phi_{jk}^+(x_1) = \Phi_{jk}^-(x_1) = \Phi_{jk}(x_1)$ ($j = 1, 4, k = 1, 2$) for $|x_1| > c$ and using equations (15), we obtain the relations

$$\begin{aligned} &\sigma_{33}(x_1, 0) + m_{14}D_3(x_1, 0) + im_{11}\sigma_{13}(x_1, 0) \\ &= \frac{1}{Y_1(x_1)} \left\{ (\sigma_{33}^\infty + m_{14}D_3^\infty)(x_1 - 2ci\varepsilon_1) + (1+\gamma_1)(\sigma_0 + m_{14}D_s - im_{11}\tau_0)\Phi_{11}(x_1) + (1+\gamma_1)(\sigma_0 + m_{14}D_s + im_{11}\tau_0)\Phi_{12}(x_1) \right\} \quad (27) \end{aligned}$$

and

$$\sigma_{33}(x_1, 0) + m_{44}D_3(x_1, 0) = \frac{1}{Y_4(x_1)} \left\{ x_1(\sigma_{33}^\infty + m_{44}D_3^\infty) + 2(\sigma_0 + m_{44}D_s)(\Phi_{41}(x_1) + \Phi_{42}(x_1)) \right\}. \quad (28)$$

for the stresses and electrical displacements.

Furthermore, we employ the finite value conditions at the interface for $x_1 \rightarrow c + 0$ for the stresses and electrical displacements formulated in the first and third of equations (19)–(21). These conditions are satisfied if the equations

$$\begin{aligned} &c(\sigma_{33}^\infty + m_{14}D_3^\infty)(1 - 2i\varepsilon_1) + (1+\gamma_1) \left\{ (\sigma_0 + m_{14}D_s - im_{11}\tau_0)\Phi_{11}^c + (\sigma_0 + m_{14}D_s + im_{11}\tau_0)\Phi_{12}^c \right\} = 0, \\ &c(\sigma_{33}^\infty + m_{44}D_3^\infty) + 2(\sigma_0 + m_{44}D_s)(\Phi_{41}^c + \Phi_{42}^c) = 0, \end{aligned} \quad (29)$$

hold, where $\Phi_{jk}^c = \lim_{x_1 \rightarrow c+0} \Phi_{jk}(x_1)$ ($j = 1, 4, k = 1, 2$). The integrals Φ_{jk}^c can be calculated exactly:

$$\begin{aligned} \Phi_{11}^c &= \frac{1}{2\pi i \gamma_1 (1.5 - i\varepsilon_1)} (a+c)^{-0.5+i\varepsilon_1} (a-c)^{1.5-i\varepsilon_1} {}_2F_1\left(1, \frac{1}{2} - i\varepsilon_1, \frac{5}{2} - i\varepsilon_1, \frac{a-c}{a+c}\right), \\ \Phi_{12}^c &= -\frac{1}{2\pi i (0.5 + i\varepsilon_1)} (a+c)^{0.5-i\varepsilon_1} (a-c)^{0.5+i\varepsilon_1} {}_2F_1\left(1, -\frac{1}{2} + i\varepsilon_1, \frac{3}{2} + i\varepsilon_1, \frac{a-c}{a+c}\right), \\ \Phi_{41}^c + \Phi_{42}^c &= -\frac{c}{\pi} \cos^{-1}\left(\frac{a}{c}\right), \end{aligned}$$

where

$${}_2F_1(\alpha, \beta, \gamma, z) = \sum_{m=0}^{\infty} \frac{(\alpha)_m (\beta)_m z^m}{(\gamma)_m m!}$$

is the Gauss hypergeometric function.

From the system (29), we derive the equality

$$\frac{c(\omega_{22} + 2\varepsilon_1\omega_{12})(\sigma_{33}^\infty + m_{14}D_3^\infty)}{(1 + \gamma_1)(\omega_{11}\omega_{22} - \omega_{12}\omega_{21})} + \frac{\pi(\sigma_{33}^\infty + m_{44}D_3^\infty)}{2 \cos^{-1}(a/c)} - (m_{44} - m_{14})D_s = 0, \tag{30}$$

where

$$\begin{aligned} \omega_{11} &= \operatorname{Re} \Phi_{11}^c + \operatorname{Re} \Phi_{12}^c, & \omega_{12} &= \operatorname{Im} \Phi_{11}^c - \operatorname{Im} \Phi_{12}^c, \\ \omega_{21} &= \operatorname{Im} \Phi_{11}^c + \operatorname{Im} \Phi_{12}^c, & \omega_{22} &= \operatorname{Re} \Phi_{12}^c - \operatorname{Re} \Phi_{11}^c; \end{aligned}$$

solving (30) for c (which in general has to be done numerically) one obtains the value of c . After substituting this value into the system (29), one arrives the expressions

$$\begin{aligned} \tau_0 &= \frac{c(\omega_{21} + 2\varepsilon_1\omega_{11})(\sigma_{33}^\infty + m_{14}D_3^\infty)}{m_{11}(1 + \gamma_1)(\omega_{11}\omega_{22} - \omega_{12}\omega_{21})}, \\ \sigma_0 &= \frac{1}{m_{14} - m_{44}} \left\{ \frac{cm_{44}(\omega_{22} + 2\varepsilon_1\omega_{12})(\sigma_{33}^\infty + m_{14}D_3^\infty)}{(1 + \gamma_1)(\omega_{11}\omega_{22} - \omega_{12}\omega_{21})} + \frac{\pi m_{14}(\sigma_{33}^\infty + m_{44}D_3^\infty)}{2 \cos^{-1}(a/c)} \right\} \end{aligned}$$

for the stresses in the prefracture zones.

When, for a given D_s , the prefracture zone length in terms of c and the appropriate values of σ_0 and τ_0 have been found, we are able to calculate the stresses and electrical displacement for $|x_1| > c$ from (27) and (28). In this case, the integrals $\Phi_{41}(x_1)$ and $\Phi_{42}(x_1)$ can be calculated analytically, while $\Phi_{11}(x_1)$ and $\Phi_{12}(x_1)$ can be represented via hypergeometric functions as

$$\begin{aligned} \Phi_{11}(x_1) &= \frac{1}{4\pi ic\gamma_1(1.5 - i\varepsilon_1)}(a + c)^{1.5 + i\varepsilon_1}(a - c)^{1.5 - i\varepsilon_1} \frac{1}{a + x_1} F_1\left(1, 2, 1, \frac{5}{2} - i\varepsilon_1, \frac{c - a}{2c}, \frac{(x_1 - c)(c - a)}{2c(a + x_1)}\right) \\ &\quad - \frac{1}{1 + \gamma_1} \left\{ (x_1 - c)^{0.5 + i\varepsilon_1} (2c)^{0.5 - i\varepsilon_1} {}_2F_1\left(\frac{3}{2} + i\varepsilon_1, -\frac{1}{2} + i\varepsilon_1, \frac{3}{2} + i\varepsilon_1, \frac{c - x_1}{2c}\right) - (x_1 + c)^{0.5 - i\varepsilon_1} (x_1 - c)^{0.5 + i\varepsilon_1} \right\}, \\ \Phi_{12}(x_1) &= \frac{1}{2\pi i(1.5 + i\varepsilon_1)}(a + c)^{0.5 - i\varepsilon_1}(a - c)^{1.5 + i\varepsilon_1} \frac{1}{x_1 - a} F_1\left(1, -\frac{1}{2} + i\varepsilon_1, 1, \frac{5}{2} + i\varepsilon_1, \frac{a - c}{a + c}, \frac{c - a}{x_1 - a}\right), \\ \Phi_{41}(x_1) + \Phi_{42}(x_1) &= -\frac{x_1}{\pi} \left\{ \cos^{-1}\left(\frac{a}{c}\right) - \frac{\sqrt{x_1^2 - c^2}}{x_1} \cot^{-1}\left(\frac{a}{x_1} \sqrt{\frac{x_1^2 - c^2}{c^2 - a^2}}\right) \right\}, \end{aligned}$$

where

$$F_1(\alpha, \beta_1, \beta_2, \gamma, x, y) = \sum_{m,n} \frac{(\alpha)_{m+n}(\beta_1)_m(\beta_2)_n}{(\gamma)_{m+n}m!n!} x^m y^n$$

is the Appell hypergeometric function.

Now consider the jumps in displacement and electrical potential at the crack faces. From (23) we have

$$F_1^-(x_1) = \frac{1}{\gamma_1} p_1(x_1) - F_1^+(x_1) \quad \text{and} \quad F_4^-(x_1) = p_4(x_1) - F_4^+(x_1)$$

for $|x_1| < c$. Substituting this into (16) and (17), one arrives at the equations

$$n_{11}[[u'_1(x_1, 0)]] + in_{13}[[u'_3(x_1, 0)]] + in_{14}[[\varphi'(x_1, 0)]] = \frac{1 + \gamma_1}{\gamma_1} F_1^+(x_1) - \frac{1}{\gamma_1} p_1(x_1), \tag{31}$$

$$in_{43}[[u'_3(x_1, 0)]] + in_{44}[[\varphi'(x_1, 0)]] = 2F_4^+(x_1) - p_4(x_1), \quad |x_1| < c. \tag{32}$$

Then, substituting (25)–(26) into (31) and (32), we arrive at

$$\begin{aligned}
 & n_{11} \llbracket u'_1(x_1, 0) \rrbracket + in_{13} \llbracket u'_3(x_1, 0) \rrbracket + in_{14} \llbracket \varphi'(x_1, 0) \rrbracket \\
 &= \frac{1}{\gamma_1 Y_1^+(x_1)} \left\{ (\sigma_{33}^\infty + m_{14} D_3^\infty)(x_1 - 2ic\varepsilon_1) + (1 + \gamma_1)(\sigma_0 + m_{14} D_s - im_{11} \tau_0) \Phi_{11}^+(x_1) \right. \\
 & \qquad \qquad \qquad \left. + (1 + \gamma_1)(\sigma_0 + m_{14} D_s + im_{11} \tau_0) \Phi_{12}^+(x_1) \right\} \quad (33)
 \end{aligned}$$

and

$$n_{43} \llbracket u'_3(x_1, 0) \rrbracket + n_{44} \llbracket \varphi'(x_1, 0) \rrbracket = \frac{\sigma_0 + m_{44} D_s}{2\pi} \{ \Gamma(c, x_1, a) - \Gamma(c, x_1, -a) \}, \quad |x_1| < c, \quad (34)$$

where

$$\Gamma(b, x_1, \zeta) = \ln \frac{b^2 - x_1 \zeta - \sqrt{(b^2 - x_1^2)(b^2 - \zeta^2)}}{b^2 - x_1 \zeta + \sqrt{(b^2 - x_1^2)(b^2 - \zeta^2)}}.$$

One can evaluate Appell’s F_1 hypergeometric function using the approach of [Colavecchia et al. 2001], which is based on analytic continuations of F_1 outside the region of convergence of the series. Thus one can write for $|x_1| < c$

$$\begin{aligned}
 \Phi_{11}^+(x_1) &= \frac{1}{4\pi ic\gamma_1(1.5 - i\varepsilon_1)} (a+c)^{1.5+i\varepsilon_1} (a-c)^{1.5-i\varepsilon_1} \frac{1}{x_1+a} F_1\left(1, 2, 1, \frac{5}{2} - i\varepsilon_1, \frac{c-a}{2c}, \frac{(x_1-c)(c-a)}{2c(a+x_1)}\right) \\
 & \quad - \frac{1}{1+\gamma_1} (x_1-c)^{0.5+i\varepsilon_1} \left\{ (2c)^{0.5-i\varepsilon_1} {}_2F_1\left(\frac{3}{2} + i\varepsilon_1, -\frac{1}{2} + i\varepsilon_1, \frac{3}{2} + i\varepsilon_1, \frac{c-x_1}{2c}\right) - (x_1+c)^{0.5-i\varepsilon_1} \right\},
 \end{aligned}$$

while for $|x_1| < a$

$$\Phi_{12}^+(x_1) = \frac{(2c)^{0.5-i\varepsilon_1}}{2\pi i(1.5 + i\varepsilon_1)} (a-c)^{1.5+i\varepsilon_1} \frac{1}{x_1-c} F_1\left(\frac{3}{2} + i\varepsilon_1, -\frac{1}{2} + i\varepsilon_1, 1, \frac{5}{2} + i\varepsilon_1, \frac{c-a}{2c}, \frac{c-a}{c-x_1}\right),$$

and for $a < |x_1| < c$

$$\begin{aligned}
 \Phi_{12}^+(x_1) &= \frac{0.5 + i\varepsilon_1}{i \exp(-\pi\varepsilon_1)(1 + \gamma_1)} (x_1 - c)^{0.5+i\varepsilon_1} (2c)^{0.5-i\varepsilon_1} {}_2F_1\left(\frac{3}{2} + i\varepsilon_1, -\frac{1}{2} + i\varepsilon_1, \frac{1}{2} + i\varepsilon_1, \frac{c+x_1}{2c}\right) \\
 & \quad + \frac{(a-c)^{1.5+i\varepsilon_1} (a+c)^{1.5-i\varepsilon_1}}{4\pi ic(1.5 - i\varepsilon_1)(a-x_1)} F_1\left(1, 2, 1, \frac{5}{2} - i\varepsilon_1, \frac{c+a}{2c}, \frac{(c+a)(c-x_1)}{2c(a-x_1)}\right).
 \end{aligned}$$

Integrating (33) and (34) gives for the jumps in displacement and electrical potential the expressions

$$\begin{aligned}
 & n_{11} \llbracket u_1(x_1, 0) \rrbracket + in_{13} \llbracket u_3(x_1, 0) \rrbracket + in_{14} \llbracket \varphi(x_1, 0) \rrbracket \\
 &= \frac{1}{\gamma_1} (\sigma_{33}^\infty + m_{14} D_3^\infty)(x_1 + c)^{0.5+i\varepsilon_1} (x_1 - c)^{0.5-i\varepsilon_1} \\
 & \quad + \frac{1 + \gamma_1}{\gamma_1} \{ (\sigma_0 + m_{14} D_s - im_{11} \tau_0) J_{11}(x_1) + (\sigma_0 + m_{14} D_s + im_{11} \tau_0) J_{12}(x_1) \} \quad (35)
 \end{aligned}$$

and, for $|x_1| < c$,

$$n_{43} \llbracket u_3(x_1, 0) \rrbracket + n_{44} \llbracket \varphi(x_1, 0) \rrbracket = \frac{\sigma_0 + m_{44} D_s}{2\pi} \{ (x_1 - a) \Gamma(c, x_1, a) - (x_1 + a) \Gamma(c, x_1, -a) \}, \quad (36)$$

where

$$J_{11}(x_1) = \int_{-c}^{x_1} \frac{\Phi_{11}^+(t) dt}{Y_1^+(t)}, J_{12}(x_1) = \int_{-c}^{x_1} \frac{\Phi_{12}^+(t) dt}{Y_1^+(t)}.$$

The most important quantities, namely the crack opening displacements and potential at the initial crack tips, are written

$$\delta_{u_1} = \llbracket u_1(a, 0) \rrbracket, \quad \delta_{u_3} = \llbracket u_3(a, 0) \rrbracket, \quad \delta_\varphi = \llbracket \varphi(a, 0) \rrbracket.$$

Because (35) and (36), we get among these quantities the relations

$$\begin{aligned} n_{11}\delta_{u_1} + in_{13}\delta_{u_3} + in_{14}\delta_\varphi &= \frac{1}{\gamma_1}(\sigma_{33}^\infty + m_{14}D_3^\infty)(a+c)^{0.5+i\varepsilon_1}(a-c)^{0.5-i\varepsilon_1} \\ &+ \frac{1+\gamma_1}{\gamma_1} \{(\sigma_0 + m_{14}D_s - im_{11}\tau_0)J_{11}(a) + (\sigma_0 + m_{14}D_s + im_{11}\tau_0)J_{12}(a)\} \end{aligned} \quad (37)$$

and

$$n_{43}\delta_{u_3} + n_{44}\delta_\varphi = -\frac{a(\sigma_0 + m_{44}D_s)}{2\pi} \Gamma(c, a, -a). \quad (38)$$

The crack opening displacement (COD)

$$\delta = \sqrt{(\delta_{u_1})^2 + (\delta_{u_3})^2}$$

can be considered as a fracture criterion for crack growth. Following Gao et al. [1997], we use a contour Γ enclosing points a and c . The energy release rate at the crack tip, as the driving force of fracture, can then be calculated from the J -integral

$$J = \oint_\Gamma \{Wn_1 - \sigma_{ij}n_iu_{j,i} - D_in_i\varphi_{,i}\} ds,$$

where W is the electric enthalpy. Using the property of path-independence of J , we reduce the contour Γ to the prefracture zone (a, c) . Taking into account that the thickness of this zone tends to zero we arrive at the formula

$$G = \sigma_0\delta_{u_3} + \tau_0\delta_{u_1} + D_s\delta_\varphi,$$

where G is the energy release rate, which here is equal to the J -integral.

As pointed out before, the solution constructed in this section corresponds to an electrical saturation zone where the stresses are constant. In addition, it is assumed that some relation

$$f(\sigma_s, \tau_s, \sigma_1) = 0$$

holds for the stresses in the prefracture zone, where $\sigma_{33} = \sigma_s, \sigma_{13} = \tau_s, \sigma_{11} = \sigma_1$. The function f , which can be interpreted as a law of interlayer material yielding or damage, may be determined experimentally or theoretically. For example, in the case of a von Mises yielding condition, we have

$$f(\sigma_s, \tau_s, \sigma_1) \equiv (\sigma_s - \sigma_1)^2 + 4\tau_s^2 - \frac{4}{3}\sigma_y^2 = 0,$$

where σ_y is the yield stress of the interface material. According to [Tvergaard and Hutchinson 1996], the stress σ_1 in front of the crack in such material is equal to $2\sigma_y$.

From the latter condition, we can now calculate for a given saturation value D_s the external loads such that the resultant stresses σ_s and τ_s reach a critical level for the onset of yielding in the prefracture zone. The conditions (29) of finite stresses and electrical displacement at the ends of prefracture zone lead to the system

$$\begin{aligned}
 (\sigma_{33}^\infty)_s + m_{14}(D_3^\infty)_s &= -\frac{1 + \gamma_1}{c(1 - 2i\varepsilon_1)} \{(\sigma_s + m_{14}D_s - im_{11}\tau_s)\Phi_{11}^c + (\sigma_s + m_{14}D_s + im_{11}\tau_s)\Phi_{12}^c\}, \\
 (\sigma_{33}^\infty)_s + m_{44}(D_3^\infty)_s &= \frac{2}{\pi}(\sigma_s + m_{44}D_s) \arccos \frac{a}{c},
 \end{aligned}
 \tag{39}$$

which suffices to determine the unknown external loads $(\sigma_{33}^\infty)_s$ and $(D_3^\infty)_s$, together with the unknown position of the point c .

After determining the value of c from the equation

$$\frac{\sigma_s + m_{14}D_s}{m_{14}} + \frac{(\omega_{22} + 2\varepsilon_1\omega_{12})m_{11}\tau_s}{m_{14}(\omega_{21} + 2\varepsilon_1\omega_{11})} = 0,
 \tag{40}$$

which is derived from equation (30), the external load can be calculated from the system (39).

5. Numerical results and discussion

Consider an electrically impermeable interface crack of length $l = 2a = 2$ mm perpendicular to the poling direction. Calculations have been performed for a bimaterial composed of materials PZT-5H (upper material) and BaTiO₃ (lower one). The parameters of these materials are given in [Pak 1992] and [Dunn and Taya 1994], respectively. The interface layer was assumed to be an elastic-perfectly plastic material with yield stress of $\sigma_y = 50$ MPa.

In Table 1, the relative length $(c - a)/l$ of the prefracture zone in front of the right crack tip is listed together with the intensity of the external load. For this, the nonlinear equation (30) has been solved. It follows that the prefracture zone length is almost independent of σ_{33}^∞ , but depends strongly and nonlinearly on D_3^∞ .

The distributions of the normalized displacement jump $\llbracket u_3(x_1, 0) \rrbracket / l$ along the material interface is shown in Figure 2, and that of the normal stress $\sigma_{33}(x_1, 0) / \sigma_y$ in Figure 3. For the interface layer, the same material properties as before have been used. The remote normal stress was taken to be equal to $\sigma_{33}^\infty / \sigma_y = 0.05$, while the remote electrical displacement has been varied. Curves 1, 2 and 3 correspond

D_3^∞ / D_s	$(c - a) / l$	
	$\sigma_{33}^\infty / \sigma_y = 0.05$	$\sigma_{33}^\infty / \sigma_y = 0.4$
0.2	0.02574	0.02554
0.3	0.06119	0.06097
0.4	0.11808	0.11785
0.5	0.20717	0.20692
0.6	0.35075	0.35047

Table 1. Relative prefracture zone length $(c - a)/l$ as a function of the intensity of the external load.

to $D_3^\infty/D_s = 0.2, 0.4$ and 0.6 , respectively. It can be seen that an increase in the remote electrical loading leads to an increase of the displacement jumps and, thus, to an increase of the prefracture zone length, while the stresses decrease in these zones.

Figure 4 shows the effect of the applied electric field E_3^∞ on the energy release rate and the COD δ . These Figures are obtained for the same material properties as before and various values of σ_{33}^∞ . Curves 1, 2 and 3 are related to $\sigma_{33}^\infty/\sigma_y = 0.2, 0.202$ and 0.204 , respectively. It can be seen from these numerical results that a fracture criterion based on the energy release rate differs essentially from one based on the COD δ . As for homogeneous piezoelectric materials [Gao et al. 1997], we can conclude that a fracture criterion based on energy release rate infers that the electric field should impede crack propagation independently of its sign. This contradicts experimental observations. This conclusion indicates that the energy release rate is not a reasonable basis for a fracture criterion and, rather, a fracture criterion

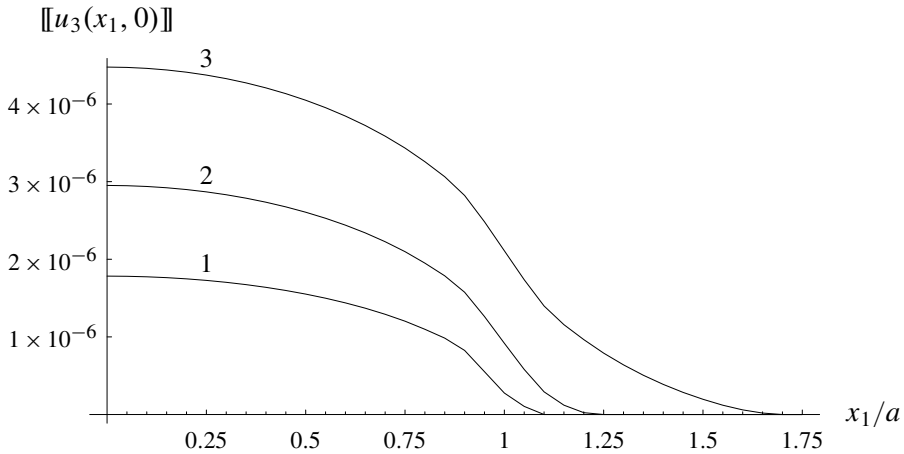


Figure 2. Distribution of normalized displacement jump $[[u_3(x_1, 0)]]/l$ along the material interface.

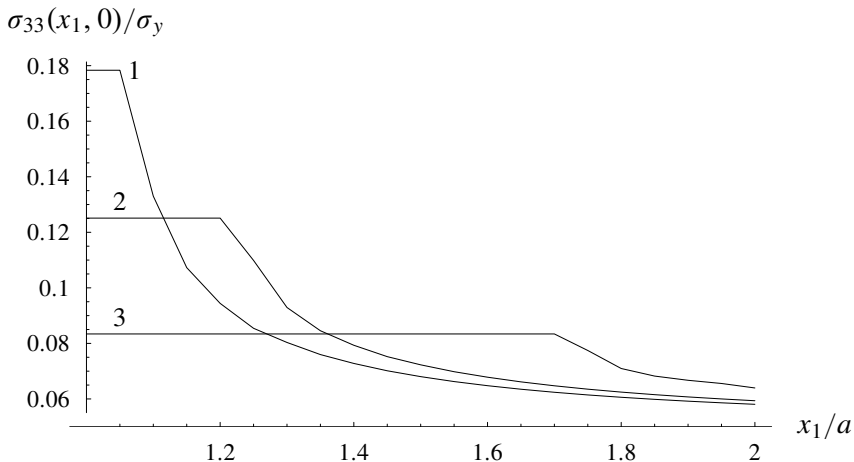


Figure 3. Distribution of normalized stress $\sigma_{33}(x_1, 0)/\sigma_y$ along the material interface.

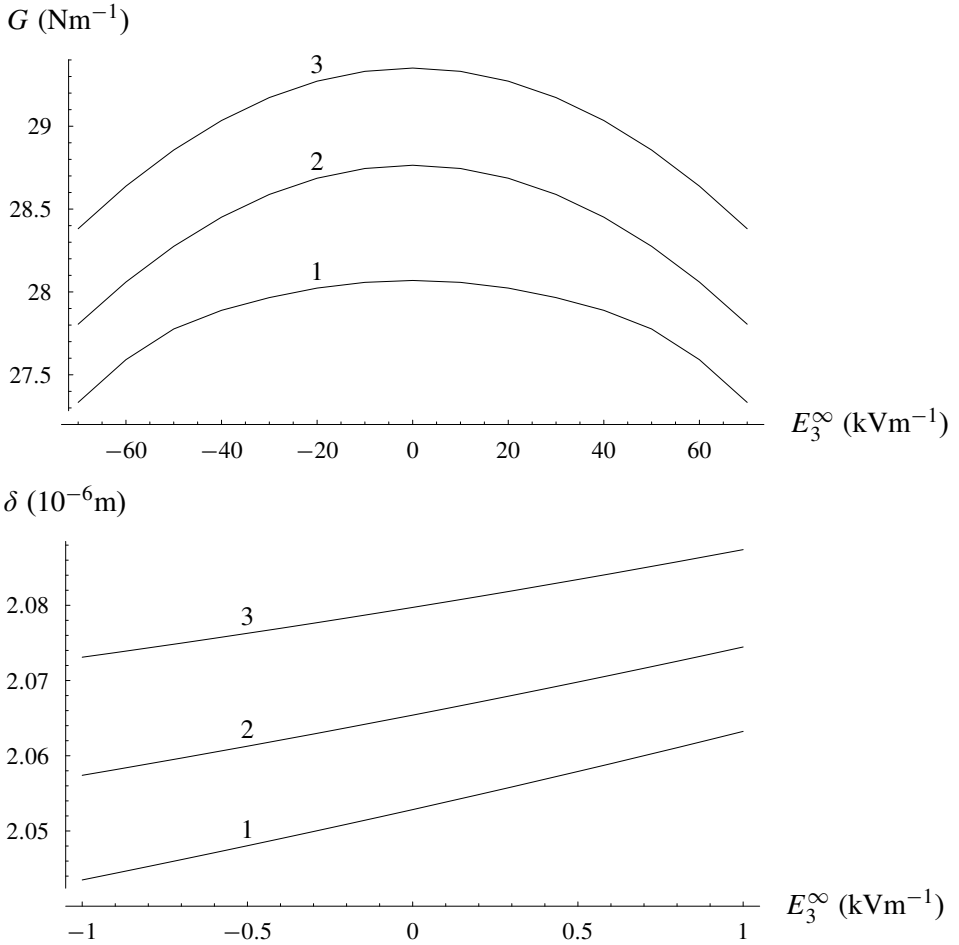


Figure 4. Energy release rate G (top) and crack opening displacement δ (bottom) as functions of the remote electric field E_3^∞ .

based on the COD might suitable. From Figure 4, we find that the COD δ would predict that fracture is enhanced by a positive applied electric field and inhibited by a negative applied electric field. This is in qualitative agreement with experimental observations for homogeneous materials [Park and Sun 1995].

External loads $(\sigma_{33}^\infty)_s / \sigma_y$ and $(D_3^\infty)_s / D_s$ as well as corresponding prefailure zone length $(c - a) / l$ belonging to given values of the yield stress of the interface layer are listed in Table 2. To this end, the

σ_y / σ_s	$(\sigma_{33}^\infty)_s / \sigma_s$	$(D_3^\infty)_s / D_s$	$(c - a) / l$
0.3333	0.0551	0.0036	0.002568
0.5000	0.0849	0.0038	0.002764
0.6667	0.1148	0.0039	0.002843
0.8333	0.1446	0.0040	0.002889

Table 2. External load $(\sigma_{33}^\infty)_s / \sigma_s$, $(D_3^\infty)_s / D_s$ and the relative prefailure zone length $(c - a) / l$ resulting from corresponding values of the yield stress of the interface layer.

system of equations (39) has been solved and equation (40) was used for calculating the prefracture zone length. It follows from Table 2 that increasing the yield stress of the interface layer leads to a grow of both the external loading magnitude and the prefracture zone length.

6. Conclusion

A plane strain problem for two piezoelectric half-spaces adhered by means of some thin interlayer has been considered. This system is subject to the action of a symmetrical remote mechanical and electrical loading. An electrically impermeable crack, which may either be located between the interlayer and one of the piezoelectric materials or completely in the interlayer, is studied.

It is assumed that the piezoelectric bimaterial components are much stiffer than the intermediate layer. Therefore, prefracture zones may develop in the interlayer in front of the crack tip. The problem is reduced to one of linear fracture mechanics by neglecting the interlayer thickness and modeling the prefracture zones as continuations of the crack where electrical polarization reaches a saturation limit and stresses are constant with respect to position.

By assuming that the displacements and the electrical potential fields are independent of out of plane coordinate x_2 , we were able to represent stresses and electrical displacements as well as the derivatives of the mechanical displacement and electrical potential jumps by a sectionally holomorphic vector function. This function is analytically continued across the mechanically and electrically bonded parts of the material interface. Furthermore, the problem is reduced to a Hilbert problem and solved exactly. From the condition of stress and electrical displacement to be finite at the end of the prefracture zone towards the undamaged interface layer, algebraic and transcendental equations have been formulated for the determination of the prefracture zone length and the stress magnitude in this zone. For the stresses and the electric displacement, the analytical relations (27) and (28) were derived. The electromechanical nonlinear effects on the structure of stress and electric displacement fields are investigated for different loading conditions. In addition, equations (35) and (36) for the crack opening at the crack tip were deduced.

In this paper, we focus on the special case, when the electrical saturation zone and mechanical yielding zone have the same length. The interface layer is assumed to be elastic perfectly-plastic according to the von Mises yield condition. For this situation, the prefracture zone length and the critical external loading corresponding to yielding are determined by system (39) and transcendental equation (40).

Numerical results for a bimaterial composed of piezoelectric materials PZT-5H and BaTiO₃ are obtained. The prefracture zone length, stresses in this zone and the crack opening at the crack tip corresponding to the respective remote loading are calculated. Note that, due to the suggested model, all mechanical and electrical quantities in the near-crack tip region are finite, i.e., all singularities connected with the crack are eliminated. The analysis of energy release rate and crack opening displacements indicates that a fracture criterion based on the crack opening displacements appears to be more appropriate from physical point of view.

Acknowledgement

Financial support by the Deutsche Forschungsgemeinschaft (DFG) is gratefully acknowledged.

References

- [Bakirov and Gol'dshtein 2004] V. F. Bakirov and R. V. Gol'dshtein, “The Leonov–Panasyuk–Dugdale model for a crack at the interface of the joint of materials”, *J. Appl. Math. Mech.* **68**:1 (2004), 153–161.
- [Beom and Atluri 2003] H. G. Beom and S. N. Atluri, “Effect of electric fields on fracture behavior of ferroelectric ceramics”, *J. Mech. Phys. Solids* **51**:6 (2003), 1107–1125.
- [Colavecchia et al. 2001] F. D. Colavecchia, G. Gasaneo, and J. E. Miraglia, “Numerical evaluation of Appell’s F1 hypergeometric function”, *Comput. Phys. Commun.* **138**:1 (2001), 29–43.
- [Comninou 1977] M. Comninou, “The interface crack”, *J. Appl. Mech. (ASME)* **44** (1977), 631–636.
- [Dugdale 1960] D. S. Dugdale, “Yielding of steel sheets containing slits”, *J. Mech. Phys. Solids* **8**:2 (1960), 100–104.
- [Dunn 1994] M. L. Dunn, “The effects of crack face boundary conditions on the fracture mechanics of piezoelectric solids”, *Eng. Fract. Mech.* **48**:1 (1994), 25–39.
- [Dunn and Taya 1994] M. L. Dunn and M. Taya, “Electroelastic field concentrations in and around inhomogeneities in piezoelectric solids”, *J. Appl. Mech. (ASME)* **61**:2 (1994), 474–475.
- [Gao et al. 1997] H. Gao, T. Y. Zhang, and P. Tong, “Local and global energy release rates for an electrically yielded crack in piezoelectric ceramic”, *J. Mech. Phys. Solids* **45**:4 (1997), 491–510.
- [Govorukha et al. 2006] V. B. Govorukha, V. V. Loboda, and M. Kamlah, “On the influence of the electric permeability on an interface crack in a piezoelectric bimaterial compound”, *Int. J. Solids Struct.* **43**:7-8 (2006), 1979–1990.
- [Herrmann and Loboda 2000] K. P. Herrmann and V. V. Loboda, “Fracture-mechanical assessment of electrically permeable interface cracks in piezoelectric bimaterials by consideration of various contact zone models”, *Arch. Appl. Mech.* **70**:1-3 (2000), 127–143.
- [Huang 1992] N. C. Huang, “An estimation of the plastic zone size for a bimaterial interfacial crack”, *Eng. Fract. Mech.* **41**:6 (1992), 935–938.
- [Kaminsky et al. 1999] A. A. Kaminskii, L. A. Kipnis, and V. A. Kolmakova, “On the Dugdale model for a crack at the interface of different media”, *Priklad. Mekh.* **35**:1 (1999), 63–68. In Russian; translated in *Int. Appl. Mech.* **35**:1 (58–63).
- [Li 2003] S. Li, “On saturation-strip model of a permeable crack in a piezoelectric ceramic”, *Acta Mech.* **165**:1-2 (2003), 47–71.
- [Loboda et al. 2007] V. Loboda, Y. Lapusta, and A. Sheveleva, “Electro-mechanical pre-fracture zones for an electrically permeable interface crack in a piezoelectric bimaterial”, *Int. J. Solids Struct.* **44**:17 (2007), 5538–5553.
- [McMeeking 2001] R. M. McMeeking, “Towards a fracture mechanics for brittle piezoelectric and dielectric materials”, *Int. J. Fract.* **108**:1 (2001), 25–41.
- [Muskhelishvili 1953] N. I. Muskhelishvili, *Some basic problems of the mathematical theory of elasticity: fundamental equations, plane theory of elasticity, torsion, and bending*, P. Noordhoff, Groningen, 1953.
- [Narita and Shindo 2001] F. Narita and Y. Shindo, “Mode I crack growth rate for yield strip model of a narrow piezoelectric ceramic body”, *Theor. Appl. Fract. Mech.* **36**:1 (2001), 73–85.
- [Needleman 1990] A. Needleman, “An analysis of tensile decohesion along an interface”, *J. Mech. Phys. Solids* **38**:3 (1990), 289–324.
- [Pak 1992] Y. E. Pak, “Linear electro-elastic fracture mechanics of piezoelectric materials”, *Int. J. Fract.* **54**:1 (1992), 79–100.
- [Park and Sun 1995] S. Park and C. T. Sun, “Fracture criteria for piezoelectric ceramics”, *J. Am. Ceram. Soc.* **78**:6 (1995), 1475–1480.
- [Parton 1976] V. Z. Parton, “Fracture mechanics of piezoelectric materials”, *Acta Astronaut.* **3**:9-10 (1976), 671–683.
- [Pickthall et al. 2002] C. Pickthall, C. Wang, and L. R. F. Rose, “Plasticity in constrained layers: model with point forces”, *Eng. Fract. Mech.* **69**:5 (2002), 647–658.
- [Qin and Mai 1999] Q. H. Qin and Y. W. Mai, “A closed crack tip model for interface cracks in thermopiezoelectric materials”, *Int. J. Solids Struct.* **36**:16 (1999), 2463–2479.
- [Ru 1999] C. Q. Ru, “Effect of electrical polarization saturation on stress intensity factors in a piezoelectric ceramic”, *Int. J. Solids Struct.* **36**:6 (1999), 869–883.

- [Shen et al. 2000] S. Shen, T. Nishioka, Z. B. Kuang, and Z. Liu, “Nonlinear electromechanical interfacial fracture for piezoelectric materials”, *Mech. Mater.* **32**:1 (2000), 57–64.
- [Sosa 1992] H. Sosa, “On the fracture mechanics of piezoelectric solids”, *Int. J. Solids Struct.* **29**:21 (1992), 2613–2622.
- [Suo et al. 1992] Z. Suo, C. M. Kuo, D. M. Barnett, and J. R. Willis, “Fracture mechanics for piezoelectric ceramics”, *J. Mech. Phys. Solids* **40**:4 (1992), 739–765.
- [Tvergaard 2001] V. Tvergaard, “Resistance curves for mixed mode interface crack growth between dissimilar elastic-plastic solids”, *J. Mech. Phys. Solids* **49**:11 (2001), 2689–2703.
- [Tvergaard and Hutchinson 1996] V. Tvergaard and J. W. Hutchinson, “On the toughness of ductile adhesive joints”, *J. Mech. Phys. Solids* **44**:5 (1996), 789–800.
- [Wang 2000] T. C. Wang, “Analysis of strip electric saturation model of crack problem in piezoelectric materials”, *Int. J. Solids Struct.* **37**:42 (2000), 6031–6049.
- [Wang and Shen 1993] X. M. Wang and Y. P. Shen, “The Dugdale crack on bimaterial interface”, *Int. J. Fract.* **59**:2 (1993), R25–R32.
- [Zhang 2004] T. Y. Zhang, “Dielectric breakdown model for an electrically impermeable crack in a piezoelectric material”, *CMC* **1**:1 (2004), 107–116.
- [Zhang and Gao 2004] T. Y. Zhang and C. F. Gao, “Fracture behaviors of piezoelectric materials”, *Theor. Appl. Fract. Mech.* **41**:1-3 (2004), 339–379.

Received 7 Apr 2008. Revised 21 May 2008. Accepted 29 Jun 2008.

VLADIMIR B. GOVORUKHA: govorukhvb@yahoo.com

Department of Computational Mathematics, Dniepropetrovsk National University, Nauchny str. 13, Dniepropetrovsk 49050, Ukraine

MARC KAMLAH: Marc.Kamlah@imf.fzk.de

Forschungszentrum Karlsruhe, Institute for Materials Research II, Postfach 3640, 76021 Karlsruhe, Germany

A GENERALIZED COSSERAT POINT ELEMENT (CPE) FOR ISOTROPIC NONLINEAR ELASTIC MATERIALS INCLUDING IRREGULAR 3-D BRICK AND THIN STRUCTURES

M. JABAREEN AND M. B. RUBIN

A generalized form for the strain energy of inhomogeneous deformations is developed for a 3-D brick Cosserat Point Element (CPE) which includes full coupling of bending and torsional modes of deformation. The constitutive coefficients, which depend on the reference geometry of the element, are determined by solving eighteen bending problems and six torsion problems on special elements that are parallelepipeds with two right angles. The resulting constitutive coefficients ensure that the strain energy for inhomogeneous deformations remains a positive definite function of the inhomogeneous strain measures for all reference element shapes. A number of example problems are considered which show that the generalized CPE produces results as accurate as enhanced strain and incompatible elements for thin structures and is free of hourglass instabilities typically predicted by these enhanced elements in regions experiencing combined high compression with bending.

1. Introduction

Recently, [Nadler and Rubin \[2003\]](#) developed a 3-D eight noded brick element based on the theory of a Cosserat point [[Rubin 1995; 2000](#)]. This Cosserat point element (CPE) can be used to formulate the numerical solution of dynamic problems for nonlinear hyperelastic materials. The kinematics of the CPE are characterized by eight element director vectors and the kinetics propose eight balance laws of director momentum to determine the dynamic response of the element. The locations of the nodes in the current deformed configuration are characterized by eight nodal director vectors and the element directors are related to the nodal directors by standard tri-linear shape functions. Moreover, the CPE theory considers the element as a structure and introduces a strain energy function which characterizes the response of the structure. Also, the nodal forces are related to derivatives of the strain energy function through algebraic relations in a similar manner to the relationship of the stress to derivatives of the strain energy function in the full three-dimensional theory of hyperelastic materials.

The CPE can easily be implemented into standard finite element programs. Specifically, the nodal positions (nodal director vectors) are used as input variables to determine the nodal forces and tangent stiffness as output variables. Here, the element assembly and solution procedures in the computer program FEAP [[Taylor 2005](#)] were used to satisfy the equilibrium equations by updating the present nodal director vectors.

In the standard finite element procedures for hyperelastic materials the response of the element is determined by integrals over the element region which assume that the kinematic approximation is valid pointwise. This is in contrast with the CPE which needs no integration over the element region. In

Keywords: Cosserat point, element irregularity, finite element, nonlinear elasticity.

this regard, the nodal forces in the CPE are not determined by integration of a displacement field based on shape functions. However, the CPE approach does not use a mixed approach based on separate shape functions for kinematic and kinetic quantities. Specifically, the nodal forces are determined by the nodal directors through algebraic constitutive equations characterizing the structural response of the element. Furthermore, it is known [Zienkiewicz and Taylor 2005] that the standard element based on full integration is robust but that it exhibits unphysical locking for thin structures with poor element aspect ratios and for nearly incompressible materials. Special methods based on enhanced strains, incompatible modes and reduced integration with hourglass control have been developed to overcome these problems; see, e.g., [Belytschko et al. 1984; Simo and Rifai 1990; Simo and Armero 1992; Belytschko and Bindeman 1993; Simo et al. 1993; Bonet and Bhargava 1995; Reese and Wriggers 1996; 2000; Reese et al. 2000; Hutter et al. 2000]. However, these improved formulations can exhibit unphysical hourglassing in regions experiencing combined high compression with bending; see, for example, [Reese and Wriggers 1996; 2000; Loehnert et al. 2005; Jabareen and Rubin 2007a; 2008c]. Furthermore, it was shown in [Jabareen and Rubin 2007a] that some of these improved element formulations in commercial codes can exhibit inelastic response even though they attempt to model a hyperelastic material with a strain energy function.

Restrictions were developed on the strain energy function for the CPE which ensure that the element reproduces exact solutions for all homogeneous deformations [Nadler and Rubin 2003]. Consequently, the CPE automatically satisfies a nonlinear form of the patch test. Also, a functional form of the strain energy for the CPE was proposed with specific dependence on the strain energy of the three-dimensional material and the reference geometry of the CPE element. In addition, a strain energy function for inhomogeneous deformations was introduced as a quadratic function of inhomogeneous strain measures.

In the original CPE formulation [Nadler and Rubin 2003] the coefficients in the strain energy function for inhomogeneous deformations were determined by comparing linear solutions of a rectangular parallelepiped CPE with exact solutions of the linear three-dimensional equations for pure bending, pure torsion and higher-order hourglass modes of deformation. Loehnert et al. [2005] implemented the CPE formulation into the finite element code FEAP [Taylor 2005] and considered specific example problems which showed that the response of the original CPE was robust and locking free for thin structures. However, it was also shown that the accuracy of the original CPE degraded with increased irregularity of the reference element shape.

Recently, Boerner et al. [2007] have proposed a numerical method for determining coefficients in a quadratic form of the strain energy function for inhomogeneous deformations which improve the response of the CPE for 2-D plane strain problems with irregular elements. In [Jabareen and Rubin 2007b] analytical expressions were developed for constitutive coefficients in an improved CPE for 3-D deformations by generalizing the quadratic form of the strain energy function for inhomogeneous deformations to include additional coupling of the inhomogeneous strains active in bending modes. Functional forms for the additional coefficients were determined by considering four bending solutions for special shaped reference elements which are parallelepipeds with two right angles. In [Jabareen and Rubin 2008c] improved coefficients were developed for torsion by considering an exact torsion-like solution of the linear elastic equations for an isotropic elastic material.

In this paper, exact linear solutions of bending and simple torsion of these special elements are re-examined and it is shown that by including more general coupling of bending and torsional modes it

is possible to match solutions of the two additional bending modes not handled in [Jabareen and Rubin 2007b] as well as the simple torsion solutions. Matching these additional two bending modes significantly improves the response of the generalized CPE for the problem of bending of a thin rhombic plate, which was shown to be inaccurate in [Ehrlich 2007].

Here is an outline of this paper. Section 2 presents the basic equations of the CPE. Section 3 describes the procedure to use eighteen bending solutions and six torsions solutions to determine the functional forms of the constitutive coefficients in the strain energy function for inhomogeneous deformations. Section 4 considers a number of examples that demonstrate the response of the generalized CPE. Finally, Section 5 presents conclusions.

2. Basic equations of a Cosserat point element (CPE)

Here attention is focused on an eight noded 3-D brick CPE as developed in [Nadler and Rubin 2003] and modified in [Jabareen and Rubin 2008c; Jabareen and Rubin 2007b]. Moreover, for the present discussion it is sufficient to confine attention to the equilibrium equations. Within the context of this theory the kinematics of the CPE are characterized by

$$\{\mathbf{D}_i, \mathbf{d}_i\} \quad (i = 0, 1, 2 \dots, 7), \tag{2.1}$$

where \mathbf{D}_i are constant reference directors associated with the reference configuration and \mathbf{d}_i are present directors associated with the deformed present configuration. These element director vectors are related to the nodal director vectors [which locate the nodes of a brick element (see Figure 1) relative to a fixed origin] by a constant matrix and details can be found in [Nadler and Rubin 2003].

Without loss in generality, the three-dimensional position vector \mathbf{X}^* associated with material points in the reference configuration of the element can be expressed in the form

$$\mathbf{X}^*(\theta^1, \theta^2, \theta^3) = \sum_{j=0}^7 N^j(\theta^1, \theta^2, \theta^3) \mathbf{D}_j, \quad |\theta^1| \leq \frac{H_1}{2}, \quad |\theta^2| \leq \frac{H_2}{2}, \quad |\theta^3| \leq \frac{H_3}{2}, \tag{2.2}$$

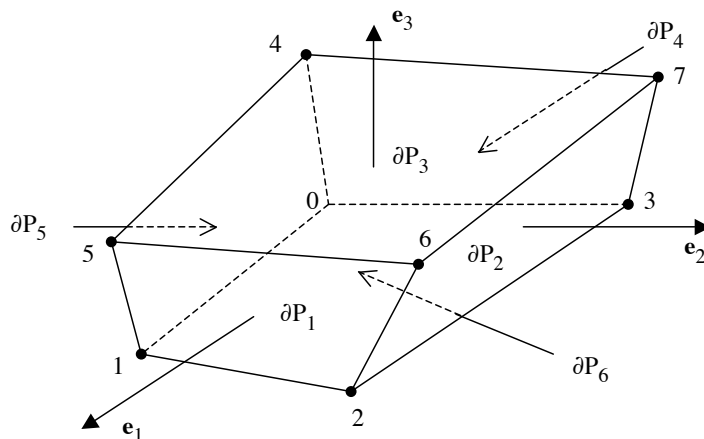


Figure 1. Sketch of a general brick CPE showing the numbering of the nodes and the surfaces.

where θ^i ($i = 1, 2, 3$) are convected material coordinates having the units of lengths, H_i are constant lengths characterizing the element defined by

$$|\mathbf{D}_1| = 1, \quad |\mathbf{D}_2| = 1, \quad |\mathbf{D}_3| = 1, \tag{2.3}$$

and N^i are shape functions

$$N^0 = 1, \quad N^1 = \theta^1, \quad N^2 = \theta^2, \quad N^3 = \theta^3, \quad N^4 = \theta^1\theta^2, \quad N^5 = \theta^1\theta^3, \quad N^6 = \theta^2\theta^3, \quad N^7 = \theta^1\theta^2\theta^3. \tag{2.4}$$

Moreover, the region P_0 associated with the reference configuration is mapped to the region P associated with the present configuration, which is bounded by ∂P which is characterized by the six surfaces ∂P_J ($J = 1, 2, \dots, 6$), such that

$$\begin{aligned} \partial P &= \partial P_1 \cup \partial P_2 \cup \partial P_3 \cup \partial P_4 \cup \partial P_5 \cup \partial P_6, \\ \theta^1 &= +\frac{H_1}{2} \quad \text{on } \partial P_1, \quad \theta^2 = +\frac{H_2}{2} \quad \text{on } \partial P_2, \quad \theta^3 = +\frac{H_3}{2} \quad \text{on } \partial P_3, \\ \theta^1 &= -\frac{H_1}{2} \quad \text{on } \partial P_4, \quad \theta^2 = -\frac{H_2}{2} \quad \text{on } \partial P_5, \quad \theta^3 = -\frac{H_3}{2} \quad \text{on } \partial P_6. \end{aligned} \tag{2.5}$$

The element directors and nodal directors are related using a tri-linear form like (2.2) for the position vector \mathbf{x}^* of material points in the present configuration. This causes the displacement field to be continuous across element boundaries. However, it is important to emphasize that the constitutive equations in the CPE approach are determined by a strain energy function for the structure and do not depend on the pointwise validity of this approximate expression for \mathbf{x}^* .

Now, in the absence of body force, the equilibrium forms of the balances of director momentum become

$$\mathbf{m}^i = \mathbf{t}^i \quad \text{with } (\mathbf{t}^0 = 0) \text{ and } (i = 0, 1, 2, \dots, 7), \tag{2.6}$$

where \mathbf{m}^i are director couples due to surface tractions on the boundaries of the element, and \mathbf{t}^i are intrinsic director couples which require constitutive equations. In this regard, it is mentioned that director couples are kinetic quantities conjugate to the element directors and they do not necessarily have the units of mechanical moment.

For the CPE it is convenient to introduce the deformation measures

$$\mathbf{F} = \sum_{i=1}^3 \mathbf{d}_i \otimes \mathbf{D}^i, \quad \boldsymbol{\beta}_i = \mathbf{F}^{-1} \mathbf{d}_{i+3} - \mathbf{D}_{i+3} \quad (i = 1, 2, 3, 4), \quad \bar{\mathbf{F}} = \mathbf{F} \left(\mathbf{I} + \sum_{i=1}^4 \boldsymbol{\beta}_i \otimes \mathbf{V}^i \right), \tag{2.7}$$

where $\{\mathbf{D}^i, \mathbf{d}^i\}$ ($i = 1, 2, 3$) are the reciprocal vectors of $\{\mathbf{D}_i, \mathbf{d}_i\}$, respectively, and $\{V, \mathbf{V}^i\}$ characterize the reference configuration of the element and are defined in [Nadler and Rubin 2003, Appendix B]. Specifically, when the reference CPE is a rectangular parallelepiped then V represents the volume of the CPE and \mathbf{V}^i vanish. Nadler and Rubin [2003] developed restrictions on the strain energy of an elastic CPE which ensure that the element satisfies a nonlinear form of the patch test for all uniform homogeneous nonlinear elastic anisotropic materials. In particular, the specific (per unit mass) strain energy Σ of the CPE can be expressed in terms of the specific strain energy Σ^* of the three-dimensional material and the specific strain energy Ψ associated with inhomogeneous deformations, such that

$$\Sigma = \Sigma^*(\bar{\mathbf{C}}) + \Psi(\bar{\mathbf{C}}, \kappa_j^i), \tag{2.8}$$

where the kinematic quantities $\{\bar{\mathbf{C}}, \kappa_j^i\}$ are defined by

$$\begin{aligned} \bar{\mathbf{C}} &= \bar{\mathbf{F}}^T \bar{\mathbf{F}}, \\ \kappa_1^1 &= H_2 \boldsymbol{\beta}_1 \cdot \mathbf{D}^1, & \kappa_1^2 &= H_1 \boldsymbol{\beta}_1 \cdot \mathbf{D}^2, & \kappa_1^3 &= H_3 \boldsymbol{\beta}_1 \cdot \mathbf{D}^3, \\ \kappa_2^1 &= H_3 \boldsymbol{\beta}_2 \cdot \mathbf{D}^1, & \kappa_2^2 &= H_2 \boldsymbol{\beta}_2 \cdot \mathbf{D}^2, & \kappa_2^3 &= H_1 \boldsymbol{\beta}_2 \cdot \mathbf{D}^3, \\ \kappa_3^1 &= H_1 \boldsymbol{\beta}_3 \cdot \mathbf{D}^1, & \kappa_3^2 &= H_3 \boldsymbol{\beta}_3 \cdot \mathbf{D}^2, & \kappa_3^3 &= H_2 \boldsymbol{\beta}_3 \cdot \mathbf{D}^3, \\ \kappa_4^1 &= H_2 H_3 \boldsymbol{\beta}_4 \cdot \mathbf{D}^1, & \kappa_4^2 &= H_1 H_3 \boldsymbol{\beta}_4 \cdot \mathbf{D}^2, & \kappa_4^3 &= H_1 H_2 \boldsymbol{\beta}_4 \cdot \mathbf{D}^3. \end{aligned} \tag{2.9}$$

Here, it is convenient to introduce the alternative variables b_i ($i = 1, 2, \dots, 12$) by

$$b_i = \{\kappa_1^1, \kappa_3^3, \kappa_1^2, \kappa_2^3, \kappa_2^1, \kappa_3^2, \kappa_1^3, \kappa_2^2, \kappa_3^1, \kappa_4^1, \kappa_4^2, \kappa_4^3\}. \tag{2.10}$$

Then, following [Jabareen and Rubin 2008c; Jabareen and Rubin 2007b], the strain energy Ψ for inhomogeneous deformations is expressed in the form

$$2m\Psi = \frac{D^{1/2}V\mu}{6(1-\nu)} \left(\sum_{i=1}^{12} \sum_{j=1}^{12} B_{ij} b_i b_j \right), \tag{2.11}$$

where m is the mass of the element, $\{\mu, \nu\}$ are the shear modulus and Poisson’s ratio associated with the small deformation response, B_{ij} is a constant symmetric matrix with the response to higher order hourglassing being uncoupled from that to bending and torsion so that B_{ij} has the following zero components:

$$\begin{aligned} B_{ij} &= 0 \quad \text{for } i = 10 \text{ and } j \neq 10, \\ B_{ij} &= 0 \quad \text{for } i = 11 \text{ and } j \neq 11, \\ B_{ij} &= 0 \quad \text{for } i = 12 \text{ and } j \neq 12, \end{aligned} \tag{2.12}$$

and the values of $\{B_{(10,10)}, B_{(11,11)}, B_{(12,12)}\}$ are given by the expressions associated with higher order hourglassing in [Nadler and Rubin 2003]. It then can be shown (loc. cit.) that the constitutive equations for a hyperelastic CPE become

$$\begin{aligned} d^{1/2} \mathbf{T} &= 2m \bar{\mathbf{F}} \frac{\partial \Sigma^*(\bar{\mathbf{C}})}{\partial \bar{\mathbf{C}}} \bar{\mathbf{F}}^T, \\ \mathbf{t}^4 &= \left(m \frac{\partial \Psi}{\partial b_1} H_2 \mathbf{d}^1 + m \frac{\partial \Psi}{\partial b_3} H_1 \mathbf{d}^2 + m \frac{\partial \Psi}{\partial b_7} H_3 \mathbf{d}^3 \right) + (d^{1/2} \mathbf{T})(\bar{\mathbf{F}}^{-T} \mathbf{V}^1), \\ \mathbf{t}^5 &= \left(m \frac{\partial \Psi}{\partial b_5} H_3 \mathbf{d}^1 + m \frac{\partial \Psi}{\partial b_8} H_2 \mathbf{d}^2 + m \frac{\partial \Psi}{\partial b_4} H_1 \mathbf{d}^3 \right) + (d^{1/2} \mathbf{T})(\bar{\mathbf{F}}^{-T} \mathbf{V}^2), \\ \mathbf{t}^6 &= \left(m \frac{\partial \Psi}{\partial b_9} H_1 \mathbf{d}^1 + m \frac{\partial \Psi}{\partial b_6} H_3 \mathbf{d}^2 + m \frac{\partial \Psi}{\partial b_2} H_2 \mathbf{d}^3 \right) + (d^{1/2} \mathbf{T})(\bar{\mathbf{F}}^{-T} \mathbf{V}^3), \\ \mathbf{t}^7 &= \left(m \frac{\partial \Psi}{\partial b_{10}} H_2 H_3 \mathbf{d}^1 + m \frac{\partial \Psi}{\partial b_{11}} H_1 H_3 \mathbf{d}^2 + m \frac{\partial \Psi}{\partial b_{12}} H_1 H_2 \mathbf{d}^3 \right), \end{aligned} \tag{2.13}$$

and the remaining quantities \mathbf{t}^i are determined by

$$\mathbf{t}^i = \left(d^{1/2} \mathbf{T} - \sum_{j=4}^7 \mathbf{t}^j \otimes \mathbf{d}_j \right) \cdot \mathbf{d}^i \quad (i = 1, 2, 3). \quad (2.14)$$

These constitutive equations automatically satisfy a nonlinear form of the patch test [Nadler and Rubin 2003].

Next, for elastically isotropic materials it is convenient to use the work of Flory [1961] to introduce the dilation \bar{J} , the pure measures of distortion $\{\bar{\mathbf{F}}', \bar{\mathbf{C}}'\}$ and the scalar measures of distortion $\{\alpha_1, \alpha_2\}$

$$\bar{J} = \det(\bar{\mathbf{F}}), \quad \bar{\mathbf{F}}' = \bar{J}^{-1/3} \bar{\mathbf{F}}, \quad \bar{\mathbf{C}}' = \bar{\mathbf{F}}'^T \bar{\mathbf{F}}', \quad \alpha_1 = \bar{\mathbf{C}}' \cdot \mathbf{I}, \quad \alpha_2 = \bar{\mathbf{C}}' \cdot \bar{\mathbf{C}}'. \quad (2.15)$$

Then, the strain energy function Σ^* can be written in the form

$$\Sigma^* = \hat{\Sigma}^*(\bar{J}, \alpha_1, \alpha_2), \quad (2.16)$$

so that

$$\frac{\partial \Sigma^*}{\partial \bar{\mathbf{C}}} = \frac{\partial \hat{\Sigma}^*}{\partial \bar{J}} \left(\frac{1}{2} \bar{J} \bar{\mathbf{C}}^{-1} \right) + \frac{\partial \hat{\Sigma}^*}{\partial \alpha_1} \left(\bar{J}^{-2/3} \left(\mathbf{I} - \frac{1}{3} (\bar{\mathbf{C}} \cdot \mathbf{I}) \bar{\mathbf{C}}^{-1} \right) \right) + \frac{\partial \hat{\Sigma}^*}{\partial \alpha_2} \left(2 \bar{J}^{-4/3} \left(\bar{\mathbf{C}} - \frac{1}{3} (\bar{\mathbf{C}} \cdot \bar{\mathbf{C}}) \bar{\mathbf{C}}^{-1} \right) \right). \quad (2.17)$$

Also, for the example problems considered later Σ^* is specified in terms of the small deformation bulk modulus K and shear modulus μ , such that

$$\rho_0^* \Sigma^* = \frac{1}{2} K (\bar{J} - 1)^2 + \mu (\alpha_1 - 3), \quad (2.18)$$

where ρ_0^* is the constant reference density of the material, the mass m of the CPE is given by

$$m = \rho_0^* D^{1/2} V. \quad (2.19)$$

and K and Young's modulus E associated with the small deformation response satisfy the equations

$$K = \frac{2\mu(1+\nu)}{3(1-2\nu)}, \quad E = 2\mu(1+\nu). \quad (2.20)$$

Furthermore, for later reference it can be shown [Nadler and Rubin 2003] that the director couples \mathbf{m}^i are related to the traction vector \mathbf{t}^* applied to the boundary ∂P by the integrals

$$\mathbf{m}^i = \int_{\partial P} N^i \mathbf{t}^* da^* \quad (i = 0, 1, \dots, 7), \quad (2.21)$$

where da^* is the current element of area. Also, it can be shown [Loehnert et al. 2005] that $d^{1/2} \mathbf{T}$ is equal to the volume integral of the three-dimensional Cauchy stress \mathbf{T}^*

$$d^{1/2} \mathbf{T} = \int_P \mathbf{T}^* dv^*, \quad (2.22)$$

where dv^* is the current element of volume.

3. Determination of the constitutive coefficients

In this paper the constitutive coefficients B_{ij} in (2.11) are determined by matching solutions of the linearized equations for the CPE with exact solutions of the linear theory of elasticity for special element shapes. Specifically, the classical pure bending solution (e.g., [Sokolnikoff 1956]) of the three dimensional equations of elasticity for a rectangular parallelepiped can be written in the form

$$\begin{aligned} \mathbf{X}^* &= X_i^{*'} \mathbf{e}'_i, & \mathbf{u}^* &= u_i^{*'} \mathbf{e}'_i, & \mathbf{T}^* &= T_{ij}^{*'} (\mathbf{e}'_i \otimes \mathbf{e}'_j), & (i, j = 1, 2, 3) \\ u_1^{*'} &= \gamma X_1^{*'} X_2^{*'}, & u_2^{*'} &= -\frac{1}{2} \gamma ((X_1^{*'})^2 + \nu (X_2^{*'})^2 - \nu (X_3^{*'})^2), & u_3^{*'} &= -\gamma \nu X_2^{*'} X_3^{*'}, \\ T_{11}^{*'} &= 2\mu(1 + \nu^*) \gamma X_2^{*'}, & \text{all other } T_{ij}^{*'} &= 0. \end{aligned} \quad (3.1)$$

In this solution, \mathbf{X}^* locates a material point in the reference configuration, \mathbf{u}^* is the displacement vector, \mathbf{T}^* is the stress tensor, the constant γ controls the magnitude of the bending field and the components of the tensors are referred to the right-handed orthonormal base vectors \mathbf{e}'_i ($i = 1, 2, 3$). Also, the simple torsion-like solution in [Jabareen and Rubin 2008c] can be expressed in the form

$$\begin{aligned} \mathbf{u}^* &= (-\omega \phi X_2^{*'} X_3^{*'}) \mathbf{e}'_1 + (-\omega X_1^{*'} X_3^{*'}) \mathbf{e}'_2 + (\omega X_1^{*'} X_2^{*'}) \mathbf{e}'_3, \\ \mathbf{T}^* &= \mu \omega [-(1 + \phi) X_3^{*'} (\mathbf{e}'_1 \otimes \mathbf{e}'_2 + \mathbf{e}'_2 \otimes \mathbf{e}'_1) + (1 - \phi) X_2^{*'} (\mathbf{e}'_1 \otimes \mathbf{e}'_3 + \mathbf{e}'_3 \otimes \mathbf{e}'_1)], \end{aligned} \quad (3.2)$$

where the constant ω is the twist per unit length in the \mathbf{e}'_1 direction and the constant ϕ controls the warping of the cross-section with unit normal \mathbf{e}'_1 .

In order to determine values of the coefficients B_{ij} it is convenient to consider the following three elements shapes, which are defined in terms of another fixed rectangular Cartesian triad \mathbf{e}_i as follows:

Element E1 ($D_{12} \neq 0, D_{13} = 0, D_{23} = 0$)

$$\mathbf{D}_1 = \mathbf{e}_1, \quad \mathbf{D}_2 = D_{12} \mathbf{e}_1 + \sqrt{1 - D_{12}^2} \mathbf{e}_2, \quad \mathbf{D}_3 = \mathbf{e}_3, \quad \mathbf{D}_i = 0 \quad (i = 0, 4, 5, 6, 7), \quad (3.3a)$$

Element E2 ($D_{12} = 0, D_{13} \neq 0, D_{23} = 0$)

$$\mathbf{D}_1 = \mathbf{e}_1, \quad \mathbf{D}_2 = \mathbf{e}_2, \quad \mathbf{D}_3 = D_{13} \mathbf{e}_1 + \sqrt{1 - D_{13}^2} \mathbf{e}_3, \quad \mathbf{D}_i = 0 \quad (i = 0, 4, 5, 6, 7), \quad (3.3b)$$

Element E3 ($D_{12} = 0, D_{13} = 0, D_{23} \neq 0$)

$$\mathbf{D}_1 = \mathbf{e}_1, \quad \mathbf{D}_2 = \mathbf{e}_2, \quad \mathbf{D}_3 = D_{23} \mathbf{e}_2 + \sqrt{1 - D_{23}^2} \mathbf{e}_3, \quad \mathbf{D}_i = 0 \quad (i = 0, 4, 5, 6, 7), \quad (3.3c)$$

where the metric D_{ij} is defined by

$$D_{ij} = \mathbf{D}_i \cdot \mathbf{D}_j. \quad (3.4)$$

Each of these element shapes is a parallelepiped with two right angles. Now, from [Nadler and Rubin 2003] it follows that for these element shapes the reference geometry is characterized by

$$V = H_1 H_2 H_3, \quad V^i = 0 \quad (i = 1, 2, 3, 4), \quad (3.5)$$

and the position vector \mathbf{X}^* in (2.2) and the Cartesian coordinates $X_i^{*'}$ can be expressed in the forms

$$\mathbf{X}^* = \sum_{j=1}^3 \theta^j \mathbf{D}_j, \quad X_i^{*'} = \sum_{j=1}^3 \theta^j (\mathbf{e}'_i \cdot \mathbf{D}_j). \quad (3.6)$$

Consequently, the exact displacements \mathbf{u}^* and stresses \mathbf{T}^* in (3.1) and (3.2) can be rewritten as functions of the convected coordinates θ^i ($i = 1, 2, 3$).

Within the context of the linear theory of a CPE [Nadler and Rubin 2003] the director displacements δ_i are defined such that

$$\mathbf{d}_i = \mathbf{D}_i + \delta_i, \quad (i = 0, 1, \dots, 7), \tag{3.7}$$

and for the special elements defined by (3.3) the linearized forms of the inhomogeneous strains β_i become

$$\beta_i = \delta_{i+3} \quad (i = 1, 2, 3, 4). \tag{3.8}$$

As explained in [Nadler and Rubin 2003], the values δ_i^* of the element director displacements δ_i which correspond to the exact displacement field \mathbf{u}^* need to be properly defined. Specifically, for these element shapes the values δ_i^* are determined by the equations in [Nadler and Rubin 2003] which connect δ_i^* to integrals over the reference element region of derivatives of \mathbf{u}^* with respect to the convected coordinates. In particular, for the exact solutions (3.1) and (3.2) and the element shapes (3.3) it can be shown that these expressions yield

$$\delta_1^* = \delta_2^* = \delta_3^* = \delta_7^* = 0, \tag{3.9}$$

so that when δ_i are replaced by the exact values δ_i^* the linearized values of κ_4^i vanish

$$\kappa_4^1 = \kappa_4^2 = \kappa_4^3 = 0, \tag{3.10}$$

and the linearized forms of the constitutive equations (2.13) and (2.14) reduce to

$$\begin{aligned} d^{1/2} \mathbf{T} &= 0, \quad \mathbf{t}^i = 0 \quad (i = 0, 1, 2, 3, 7), \\ \mathbf{t}^4 &= \left(m \frac{\partial \Psi}{\partial b_1} H_2 \mathbf{D}^1 + m \frac{\partial \Psi}{\partial b_3} H_1 \mathbf{D}^2 + m \frac{\partial \Psi}{\partial b_7} H_3 \mathbf{D}^3 \right), \\ \mathbf{t}^5 &= \left(m \frac{\partial \Psi}{\partial b_5} H_3 \mathbf{D}^1 + m \frac{\partial \Psi}{\partial b_8} H_2 \mathbf{D}^2 + m \frac{\partial \Psi}{\partial b_4} H_1 \mathbf{D}^3 \right), \\ \mathbf{t}^6 &= \left(m \frac{\partial \Psi}{\partial b_9} H_1 \mathbf{D}^1 + m \frac{\partial \Psi}{\partial b_6} H_3 \mathbf{D}^2 + m \frac{\partial \Psi}{\partial b_2} H_2 \mathbf{D}^3 \right) \end{aligned} \tag{3.11}$$

where \mathbf{d}^i have been replaced by the reference values \mathbf{D}^i . Also, the values of \mathbf{m}^i in (2.21) associated with the exact solutions (3.1) and (3.2) are given by

$$\mathbf{m}^i = 0 \quad (i = 0, 1, 2, 3, 7), \quad \mathbf{m}^i = \int_{\partial P_0} N^i \mathbf{T}^* N^* dA^* \quad (i = 4, 5, 6), \tag{3.12}$$

where ∂P_0 is the reference boundary of the CPE, N^* is the unit outward normal to ∂P_0 and dA^* is the reference element of area. It then follows that within the context of the linearized theory, the equations of equilibrium associated with the bending (3.1) and torsion (3.2) solutions reduce to three vector equations

$$\mathbf{t}^i - \mathbf{m}^i = 0 \quad (i = 4, 5, 6). \tag{3.13}$$

Analytical expressions for B_{ij} can be developed by matching the solutions (3.1) and (3.2) for each of the element shapes (3.3). Then, the resulting coefficients are combined in a manner that ensures that B_{ij}

is a positive definite tensor. Specifically, with reference to the element shape E1 in (3.3a) consider six bending solutions associated with specifications of the orientation of e'_i relative to D_i

$$\text{Bending B1 : } e'_1 = D_1, \quad e'_3 = D_3, \tag{3.14a}$$

$$\text{Bending B2 : } e'_1 = D_1, \quad e'_2 = D_3 \tag{3.14b}$$

$$\text{Bending B3 : } e'_1 = D_2, \quad e'_3 = D_3 \tag{3.14c}$$

$$\text{Bending B4 : } e'_1 = D_2, \quad e'_2 = D_3 \tag{3.14d}$$

$$\text{Bending B5 : } e'_1 = D_3, \quad e'_3 = D_2 \tag{3.14e}$$

$$\text{Bending B6 : } e'_1 = D_3, \quad e'_3 = -D_1 \tag{3.14f}$$

Also, consider two torsion solutions associated with specifications

$$\text{Torsion T1 : } e'_1 = D_1, \quad e'_3 = D_3, \tag{3.15a}$$

$$\text{Torsion T2 : } e'_1 = D_2, \quad e'_3 = D_3, \tag{3.15b}$$

For each bending and torsion solution the exact displacements u^* are used to determine the exact values δ_i^* . Then, the linearized values of κ_j^i are determined using (2.9) and (3.8) with δ_i replaced by δ_i^* and the resulting constitutive equations for t^i are determined by (3.11). Similarly, the values of m^i are determined by using the exact stress T^* in the equations (3.12). Also, the values of the warping constant ϕ which corresponds to nearly pure torsion [Jabareen and Rubin 2008c] are determined by

$$\text{Torsion T1 : } m^6 \cdot D_1 = 0 \Rightarrow \phi = \frac{H_2^2(1 - D_{12}^2) - H_3^2}{H_2^2(1 - D_{12}^2) + H_3^2}, \tag{3.16a}$$

$$\text{Torsion T2 : } m^5 \cdot D_2 = 0 \Rightarrow \phi = \frac{H_1^2(1 - D_{12}^2) - H_3^2}{H_1^2(1 - D_{12}^2) + H_3^2}, \tag{3.16b}$$

In these expressions it can be seen that $\{m^6, D_1\}$ are associated with the cross-sectional coordinates $\{\theta^2, \theta^3\}$ and $\{m^5, D_2\}$ are associated with the cross-sectional coordinates $\{\theta^1, \theta^3\}$. With reference to Figure 2 it can also be seen that these expressions are similar to those in [Nadler and Rubin 2003] since the cross-section normal to D_1 has lengths $\{H_2\sqrt{1 - D_{12}^2}, H_3\}$ and the cross-section normal to D_2 has

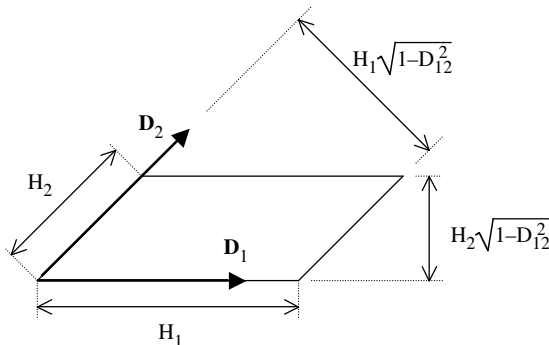


Figure 2. Cross-section of the parallelepiped element E1.

lengths $\{H_1\sqrt{1 - D_{12}^2}, H_3\}$. For each bending solution the value of γ can be eliminated in the resulting equations of equilibrium (3.13) and the value of ω can be eliminated from each of the equations of equilibrium associated with the torsion solutions. Also, the values (3.16) are used in the resulting torsion equations. It therefore follows that each of the solutions (B1)-(B6), (T1) and (T2) yield nine scalar equations of equilibrium which total 72 scalar equations to determine the values of B_{ij} as functions of H_i and D_{12} . Some of these scalar equations are trivially satisfied and others are redundant. In particular, using a symbolic program like Maple it can be shown that the equations associated with the bending solutions (3.14) can be solved for B_{ij} ($i, j = 1, 2, \dots, 5$) in terms of

$$\{B_{77}, B_{78}, B_{79}, B_{88}, B_{89}, B_{99}\}. \tag{3.17}$$

Then, these expressions can be substituted into the equations for torsion to determine all of the values of B_{ij} ($i, j = 1, 2, \dots, 9$) in terms of one of the values $\{B_{77}, B_{88}, B_{99}\}$, say B_{77} .

Next, it is noted that the strain energy function Ψ in (2.11) will be positive definite provided that the coefficient matrix B_{ij} is positive definite. The results of the calculations just described yield a form for B_{ij} which separates into two matrices $[B_{ij}$ ($i, j = 1, 2, 3, 4$)] and $[B_{ij}$ ($i, j = 5, 6, \dots, 9$)]. In particular, it can be shown that

$$\det(B_{ij}) = (1 - \nu)^2(1 + \nu)^2(1 - D_{12}^2)^2 > 0, \quad (i, j = 1, 2, 3, 4) \tag{3.18}$$

which is independent of the lengths H_i and is positive for the full range of Poisson's ratio and D_{12}

$$-1 < \nu < \frac{1}{2}, \quad -1 < D_{12} < 1. \tag{3.19}$$

Moreover, the $\det(B_{ij})$ for ($i, j = 5, 6, \dots, 9$) is a linear function of B_{77} , which has the value

$$\det(B_{ij}) = \frac{1}{2}(1 - \nu)^4(1 + \nu) \text{ for } (i, j = 5, 6, \dots, 9) \quad \text{and} \quad D_{12} = 0. \tag{3.20}$$

It was found that if the value of B_{77} is specified so that

$$\det(B_{ij}) = \frac{1}{2}(1 - \nu)^4(1 + \nu)(1 - D_{12}^2) \quad \text{for } (i, j = 5, 6, \dots, 9), \tag{3.21}$$

then the expressions for B_{ij} are quite simple and

$$\det(B_{ij}) = \frac{1}{2}(1 - \nu)^6(1 + \nu)^3(1 - D_{12}^2)^3 \quad \text{for } (i, j = 1, 2, \dots, 9), \tag{3.22}$$

which is positive for the range of values (3.19).

Similar procedures can be used to define bending and torsion solutions for the element shapes E2 and E3 and the resulting equations can be solved for B_{ij} to determine the dependence on the metrics D_{13} and D_{23} . Next, define auxiliary variables $\{\lambda_{12}, \lambda_{13}, \lambda_{23}\}$ as follows:

For $D_{12}^2 + D_{13}^2 + D_{23}^2 = 0$:

$$\lambda_{12} = \lambda_{13} = \lambda_{23} = 0, \tag{3.23a}$$

For $D_{12}^2 + D_{13}^2 + D_{23}^2 > 0$:

$$\lambda_{12} = \frac{D_{12}^2}{D_{12}^2 + D_{13}^2 + D_{23}^2}, \lambda_{13} = \frac{D_{13}^2}{D_{12}^2 + D_{13}^2 + D_{23}^2}, \lambda_{23} = \frac{D_{23}^2}{D_{12}^2 + D_{13}^2 + D_{23}^2}. \tag{3.23b}$$

Then it is possible to denote the values of B_{ij} associated with the solutions of the three elements E1-E3 in (3.3) by B_{ij}^{12} for E1, by B_{ij}^{13} for E2, and by B_{ij}^{23} for E3. Moreover, the matrix B_{ij}^0 is defined so that it yields a strain energy function Ψ equivalent to that obtained in [Nadler and Rubin 2003] for a rectangular parallelepiped, when the value of the torsion function $b^*(1)$ is taken to be 1/2 as suggested in [Jabareen and Rubin 2008c]. Then, the general expression $B_{ij}(D_{12}, D_{13}, D_{23})$ combining these solutions is

$$B_{ij}(D_{12}, D_{13}, D_{23}) = (1 - \lambda_{12} - \lambda_{13} - \lambda_{23})B_{ij}^0 + \lambda_{12}B_{ij}^{12} + \lambda_{13}B_{ij}^{13} + \lambda_{23}B_{ij}^{23}. \quad (3.24)$$

Now, using the definitions (3.23) it follows that each of the coefficients $\{(1 - \lambda_{12} - \lambda_{13} - \lambda_{23}), \lambda_{12}, \lambda_{13}, \lambda_{23}\}$ is non-negative and that at least one of them is positive. Also, each of the matrices $\{B_{ij}^0, B_{ij}^{12}, B_{ij}^{13}, B_{ij}^{23}\}$, given in Appendix A, is positive definite so that the combined matrix $B_{ij}(D_{12}, D_{13}, D_{23})$ is also positive definite for all reference element shapes.

4. Examples

For planar problems (in the D_1 - D_2 plane with $D_{13} = D_{23} = 0$) it was shown in [Jabareen and Rubin 2008a] that

$$b_5 = b_6 = b_7 = b_8 = b_9 = b_{10} = b_{11} = 0. \quad (4.1)$$

Moreover, since the values of B_{ij} ($i, j = 1, 2, 3, 4$) for these planar problems reduce to those of the improved CPE in [Jabareen and Rubin 2007b], the results of the improved and generalized CPE will be identical for all planar problems. Consequently, the results of the example problems of a Cook’s membrane, a Kirsch problem and buckling of a block considered in [Jabareen and Rubin 2007a; 2007b] are identical to those that would be predicted by the generalized CPE of Sections 2 and 3. In particular, it follows that the generalized CPE is free of the unphysical hourglassing that is predicted by the elements in ABAQUS, ADINA, ANSYS and FEAP [Taylor 2005] based on enhanced strain and incompatible mode methods.

In this section a number of example problems are considered to examine the predictions of the generalized CPE which show that it is more accurate than the improved CPE in [Jabareen and Rubin 2007b]. For all of the example problems the full nonlinear equations are solved using the constitutive equations (2.13) and (2.14) with strain energy specified by (2.8), (2.13), (2.14) and (2.18), even when the loads are small and the deformations remain small. Also, for irregular shaped elements the values of V^i in (2.7) and (2.13) can be nonzero so the response is examined for more general conditions than those used in the last section used to develop expressions for the constitutive coefficients B_{ij} . Unless otherwise stated the material is taken to be compressible with

$$K = 1 \text{ GPa}, \quad \mu = 0.6 \text{ GPa}, \quad \nu = 0.25. \quad (4.2)$$

For the special examples which consider a nearly incompressible the material constants are specified by

$$K = 1000 \text{ GPa}, \quad \mu = 0.6 \text{ GPa}, \quad \nu \approx 0.4997. \quad (4.3)$$

Furthermore, it was shown in [Jabareen and Rubin 2007a; 2007b] that the enhanced strain element in FEAP produces results similar to the enhanced strain or incompatible mode elements in ABAQUS, ADINA and ANSYS so that comparison with these types of elements will be limited to the element in FEAP.

For the calculations with the improved CPE presented here use is made of the modified torsion coefficients discussed in [Jabareen and Rubin 2008c]. In addition, for the improved CPE the matrices B_{ij} associated with the individual metrics $\{D_{12}, D_{13}, D_{23}\}$ are combined using an expression of the form (3.24) instead of using the method described in [Jabareen and Rubin 2007b] for ensuring that B_{ij} remains positive definite.

Furthermore, in the following figures the symbols {G, I, F, Q1, Q1P0, HO9} denote predictions of: the generalized CPE developed here; the improved CPE developed in [Jabareen and Rubin 2007b]; the enhanced strain, full integration, mixed element for nearly incompressible materials and the mixed higher order 9 node quadrilateral in FEAP, respectively. Also, it is noted that when the elements are rectangular parallelepipeds with $(D_{12} = D_{13} = D_{23} = 0)$ the predictions of (G) and (I) are identical.

4.1. Shear load on a thin cantilever beam (small deformations). Figure 3 shows a sketch of a thin cantilever beam with dimensions

$$L = 200 \text{ mm}, \quad H = W = 10 \text{ mm}, \tag{4.4}$$

which is fully clamped at its end $X_1^* = 0$ and is subjected to a shear force P (modeled by a uniform shear stress) applied in the e_2 direction to its end $X_1^* = L$. The lateral surfaces are traction free. The mesh $\{20n \times n \times n\}$ is defined by distorting the middle cross-section in its reference configuration (using the parameters a_1, a_2, a_3, a_4 shown in Figure 3), with $10n$ elements on each side of this cross-section and n elements in each of the e_2 and e_3 directions. Two cases of element distortion are considered:

$$\begin{aligned} \text{Case I: } & a_1 = a, \quad a_2 = -a, \quad a_3 = a, \quad a_4 = -a, \\ \text{Case II: } & a_1 = a, \quad a_2 = a, \quad a_3 = -a, \quad a_4 = -a, \end{aligned} \tag{4.5}$$

and the parameter a/H defines the element irregularity. Both of these cases cause the middle surface to remain planar with the normal to that surface being in the e_1 - e_2 plane for Case I and in the e_1 - e_3 plane for Case II. The value

$$u_{A2}^* = 0.21310 \text{ mm} \quad \text{for } P = 0.1 \text{ N} \tag{4.6}$$

of the e_2 component of the displacement of point A (see Figure 3) predicted by (G) with the most refined mesh ($n = 5$) and a regular mesh ($a/H = 0$) is considered to be exact and the error E associated with

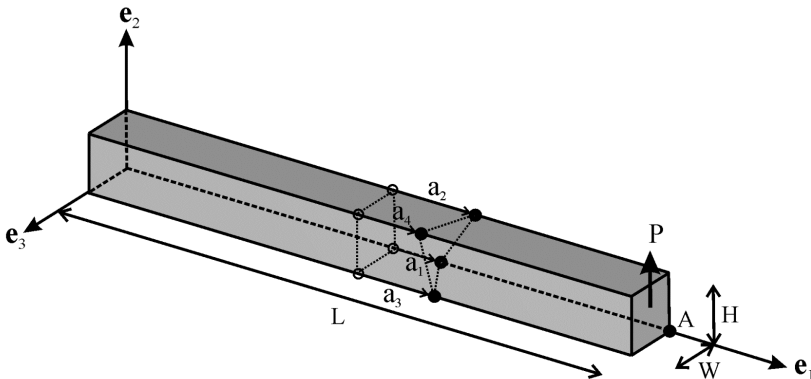


Figure 3. Shear load on a thin cantilever beam. The irregular element mesh is based on the distorted center cross-section.

the predictions u_{A2} of other calculations for the same value of P is defined by

$$E = \frac{u_{A2} - u_{A2}^*}{|u_{A2}^*|} \tag{4.7}$$

Figure 4a shows the error as a function of the irregularity parameter a/H for Case I with $n = 1$. Ideally the response should be nearly insensitive to the value of a/H . This figure shows that the predictions of (G) and (I) are identical and are slightly more accurate than those of (F) for large values of irregularity. Figure 4b shows that the three elements converge to the same value for Case I with the refined mesh ($n = 5$) and large irregularity $a/H = 2$. The results for Case II shown in Figures 4c,d indicate that (G) is again slightly more accurate than (F) and that they both converge to the same solution. In contrast, Figures 4c,d show that (I) predicts significant errors and converges slowly for large irregularities. It will be shown later that this deficiency for Case II causes (I) to be inaccurate for out-of-plane bending of a rhombic plate.

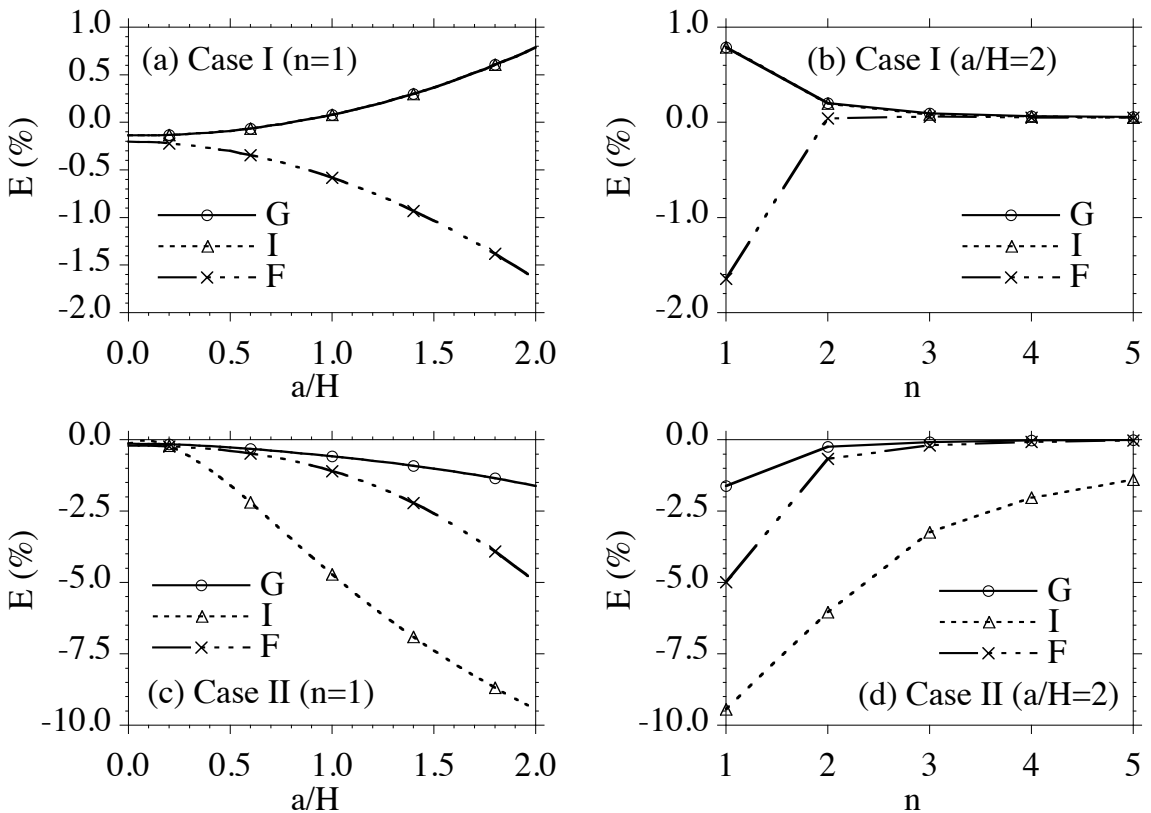


Figure 4. Shear load on a thin cantilever beam (small deformations). (a,c) Errors in the displacement of the point A in the e_2 direction versus the distortion parameter a/H and; (b,d) the errors versus n for the mesh $\{20n \times n \times n\}$ defined for two cases of element distortion.

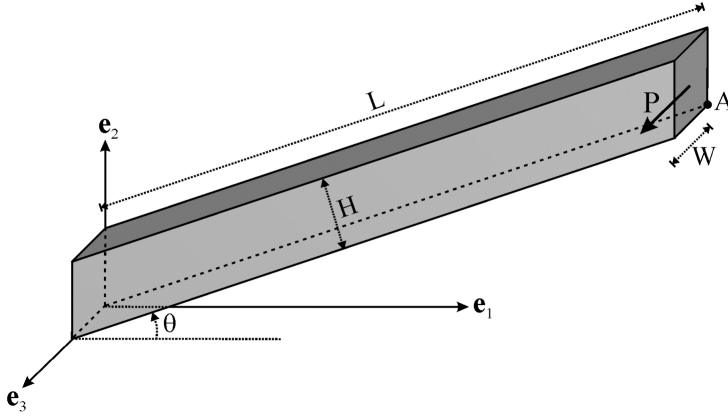


Figure 5. Shear load on a thin slanted cantilever beam.

4.2. *Shear load on a thin slanted cantilever beam (small deformations).* Figure 5 shows a sketch of a thin slanted cantilever beam with dimensions (4.4) and with the slanting angle θ . The boundary conditions are the same as those for the previous example except that the shear load P is applied in the e_3 direction to emphasize differences between the predictions of (G) and (I). Again the mesh is taken to be $\{20n \times n \times n\}$ with $20n$ elements in axial direction of the beam. All of the elements have parallelogram cross-sections in the e_1 - e_2 plane with sides parallel to the ends of the beam.

Figure 6a shows the displacement component u_{A3} of point A (see Figure 5) in the e_3 direction as a function of θ for the most refined mesh ($n = 5$). The error E in u_{A3} is defined in a similar manner to (4.7) with the exact value u_{A3}^* taken to be that predicted by (G) for each value of θ with $n = 5$ and with the load P given by (4.6). Figures 6b,c show that (G) and (F) converge to the same values and that (G) is slightly more accurate than (F) for $n=1$ and large values of θ . Also, it can be seen that (I) predicts significant errors with slow convergence.

4.3. *Shear load on a thin twisted cantilever beam (small deformations).* The problem of shear loading of a thin twisted beam provides a severe test of the accuracy of an element formulation since the elements have irregular shapes and the response couples torsion and bending modes of deformation. In its unstressed reference configuration the twisted beam has length L and a rectangular cross-section with height H and width W given by

$$L = 200 \text{ mm}, \quad H = 10 \text{ mm}, \quad W = 2 \text{ mm}. \tag{4.8}$$

Also, each of the cross-sections is twisted by the angle θ such that the position of a material point X^* in the reference configuration is given by

$$\begin{aligned} X^* &= X_i^{*'} e_i', & \theta &= \frac{X_1^{*'}}{L} \Theta, \\ e_1' &= e_1, & e_2' &= \cos \theta e_2 + \sin \theta e_3, & e_3' &= -\sin \theta e_2 + \cos \theta e_3, \end{aligned} \tag{4.9}$$

where Θ controls the magnitude of the twist. Furthermore, the influence of irregular element meshes is explored by applying the twist θ to the cross-sections of the beam shown in Figure 3 and in Figure 7 using the element irregularity specified by Case I in (4.5). The surface $X_1^{*'} = 0$ is fully clamped, a shear

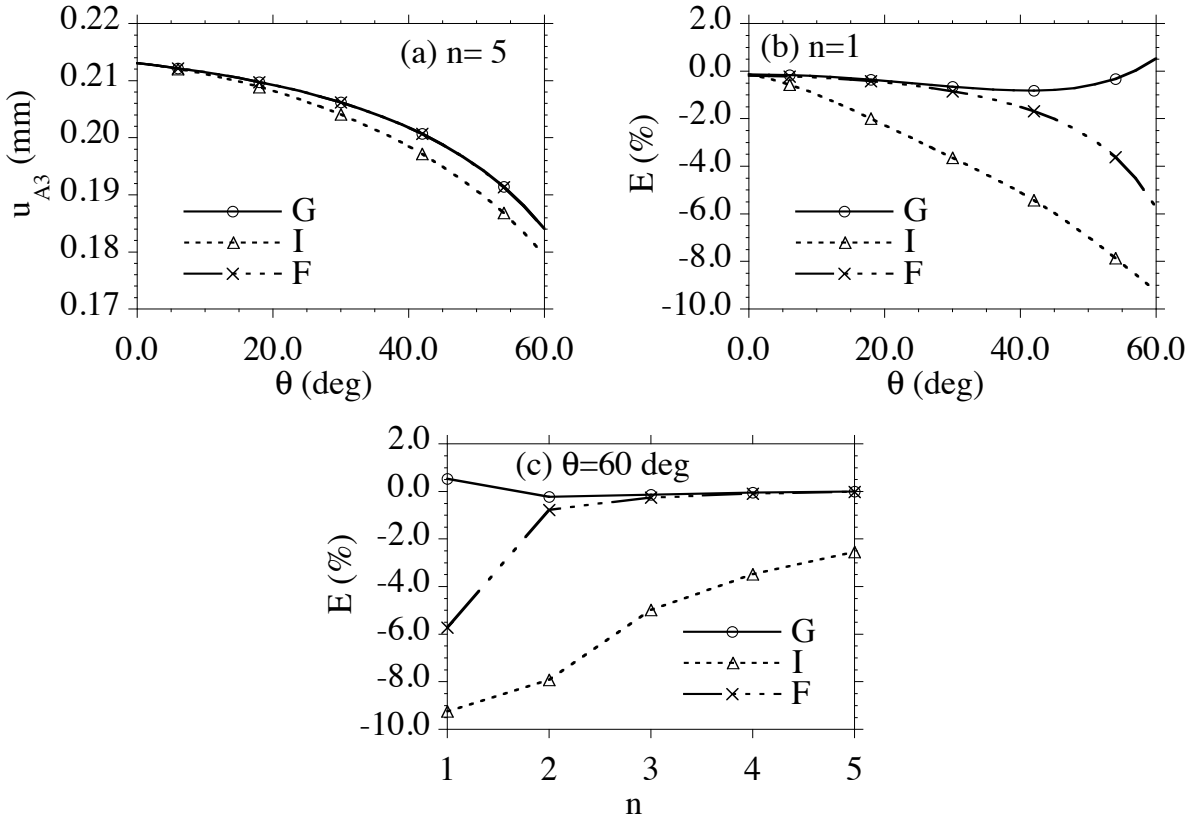


Figure 6. Shear load on a thin slanted cantilever beam (small deformations). (a) Displacement u_{A3} of the point A in the e_3 direction versus the angle θ for $n = 5$ with the mesh $\{20n \times n \times n\}$; (b) errors in u_{A3} versus θ for $n = 1$; (c) errors in u_{A3} versus n for $\theta = 60$ deg.

force P (modeled by a uniform shear stress) is applied to the end $X_1^* = L$ in the constant e_2' direction (defined by its direction in the reference configuration) and the remaining lateral surfaces are traction free. Also, the element mesh for this problem is specified by $\{20n \times n \times n\}$ with $20n$ elements along the length of the beam.

Figure 8a shows the component u'_{B2} of the displacement of the point B (see Figure 7) in the e_2' direction

$$u'_{B2} = \mathbf{u}_B \cdot \mathbf{e}'_2, \tag{4.10}$$

versus the pre-twist Θ for the most refined mesh with $n = 5$, no element irregularity ($a/H = 0$) and the load given by

$$P = 0.01 \text{ N}. \tag{4.11}$$

This value of load is used for all calculations in this subsection. It can be seen that $\{G, I, F\}$ converge to the same results. Thus, the value u'^*_{B2} of u'_{B2} predicted by (G) for $n = 5$ is considered to be exact and the error E of other calculations is defined in a similar manner to (4.7). Figures 8b,c show the influence of element irregularity for the coarse mesh with $n = 1$ and Figures 8d,e consider a finer mesh

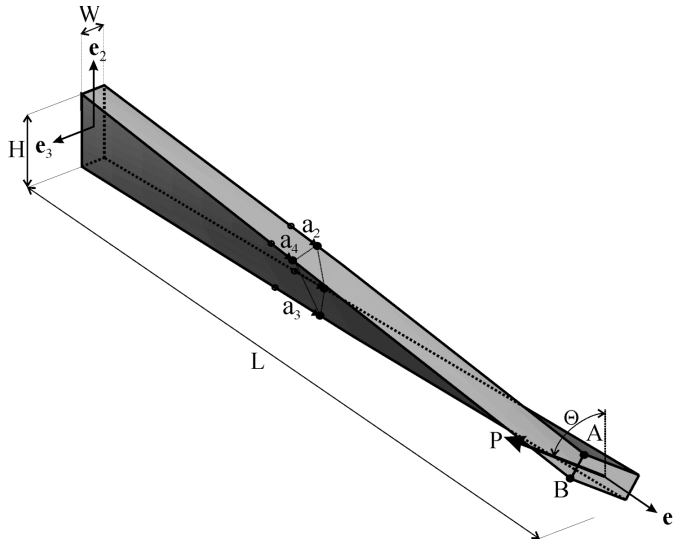


Figure 7. Shear load on a thin twisted cantilever beam. The element mesh is based on the distorted center cross-section.

with $n = 2$. From these figures it can be seen that (G) is as accurate as (F) and is much more accurate than (I), especially for irregular shaped elements.

4.4. Lateral torsional buckling of a thin cantilever beam (large deformations). For this example the beam and element mesh are characterized by the same parameters as used in Section 4.3 with the shear force P being applied in the e'_2 direction. To investigate rotation of the beam's end it is convenient to consider the difference in the displacements of the points A and B shown in Figure 7. Specifically, the quantity Δu is defined by

$$\Delta u = (\mathbf{u}_B - \mathbf{u}_A) \cdot \mathbf{e}'_2. \tag{4.12}$$

Figure 9 shows the results for large deformation lateral torsional buckling of a thin cantilever beam. Again it is emphasized that the direction e'_2 of the load is held constant during loading. The buckling process is triggered by the small pre-twist

$$\Theta = 0.1 \text{ deg}, \tag{4.13}$$

which smoothes out the bifurcation that would occur for a perfect beam with $\Theta = 0$. Figure 10 shows the results for shear loading with a large pre-twist

$$\Theta = 30 \text{ deg}. \tag{4.14}$$

Moreover, the curves in Figures 9 and 10 denoted by (E) are predicted by (G) with $n = 5$ and $a/H = 0$ and are considered to be exact.

The results in Figure 9 show that for $n = 2$ (Figures 9a,b) the predictions are not yet converged and are sensitive to element irregularity with large errors being predicted by (I). Figures 9c,d show that for $n = 3$ the predictions are reasonably converged and that the sensitivity of element irregularity is reduced for {G, F} but that (I) still predicts large errors.

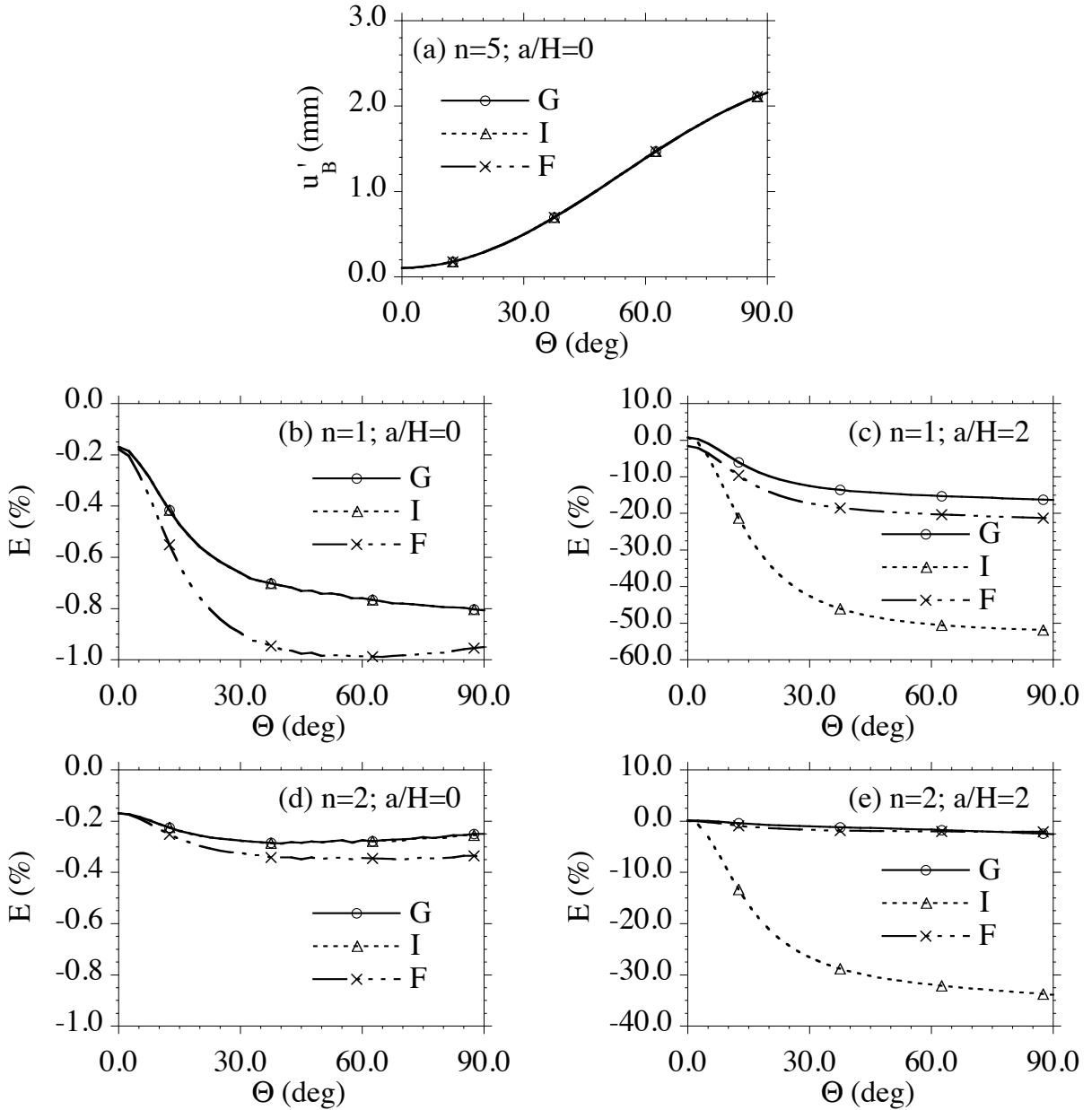


Figure 8. Shear loading of a thin twisted cantilever beam with a pre-twist Θ and the mesh $\{20n \times n \times n\}$ (small deformations). The influence of element irregularity is shown in the middle row graphs for $n = 1$ and in the bottom graphs for $n = 2$.

The results in [Figure 10](#) for shearing of a thin cantilever beam with a large pre-twist again show that the predictions of $\{G, F\}$ are relatively accurate but that the predictions of $\{I\}$ are inaccurate for the irregular shaped elements even for the mesh with $n = 3$ ([Figure 10d](#)). This result is consistent with that in [[Jabareen and Rubin 2007b](#), [Figure 8b](#)], which showed that the error of out-of-plane bending of a beam

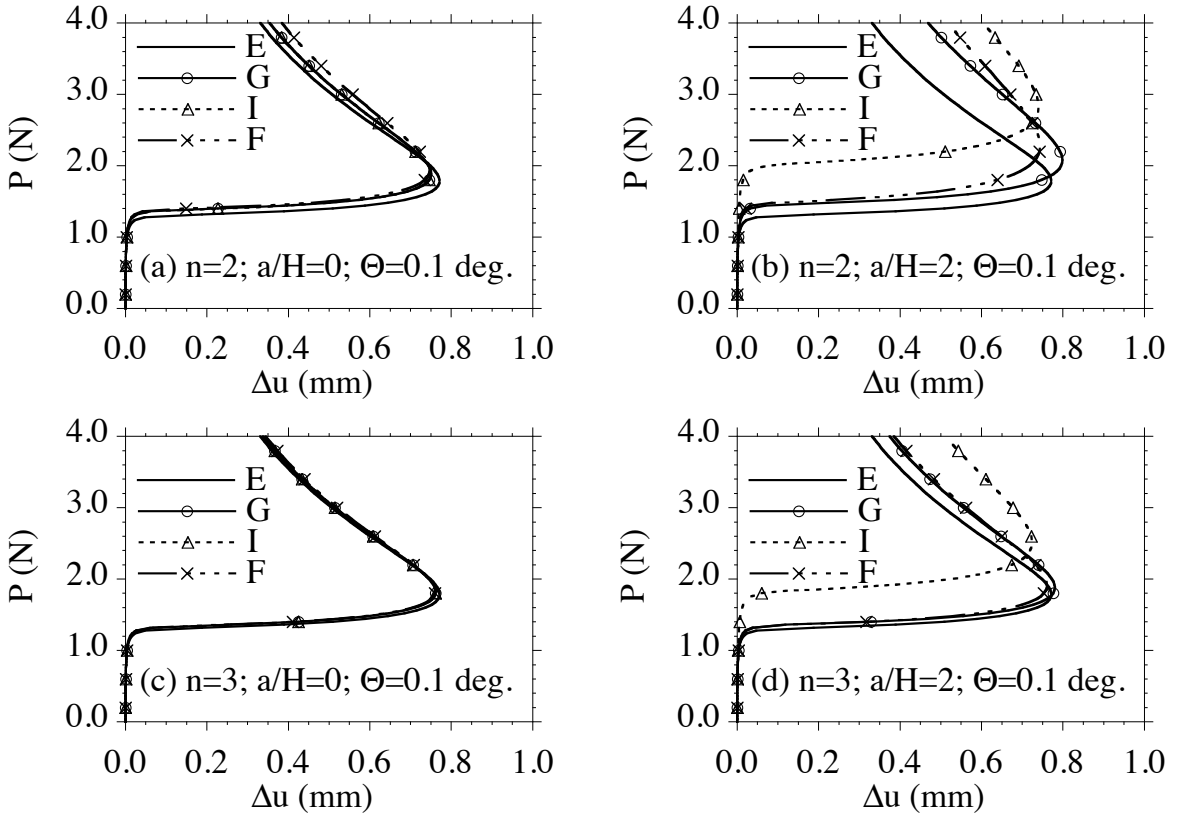


Figure 9. Large deformation lateral torsional buckling of a thin cantilever beam with a small pre-twist $\Theta = 0.1$ deg. using the mesh $\{20n \times n \times n\}$. The influence of element irregularity is shown in the top two graphs for $n = 2$ and in the bottom two for $n = 3$.

with the element irregularity of Case I [(4.5) here] does not have a zero slope as a/H approaches zero. Furthermore, this error causes (I) to predict inaccurate results for out-of-plane bending of a rhombic plate, as will be shown next.

4.5. Point load on the corner of a thin partially clamped rhombic plate (small deformations). Figure 11 shows a sketch of one quarter of a thin fully clamped rhombic plate with dimensions

$$L = 500 \text{ mm}, \quad H = 10 \text{ mm}, \tag{4.15}$$

with two clamped and two free edges and which is loaded at its corner by a point force. The length of each edge is L and the load is specified by

$$P = 1 \text{ N}. \tag{4.16}$$

The mesh used for the plate is defined by $\{10n \times 10n \times n\}$ with n elements through the thickness.

Figure 12a shows the component u_{A3} of the displacement of the point A in the e_3 direction as a function of θ for the most refined mesh ($n = 5$). The error E in this displacement is defined in a similar

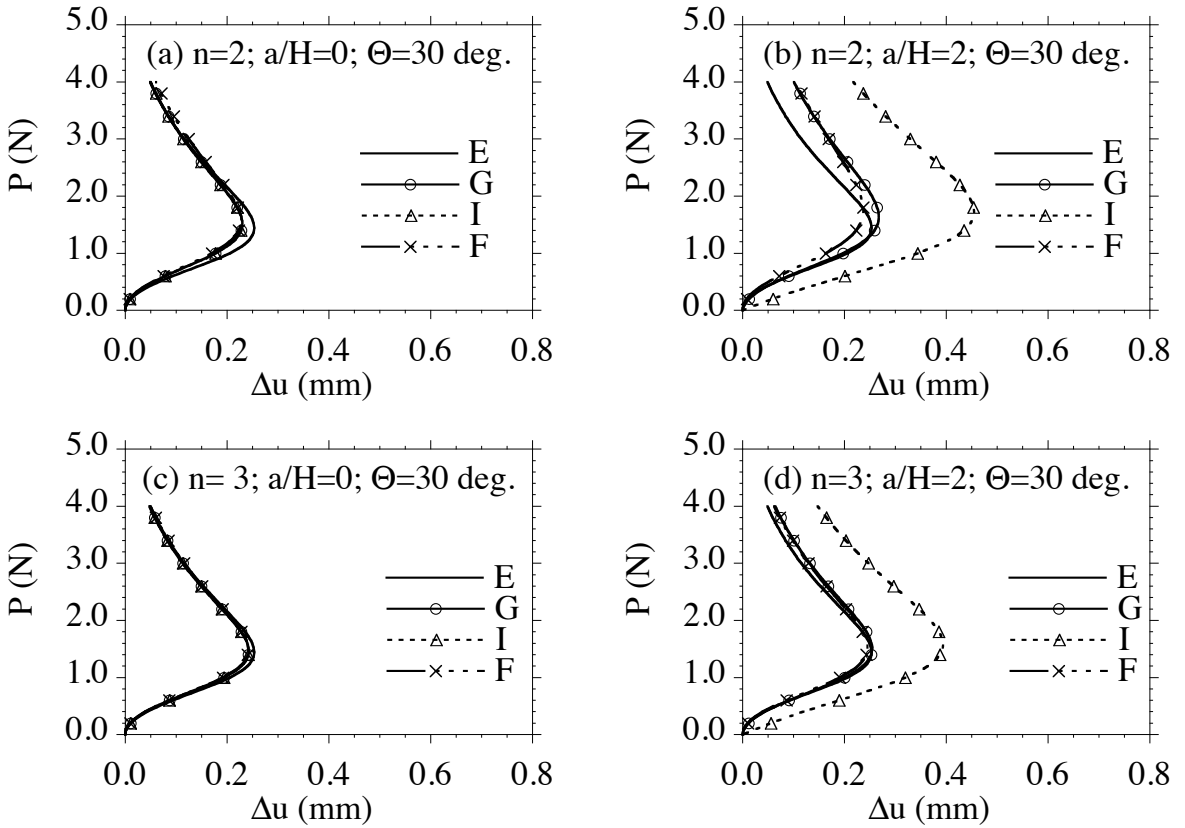


Figure 10. Large deformation shear loading of a thin cantilever beam with a pre-twist $\Theta = 30$ deg using the mesh $\{20n \times n \times n\}$. The influence of element irregularity is shown in the top two graphs for $n = 2$ and in the bottom two for $n = 3$.

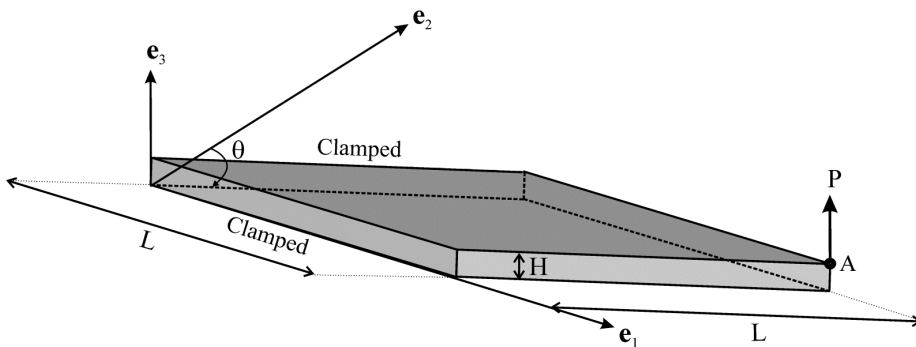


Figure 11. Point load on the corner of a thin partially clamped rhombic plate.

manner to (4.7) with the exact value u_{A3}^* taken to be that predicted by (G) for each value of θ with $n = 5$ and the load P given by (4.16). Figures 12b,c show that $\{G, F\}$ predict nearly the same values, that (I) predicts significant errors for $n = 1$ (especially for the angle $\theta = 60$ deg) and that (I) exhibits slow convergence.

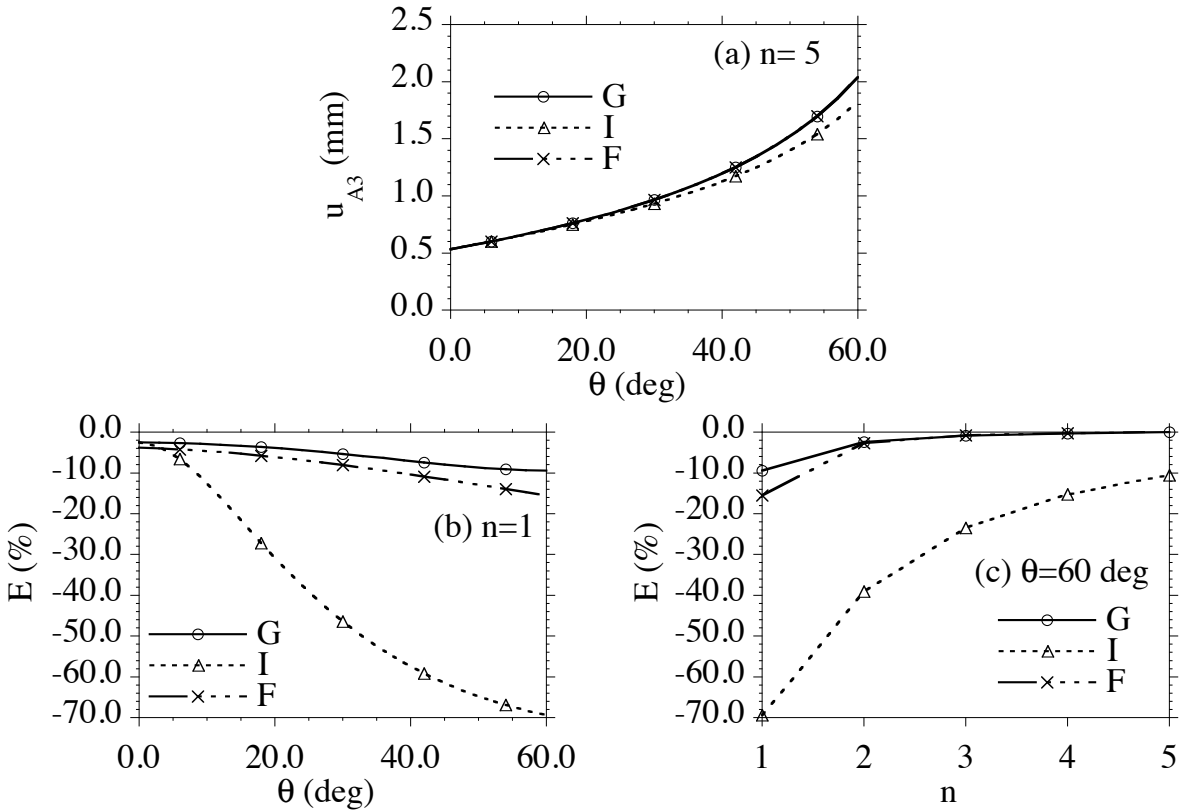


Figure 12. Point load on the center of a thin fully clamped rhombic plate (small deformations). Displacement u_{A3} of the point A in the e_3 direction versus the angle θ for $n = 5$ with the mesh $\{10n \times 10n \times n\}$; (b) errors in u_{A3} versus θ for $n = 1$; (c) errors in u_{A3} versus n for $\theta = 60$ deg.

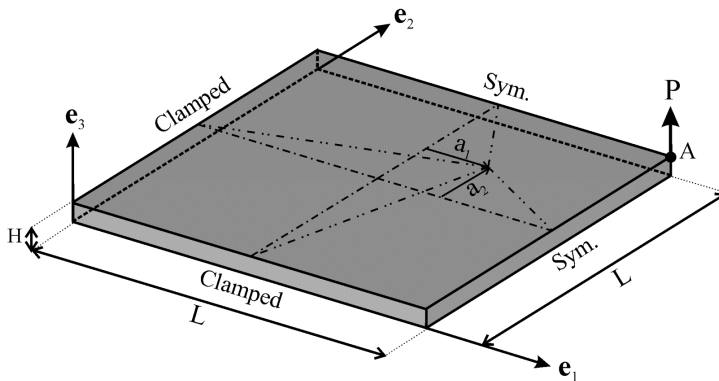


Figure 13. Point load on the center of a thin fully clamped square plate with an irregular element mesh.

4.6. Point load on the center of a thin fully clamped square plate with an irregular element mesh (small deformations). Figure 13 shows a sketch of one quarter of a thin fully clamped square plate with dimensions (4.8) that is loaded by a point force at its center. Only one quarter of the plate is modeled and

the value P given by (4.16) corresponds to one quarter of the load that would be applied to the center of the entire plate. Irregular elements are specified by moving the center point of the quarter section to the position characterized by the lengths $\{a_1, a_2\}$ (shown in Figure 13) defined by two cases:

$$\text{Case I: } a_1 = a_2 = a, \quad -1 \leq \frac{4a}{L} \leq 1, \tag{4.17}$$

$$\text{Case II: } a_1 = \frac{L}{4} \cos(\theta), \quad a_2 = \frac{L}{4} \sin(\theta), \quad 0 \leq \theta \leq 2\pi.$$

The quarter section of the plate is meshed by $\{10n \times 10n \times n\}$ with each subsection being meshed by $\{5n \times 5n \times n\}$ and with n elements through the thickness. The error E in the displacement component u_{A3} of point A in the e_3 direction is defined in a similar manner to (4.7) with the exact value u_{A3}^* taken to be that predicted by (G) for regular elements ($a/L = 0$) with $n = 5$

$$u_{A3}^* = 0.16893 \text{ mm} \quad \text{for } P = 1 \text{ N.} \tag{4.18}$$

Figures 14a,b show the error for $n = 1$ as a function of the irregularity parameters $4a/L$ for Case I (Figure 14a) and as a function of $\theta/(2\pi)$ for Case II (Figure 14b). From these figures it can be seen that that {G, F} are relatively insensitive to the magnitude and type of element irregularity but that (I) predicts significant errors for irregular elements.

4.7. Point load on the corner of a thin partially clamped rhombic plate (large deformations). Figure 15 shows the deformed shapes of a thin partially clamped rhombic plate subjected to a point load on its corner for two different angles θ and the same value P of load. The plate is fully clamped on two edges and the other edges and major surfaces are traction free. The dimensions are given by (4.8) as shown in Figure 11 (with L now being the length of the plate’s edge) and the point force P is specified by

$$P = 1 \text{ kN.} \tag{4.19}$$

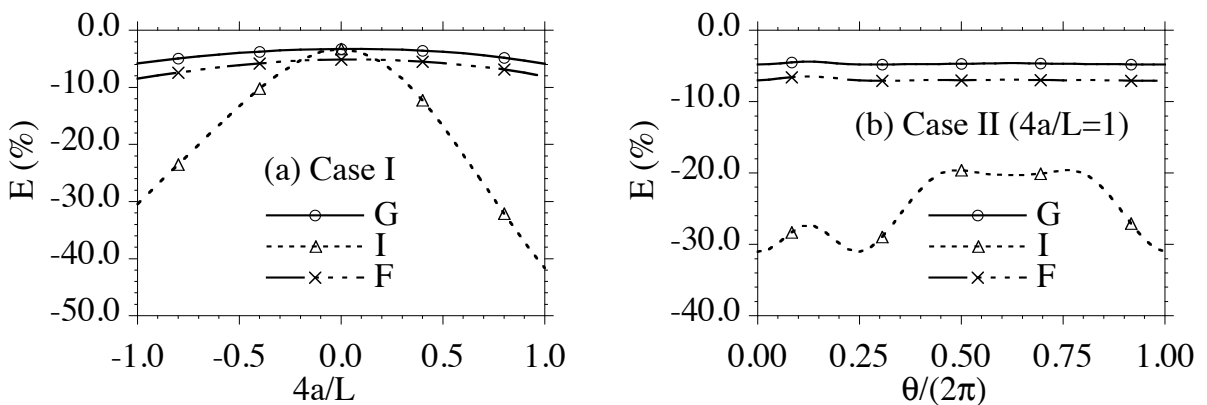


Figure 14. Point load on the center of a thin fully clamped square plate (small deformations). Errors in the displacement of the point A in the e_3 direction versus the distortion parameters (a) $4a/L$ and; (b) the angle θ for two cases of element irregularity with the mesh $\{10 \times 10 \times 1\}$.

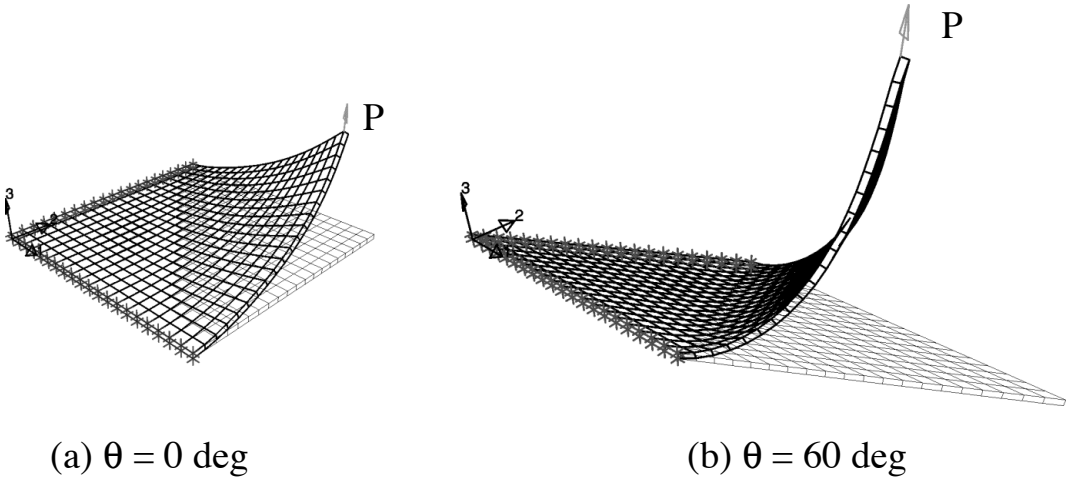


Figure 15. Point load on a partially clamped rhombic plate (large deformations). Predictions of the generalized CPE for the mesh $\{10n \times 10n \times 1\}$ with $n = 2$ and $P = 1$ kN.

The mesh is specified by $\{10n \times 10n \times 1\}$ and the exact value u_3^* of the displacement of the corner in the e_3 direction is determined by the most refined solution (G) with $n = 5$

$$u_3^* = 0.21084 \text{ m} \quad \text{for } \theta = 0 \text{ deg}, \quad u_3^* = 0.39306 \text{ m} \quad \text{for } \theta = 60 \text{ deg}. \quad (4.20)$$

Figures 16 show the load P versus displacement curves for $n = 2$ and the convergence curves for two values of the angle θ . Comparison of Figures 16a,c shows that the rhombic plate with angle $\theta = 60$ deg is more flexible than that for $\theta = 0$ deg and that {G, F} predict nearly the same values, whereas (I) predicts significant errors for the angle $\theta = 60$ deg. Also, Figure 16d shows that the convergence properties of (G) are slightly better than those of (F) for the case when $\theta = 60$ deg.

4.8. A pair of opposing point loads applied to a complete circular cylindrical shell (large deformations). Figure 17 is a sketch of one eighth of a thin circular cylindrical shell that is subjected to a pair of opposing point loads P . The entire shell has length $2L$, middle surface radius R , and thickness H , with

$$L = 300 \text{ mm}, \quad R = 300 \text{ mm}, \quad H = 3 \text{ mm}. \quad (4.21)$$

All nodes (except for one) on the circular edges of the shell are allowed to move freely in the axial direction but their radial and circumferential positions are fixed. Also, the eighth region of the shell is modeled by the mesh $\{10n \times 10n \times 1\}$ in the axial, circumferential and radial directions, respectively.

Figure 18 plots the force P versus radial displacement u_r of the point A under the load for different mesh refinements. Curves are presented for (G) for the most refined mesh of $n = 10$ and for {G, F} for $n = 3$ (Figure 18a) and $n = 5$ (Figure 18b). It can be seen from Figure 18a that for the coarser mesh ($n = 3$) the load-deflection curve exhibits ratcheting due to localized limit points whereas for the more refined mesh ($n = 5$) in Figure 18b the load-deflection curve is smooth. It can also be seen that the predictions of {G, F} tend to converge to the same solutions. Figure 19 shows the deformed shape of one eighth of the circular shell predicted by (G) for $n = 5$ and $P = 1.73$ kN with no enhancement of the

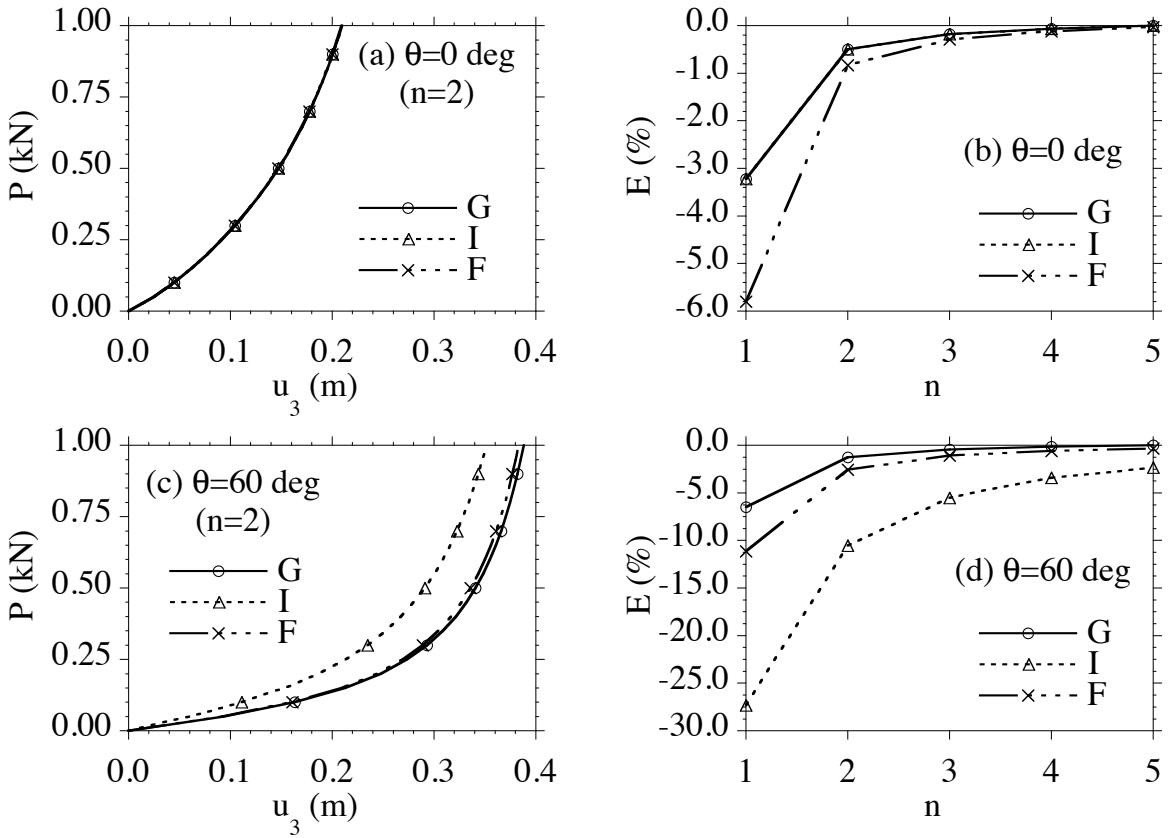


Figure 16. Point load on a partially clamped rhombic plate (large deformations). Predictions of the load P versus displacement u_3 at the loaded corner and convergence of the error in the displacement for the mesh $\{10n \times 10n \times 1\}$ with the load $P = 1$ kN and different angles θ .

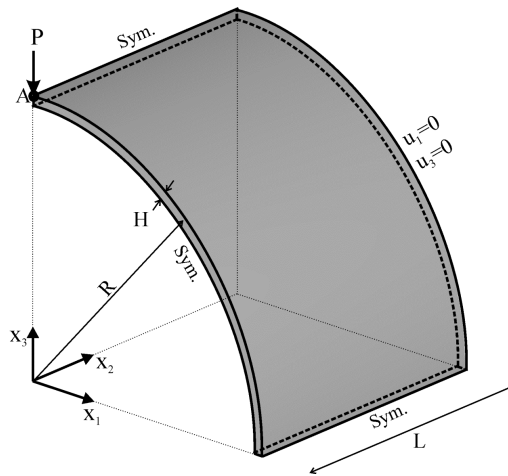


Figure 17. Sketch of one eighth of a thin circular cylindrical shell that is subjected to a pair of opposing point loads P .

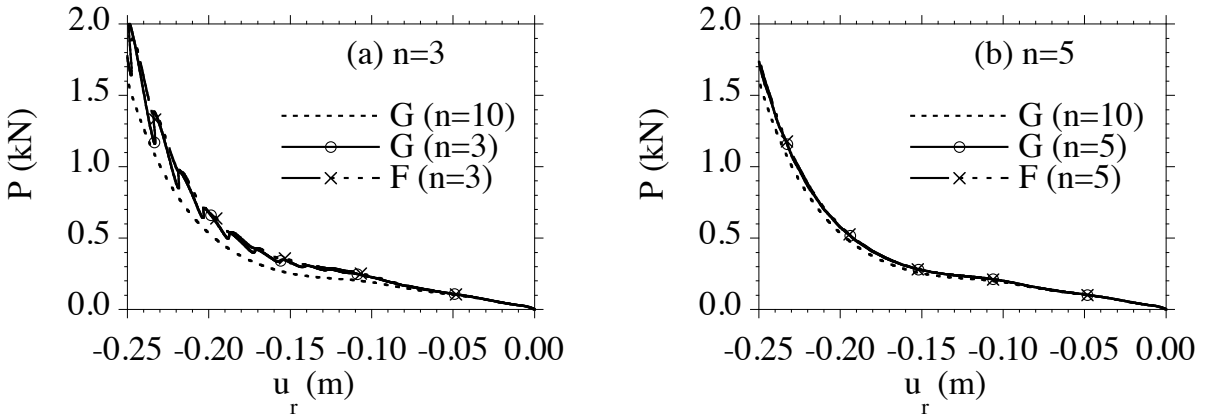


Figure 18. A pair of opposing concentrated loads P applied to a thin circular cylindrical shell with the mesh $\{10n \times 10n \times 1\}$.

displacements. In particular, it is noted that the inability of the coarse mesh to capture the high curvature of the middle of the shell far away from the load is most likely the cause of the ratcheting shown in Figure 18a.

4.9. Plane strain indentation of a rigid plate into a nearly incompressible block (large deformations). Crisfield et al. [1995] and César de Sá et al. [2001] considered the example of plane strain indentation of a rigid plate into a block and showed limitations of enhanced strain elements for elastic and elastic-plastic response. Figure 20 shows a sketch of the dimensions and boundary conditions for this problem with a

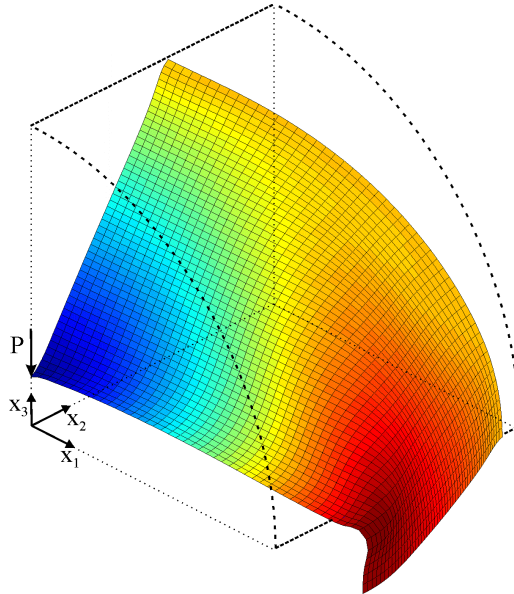


Figure 19. Deformed shape of an eighth of a thin circular cylindrical shell subjected to a pair of opposing concentrated point loads P for the mesh $\{10n \times 10n \times 1\}$ with $n=5$ and $P=1.73$ kN.

nearly incompressible elastic material. The block has length $2L$, height L and depth W . Material points on its sides and bottom remain in contact with a rigid container and are allowed to slide freely. The top surface of the block is loaded by a rigid plate (AB) of length L which makes perfect contact with the block so that material points in contact with the rigid plate move only vertically. The remaining half of the block's top surface is traction free. The dimensions of the block are given by

$$L = W = 1 \text{ m.} \tag{4.22}$$

Irregular meshes are defined by dividing the block into four subsections with the central node moving to the position characterized by the lengths $\{a_1, a_2\}$ (shown in Figure 20) defined by two cases:

$$\text{Case I: } a_1 = a, a_2 = 0, \quad -1 \leq \frac{8a}{3L} \leq 1, \quad u_{A2} = -0.1 \text{ m}, \quad n = 5, \tag{4.23}$$

$$\text{Case II: } a_1 = 0, a_2 = a, \quad -1 \leq \frac{8a}{3L} \leq 1, \quad u_{A2} = -0.1 \text{ m}, \quad n = 5.$$

The entire block is meshed by $\{8n \times 4n \times 1\}$ with $4n$ elements in the e_1 direction and $2n$ elements in the e_2 in each of the subsections. The point C (shown in Figure 20) is located on the free top surface at a distance $0.25L$ from the corner B of the rigid plate.

Figure 21 shows convergence of the solution for the regular ($a = 0$) mesh $\{8n \times 4n \times 1\}$ and $u_{A2} = -0.1 \text{ m}$. The converged value u_{C2}^* of the displacement of the point C in the e_2 direction predicted by (G) for a regular mesh with $n = 20$ is considered to be exact and is given by

$$u_{C2}^* = 0.071895 \text{ m} \quad \text{for } u_{A2} = -0.1 \text{ m with } n = 20. \tag{4.24}$$

The error E of in the values u_{C2} predicted by calculations of other elements and meshes is defined by an expression similar to (4.7). Figure 21 shows the convergence of this error predicted by {G, Q1P0, HO9}. This error is plotted relative to n for the mesh $\{8n \times 4n \times 1\}$ in Figure 21a and is plotted relative to the degrees of freedom (DOF, calculated for plane strain response) in Figure 21b. From Figure 21a it is not clear if (Q1P0) exhibits a locking behavior by converging to a value different from (G) or whether the

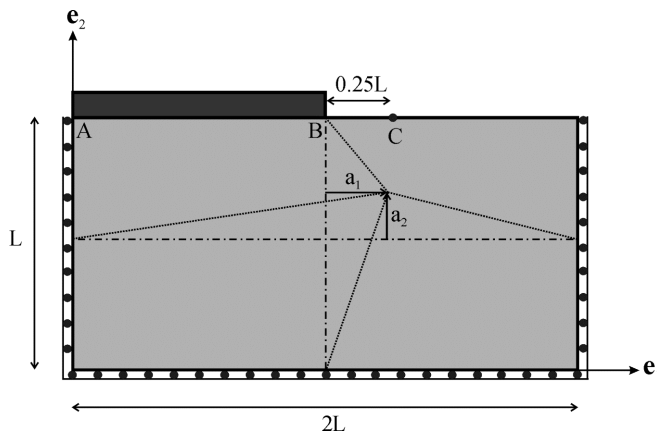


Figure 20. Plane strain indentation of a rigid plate into a block showing the boundary conditions and definition of element irregularity.

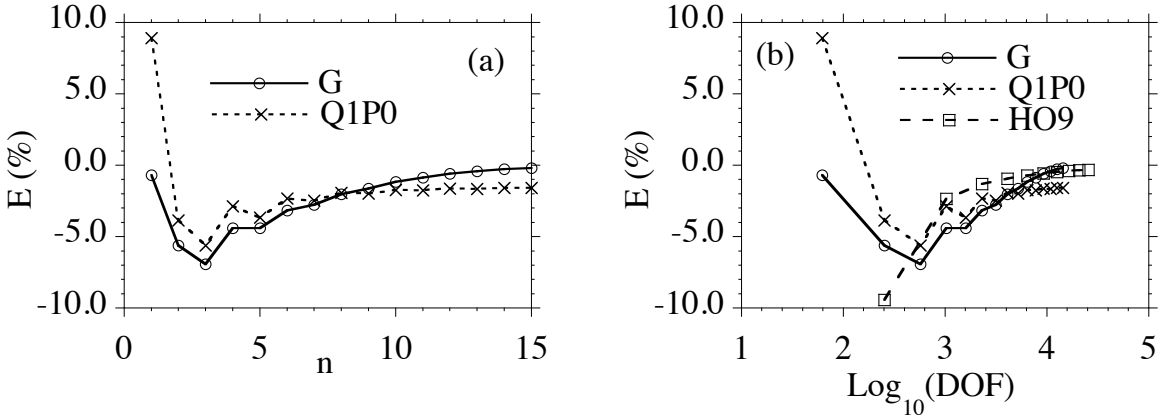


Figure 21. Plane strain indentation of a rigid plate into a nearly incompressible block. Convergence of the error E in the displacement u_{C2} of the point C using the regular mesh $\{8n \times 4n \times 1\}$ for $u_{A2} = -0.1$ m versus: (a) n ; and (b) versus the number of degrees of freedom DOF.

convergence rate is very slow. To validate the converged value of (G) for $n = 20$, calculations were also performed using the mixed higher order element (HO9) with the mesh $\{8n \times 4n \times 1\}$ up to $n = 10$. In particular, it can be seen in Figure 21b that (HO9) tends to converge to the value predicted by (G).

Figure 22 presents the errors E in the displacement u_{C2} for two cases of element irregularity and for the mesh $\{8n \times 4n \times 1\}$ with $n = 5$ and $u_{A2} = -0.1$ m. Since there is a strain concentration near the edge of the plate it is expected that a non-fully converged solution will be sensitive to element irregularity. In particular, it can be seen from Figure 22a that (Q1P0) is more sensitive to element irregularity than (G) for positive values of a for Case I which cause the elements near the plate's edge B to be more irregular. The results in Figure 22b show that the error reduces slightly for increasing positive values of a for Case II which cause the elements near the plate's edge B to be more refined.

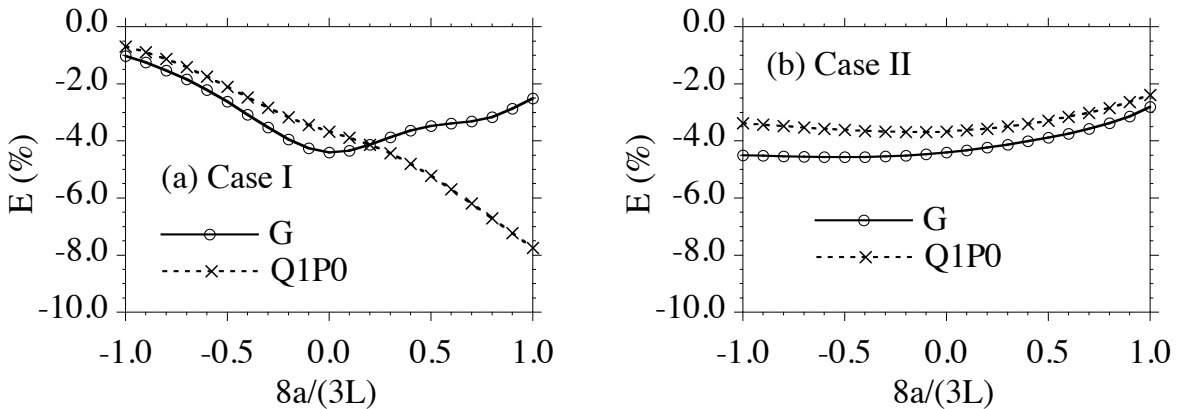


Figure 22. Plane strain indentation of a rigid plate into a nearly incompressible block. Error E in the displacement u_{C2} of the point C for two cases of element irregularity and for the mesh $\{8n \times 4n \times 1\}$ with $n = 5$ and $u_{A2} = -0.1$ m.

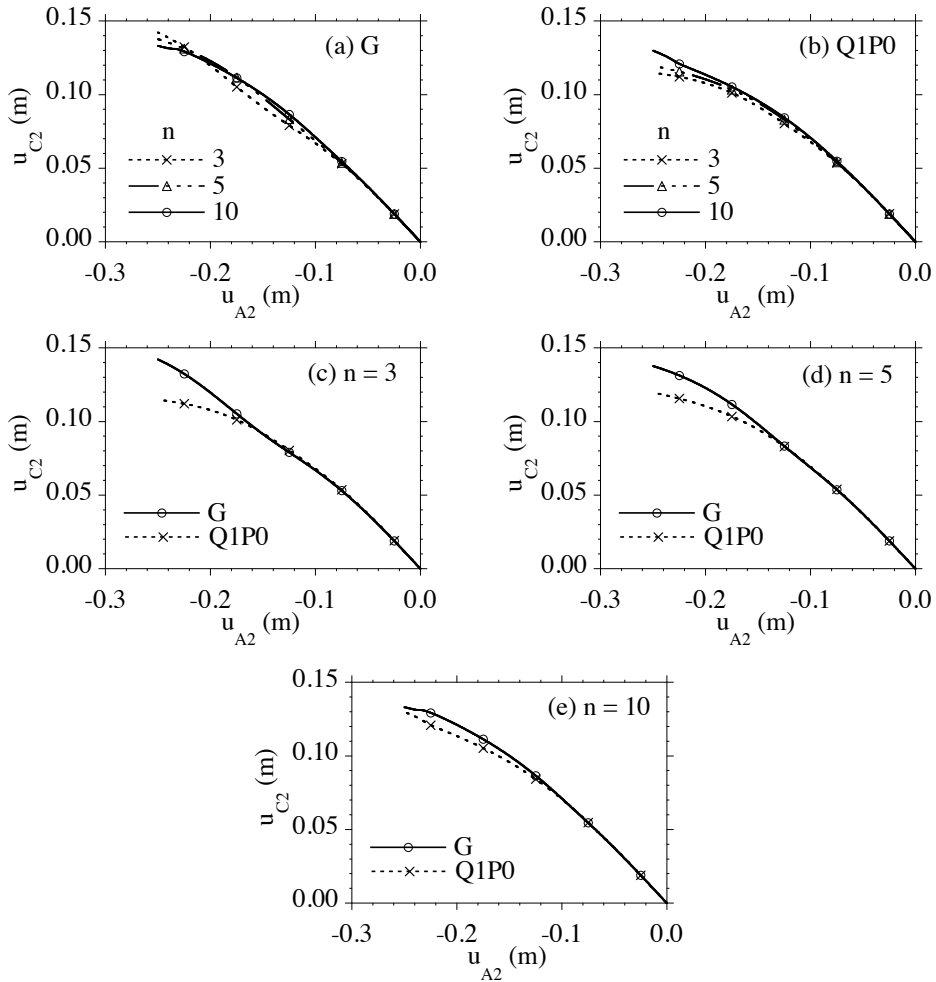


Figure 23. Plane strain indentation of a rigid plate into a nearly incompressible block showing nonlinear load curves using the regular mesh $\{8n \times 4n \times 1\}$ for 3 values of n .

Figure 23 shows nonlinear load curves using the regular mesh $\{8n \times 4n \times 1\}$ for different values of n . Again it can be seen that (G) predicts more flexible response than (Q1P0) for the coarser meshes. Figure 24 shows the deformed shapes for the regular mesh $\{8n \times 4n \times 1\}$ with $n = 3$ for different values of loads. In particular, it can be seen that the flexibility of (G) allows the elements near the plate’s corner to roll around the corner more easily than allowed by (Q1P0). Since the flexibility of (G) has been validated relative to the mixed higher order element (HO9) it is concluded that the stiffness shown by (Q1P0) is unphysical.

4.10. Indentation of a rigid plate into a nearly incompressible block (large deformations). Figure 25 shows a sketch of one fourth of a nearly incompressible block that has total length $2L$, height L and depth $2L$ with

$$L = 1 \text{ m.} \tag{4.25}$$

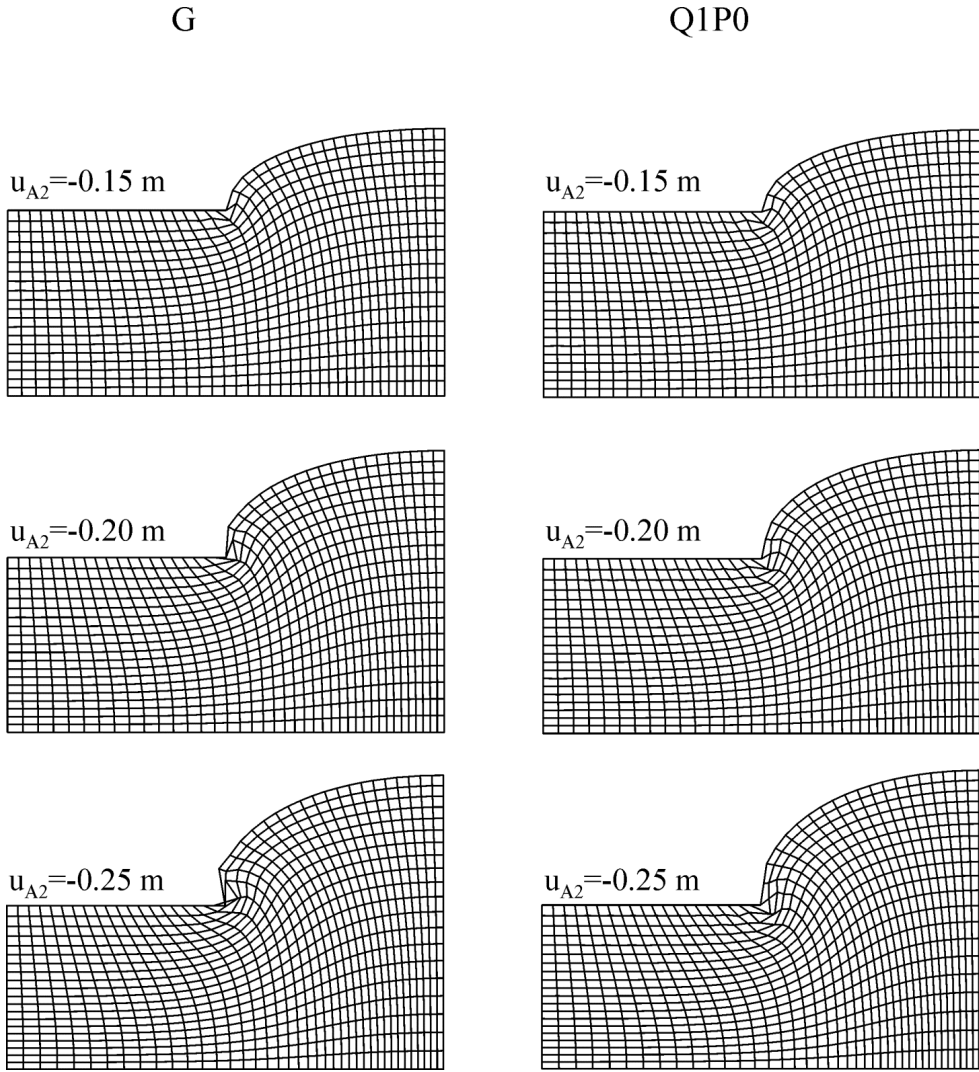


Figure 24. Plane strain indentation of a rigid plate into a nearly incompressible block showing the deformed shapes for the regular mesh $\{8n \times 4n \times 1\}$ with $n = 5$. The left column shows the results for (G) and the right column shows the results (Q1P0).

The bottom ($X_3^* = 0$) and exterior lateral surfaces ($X_1^* = \pm L, X_2^* = \pm L$) of the block remain in contact with and slide freely on smooth rigid planes. The block's top surface ($X_3^* = L$) is loaded by a rigid plate (ABCD) which makes perfect contact with the material points so that these points can only move vertically in the e_3 direction. The remaining portion of the block's top surface is traction free. Irregular elements are generated by moving the nodes of the center plane by the displacements $\{a_1, a_2, a_3, a_4\}$ as shown in Figure 25 with

$$a_1 = a, \quad a_2 = 0, \quad a_3 = -a, \quad a_4 = a, \quad -1 \leq \frac{8a}{3L} \leq 1. \tag{4.26}$$

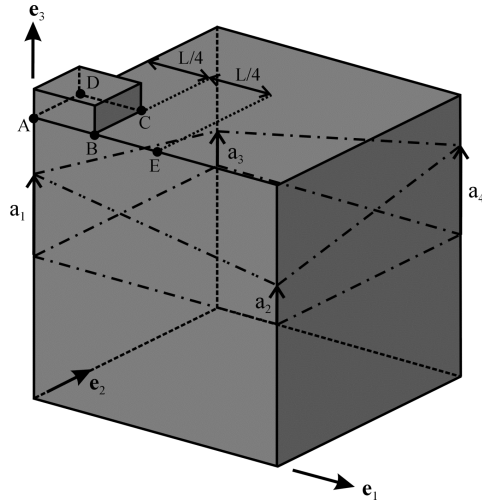


Figure 25. Indentation of a rigid plate into a block showing the boundary conditions and definition of element irregularity. Symmetry conditions are used so that only one fourth of the block is meshed.

The mesh for the one fourth region is specified by $\{4n \times 4n \times 4n\}$ with $2n$ elements below and above the distorted center surface and with $\{n \times n\}$ elements under the rigid plate. Moreover, the vertical reference locations of material points on these distorted surfaces are described by a bilinear form of the coordinates (X_1^*, X_2^*) . Furthermore, the point E is located at a distance $L/4$ from the edge of the rigid plate.

Based on the results of the previous example it is expected that the deformation will be concentrated near the edges of the plate so that a refined mesh will be required to obtain an accurate solution. Mesh refinement of this 3-D problem is beyond the capacity of the hardware being used to obtain the solution. Therefore, attention will be focused on the robustness of the solutions with relative coarse meshes.

Figure 26 explores the sensitivity of the elements $\{G, Q1P0\}$ to irregularity of the reference element shape. Since the converged value of the displacement u_{E3} is not known it is convenient to define the difference of u_{E3} relative to the value u_{E3}^* predicted for a regular mesh ($a = 0$). Specifically, the value

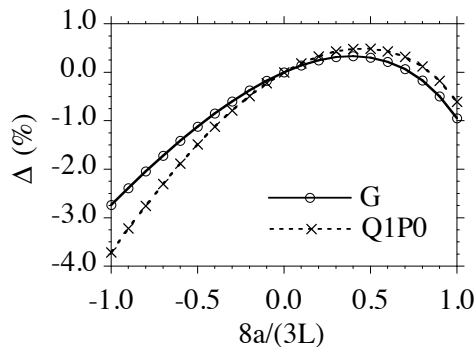


Figure 26. Indentation of a rigid plate into a nearly incompressible block. The displacement u_{E3} of the point E as a function of element irregularity for the mesh $\{4n \times 4n \times 4n\}$ with $n = 3$ and $u_{A3} = -0.1$ m.

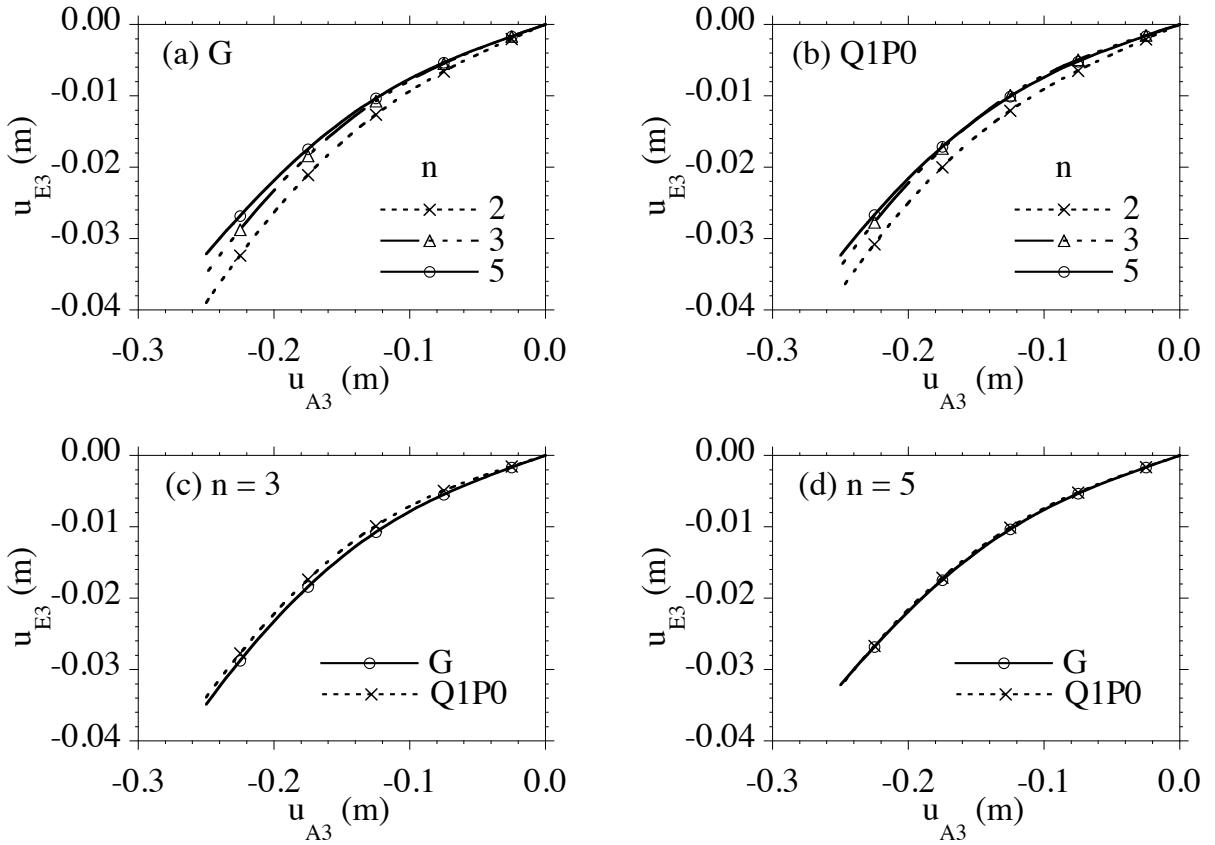


Figure 27. Indentation of a rigid plate into a nearly incompressible block. Nonlinear load curves for the regular mesh $\{4n \times 4n \times 4n\}$ with different values of n .

of u_{E3}^* for each element for the regular mesh $\{4n \times 4n \times 4n\}$ with $n = 3$ and $u_{A3} = -0.1$ m is given by

$$u_{E3}^* = -0.0078595 \text{ m for } (G), \quad u_{E3}^* = -0.0071327 \text{ m for } (Q1P0). \quad (4.27)$$

The difference Δ is then defined by a formula of the type (4.7)

$$\Delta = \frac{u_{E3} - u_{E3}^*}{|u_{E3}^*|}, \quad (4.28)$$

for each of the elements using its value of u_{E3}^* so that Δ vanishes for each element when $a = 0$. The results in Figure 26 demonstrate that (G) can be used for three-dimensional irregularity of the reference element shapes and that the predictions of (G) are similar to those of (Q1P0). Since the solution is not fully converged for this mesh it is expected that the solution will be sensitive to the value of the irregularity parameter a . In particular, the results in Figure 26 are consistent with the observation that the mesh is more refined under the rigid plate for positive values of a .

Figure 27 shows nonlinear load curves using the regular mesh $\{4n \times 4n \times 4n\}$ for different values of n . From these figures it can be seen that the results predicted by {G, Q1P0} are similar. In particular,

the unphysical stiffness exhibited by (Q1P0) in the previous plane strain problem is not detected in this three-dimensional problem.

5. Conclusions

A generalized form (2.11) for the strain energy of inhomogeneous deformations of a Cosserat point element (CPE) has been developed which includes full coupling of bending and torsional modes. The dependence of the constitutive coefficients B_{ij} on the metric D_{ij} (3.4) have been determined by matching exact small deformation solutions for pure bending (eighteen solutions) and simple torsion (6 solutions). These coefficients are then used with nonlinear strain measures to characterize the response of general irregular element shapes to large deformations.

Ideally, for a fully converged solution the response of a structure to a specified load should be insensitive to irregularities in the element shapes used to mesh the structure. The results here indicate that the main features of this desired response for general shaped elements can be obtained by properly modeling pure bending and simple torsion of parallelepipeds with two right angles. Also, it is recalled [Jabareen and Rubin 2007b] that insensitivity to element irregularity can best be exhibited by focusing attention on a thin structure that is loaded so that inhomogeneous deformations (like bending and torsion) dominate homogeneous deformations. In particular, plots like Figure 4c for (I) clearly emphasize undesirable sensitivity to element irregularity.

In contrast with standard finite elements, the nodal forces in the generalized CPE are determined by algebraic expressions in terms of derivatives of a strain energy function and no integration is needed over the element region. A number of example problems (also see [Jabareen and Rubin 2007a; Jabareen and Rubin 2007b]) have been considered which show that the generalized CPE is as accurate as elements based on enhanced strain and incompatible modes and is as robust as elements based on full integration. The plane strain example of indentation of a rigid plate into a nearly incompressible block showed that the flexibility exhibited by the CPE is physical and that the mixed Q1P0 element predicts unphysical stiffness. Furthermore, the generalized CPE can be used to model 3-D bodies, thin shells and rods and nearly incompressible materials. In addition, the generalized CPE is free of hourglass instabilities that are observed in other element formulations in regions experiencing combined high compression with bending. Consequently, the generalized CPE is truly a robust user friendly element that can be used with confidence to model problems in nonlinear elasticity.

Appendix A. Values of the constitutive coefficients B_{ij}

The equations of the bending and torsion problems discussed in Section 3 for the element shapes can be solved for the values of B_{ij} in the strain energy function (2.11) for inhomogeneous deformations and the results were reported in [Jabareen and Rubin 2008b]. Specifically, the nonzero components of the upper diagonal of the symmetric matrices $\{B_{ij}^0, B_{ij}^{12}, B_{ij}^{13}, B_{ij}^{23}, i, j = 1, 2, \dots, 9\}$ in (3.24) for a general shaped element are specified by

$$B_{11}^0 = 1, \quad B_{11}^{12} = 1 + \frac{H_1^2 D_{12}^2}{H_2^2}, \quad B_{11}^{13} = 1 + \frac{(1 - \nu)\{H_1^2(1 - D_{13}^2) + H_2^2\}D_{13}^2}{2H_2^2(1 - D_{13}^2)}, \quad B_{11}^{23} = 1,$$

$$\begin{aligned}
 B_{12}^0 &= \nu, & B_{12}^{12} &= \nu, & B_{12}^{13} &= \nu - \frac{(1-\nu)D_{13}^2}{2(1-D_{13}^2)}, & B_{12}^{23} &= \nu, & B_{13}^{12} &= \frac{(H_1^2 + H_2^2)D_{12}}{H_1 H_2}, \\
 B_{14}^{12} &= \frac{\nu H_1 D_{12}}{H_2}, & B_{16}^{23} &= \frac{\nu H_2 D_{23}}{H_3}, & B_{17}^{13} &= \frac{(1-\nu)\{H_1^2(1-D_{13}^2) + H_2^2\}D_{13}}{2H_2 H_3(1-D_{13}^2)}, \\
 B_{18}^{13} &= \frac{(1-\nu)H_1^2 D_{13}}{2H_2^2}, & B_{19}^{13} &= -\frac{(1-\nu)H_2 D_{13}}{2H_1(1-D_{13}^2)}, \\
 B_{22}^0 &= 1, & B_{22}^{12} &= 1, & B_{22}^{13} &= 1 + \frac{(1-\nu)\{H_3^2(1-D_{13}^2) + H_2^2\}D_{13}^2}{2H_2^2(1-D_{13}^2)}, & B_{22}^{23} &= 1 + \frac{H_3^2 D_{23}^2}{H_2^2}, \\
 B_{23}^{12} &= \frac{\nu H_2 D_{12}}{H_1}, & B_{25}^{23} &= \frac{\nu H_3 D_{23}}{H_2}, & B_{26}^{23} &= \frac{(H_2^2 + H_3^2)D_{23}}{H_2 H_3}, \\
 B_{27}^{13} &= -\frac{(1-\nu)H_2 D_{13}}{2H_3(1-D_{13}^2)}, & B_{28}^{13} &= \frac{(1-\nu)H_3^2 D_{13}}{2H_2^2}, & B_{29}^{13} &= \frac{(1-\nu)\{H_2^2 + H_3^2(1-D_{13}^2)\}D_{13}}{2H_1 H_2(1-D_{13}^2)}, \\
 B_{33}^0 &= 1, & B_{33}^{12} &= 1 + \frac{H_2^2 D_{12}^2}{H_1^2}, & B_{33}^{13} &= 1, & B_{33}^{23} &= 1 + \frac{(1-\nu)\{H_1^2 + H_2^2(1-D_{23}^2)\}D_{23}^2}{2H_1^2(1-D_{23}^2)}, \\
 B_{34}^0 &= \nu, & B_{34}^{12} &= \nu, & B_{34}^{13} &= \nu, & B_{34}^{23} &= \nu - \frac{(1-\nu)D_{23}^2}{2(1-D_{23}^2)}, \\
 B_{35}^{13} &= \frac{\nu H_1 D_{13}}{H_3}, & B_{37}^{23} &= \frac{(1-\nu)\{H_1^2 + H_2^2(1-D_{23}^2)\}D_{23}}{2H_1 H_3(1-D_{23}^2)}, & B_{38}^{23} &= -\frac{(1-\nu)H_1 D_{23}}{2H_2(1-D_{23}^2)}, \\
 B_{39}^{23} &= \frac{(1-\nu)H_2^2 D_{23}}{2H_1^2}, & B_{44}^0 &= 1, & B_{44}^{12} &= 1, & B_{44}^{13} &= 1 + \frac{H_3^2 D_{13}^2}{H_1^2}, \\
 B_{44}^{23} &= 1 + \frac{(1-\nu)\{H_1^2 + H_3^2(1-D_{23}^2)\}D_{23}^2}{2H_1^2(1-D_{23}^2)}, & B_{45}^{13} &= \frac{(H_1^2 + H_3^2)D_{13}}{H_1 H_3}, & B_{46}^{13} &= \frac{\nu H_3 D_{13}}{H_1}, \\
 B_{47}^{23} &= -\frac{(1-\nu)H_1 D_{23}}{2H_3(1-D_{23}^2)}, & B_{48}^{23} &= \frac{(1-\nu)\{H_1^2 + H_3^2(1-D_{23}^2)\}D_{23}}{2H_1 H_2(1-D_{23}^2)}, & B_{49}^{23} &= \frac{(1-\nu)H_3^2 D_{23}}{2H_1^2}, \\
 B_{55}^0 &= 1, & B_{55}^{12} &= 1 + \frac{(1-\nu)\{H_1^2(1-D_{12}^2) + H_3^2\}D_{12}^2}{2H_3^2(1-D_{12}^2)}, & B_{55}^{13} &= 1 + \frac{H_1^2 D_{13}^2}{H_3^2}, & B_{55}^{23} &= 1, \\
 B_{56}^0 &= \nu, & B_{56}^{12} &= \nu - \frac{(1-\nu)D_{12}^2}{2(1-D_{12}^2)}, & B_{56}^{13} &= \nu, & B_{56}^{23} &= \nu, \\
 B_{57}^{12} &= \frac{(1-\nu)H_1^2 D_{12}}{2H_3^2}, & B_{58}^{12} &= \frac{(1-\nu)\{H_1^2(1-D_{12}^2) + H_3^2\}D_{12}}{2H_2 H_3(1-D_{12}^2)}, & B_{59}^{12} &= -\frac{(1-\nu)H_3 D_{12}}{2H_1(1-D_{12}^2)}, \\
 B_{66}^0 &= 1, & B_{66}^{12} &= 1 + \frac{(1-\nu)\{H_2^2(1-D_{12}^2) + H_3^2\}D_{12}^2}{2H_3^2(1-D_{12}^2)}, & B_{66}^{13} &= 1, & B_{66}^{23} &= 1 + \frac{H_2^2 D_{23}^2}{H_3^2}, \\
 B_{67}^{12} &= \frac{(1-\nu)H_2^2 D_{12}}{2H_3^2}, & B_{68}^{12} &= -\frac{(1-\nu)H_3 D_{12}}{2H_2(1-D_{12}^2)}, & B_{69}^{12} &= \frac{(1-\nu)\{H_2^2(1-D_{12}^2) + H_3^2\}D_{12}}{2H_1 H_3(1-D_{12}^2)},
 \end{aligned}$$

$$\begin{aligned}
 B_{77}^0 &= \frac{(1-\nu)(H_1^2 + H_2^2)}{2H_3^2}, & B_{77}^{12} &= B_{77}^0, & B_{77}^{13} &= B_{77}^0 + \frac{(1-\nu)H_2^2 D_{13}^2}{2H_3^2(1-D_{13}^2)}, & B_{77}^{23} &= B_{77}^0 + \frac{(1-\nu)H_1^2 D_{23}^2}{2H_3^2(1-D_{23}^2)}, \\
 B_{78}^0 &= \frac{(1-\nu)H_1^2}{2H_2 H_3}, & B_{78}^{12} &= B_{78}^0, & B_{78}^{13} &= B_{78}^0, & B_{78}^{23} &= B_{78}^0 - \frac{(1-\nu)H_1^2 D_{23}^2}{2H_2 H_3(1-D_{23}^2)}, \\
 B_{79}^0 &= \frac{(1-\nu)H_2^2}{2H_1 H_3}, & B_{79}^{12} &= B_{79}^0, & B_{79}^{13} &= B_{79}^0 - \frac{(1-\nu)H_2^2 D_{13}^2}{2H_1 H_3(1-D_{13}^2)}, & B_{79}^{23} &= B_{79}^0, \\
 B_{88}^0 &= \frac{(1-\nu)(H_1^2 + H_3^2)}{2H_2^2}, & B_{88}^{12} &= B_{88}^0 + \frac{(1-\nu)H_3^2 D_{12}^2}{2H_2^2(1-D_{12}^2)}, & B_{88}^{13} &= B_{88}^0, & B_{88}^{23} &= B_{88}^0 + \frac{(1-\nu)H_1^2 D_{23}^2}{2H_2^2(1-D_{23}^2)}, \\
 B_{89}^0 &= \frac{(1-\nu)H_3^2}{2H_1 H_2}, & B_{89}^{12} &= B_{89}^0 - \frac{(1-\nu)H_3^2 D_{12}^2}{2H_1 H_2(1-D_{12}^2)}, & B_{89}^{13} &= B_{89}^0, & B_{89}^{23} &= B_{89}^0, \\
 B_{99}^0 &= \frac{(1-\nu)(H_2^2 + H_3^2)}{2H_1^2}, & B_{99}^{12} &= B_{99}^0 + \frac{(1-\nu)H_3^2 D_{12}^2}{2H_1^2(1-D_{12}^2)}, & B_{99}^{13} &= B_{99}^0 + \frac{(1-\nu)H_2^2 D_{13}^2}{2H_1^2(1-D_{13}^2)}, & B_{99}^{23} &= B_{99}^0,
 \end{aligned}$$

with $\{\lambda_{12}, \lambda_{13}, \lambda_{23}\}$ defined by (3.23).

Acknowledgements

This research was partially supported by M. B. Rubin’s Gerard Swope Chair in Mechanics and by the fund for the promotion of research at the Technion. The authors would like to thank D. Ehrlich for directing our attention to the example of bending of a rhombic plate.

References

[ABAQUS] *ABAQUS*, Version 6.5-1, ABAQUS, Providence, RI.

[ADINA] *ADINA*, Version 8.3.1, ADINA R & D, Watertown, MA.

[ANSYS] *ANSYS*, University Advanced Version 9, ANSYS, Canonsburg, PA.

[Belytschko and Bindeman 1993] T. Belytschko and L. P. Bindeman, “Assumed strain stabilization of the eight node hexahedral element”, *Comput. Methods Appl. Mech. Eng.* **105**:2 (1993), 225–260.

[Belytschko et al. 1984] T. Belytschko, J. S.-J. Ong, W. K. Liu, and J. M. Kennedy, “Hourglass control in linear and nonlinear problems”, *Comput. Methods Appl. Mech. Eng.* **43**:3 (1984), 251–276.

[Boerner et al. 2007] E. F. I. Boerner, S. Loehnert, and P. Wriggers, “A new finite element based on the theory of a Cosserat point: extension to initially distorted elements for 2D plane strain”, *Int. J. Numer. Methods Eng.* **71**:4 (2007), 454–472.

[Bonet and Bhargava 1995] J. Bonet and P. Bhargava, “A uniform deformation gradient hexahedron element with artificial hourglass control”, *Int. J. Numer. Methods Eng.* **38**:16 (1995), 2809–2828.

[Crisfield et al. 1995] M. A. Crisfield, G. F. Moita, L. P. R. Lyons, and G. Jelenić, “Enhanced lower-order element formulations for large strains”, *Comput. Mech.* **17**:1–2 (1995), 62–73.

[Ehrlich 2007] D. Ehrlich, Personal communication, 2007.

[Flory 1961] P. J. Flory, “Thermodynamic relations for high elastic materials”, *T. Faraday Soc.* **57** (1961), 829–838.

[Hutter et al. 2000] R. Hutter, P. Hora, and P. Niederer, “Total hourglass control for hyperelastic materials”, *Comput. Methods Appl. Mech. Eng.* **189**:3 (2000), 991–1010.

[Jabareen and Rubin 2007a] M. Jabareen and M. B. Rubin, “Hyperelasticity and physical shear buckling of a block predicted by the Cosserat point element compared with inelasticity and hourglassing predicted by other element formulations”, *Comput. Mech.* **40**:3 (2007), 447–459.

- [Jabareen and Rubin 2007b] M. Jabareen and M. B. Rubin, “An improved 3-D brick Cosserat point element for irregular shaped elements”, *Comput. Mech.* **40**:6 (2007), 979–1004.
- [Jabareen and Rubin 2008a] M. Jabareen and M. B. Rubin, “A Cosserat point element (CPE) for nearly planar problems (including thickness changes) in nonlinear elasticity”, *Int. J. Eng. Sci.* **46**:10 (2008), 986–1010.
- [Jabareen and Rubin 2008b] M. Jabareen and M. B. Rubin, “A generalized Cosserat point element (CPE) for isotropic nonlinear elastic materials including irregular 3-D brick and thin structures”, United States Patent and Trademark Office, 2008.
- [Jabareen and Rubin 2008c] M. Jabareen and M. B. Rubin, “Modified torsion coefficients for a 3-D brick Cosserat point element”, *Comput. Mech.* **41**:4 (2008), 517–525.
- [Loehnert et al. 2005] S. Loehnert, E. F. I. Boerner, M. B. Rubin, and P. Wriggers, “Response of a nonlinear elastic general Cosserat brick element in simulations typically exhibiting locking and hourglassing”, *Comput. Mech.* **36**:4 (2005), 255–265.
- [Nadler and Rubin 2003] B. Nadler and M. B. Rubin, “A new 3-D finite element for nonlinear elasticity using the theory of a Cosserat point”, *Int. J. Solids Struct.* **40**:17 (2003), 4585–4614.
- [Reese and Wriggers 1996] S. Reese and P. Wriggers, “Finite element calculation of the stability behaviour of hyperelastic solids with the enhanced strain methods”, *Z. Angew. Math. Mech.* **76**:S5 (1996), 415–416.
- [Reese and Wriggers 2000] S. Reese and P. Wriggers, “A stabilization technique to avoid hourglassing in finite elasticity”, *Int. J. Numer. Methods Eng.* **48**:1 (2000), 79–109.
- [Reese et al. 2000] S. Reese, P. Wriggers, and B. D. Reddy, “A new locking-free brick element technique for large deformation problems in elasticity”, *Compos. Struct.* **75**:3 (2000), 291–304.
- [Rubin 1995] M. B. Rubin, “Numerical solution of two- and three-dimensional thermomechanical problems using the theory of a Cosserat point”, pp. 308–334 in *Theoretical, experimental, and numerical contributions to the mechanics of fluids and solids: a collection of papers in honor of Paul M. Naghdi*, edited by J. Casey and M. J. Crochet, Birkhäuser, Basel, 1995. Special issue of *Z. Angew. Math. Phys.* **46**.
- [Rubin 2000] M. B. Rubin, *Cosserat theories: shells, rods and points*, Solid Mechanics and its Applications **79**, Kluwer, Dordrecht, 2000.
- [César de Sá et al. 2001] J. M. A. César de Sá, P. M. A. Areias, and R. M. N. Jorge, “Quadrilateral elements for the solution of elasto-plastic finite strain problems”, *Int. J. Numer. Methods Eng.* **51**:8 (2001), 883–917.
- [Simo and Armero 1992] J. C. Simo and F. Armero, “Geometrically non-linear enhanced strain mixed methods and the method of incompatible modes”, *Int. J. Numer. Methods Eng.* **33**:7 (1992), 1413–1449.
- [Simo and Rifai 1990] J. C. Simo and M. S. Rifai, “A class of mixed assumed strain methods and the method of incompatible modes”, *Int. J. Numer. Methods Eng.* **29**:8 (1990), 1595–1638.
- [Simo et al. 1993] J. C. Simo, F. Armero, and R. L. Taylor, “Improved versions of assumed enhanced strain tri-linear elements for 3D finite deformation problems”, *Comput. Methods Appl. Mech. Eng.* **110**:3–4 (1993), 359–386.
- [Sokolnikoff 1956] I. S. Sokolnikoff, *Mathematical theory of elasticity*, McGraw-Hill, New York, 1956.
- [Taylor 2005] R. L. Taylor, “FEAP - a finite element analysis program, Version 7.5”, University of California, Berkeley, 2005.
- [Zienkiewicz and Taylor 2005] O. C. Zienkiewicz and R. L. Taylor, *The finite element method for solid and structural mechanics*, 6th ed., Elsevier, Amsterdam, 2005.

Received 22 Dec 2007. Revised 26 Jun 2008. Accepted 29 Jun 2008.

M. JABAREEN: mahmood.jabareen@imes.mavt.ethz.ch

Institute of Mechanical Systems, Department of Mechanical Engineering, ETH Zentrum, 8092 Zürich, Switzerland

M. B. RUBIN: mbrubin@tx.technion.ac.il

Faculty of Mechanical Engineering, Technion – Israel Institute of Technology, 32000 Haifa, Israel

AXISYMMETRIC INDENTATION OF A RIGID CYLINDER ON A LAYERED COMPRESSIBLE AND INCOMPRESSIBLE HALFSPACE

LUIGI LA RAGIONE, FRANCESCO MUSCEO AND ALFREDO SOLLAZZO

We propose a solution for an elastic, axisymmetric, indentation problem. The indenter is a rigid cylinder on an elastic layer in contact with an elastic substrate. The goal is to provide a contact law between the applied force and the displacement of the coating in two cases: frictionless interaction and perfect binding between the coating and the substrate. As examples we have considered situations in which the substrate is either softer, similarly stiff, or stiffer than the coating, both for compressible or incompressible materials.

1. Introduction

Problems concerning the investigation of strain and stress in elastic bodies in contact are the goal of researches devoted to theoretical models and applications in the industry; see, for example, [Li and Chou 1997; Johnson and Sridhar 2001; Wang et al. 2004; Sburlati 2006].

A relative recent interest in contact mechanics (an exhaustive treatise of contact problems can be found in [Johnson 1985]) has focused on indentation problems upon layered solids with coating different from the substrate. This is of interest, for example, in the measurement of mechanical properties, such as hardness and elastic moduli, of surface films in not destructive experimental tests, also on the micro- or nanoscale.

In this paper we focus our attention on the case of a rigid cylinder with circular section indenting a layered body formed by an isotropic halfspace with an isotropic surface coating having different mechanical characteristic from the substrate: this is an axisymmetric problem for compressible or incompressible layers.

From the general case, in which no restriction is made on the elastic properties of the bodies in contact, we deduce a limit condition for the case where the substrate is stiffer than the surface coating. (An example of a solution in the case of a rigid foundation can be found in [Matthewson 1981; Yang 1998; 2003].)

Our solution is based on Hankel integral transforms, developed by Harding and Sneddon [1945] and applied by Sneddon [1946] to the case of half space, that leads to a second kind Fredholm integral equation numerically solvable.

We make the following hypotheses to approach the problem: the friction influences in a negligible way the normal stress distribution on the interface between the layer and the cylinder (see [Johnson 1985], for example); and we consider only the limit contact cases between the layer and the elastic substrate, that is, either perfect bonding or absence of friction.

Keywords: contact mechanics, elasticity, indentation, Hankel transform.

We believe that the model allows to highlight characteristics of solution that are unlikely to be noticed through numerical simulations alone (as in [Komvopoulos 1988]), especially in the inherent case of a rigid foundation where we obtain a solution normalized by all mechanical parameters.

2. Problem formulation

We study the quasistatic axisymmetric indentation of a rigid circular cylinder with radius a , in the context of small deformation. The cylinder produces a normal force F upon an elastic body made by an isotropic surface layer with moduli E_1 and ν_1 and thickness h , and a semi-indefinite isotropic substrate with moduli E_2 and ν_2 (see Figure 1). For the interface between the layer and the elastic substrate we consider two limit conditions: perfect bonding and absence of friction. The contact area does not vary with the loading and it is a circle with radius a . The normal acting force is fixed and the displacement for all points of the contact surface, δ , is the same.

We take two cylindrical frames of reference: the triplet (r, ϑ, z) refers to the surface layer, with r and ϑ belonging to the upper surface of the coating and the z axis that coincides with the axis of symmetry; the triplet (r', ϑ', z') refers to the substrate with r' and ϑ' belonging to the interface layer-substrate surface and the z' axis superimposed on z . That is, the two frames of reference differ for a translation h in the positive z direction.

Because of the symmetry, the problem can be simplified by focusing only on the positive quadrants (O, r, z) , $r \geq 0, z \geq 0$, and (O, r', z') , $r' \geq 0, z' \geq 0$.

We first consider Mitchell's theory [Sneddon 1951] for isotropic bodies deformed in axisymmetry condition where stress and strain can be expressed through a single function. We refer to the generic frame of reference (O, r, ϑ, z) and we introduce a potential $\Phi(r, z)$ related to the nonzero components of the strain such that

$$u_r(r, z) = -\frac{(1 + \nu)}{E} \frac{\partial}{\partial r} \frac{\partial \Phi(r, z)}{\partial z}, \tag{1}$$

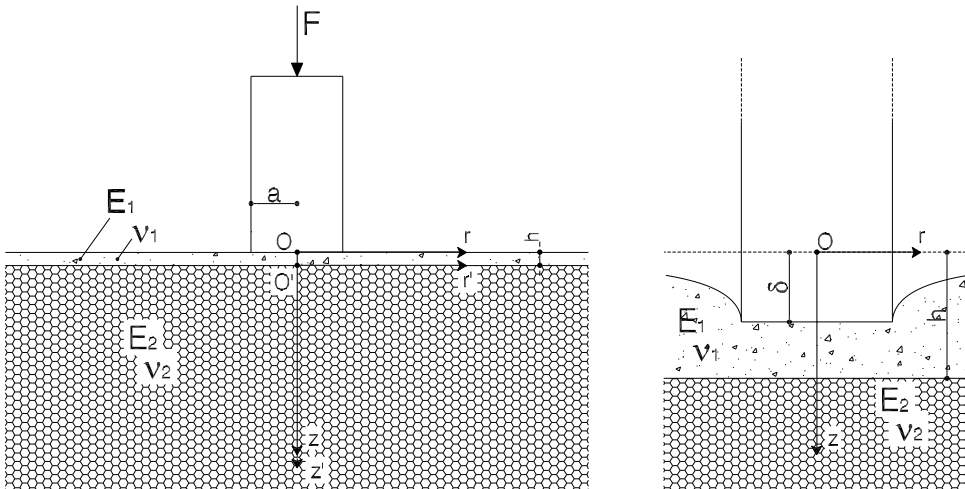


Figure 1. Cylindrical indenter on layered halfspace.

$$u_z(r, z) = \frac{2(1 - \nu^2)}{E} \nabla^2 \Phi(r, z) - \frac{(1 + \nu)}{E} \frac{\partial^2 \Phi(r, z)}{\partial z^2}. \tag{2}$$

It is then straightforward to obtain the following expressions for the component of stress:

$$\sigma_z(r, z) = \frac{\partial}{\partial z} \left[(2 - \nu) \nabla^2 \Phi(r, z) - \frac{\partial^2 \Phi(r, z)}{\partial z^2} \right], \tag{3}$$

$$\sigma_r(r, z) = \frac{\partial}{\partial z} \left[\nu \nabla^2 \Phi(r, z) - \frac{\partial^2 \Phi(r, z)}{\partial r^2} \right], \tag{4}$$

$$\sigma_{\theta}(r, z) = \frac{\partial}{\partial z} \left[\nu \nabla^2 \Phi(r, z) - \frac{1}{r} \frac{\partial \Phi(r, z)}{\partial r} \right], \tag{5}$$

$$\tau_{zr}(r, z) = \frac{\partial}{\partial r} \left[(1 - \nu) \nabla^2 \Phi(r, z) - \frac{\partial^2 \Phi(r, z)}{\partial z^2} \right], \tag{6}$$

with

$$\nabla^2 = \frac{\partial^2}{\partial r^2} + \frac{\partial}{r \partial r} + \frac{\partial^2}{\partial z^2}.$$

If we apply Hankel transform theory [Sneddon 1951] to (1)–(6) indicating the transform with $\tilde{}$, and introduce the parameter ξ instead of r , all the listed quantities can be written as function of the zeroth order Hankel transform of the potential $\tilde{\Phi}_0(\xi, z)$:

$$u_r(r, z) = \int_0^\infty \frac{(1 + \nu)}{E} \xi^2 \frac{d\tilde{\Phi}_0(\xi, z)}{dz} J_1(\xi r) d\xi, \tag{7}$$

$$u_z(r, z) = \int_0^\infty \xi \left[\frac{(1 - 2\nu)(1 + \nu)}{E} \frac{d^2 \tilde{\Phi}_0(\xi, z)}{dz^2} - \frac{2(1 - \nu^2)}{E} \xi^2 \tilde{\Phi}_0(\xi, z) \right] J_0(\xi r) d\xi, \tag{8}$$

$$\sigma_z(r, z) = \int_0^\infty \xi \left[(1 - \nu) \frac{d^3 \tilde{\Phi}_0(\xi, z)}{dz^3} - (2 - \nu) \xi^2 \frac{d\tilde{\Phi}_0(\xi, z)}{dz} \right] J_0(\xi r) d\xi, \tag{9}$$

$$\sigma_r(r, z) = \int_0^\infty \xi \left(\nu \frac{d^3 \tilde{\Phi}_0(\xi, z)}{dz^3} + (1 - \nu) \xi^2 \frac{d\tilde{\Phi}_0(\xi, z)}{dz} \right) J_0(\xi r) d\xi - \frac{1}{r} \int_0^\infty \xi^2 \frac{d\tilde{\Phi}_0(\xi, z)}{dz} J_1(\xi r) d\xi, \tag{10}$$

$$\sigma_{\theta}(r, z) = \int_0^\infty \xi \nu \left(\frac{d^3 \tilde{\Phi}_0(\xi, z)}{dz^3} - \xi^2 \frac{d\tilde{\Phi}_0(\xi, z)}{dz} \right) J_0(\xi r) d\xi + \frac{1}{r} \int_0^\infty \xi^2 \frac{d\tilde{\Phi}_0(\xi, z)}{dz} J_1(\xi r) d\xi, \tag{11}$$

$$\tau_{zr}(r, z) = \int_0^\infty \xi^2 \left[\nu \frac{d^2 \tilde{\Phi}_0(\xi, z)}{dz^2} + (1 - \nu) \xi^2 \tilde{\Phi}_0(\xi, z) \right] J_1(\xi r) d\xi. \tag{12}$$

where $J_m(r\xi)$ represents the m order Bessel function of first kind, in the variable $r\xi$.

On this basis, the indefinite balance equations are automatically satisfied, while compatibility gives the equation

$$\left(\frac{d^2}{dz^2} - \xi^2 \right)^2 \tilde{\Phi}_0(\xi, z) = 0,$$

whose solution is

$$\tilde{\Phi}_0(\xi, z) = [L(\xi) + M(\xi)z] \sinh(\xi z) + [N(\xi) + P(\xi)z] \cosh(\xi z), \tag{13}$$

in the unknown functions $L(\xi)$, $M(\xi)$, $N(\xi)$ e $P(\xi)$.

Note that the potential function introduced agrees with the one considered in [Timoshenko and Goodier 1970], and differs from that indicated in [Love 1944] and in [Sneddon 1951] by a term $(1 + \nu)(1 - 2\nu)/E$. The former form allows us to determine a solution for the special case of incompressible materials ($\nu = 1/2$).

As the layered halfspace is axisymmetric deformed, the present theory is applicable to both upper layer and substrate.

We label with the apex ^(c) terms related to the surface coating, and with apex ^(s) those related to the substrate. The zeroth order Hankel transform for the potential of the coating, in the frame of reference (O, r, z) , is given by:

$$\tilde{\Phi}_0^{(c)}(\xi, z) = [A(\xi) + B(\xi)z] \cosh(\xi z) + [C(\xi) + D(\xi)z] \sinh(\xi z), \tag{14}$$

where $A(\xi)$, $B(\xi)$, $C(\xi)$ and $D(\xi)$ are unknowns. In the frame of reference (O, r', z') , the potential for the substrate is given by

$$\tilde{\Phi}_0^{(s)}(\xi, z') = -[S(\xi)z' + T(\xi)] \sinh(\xi z') + [S(\xi)z' + T(\xi)] \cosh(\xi z'), \tag{15}$$

in the unknowns $S(\xi)$ and $T(\xi)$ where we have imposed the vanishing of stresses and displacements as z' goes to ∞ . The equilibrium equation along the z axis can be phrased as

$$2\pi \int_0^a [\sigma_z]_{z=0}^{(c)} r dr = -F. \tag{16}$$

The boundary condition at the external surface of the layer are

$$[\tau_{zr}]_{z=0}^{(c)} = 0 \quad \text{for } r > 0, \tag{17}$$

$$[u_z]_{z=0}^{(c)} = \delta \quad \text{for } 0 \leq r \leq a, \tag{18}$$

$$[\sigma_z]_{z=0}^{(c)} = 0 \quad \text{for } r > a. \tag{19}$$

The interaction between the layer and the substrate, keeping in mind the relation $z = z' + h$, can be expressed, in the case of a perfect bond, through the equations

$$[u_z]_{z=h}^{(c)} = [u_z]_{z'=0}^{(s)}, \tag{20}$$

$$[u_r]_{z=h}^{(c)} = [u_r]_{z'=0}^{(s)}, \tag{21}$$

$$[\tau_{zr}]_{z=h}^{(c)} = [\tau_{zr}]_{z'=0}^{(s)}, \tag{22}$$

$$[\sigma_z]_{z=h}^{(c)} = [\sigma_z]_{z'=0}^{(s)}. \tag{23}$$

For the frictionless case we replace the conditions (21) and (22), that refer to the continuity of the radial displacement and stress, with

$$[\tau_{zr}]_{z=h}^{(c)} = 0, \quad [\tau_{zr}]_{z'=0}^{(s)} = 0,$$

which accounts for the absence of tangential traction between the layer and the substrate.

2.1. Solution. With the boundary conditions above, except for equations (16), (18), (19) and with equations (14), (15), we express $B(\zeta)$, $C(\zeta)$, $D(\zeta)$, $S(\zeta)$, $T(\zeta)$ as functions of $A(\zeta)$ by means of Hankel transforms (see Appendix A). Therefore we write

$$D(\zeta) = -\frac{\zeta A(\zeta)}{2\nu_1}, \tag{24}$$

$$S(\zeta) = \frac{S(\zeta)_{(N)}}{S(\zeta)_{(D)}}, \quad T(\zeta) = \frac{T(\zeta)_{(N)}}{T(\zeta)_{(D)}}, \quad B(\zeta) = \frac{B(\zeta)_{(N)}}{B(\zeta)_{(D)}}, \quad C(\zeta) = \frac{C(\zeta)_{(N)}}{C(\zeta)_{(D)}}, \tag{25}$$

where, in the case of a perfect bond, we obtain

$$S(\zeta)_{(N)} = 2A(\zeta)E_2\zeta(1-\nu_1^2)\{(E_2(1+\nu_1)(-2+h\zeta+2\nu_1)-hE_1\zeta(1+\nu_2))\cosh(\zeta h) + (-E_2(1+h\zeta-2\nu_1)(1+\nu_1)+E_1(-1+h\zeta)(1+\nu_2))\sinh(\zeta h)\},$$

$$T(\zeta)_{(N)} = 2A(\zeta)E_2(1-\nu_1^2)\{(4E_2(-1+\nu_1^2)\nu_2-h\zeta[E_1+E_2+E_2\nu_1+\nu_2(E_1-2E_2(1+\nu_1))])\cosh(\zeta h) + (E_1(1+\nu_2)[-1+2h\zeta(-1+2\nu_2)]+E_2(1+\nu_1)[1-2(1+h\zeta)\nu_2+\nu_1(-2+4\nu_2)])\sinh(\zeta h)\},$$

$$B(\zeta)_{(N)} = \frac{1}{2}A(\zeta)\zeta\{[E_2(1+\nu_1)-E_1(1+\nu_2)][-E_2(1+\nu_1)+E_1(-3+\nu_2+4\nu_2^2)] + [E_2^2(1+\nu_1)^2(-3+4\nu_1)+E_1^2(1+\nu_2)^2(-3+4\nu_2)-2E_1E_2(-1+\nu_1+2\nu_1^2)(-1+\nu_2+2\nu_2^2)]\cosh(2\zeta h) - 8E_1E_2(-1+\nu_1^2)(-1+\nu_2^2)\sinh(2\zeta h)\},$$

$$C(\zeta)_{(N)} = A(\zeta)\{E_2^2(1+\nu_1)^2[2+h^2\zeta^2+\nu_1(-5+4\nu_1)]+E_1^2(h^2\zeta^2+\nu_1)(1+\nu_2)^2(-3+4\nu_2) - 2E_1E_2(1+\nu_1)(-1+h^2\zeta^2+2\nu_1)(-1+\nu_2+2\nu_2^2) + \nu_1[-E_2^2(1+\nu_1)^2(-3+4\nu_1)-E_1^2(1+\nu_2)^2(-3+4\nu_2)+2E_1E_2(-1+\nu_1+2\nu_1^2)(-1+\nu_2+2\nu_2^2)]\cosh(2\zeta h) + 8E_1E_2\nu_1(-1+\nu_1^2)(-1+\nu_2^2)\sinh(2\zeta h)\},$$

$$T(\zeta)_{(D)} = B(\zeta)_{(D)} = C(\zeta)_{(D)} = S(\zeta)_{(D)},$$

$$S(\zeta)_{(D)} = \nu_1\{2h\zeta[-E_2(1+\nu_1)+E_1(1+\nu_2)][-E_2(1+\nu_1)+E_1(-3+\nu_2+4\nu_2^2)] - 8E_1E_2(-1+\nu_1^2)(-1+\nu_2^2)\cosh(2\zeta h) + [E_2^2(1+\nu_1)^2(-3+4\nu_1)+E_1^2(1+\nu_2)^2(-3+4\nu_2)-2E_1E_2(-1+\nu_1+2\nu_1^2)(-1+\nu_2+2\nu_2^2)]\sinh(2\zeta h)\},$$

while the frictionless case leads to

$$S(\zeta)_{(N)} = A(\zeta)\zeta E_2(-1+\nu_1^2)[h\zeta\cosh(h\zeta)+\sinh(\zeta h)],$$

$$T(\zeta)_{(N)} = A(\zeta)2E_2\nu_2(-1+\nu_1^2)[h\zeta\cosh(h\zeta)+\sinh(\zeta h)],$$

$$B(\zeta)_{(N)} = A(\zeta)\zeta\sinh(\zeta h)[E_2(-1+\nu_1^2)\cosh(h\zeta)+E_1(-1+\nu_2^2)\sinh(\zeta h)],$$

$$C(\zeta)_{(N)} = A(\zeta)[-E_2\zeta h(-1+\nu_1^2)+E_1\zeta^2h^2(-1+\nu_2^2)+E_1\nu_1(-1+\nu_2^2) - E_1\nu_1(-1+\nu_2^2)\cosh(2h\zeta)-E_2\nu_1(-1+\nu_1^2)\sinh(2\zeta h)],$$

$$T(\zeta)_{(D)} = B(\zeta)_{(D)} = C(\zeta)_{(D)} = S(\zeta)_{(D)},$$

$$S(\zeta)_{(D)} = \nu_1[E_2(1-\nu_1^2)-2\zeta hE_1(1-\nu_2^2)-E_2(1-\nu_1^2)\cosh(2h\zeta)-E_1(1-\nu_2^2)\sinh(2h\zeta)].$$

Conditions (18) and (19), which refer to parts of the domain, represent the dual integral equation that allows us to determine the unknown function $A(\zeta)$.

In terms of Hankel transforms, equations (18) and (19) can be written as

$$\int_0^\infty \zeta [\tilde{u}_{z_0}]_{z=0}^{(c)} J_0(\zeta r) d\zeta = \delta \quad \text{for } 0 \leq r \leq a, \tag{26}$$

$$\int_0^\infty \zeta [\tilde{\sigma}_{z_0}]_{z=0}^{(c)} J_0(\zeta r) d\zeta = 0 \quad \text{for } r > a, \tag{27}$$

with $[\tilde{u}_{z_0}]^{(c)}$ and $[\tilde{\sigma}_{z_0}]^{(c)}$ function of $\tilde{\Phi}_0^{(c)}(\zeta, z)$ as specified in Appendix A.

If we write

$$[\tilde{u}_{z_0}]_{z=0}^{(c)} = -\zeta^2 A(\zeta) k_u, \tag{28}$$

$$[\tilde{\sigma}_{z_0}]_{z=0}^{(c)} = \zeta^3 A(\zeta) k_s, \tag{29}$$

where

$$k_u = \frac{(1 - \nu_1^2)}{E_1 \nu_1} \quad \text{and} \quad k_s(\zeta) = \frac{k_{s(N)}}{k_{s(D)}}, \tag{30}$$

with, in the case of a perfect bond

$$\begin{aligned} k_{s(N)} = & -\{E_2^2(1+\nu_1)^2(5+2h^2\zeta^2+4\nu_1(-3+2\nu_1)) - E_1^2(1+2h^2\zeta^2)(1+\nu_2)^2(-3+4\nu_2) \\ & + 2E_1E_2(1+\nu_1)(-1+2h^2\zeta^2+2\nu_1)(-1+\nu_2+2\nu_2^2) \\ & + [E_2^2(1+\nu_1)^2(-3+4\nu_1) + E_1^2(1+\nu_2)^2(-3+4\nu_2) - 2E_1E_2(-1+\nu_1+2\nu_1^2)(-1+\nu_2+2\nu_2^2)] \cosh(2h\zeta) \\ & - 8E_1E_2(-1+\nu_1^2)(-1+\nu_2^2) \sinh(2h\zeta)\}, \end{aligned}$$

$$k_{s(D)} = 2S(\zeta)_{(D)},$$

and, in the frictionless case,

$$\begin{aligned} k_{s(N)} = & -2\zeta h E_2(1 - \nu_1^2) - E_1(1 + 2\zeta^2 h^2)(1 - \nu_2^2) - E_1(1 - \nu_2^2) \cosh(2h\zeta) - E_2(1 - \nu_1^2) \sinh(2h\zeta), \\ k_{s(D)} = & 2S(\zeta)_{(D)}, \end{aligned}$$

then equations (26) and (27) become

$$\int_0^\infty -\zeta^3 A(\zeta) k_u J_0(\zeta r) d\zeta = \delta \quad \text{for } 0 \leq r \leq a, \tag{31}$$

$$\int_0^\infty \zeta^4 A(\zeta) k_s(\zeta) J_0(\zeta r) d\zeta = 0 \quad \text{for } r > a. \tag{32}$$

Equations (31) and (32) represent the dual integral equation that solves the problem. At this point we search for a numerical solution instead of treating the problem analytically. From (31) and (32) we can find solutions in the case of an incompressible layer; this special case is not treatable if we adopt Sneddon's expression (for $\nu = 1/2$ we have $k_s(\zeta) = \infty$).

In Appendix B we show that if the thickness of the coating tends to infinite the potential of surface layer converges to the one related to the indefinite isotropic halfspace with moduli E_1 and ν_1 , while

when the thickness vanishes the potential of substrate converge to that related to the indefinite isotropic halfspace with moduli E_2 and ν_2 .

3. Numerical solutions

The dual integral equation (31)–(32), for the Erdélyi–Sneddon solution method [Sneddon 1966], can be converted in a second kind Fredholm equation whose kernels, in our cases, have only singularity in the integration limits.

With

$$A^*(\zeta) = \zeta^4 A(\zeta) k_s(\zeta), \quad \bar{\zeta} = a\zeta, \quad \bar{r} = r/a,$$

$$\frac{\varrho}{k_s(\bar{\zeta})} = 1 + I(\bar{\zeta}), \tag{33}$$

$$\overline{A^*}(\bar{\zeta}) = A^*(\bar{\zeta}) \frac{k_u}{\varrho \delta},$$

the dual integral equation (31)–(32) becomes

$$\int_0^\infty \zeta^{-1} \overline{A^*}(\bar{\zeta}) [1 + I(\bar{\zeta})] J_0(\bar{\zeta}\bar{r}) d\bar{\zeta} = -1 \quad 0 < \bar{r} < 1, \tag{34}$$

$$\int_0^\infty \overline{A^*}(\bar{\zeta}) J_0(\bar{\zeta}\bar{r}) d\bar{\zeta} = 0 \quad \bar{r} > 1. \tag{35}$$

The parameter ϱ has to be chosen so that the Fourier cosine transform of function $I(t)$ exists with the auxiliary parameters $|x - u|$ e $|x + u|$; that is, the following integrals converge

$$\int_0^\infty I(t) \cos(t|x - u|) dt + \int_0^\infty I(t) \cos(t|x + u|) dt.$$

This condition implies that

$$\lim_{\bar{\zeta} \rightarrow \infty} \frac{\varrho}{k_s(\bar{\zeta})} = 1,$$

which means, either for perfect bond or frictionless case, that $\varrho = 1/2\nu_1$.

The solution of (34)–(35) is

$$\overline{A^*}(\bar{\zeta}) = \frac{\bar{\zeta}}{\sqrt{\pi}} \int_0^1 h_1(t) \cos(\bar{\zeta}t) dt, \tag{36}$$

where $h_1(t)$ is the solution of the following Fredholm integral equation [Sneddon 1966]

$$h_1(x) + \int_0^1 h_1(u) k(x, u) du = H(x), \tag{37}$$

with

$$k(x, u) = \frac{u}{x\sqrt{2\pi}} \left(\sqrt{\frac{2}{\pi}} \int_0^\infty I(t) \cos(t|x - u|) dt + \sqrt{\frac{2}{\pi}} \int_0^\infty I(t) \cos(t|x + u|) dt \right) \tag{38}$$

and

$$H(x) = -\frac{2}{x\sqrt{\pi}}.$$

Once we have solved Equation (37) numerically, together with (36), we obtain the dimensionless normal stress distribution inside the contact area

$$\overline{[\sigma_z(\bar{r})]}_{z=0}^{(c)} = [\sigma_z(\bar{r})]_{z=0}^{(c)} \frac{ak_u}{\rho\delta} = \int_0^\infty \overline{A^*(\bar{\xi})} J_0(\bar{\xi}\bar{r}) d\bar{\xi} \quad [0 < \bar{r} < 1]. \tag{39}$$

Next we impose the translation balance, Equation (16), and obtain the dimensionless force-displacement relation

$$\bar{F} = F \frac{k_u}{\rho\delta a} = -2\pi \int_0^1 \overline{[\sigma_z(\bar{r})]}_{z=0}^{(c)} \bar{r} d\bar{r}, \tag{40}$$

which allows us to obtain a symbolic solution in E_1 and ν_1 in the case of elastic layer, with no friction, on a rigid substrate. In order to solve Equation (38) numerically we use the Newton–Cotes method, with the exclusion of the integration limits (see [Davis and Rabinowitz 1984], for example). We replace the integral in (37) by a series by dividing the range $[0, 1]$ into N parts, so that

$$h_1(x_i) + \sum_{j=1}^{N-1} h_1(u_j)k(x_i, u_j)w_j = H(x_i), \tag{41}$$

where w_j represents the weight to be considered for the chosen integration method. Varying x_i and u_j with the same step, Equation (41) is equivalent to a linear system of equations in the variable $h_1(x_i)$:

$$(K + V)H_1 = H,$$

where H_1 is the variable array $h_1(x_i)$, K the coefficients matrix $k(x_i, u_j)w_j$, V the $(N - 1)$ th order identity matrix and H the known terms array $H(x_i)$. When we get $h_1(x_i)$ we can then evaluate numerically the expressions (36), (39) and (40).

4. Applications

We note that with $k_s(\xi)$ in (30) in both cases, perfect bond and frictionless condition, we do not have a symbolic solution. Therefore we take some values for all mechanical properties of the two elastic bodies. As examples of our activity we consider four cases of interacting materials; in particular we take a steel layer above a polystyrene substrate such that $E_1 = 210$ GPa, $\nu_1 = 0.3$ and $E_2 = 2$ GPa, $\nu_2 = 0.4$. This represents an application for a case in which the substrate is softer than the coating. Then we take a steel layer above a glass substrate such that $E_1 = 210$ GPa, $\nu_1 = 0.3$ and $E_2 = 70$ GPa, $\nu_2 = 0.22$; the opposite case is also treated such that $E_1 = 70$ GPa, $\nu_1 = 0.22$ and $E_2 = 210$ GPa, $\nu_2 = 0.3$. These represent an application for a case in which the substrate and the coating have similar stiffness. As last case, in the next section, we deal with the case of substrate much stiffer than the upper layer that can be treated as a limit case of rigid foundation.

In Figure 2 we plot the dimensionless force \bar{F} for different values of the ratio $\bar{h} = h/a$, in the case of a perfect bond of a steel layer above a polystyrene substrate (top) and in the frictionless case (bottom). Figure 3 deals with the case of a steel layer above a glass substrate, and Figure 4 with that of a glass layer above a steel substrate.

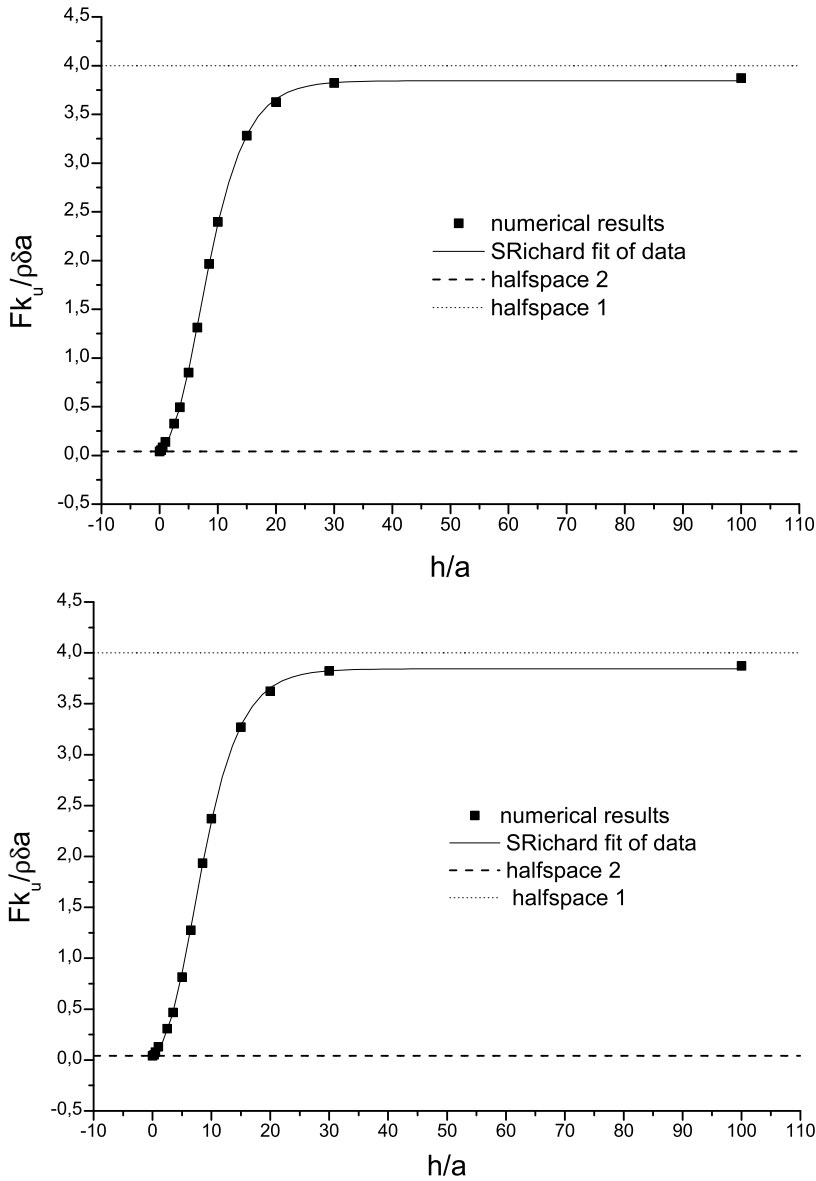


Figure 2. Elastic substrate (steel on polystyrene): contact law for perfect-bond (top) and frictionless case (bottom). Parameters: $E_1=210$ GPa, $\nu_1=0.3$, $E_2=2$ GPa, $\nu_2=0.4$).

In all figures we have also considered the limit values of \bar{F} related to the elastic halfspace 1, with moduli E_1 and ν_1 , and to the elastic halfspace 2, with moduli E_2 and ν_2 . (For the half space with moduli E and ν , we have

$$\bar{F} = \frac{2}{\delta a} \frac{(1 - \nu_1^2)}{E_1} \left[\frac{2\delta E a}{(1 - \nu^2)} \right].$$

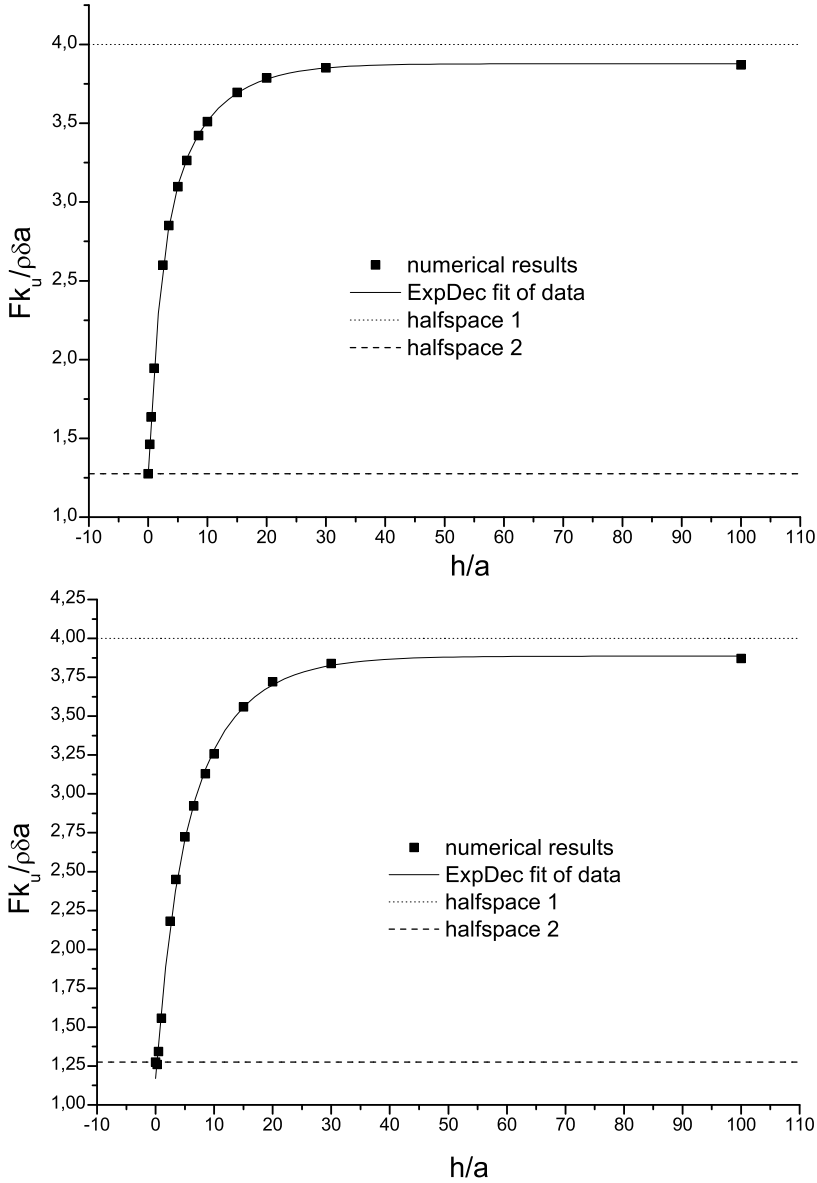


Figure 3. Elastic substrate (steel on glass): contact law for perfect-bond (top) and frictionless case (bottom). Parameters: $E_1=210$ GPa, $\nu_1=0.3$, $E_2=70$ GPa, $\nu_2=0.22$.

For the halfspace with moduli E_1 and ν_1 , we have $\bar{F}_1 = 4$. For the halfspace with moduli E_2 and ν_2 we have

$$\bar{F}_2 = 4 \frac{E_2 (1 - \nu_1^2)}{E_1 (1 - \nu_2^2)}.$$

Therefore $\bar{F}_2 = 0.04127$ for steel on polystyrene, $\bar{F}_2 = 1.275$ for steel on glass and $\bar{F}_2 = 12.549$ for glass on steel.)

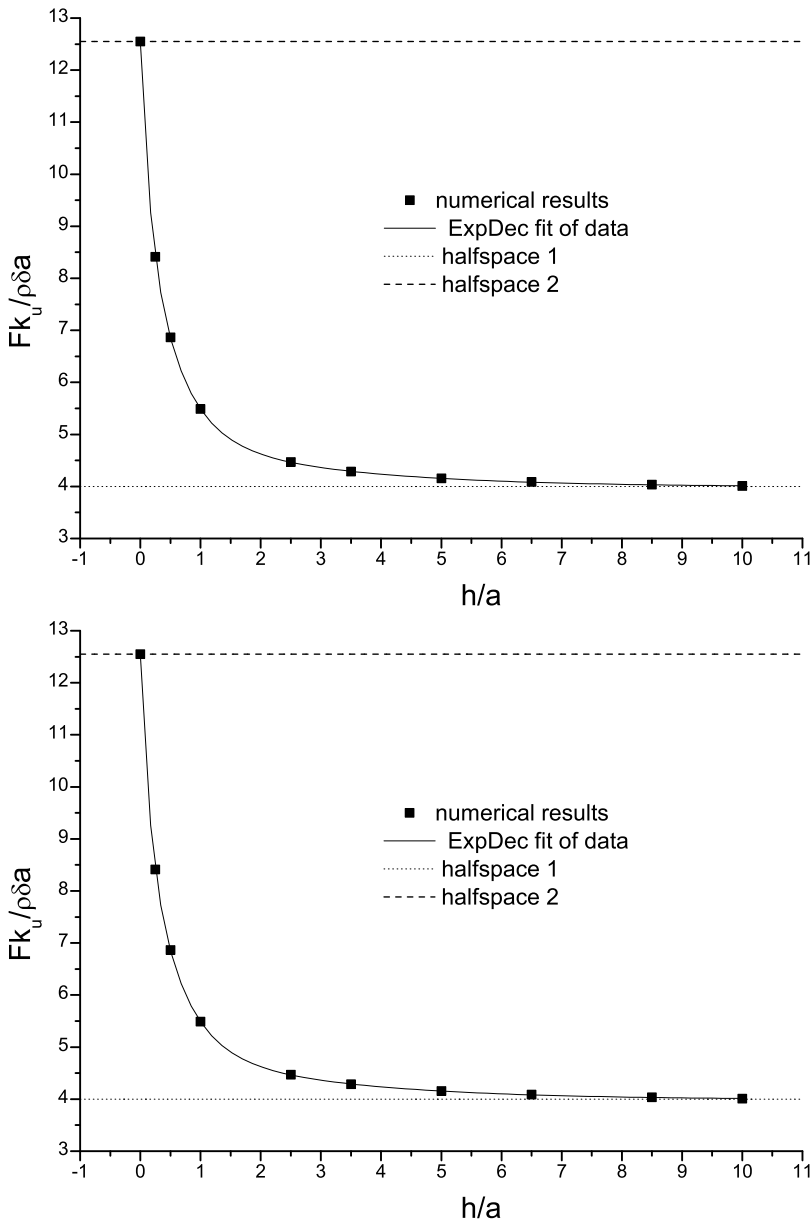


Figure 4. Elastic substrate (glass on steel): contact law for perfect-bond (top) and frictionless case (bottom). Parameters: $E_1 = 70$ GPa, $\nu_1 = 0.22$, $E_2 = 210$ GPa, $\nu_2 = 0.3$).

The numerical results have been fitted by means of the SRichards curve or ExpDec curve (see Appendix C). We also provide in Appendix C the numerical results related to Figures 2–4 in order to show more in detail the differences that emerge in the perfect-bond and frictionless cases.

We observe that for the coating’s thickness $h < 0.5a$ the solution is close to the halfspace with the same characteristic of the substrate, while, when the ratio $\bar{h} = h/a$ increases it tends to the case of the

halfspace with moduli E_1, ν_1 , such that, for $h > 10a$, we can assume that the substrate does not influence the force-displacement relation.

With fixed thickness, \bar{F} related to the frictionless case is lower than that related to perfect bond; that is, in the latter case the layer results less capable of being deformed.

5. Rigid foundation

As already underlined, if the substrate is much stiffer than the surface coating the problem can be approximated to the case of an elastic layer lying on a rigid foundation [Matthewson 1981; Yang 2003; Yang 1998]. The solution can be obtained directly by the general case developed previously by taking the limit $E_2 \rightarrow \infty$.

In the case of a perfect bond we have

$$\lim_{E_2 \rightarrow \infty} B(\zeta) = -\zeta A(\zeta) \frac{1 + (3 - 4\nu_1)\nu_1 \cosh(2\zeta h)}{4h\zeta\nu_1 + 2\nu_1(-3 + 4\nu_1) \sinh(2\zeta h)}, \tag{42}$$

$$\lim_{E_2 \rightarrow \infty} C(\zeta) = A(\zeta) \frac{2 + h^2\zeta^2 + \nu_1(-5 + 4\nu_1) + (3 - 4\nu_1)\nu_1 \cosh(2\zeta h)}{2h\zeta\nu_1 + \nu_1(-3 + 4\nu_1) \sinh(2\zeta h)}, \tag{43}$$

$$\lim_{E_2 \rightarrow \infty} D(\zeta) = -\frac{\zeta A(\zeta)}{2\nu_1}, \tag{44}$$

$$\lim_{E_2 \rightarrow \infty} [\tilde{u}_{z_0}]_{z=0}^{(c)} = -\zeta^2 A(\zeta) \frac{(1 - \nu_1^2)}{E_1\nu_1}, \tag{45}$$

$$\lim_{E_2 \rightarrow \infty} [\tilde{\sigma}_{z_0}]_{z=0}^{(c)} = -\zeta^3 A(\zeta) \frac{5 + 2h^2\zeta^2 + 4\nu_1(-3 + 2\nu_1) + (3 - 4\nu_1) \cosh(2\zeta h)}{4h\zeta\nu_1 + 2\nu_1(-3 + 4\nu_1) \sinh(2\zeta h)}. \tag{46}$$

The dual integral equation (31)–(32) seems not to be analytically solvable; however the numerical solution, for equations (45) and (46), is symbolic in the parameter E_1 . We plot in Figure 5 the dimensionless force-displacement diagrams for $\nu_1 = 0.1, 0.3$ and 0.5 . The numerical results have been fitted by means of the ExpDec curve for the compressible layer (see Appendix C). Note that, for a given thickness, when the Poisson ratio increases we need a greater force to produce the same displacement.

The same Figure 5 also shows the dimensionless force-displacement relation for the halfspace with moduli E_1 and ν_1 and for very thin layer; in this last case we have introduced in (42)–(46) the series

$$\sinh(h\zeta) = \sum_{n=0}^{\infty} \frac{(h\zeta)^{2n+1}}{(2n+1)!}, \quad \cosh(h\zeta) = \sum_{n=0}^{\infty} \frac{(h\zeta)^{2n}}{(2n)!}, \tag{47}$$

neglecting in each case the higher order terms (details of the approximations are given in Appendix D). With this approximation, we can treat the dual integral Equation (31)–(32) analytically. These equations, in fact, can be reduced to the classic Titchmarsh’s form [Sneddon 1966] if the film is incompressible (see Appendix E), while, in the case of compressible films, they can be solved by applying the inversion theorem for Hankel transforms (see Appendix E). For an incompressible film we have

$$A(\zeta) = -\frac{\delta a^2}{2\zeta^2 k_u} J_2(\zeta a),$$

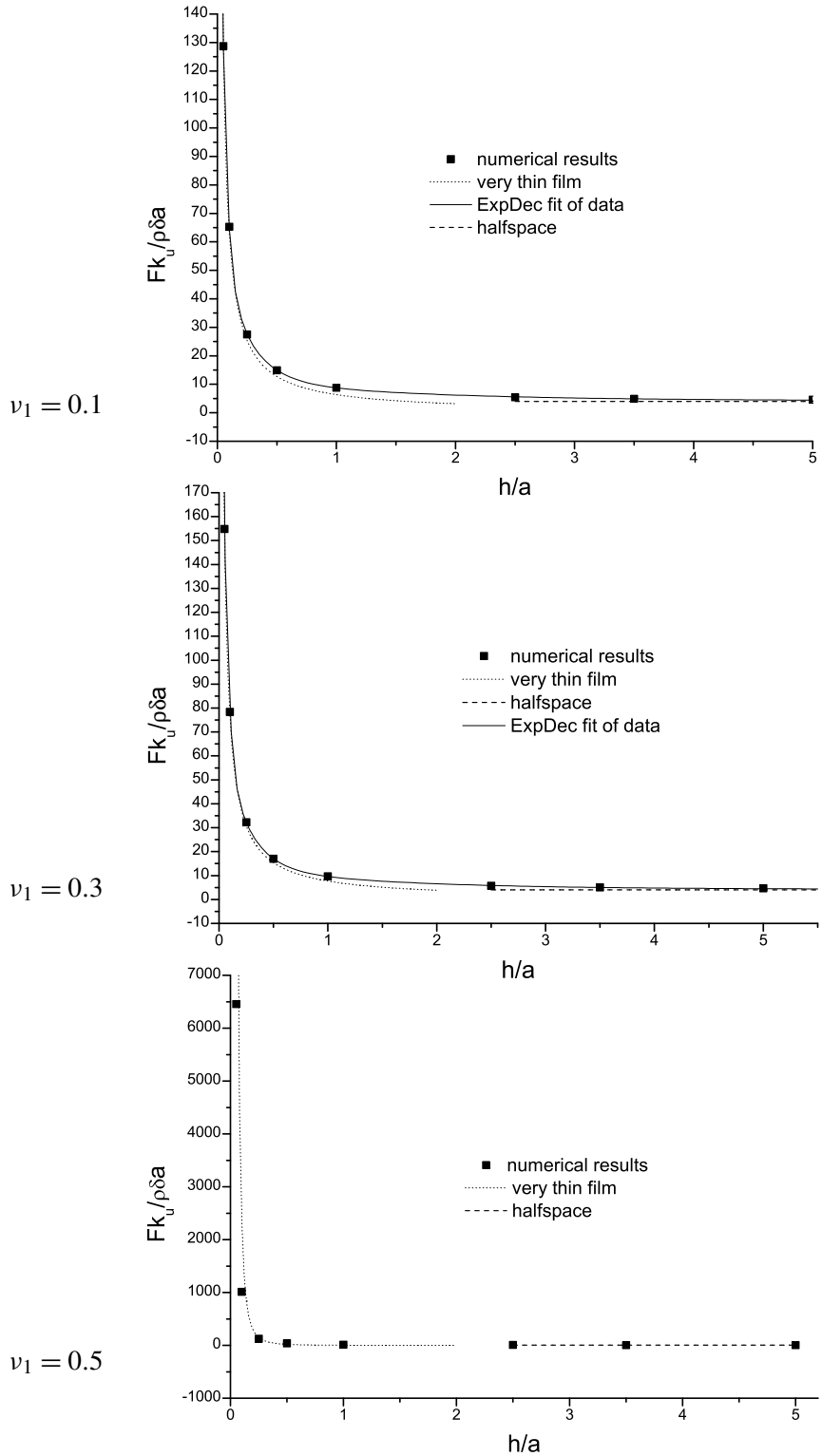


Figure 5. Rigid substrate: contact law for perfect bond case.

and, for (16), we obtain the force-displacement relation

$$\delta = \frac{8Fh^3}{a^4\pi E_1}. \tag{48}$$

For a compressible film, instead, we have

$$A(\xi) = -\frac{1}{\xi^3} \frac{a\delta}{k_u} J_1(\xi a),$$

and, for (16), we obtain the force-displacement relation

$$\delta = \frac{Fh(1+\nu_1)(1-2\nu_1)}{\pi a^2 E_1(1-\nu_1)}. \tag{49}$$

For very thin films we note a great difference between displacements δ given by (48) and (49): the former depends on h^3 while the latter varies as h .

In the frictionless case we have

$$\lim_{E_2 \rightarrow \infty} B(\xi) = \xi A(\xi) \frac{\cosh(\xi h)}{2\nu_1 \sinh(\xi h)}, \tag{50}$$

$$\lim_{E_2 \rightarrow \infty} C(\xi) = -A(\xi) \frac{[h\xi + \nu_1 \sinh(2\xi h)]}{2\nu_1 [\sinh(\xi h)]^2}, \tag{51}$$

$$\lim_{E_2 \rightarrow \infty} D(\xi) = -\frac{\xi A(\xi)}{2\nu_1}, \tag{52}$$

$$\lim_{E_2 \rightarrow \infty} [\tilde{u}_{z_0}]_{z=0}^{(c)} = -\xi^2 A(\xi) \frac{(1-\nu_1^2)}{E_1 \nu_1}, \tag{53}$$

$$\lim_{E_2 \rightarrow \infty} [\tilde{\sigma}_{z_0}]_{z=0}^{(c)} = \xi^3 A(\xi) \frac{[2h\xi + \sinh(2\xi h)]}{4\nu_1 [\sinh(\xi h)]^2}. \tag{54}$$

Unlike the case of a perfect bond, the dual integral equation (53)–(54) has a numerical symbolic solution in both mechanical parameters, E_1 and ν_1 , of the surface layer. We plot in Figure 6 the dimensionless force-displacement relation.

Moreover in this case we consider the dimensionless force-displacement relation for the halfspace with moduli E_1 and ν_1 and for very thin layer; we have also plotted the fitting ExpDec curve (see Appendix C). For thin layer we have again replaced in ((50) – (54)), the series (47) and we do not have a different significant order of infinitesimal for the compressible and incompressible film. So we then obtain a single solution for compressible and incompressible cases. Again equations (31) and (32) are solvable analytically applying the inversion theorem for Hankel transform (see Appendix E) and the solution is

$$A(\xi) = -\frac{1}{\xi^3} \frac{a\delta}{k_u} J_1(\xi a),$$

and, with (16), we obtain the force-displacement relation

$$\delta = \frac{Fh(1-\nu_1^2)}{\pi a^2 E_1}. \tag{55}$$

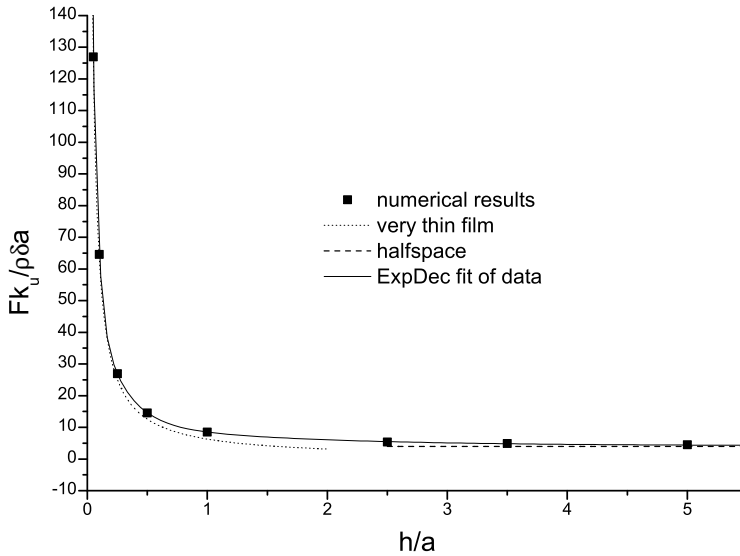


Figure 6. Rigid substrate: contact law for frictionless case.

In case of a compressible or incompressible very thin layer that is free to slide on a rigid foundation, we obtain, therefore, a direct proportionality between δ and h , as in the case of compressible films in perfect bond. Yang [1998; 2003; 2006] obtained the same results, considering the direct case of an elastic layer on a rigid foundation, again in the compressible and incompressible cases. For the latter he formulates the differential problem on the basis of the constitutive relation of incompressible materials.

6. Conclusion

We have considered an elastic, axisymmetric indentation problem under conditions that represent the upper and lower limits of real situations, for which the degree of adhesion between the layers is intermediate between the conditions of complete bond and frictionless.

From the analysis developed for an elastic coating on an elastic substrate is deduced that, varying $\bar{h} = h/a$ between 0.5 and 10, the F - δ law is influenced by all the mechanical properties of materials of the two layers. The same is true for the function $[\overline{\sigma_z(\bar{r})}]_{z=0}^{(c)}$ given by (39), for different values of the ration h/a . Therefore we have only provided the dimensionless relations F vs. δ .

A comparison of the results leads us to conclude that a given displacement δ is associated to a smaller force F for the frictionless case than for the perfect bond condition; this indicates that the frictionless on interface makes more deformable the layered body. This difference increases with the reduction of the thickness of the surface layer and when the Poisson ratio increases.

This is evident if we compare the two cases of a compressible film on a rigid foundation: the dimensionless solution in the frictionless case is slightly lower than that of perfect bond related to film with modulus ν_1 minimum among those considered ($\nu_1 = 0.1$).

The contrast is all the clearer for incompressible films, especially if the foundation is rigid and the surface layer is very thin. In fact, formulas (48) and (55), referring to the latter condition respectively

for perfect bonding and absence of friction, differ by two orders of magnitude: in one case there appears h^3 and in the other h .

We also pointed out that the choice of analytical solution highlight characteristics of the solution that are difficult to notice through a complete numerical study.

Appendix A. Hankel transforms

If we apply the inversion theorem to equations (1), (2), (3) and (6) we obtain the Hankel transforms of some components of stress and displacement as functions of $\tilde{\Phi}_0(\xi, z)$ and derivatives of $\tilde{\Phi}_0(\xi, z)$:

$$\tilde{u}_{r_1}(\xi, z) = \frac{(1 + \nu)}{E} \xi \frac{d\tilde{\Phi}_0(\xi, z)}{dz}, \tag{56}$$

$$\tilde{u}_{z_0}(\xi, z) = \frac{(1 - 2\nu)(1 + \nu)}{E} \frac{d^2\tilde{\Phi}_0(\xi, z)}{dz^2} - \frac{2(1 - \nu^2)}{E} \xi^2 \tilde{\Phi}_0(\xi, z), \tag{57}$$

$$\tilde{\sigma}_{z_0}(\xi, z) = (1 - \nu) \frac{d^3\tilde{\Phi}_0(\xi, z)}{dz^3} - (2 - \nu) \xi^2 \frac{d\tilde{\Phi}_0(\xi, z)}{dz}, \tag{58}$$

$$\tilde{\tau}_{r_1}(\xi, z) = \xi \left[\nu \frac{d^2\tilde{\Phi}_0(\xi, z)}{dz^2} + (1 - \nu) \xi^2 \tilde{\Phi}_0(\xi, z) \right], \tag{59}$$

Appendix B. Convergence for $h \rightarrow \infty$ and for $h \rightarrow 0$

The following proof of convergence to halfspace is valid either for perfect bond that for frictionless case. For $h \rightarrow \infty$, equations (28), (29) become

$$\lim_{h \rightarrow \infty} [\tilde{u}_{z_0}]_{z=0}^{(c)} = -\xi^2 A(\xi) \frac{(1 - \nu_1^2)}{E_1 \nu_1}, \quad \lim_{h \rightarrow \infty} [\tilde{\sigma}_{z_0}]_{z=0}^{(c)} = \xi^3 A(\xi) \frac{1}{2\nu_1}.$$

Consequently the dual integral (31)–(32) can be treated analytically as it reduces to the classical Titchmarsh’s form [Sneddon 1966], and give

$$A(\xi) = -\frac{2}{\pi \xi^3} \frac{E_1 \nu_1}{(1 - \nu_1^2)} \delta \sin(\xi a). \tag{60}$$

For the other functions $B(\xi)$, $C(\xi)$ and $D(\xi)$ we simply have

$$\lim_{h \rightarrow \infty} B(\xi) = \frac{\xi A(\xi)}{2\nu_1}; \quad \lim_{h \rightarrow \infty} C(\xi) = -A(\xi); \quad \lim_{h \rightarrow \infty} D(\xi) = -\frac{\xi A(\xi)}{2\nu_1}, \tag{61}$$

and, by replacing Equation (60) in (61), the potential in the layer, given by equation (14), becomes

$$\tilde{\Phi}_0^{(c)} = -\frac{\sin(\xi a)}{\xi^4} \frac{E_1 \delta}{\pi (1 - \nu_1^2)} [2\nu_1 + \xi z] e^{(-\xi z)}, \tag{62}$$

which is equivalent to the solution of the halfspace of moduli E_1 e ν_1 .

For $h \rightarrow 0$, equations (28)–(29) become

$$\lim_{h \rightarrow 0} [\tilde{u}_{z_0}]_{z=0}^{(c)} = -\xi^2 A(\xi) \frac{(1 - \nu_1^2)}{E_1 \nu_1}, \quad \lim_{h \rightarrow 0} [\tilde{\sigma}_{z_0}]_{z=0}^{(c)} = \xi^3 A(\xi) \frac{E_2 (1 - \nu_1^2)}{2E_1 \nu_1 (1 - \nu_2^2)}.$$

With these equations it is again the case that the solution of the dual integral (31)–(32) is given by (60), because the right-hand term in (32) vanishes. In the limit the unknown functions $S(\zeta)$ and $T(\zeta)$ are

$$\lim_{h \rightarrow 0} S(\zeta) = \frac{E_2(1 - \nu_1^2)}{2E_1\nu_1(1 - \nu_2^2)} \zeta A(\zeta); \quad \lim_{h \rightarrow 0} T(\zeta) = \frac{E_2\nu_2(1 - \nu_1^2)}{E_1\nu_1(1 - \nu_2^2)} A(\zeta), \quad (63)$$

and, replacing (60) in (63), the potential in the substrate, given by equation (15), becomes

$$\tilde{\Phi}_0^{(s)} = -\frac{\sin(\zeta a)}{\zeta^4} \frac{E_2\delta}{\pi(1 - \nu_2^2)} (2\nu_2 + \zeta z') e^{(-\zeta z')}, \quad (64)$$

that is equivalent to the solution of the halfspace of moduli $E_2 e \nu_2$, because for $h \rightarrow 0$ the z' axis has the same origin of z .¹

Appendix C. Numerical results and fitting curves

The following tables show the numerical results for \bar{F} , in the case of perfect bonding (pb) and no friction (nf), as well as the percent difference.

Steel on polystyrene

\bar{h}	0.25	0.5	1	2.5	3.5	5	6.5	8.5	10	15	20	30	100
\bar{F} (pb)	.0550	.0815	.1385	.3267	.4936	.8489	1.3118	1.9653	2.3968	3.2809	3.6260	3.8228	3.8717
\bar{F} (nf)	.0522	.0772	.1312	.3089	.4681	.8149	1.2757	1.9347	2.3724	3.2719	3.6227	3.8221	3.8716
$\Delta\bar{F}$ (%)	5.09	5.27	5.27	5.45	5.17	4.00	2.75	1.58	1.02	0.27	0.09	0.02	0.003

Steel on glass

\bar{h}	0.25	0.5	1	2.5	3.5	5	6.5	8.5	10	15	20	30	100
\bar{F} (pb)	1.463	1.636	1.945	2.600	2.852	3.097	3.264	3.422	3.511	3.696	3.788	3.853	3.872
\bar{F} (nf)	1.261	1.344	1.557	2.181	2.450	2.723	2.922	3.129	3.257	3.560	3.722	3.838	3.862
$\Delta\bar{F}$ (%)	13.82	17.85	19.92	16.11	14.09	12.07	10.47	8.56	7.25	3.67	1.75	0.38	0.26

Glass on steel

\bar{h}	0.25	0.5	1	2.5	3.5	5	6.5	8.5	10
\bar{F} (pb)	9.0541	7.6161	6.1548	4.7986	4.5174	4.3118	4.2043	4.1222	4.0827
\bar{F} (nf)	8.4112	6.8633	5.4886	4.4709	4.2846	4.1551	4.0864	4.0338	4.0084
$\Delta\bar{F}$ (%)	7.10	9.88	10.82	6.83	3.63	3.63	2.80	2.14	1.82

The fitting of curves was carried out based on 13 values of the ratio h/a . SRichards and ExpDec are exponential curves; the general expression for a SRichards curve is

$$\bar{F} = b[1 + (d - 1)e^{-c(\bar{h} - h_0)}]^{1/(1-d)}$$

¹The Hankel transform of Sneddon’s potential [1951] for the halfspace is equivalent to (62) or (64) times $E^{-1}(1 + \nu)(1 - 2\nu)$, in agreement with the formulation of the problem.

while the expression for the ExpDec curve is

$$\bar{F} = F_0 + b_1 e^{-(\bar{h}-h_0)/c_1} + b_2 e^{-(\bar{h}-h_0)/c_2} + b_3 e^{-(\bar{h}-h_0)/c_3}$$

The constants obtained were as follows (pb = perfect bond; nf = no friction):

Steel on polystyrene

	b	d	c	h_0
(pb)	3.8447	1.05499	0.22874	6.88795
(nf)	3.84321	1.06893	0.23112	7.02854

Steel on glass

	F_0	h_0	b_1	b_2	b_3	c_1	c_2	c_3
(pb)	3.87775	0	-1.30211	-1.31437	0	1.88306	7.68174	0
(nf)	3.88583	0	-1.73246	-0.98371	0	8.90297	3.07826	0

Glass on steel

	F_0	h_0	b_1	b_2	b_3	c_1	c_2	c_3
(pb)	3.9879	0.13699	7.44575	1.20125	6.4023	0.12538	2.60411	0.52208
(nf)	4.04243	0.14828	6.62349	1.72188	6.14044	0.12554	2.77703	0.62372

Rigid foundation

	F_0	h_0	b_1	b_2	b_3	c_1	c_2	c_3
(nf)	4.1702	0	264.127	50.342	7.86791	0.03896	0.21493	1.40524
(pb, $\nu_1 = 0.1$)	4.1947	0	270.474	51.108	8.31471	0.03942	0.21365	1.41220
(pb, $\nu_1 = 0.3$)	4.2509	0	323.156	61.805	9.99856	0.03983	0.21263	1.3695

Appendix D. Approximations on the hyperbolic functions for very thin coating

In the case of a very thin coating we have substituted the hyperbolic series (47), neglecting the higher order terms, in order to solve the dual integral equation and obtain the force-displacement law. To this end we follow the approach proposed by Yang [2003; 1998] and we report here some details of the calculation useful to derive the explicit form of the dual integral equation based upon the potentials adopted.

For a compressible very thin coating in perfect bond on a rigid foundation, if we assume

$$\sinh(h\xi) \simeq h\xi, \quad \cosh(h\xi) \simeq 1 + \frac{1}{2}(h\xi)^2, \quad (65)$$

use the identities

$$\sinh(2h\xi) = 2 \sinh(h\xi) \cosh(h\xi), \quad \cosh(2h\xi) = \sinh^2(h\xi) + \cosh^2(h\xi), \quad (66)$$

and substitute formulas (65) and (66) in (42), (43) and (46) we obtain

$$B(\xi) = A(\xi) \frac{1-\nu_1}{2h\nu_1(1-2\nu_1)}, \quad C(\xi) = -A(\xi) \frac{1-\nu_1}{2h\xi\nu_1(1-2\nu_1)}, \quad [\tilde{\sigma}_{z_0}]_{z=0}^{(c)} = \xi^2 A(\xi) \frac{(1-\nu_1)^2}{h\nu_1(1-2\nu_1)}. \quad (67)$$

With this approximation, we can treat the dual integral (31)–(32) analytically. These equations, in fact, can be solved applying the inversion theorem for Hankel transforms.

In case of an incompressible coating the expressions (67) become indeterminate and consequently we must include additional terms in the series expansion (47). If we take

$$\sinh(h\xi) \simeq h\xi + \frac{1}{6}(h\xi)^3, \quad \cosh(h\xi) \simeq 1 + \frac{1}{2}(h\xi)^2, \quad (68)$$

set $\nu = \frac{1}{2}$, and substitute formulas (68), (66) in (42), (43) and (46), we obtain

$$B(\xi) = A(\xi) \frac{3}{2h^3\xi^2}, \quad C(\xi) = -A(\xi) \frac{3}{2h^3\xi^3}, \quad [\tilde{\sigma}_{z_0}]_{z=0}^{(c)} = A(\xi) \frac{3}{2h^3}. \quad (69)$$

With this approximation we can treat the dual integral (31)–(32) analytically because it can be reduced to the classic Titchmarsh form.

For a compressible very thin coating free to slide on a rigid foundation, if we substitute formulas (65) and (66) in (50), (51) and (54) we obtain

$$B(\xi) = A(\xi) \frac{1}{2h\nu_1}, \quad C(\xi) = -A(\xi) \frac{1+2\nu_1}{2h\xi\nu_1}, \quad [\tilde{\sigma}_{z_0}]_{z=0}^{(c)} = \xi^2 A(\xi) \frac{1}{h\nu_1}. \quad (70)$$

In this case the approximation (65) is valid for incompressible upper layer too, and the dual integral (31)–(32) is solvable analytically applying the inversion theorem for Hankel transform.

Appendix E. Analytical solution of the dual integral equation for a very thin coating on a rigid foundation

For a very thin incompressible layer in perfect bond on a rigid foundation we have the transform of the surface normal stress given by (69)₃. Consequently, the dual integral equation can be written as

$$\int_0^\infty -\xi^3 A(\xi) \frac{3}{2E_1} J_0(\xi r) d\xi = \delta \quad \text{for } 0 < r < a, \\ \int_0^\infty \xi A(\xi) \frac{3}{2h^3} J_0(\xi r) d\xi = 0 \quad \text{for } r > a, \quad (71)$$

and if we assume

$$\bar{\xi} = \xi a, \quad \bar{r} = \frac{a}{r}, \quad k_u = \frac{3}{2E_1}, \quad \bar{\delta} = -a^4 \frac{\delta}{k_u}, \quad \overline{A(\bar{\xi})} = \bar{\xi} A(\bar{\xi}),$$

we have

$$\int_0^\infty \bar{\xi}^2 \overline{A(\bar{\xi})} J_0(\bar{\xi} \bar{r}) d\bar{\xi} = \bar{\delta} \quad \text{for } 0 < \bar{r} < 1, \\ \int_0^\infty \overline{A(\bar{\xi})} J_0(\bar{\xi} \bar{r}) d\bar{\xi} = 0 \quad \text{for } \bar{r} > 1. \quad (72)$$

The dual integral equation in the form

$$\int_0^\infty \bar{\xi}^{-2\alpha} A(\bar{\xi}) J_m(\bar{\xi} \bar{r}) d\bar{\xi} = f(\bar{r}) \quad \text{for } 0 < \bar{r} < 1,$$

$$\int_0^\infty A(\bar{\xi}) J_m(\bar{\xi} \bar{r}) d\bar{\xi} = 0 \quad \text{for } \bar{r} > 1,$$

with $\alpha < 0$, was solved by Titchmarsh; the solution is

$$A(\bar{\xi}) = \frac{(2\bar{\xi})^{1+\alpha}}{\Gamma(-\alpha)} \int_0^1 t^{1-\alpha} J_{m-\alpha}(\bar{\xi} t) \left(\int_0^1 (1-s^2)^{-1-\alpha} s^{m+1} f(ts) ds \right) dt.$$

Therefore, the solution for the dual (72) is

$$\overline{A(\bar{\xi})} = \int_0^1 \bar{r}^2 J_1(\bar{\xi} \bar{r}) \left(\int_0^1 s \bar{\delta} ds \right) d\bar{r} = -\frac{1}{\bar{\xi}} a^4 \frac{\delta}{2k_u} J_2(\bar{\xi}),$$

and then we have

$$A(\xi) = -\frac{\delta a^2}{2\xi^2 k_u} J_2(\xi a). \tag{73}$$

If we substitute (73) in (71) we deduce the normal stress distribution over the contact area

$$[\sigma_z(r, z)]_{z=0} = \int_0^\infty \frac{-3a^2 \delta}{4h^3 \xi k_u} J_2(\xi a) J_0(\xi r) d\xi = \begin{cases} 0 & \text{for } r > a, \\ -\frac{\delta E_1}{4h^3} (a^2 - r^2) & \text{for } 0 < r < a, \end{cases}$$

while, with Equation (16), we have the force-displacement law

$$\delta = \frac{8Fh^3}{a^4 \pi E_1}.$$

For a very thin compressible layer in perfect bond on a rigid foundation we have the transform of the surface normal stress given by (67)₃. The dual integral equation can be written as

$$\int_0^\infty -\xi^3 A(\xi) \frac{1-\nu_1^2}{E_1 \nu_1} J_0(\xi r) d\xi = \delta \quad \text{for } 0 < r < a,$$

$$\int_0^\infty \xi^3 A(\xi) \frac{(1-\nu_1)^2}{h \nu_1 (1-2\nu_1)} J_0(\xi r) d\xi = 0 \quad \text{for } r > a, \tag{74}$$

and then

$$\int_0^\infty -\xi^3 A(\xi) J_0(\xi r) d\xi = \begin{cases} 0 & \text{for } r > a, \\ \frac{E_1 \nu_1}{1-\nu_1^2} \delta & \text{for } 0 < r < a, \end{cases}$$

By means of the inversion theorem for the Hankel transform, we obtain

$$A(\xi) = -\frac{1}{\xi^2} \int_0^a r \frac{\delta E_1 \nu_1}{(1-\nu_1^2)} J_0(\xi r) dr = -\frac{1}{\xi^3} \frac{a \delta E_1 \nu_1}{(1-\nu_1^2)} J_1(\xi a).$$

Consequently we have

$$\begin{aligned}
 [\sigma_z(r, z)]_{z=0} &= \int_0^\infty -\frac{a\delta E_1 \nu_1}{(1-\nu_1^2)} \frac{(1-\nu_1)^2}{h\nu_1(1-2\nu_1)} J_1(\xi a) J_0(\xi r) d\xi \\
 &= \begin{cases} 0 & \text{for } r > a, \\ -\delta \frac{E_1(1-\nu_1)}{h(1+\nu_1)(1-2\nu_1)} & \text{for } 0 < r < a, \end{cases} \tag{75}
 \end{aligned}$$

and with (16) we derive

$$\delta = \frac{Fh(1+\nu_1)(1-2\nu_1)}{\pi a^2 E_1(1-\nu_1)}.$$

For a very thin compressible or incompressible layer free to slide on a rigid foundation we have the transform of the surface normal stress given by (70)₃. The dual integral equation can be written as

$$\begin{aligned}
 \int_0^\infty -\xi^3 A(\xi) \frac{(1-\nu_1^2)}{E_1 \nu_1} J_0(\xi r) d\xi &= \delta \quad 0 < r < a, \\
 \int_0^\infty \xi^3 A(\xi) \frac{1}{h\nu_1} J_0(\xi r) d\xi &= 0 \quad r > a, \tag{76}
 \end{aligned}$$

and then

$$\int_0^\infty \xi^3 A(\xi) J_0(\xi r) d\xi = \begin{cases} 0 & \text{for } r > a, \\ -\delta \frac{E_1 \nu_1}{1-\nu_1^2} & \text{for } 0 < r < a, \end{cases} \tag{77}$$

By means of the inversion theorem for the Hankel transform, we obtain

$$A(\xi) = -\frac{1}{\xi^2} \int_0^a r \frac{\delta E_1 \nu_1}{(1-\nu_1^2)} J_0(\xi r) dr = -\frac{1}{\xi^3} \frac{a\delta E_1 \nu_1}{(1-\nu_1^2)} J_1(\xi a). \tag{78}$$

Consequently

$$[\sigma_z(r, z)]_{z=0} = \int_0^\infty -\frac{a\delta E_1 \nu_1}{(1-\nu_1^2)} \frac{1}{h\nu_1} J_1(\xi a) J_0(\xi r) d\xi = 0 = \begin{cases} 0 & \text{for } r > a, \\ -\delta \frac{E_1}{h(1-\nu_1^2)} & \text{for } 0 < r < a. \end{cases} \tag{79}$$

Using (16), we then obtain

$$\delta = \frac{Fh(1-\nu_1^2)}{\pi a^2 E_1}.$$

Acknowledgement

The authors thank Prof. T. Politi (Politecnico di Bari, Italy) for his suggestions regarding the numerical solution of the Fredholm integral equation. La Ragione is grateful to G.N.F.M. and P.S.T. – Regione Puglia for financial support.

References

- [Davis and Rabinowitz 1984] P. J. Davis and P. Rabinowitz, *Methods of numerical integration*, 2nd ed., Academic Press, Orlando, 1984.
- [Harding and Sneddon 1945] J. W. Harding and I. N. Sneddon, “The elastic stress produced by indentation of the plane surface of a semi-infinite elastic solid by a rigid punch”, *Proc. Camb. Phil. Soc.* **41** (1945), 16–26.
- [Johnson 1985] K. L. Johnson, *Contact mechanics*, Cambridge University Press, New York, 1985.
- [Johnson and Sridhar 2001] K. L. Johnson and I. Sridhar, “Adhesion between a spherical indenter and an elastic solid with a compliant elastic coating”, *J. Phys. D Appl. Phys.* **34**:5 (2001), 683–689.
- [Komvopoulos 1988] K. Komvopoulos, “Finite element analysis of a layered elastic solid in normal contact with a rigid surface”, *J. Tribol. (Trans. ASME)* **110** (1988), 477–485.
- [Li and Chou 1997] J. Li and T.-W. Chou, “Elastic field of a thin-film/substrate system under an axisymmetric loading”, *Int. J. Solids Struct.* **34**:35-36 (1997), 4463–4478.
- [Love 1944] A. E. H. Love, *A treatise on the mathematical theory of elasticity*, Cambridge University Press, Cambridge, 1944.
- [Matthewson 1981] M. J. Matthewson, “Axi-symmetric contact on thin compliant coating”, *J. Mech. Phys. Solids* **29**:2 (1981), 89–113.
- [Sburlati 2006] R. Sburlati, “Elastic indentation problems in thin films on substrate systems”, *J. Mech. Mater. Struct.* **1** (2006), 541–557.
- [Sneddon 1946] I. N. Sneddon, “Boussinesq’s problem for a flat-ended cylinder”, *Proc. Camb. Phil. Soc.* **42** (1946), 29–32.
- [Sneddon 1951] I. N. Sneddon, *Fourier transforms*, McGraw-Hill, New York, 1951. Reprinted Dover, New York, 1995.
- [Sneddon 1966] I. N. Sneddon, *Mixed boundary value problems in potential theory*, North-Holland, Amsterdam, 1966.
- [Timoshenko and Goodier 1970] S. Timoshenko and J. N. Goodier, *Theory of elasticity*, McGraw Hill, New York, 1970.
- [Wang et al. 2004] M. Wang, K. M. Liechti, J. M. White, and R. M. Winter, “Nanoindentation of polymeric thin films with an interfacial force microscope”, *J. Mech. Phys. Solids* **52**:10 (2004), 2329–2354.
- [Yang 1998] F. Yang, “Indentation of an incompressible elastic film”, *Mech. Mater.* **30**:4 (1998), 275–286.
- [Yang 2003] F. Yang, “Thickness effect on the indentation of an elastic layer”, *Mat. Sci. Eng. A Struct.* **358**:1-2 (2003), 226–232.
- [Yang 2006] F. Yang, “Asymptotic solution to axisymmetric indentation of a compressible elastic thin film”, *Thin Solid Films* **515** (2006), 2274–2283.

Received 27 Mar 2008. Revised 25 Jun 2008. Accepted 25 Jun 2008.

LUIGI LA RAGIONE: l.laragione@poliba.it

Dipartimento di Ingegneria Civile e Ambientale, Politecnico di Bari, Via Re David 200, 70125 Bari, Italy

FRANCESCO MUSCEO: fmusceo@libero.it

Dipartimento di Ingegneria Civile e Ambientale, Politecnico di Bari, Via Re David 200, 70125 Bari, Italy

ALFREDO SOLLAZZO: a.sollazzo@poliba.it

Dipartimento di Ingegneria Civile e Ambientale, Politecnico di Bari, Via Re David 200, 70125 Bari, Italy

ELASTIC SOLUTIONS FOR AN INCLINED TRANSVERSELY ISOTROPIC MATERIAL DUE TO THREE-DIMENSIONAL POINT LOADS

JYH-JONG LIAO, TIN-BIN HU AND CHENG-DER WANG

We present the elastic solutions for displacements and stresses due to three-dimensional point loads in a transversely isotropic material (rock), for which the transversely isotropic full planes are inclined with respect to the horizontal loading surface. The closed-form solutions are derived by applying an efficient method, the double Fourier transform, to obtain the integral expressions for displacements and stresses. Subsequently, the double inverse Fourier transform and residue calculus are utilized to integrate the contours. Utilizing the double Fourier transform in a Cartesian coordinate system is a new approach to solving the displacement and stress components that result from three-dimensional point loads applied to an inclined transversely isotropic medium. In addition, it is the first presentation of the exact closed-form characteristic roots for this special material anisotropy. The proposed solutions demonstrate that the displacements and stresses are profoundly influenced by the rotation of the transversely isotropic planes (ϕ), the type and degree of material anisotropy (E/E' , ν/ν' , G/G'), the geometric position (r , ϕ , ζ), and the type of three-dimensional loading (P_x , P_y , P_z). The present solutions are identical to previously published solutions if the planes of transverse isotropy are parallel to the horizontal loading surface. A parametric study is conducted to elucidate the influence of the aforementioned factors on the displacements and stresses. The computed results reveal that the induced displacements and stresses in the inclined isotropic/transversely isotropic rocks by a vertical point load are quite different from the displacements that result from previous solutions in which $\phi = 0$. The numerical results presented here are interesting for their ability to describe the physical features of inclined transversely isotropic rocks. Hence, the dip at an angle of inclination should be considered in computing the displacements and stresses in a transversely isotropic material due to applied loads.

Introduction

Generally, estimates for the magnitudes of displacements and stresses in a solid are made using solutions that model a material as a homogeneous, linearly elastic, and isotropic medium. However, among geomaterials, these models are unable to describe the properties of some natural soils which have deposited by means of sedimentation over a long period of time, for example flocculated clays, varved silts or sands, or rock masses cut by discontinuities such as cleavages, foliations, stratifications, schistosity, or joints. The deformability properties of these inhomogeneous materials should result in structural anisotropy. From the standpoint of practical considerations in engineering, anisotropic bodies are often modeled as orthotropic or transversely isotropic materials. In particular, when discontinuities of rock masses dip at an angle from the horizontal surface, their effects on displacement and stress could be essential to

Keywords: displacements, stresses, inclined transversely isotropic material, double Fourier transform, residue calculus, material anisotropy.

We acknowledge the financial support of the National Science Council (Taiwan) under Grant No. 96-2628-E-239-022-MY3. Cheng-Der Wang is the corresponding author.

the design of structures. Hence, we study here the elastic loading problem for an inclined transversely isotropic material.

Elastic solutions to the problem of a point load acting on the interior of a full space are called the fundamental solutions or the elastic Green's function solutions [Tarn and Wang 1987]. These solutions in exact closed-form have always played an important role in applied mechanics and in particular numerical formulations of boundary element methods [Liew et al. 2001]. In [Liao and Wang 1998] we detailed the existing solutions for transversely isotropic full/half-spaces in which the planes of transverse isotropy are assumed to be parallel to the horizontal ground surface, subjected to three-dimensional point loads. However, recent work that was not cited in that paper should be mentioned here: [Ding et al. 1997; Hanson 1999; Pan and Tonon 2000; Pan and Yuan 2000a; Pan and Yuan 2000b; Tonon et al. 2001; Pan 2002; Fabrikant 2004; Ding et al. 2006]. Hu et al. [2007] presented the analytical solutions for displacements caused by three-dimensional point loads (P_x, P_y, P_z) in a transversely isotropic full space, where the transversely isotropic planes are inclined with respect to the horizontal loading surface. In their derivation, the triple Fourier transform was employed to yield integral expressions of Green's displacement. Subsequently, the triple inverse Fourier transform and residue calculus were performed to integrate the contours. It is known that the stress components due to three-dimensional point loads on an inclined infinite space can be obtained by employing the coordinate transformation formulae with respect to the applied loads. Nevertheless, the displacement components cannot be solved by the same approach. Hence, their solutions for the displacements in an inclined space are new and cannot be obtained directly from the aforementioned point load solutions (see [Liao and Wang 1998], for example) with a linear rotation of the Cartesian coordinate system. Nevertheless, the derivations using the triple Fourier transform were not very efficient, and the presentations were rather lengthy. Yet, to the best of our knowledge, no solutions for displacements and stresses resulting from three-dimensional point loads acting on an inclined transversely isotropic material have been performed by using the double Fourier transform in a Cartesian coordinate system. The advantage of deriving stress components by applying the double Fourier transform is that the proposed solutions for the inclined transversely isotropic infinite space are parts of the point force problem in an inclined transversely isotropic half-space, achieved by satisfying the surface boundary conditions and thus utilizing the principle of superposition. Therefore, the yielded solutions are valuable and would be straightforward to extend to the half-space/bimaterial/layered material problems.

In the solutions presented here, it is found that both the displacement and stress solutions are governed by: (1) the rotation of the transversely isotropic planes (ϕ), (2) the type and degree of material anisotropy ($E/E', \nu/\nu', G/G'$), (3) the geometric position (r, φ, ζ), and (4) the type of three-dimensional loading (P_x, P_y, P_z). Two examples are given to illustrate the generated solutions and clarify how the rotation of the transversely isotropic planes (ϕ), the geometric position (φ), and the type and degree of rock anisotropy would affect the displacements and stresses in inclined isotropic/transversely isotropic rocks subjected to a vertical point load (P_z).

1. Displacements and stresses in an inclined transversely isotropic full space due to three-dimensional point loads

We start with the generalized Hooke's law for a transversely isotropic material in a Cartesian coordinate system (x', y', z'), where z' is the rotation axis associated with elastic symmetry, and the x' and y' axes

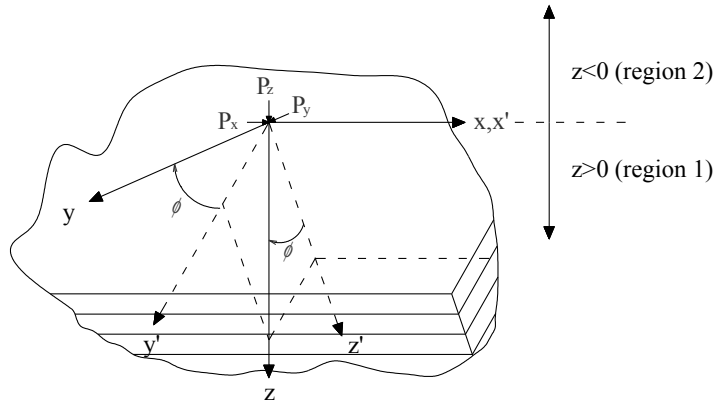


Figure 1. (P_x, P_y, P_z) acting in an inclined transversely isotropic full space.

are in the plane of transverse isotropy (see [Figure 1](#)). We have

$$\begin{bmatrix} \sigma_{x'x'} \\ \sigma_{y'y'} \\ \sigma_{z'z'} \\ \tau_{y'z'} \\ \tau_{z'x'} \\ \tau_{x'y'} \end{bmatrix} = \begin{bmatrix} C_{11} & C_{12} & C_{13} & 0 & 0 & 0 \\ C_{12} & C_{11} & C_{13} & 0 & 0 & 0 \\ C_{13} & C_{13} & C_{33} & 0 & 0 & 0 \\ 0 & 0 & 0 & C_{44} & 0 & 0 \\ 0 & 0 & 0 & 0 & C_{44} & 0 \\ 0 & 0 & 0 & 0 & 0 & C_{66} \end{bmatrix} \begin{bmatrix} \varepsilon_{x'x'} \\ \varepsilon_{y'y'} \\ \varepsilon_{z'z'} \\ \gamma_{y'z'} \\ \gamma_{z'x'} \\ \gamma_{x'y'} \end{bmatrix},$$

where $\sigma_{x'x'}$, $\sigma_{y'y'}$, $\sigma_{z'z'}$ are the normal stresses, $\varepsilon_{x'x'}$, $\varepsilon_{y'y'}$, $\varepsilon_{z'z'}$ the normal strains, $\tau_{y'z'}$, $\tau_{z'x'}$, $\tau_{x'y'}$ the shear stresses, $\gamma_{y'z'}$, $\gamma_{z'x'}$, $\gamma_{x'y'}$ the shear strains, and C_{11} , C_{12} , C_{13} , C_{33} , C_{44} , C_{66} the elastic moduli.

Because $C_{12} = C_{11} - 2C_{66}$, only C_{11} , C_{13} , C_{33} , C_{44} , C_{66} are independent for a transversely isotropic material, so it is convenient to work in terms of the constants c_1, \dots, c_5 defined in terms of the C_{ij} by

$$\begin{aligned} c_1 = C_{11} &= \frac{E(1 - (E/E')\nu^2)}{(1 + \nu)(1 - \nu - (2E/E')\nu^2)}, & c_2 = C_{33} &= \frac{E'(1 - \nu)}{1 - \nu - (2E/E')\nu^2}, & c_5 = C_{44} &= G', \\ c_3 = C_{13} + C_{44} &= \frac{Ev'}{1 - \nu - (2E/E')\nu^2} + C_{44}, & c_4 = C_{66} &= \frac{C_{11} - C_{12}}{2} = \frac{E}{2(1 + \nu)}. \end{aligned} \tag{1}$$

[Equation \(1\)](#) also displays the relation between c_1, \dots, c_5 and the traditional constants E and E' (Young's moduli in the plane of transverse isotropy and in the normal direction to it), ν and ν' (Poisson's ratios characterizing the lateral strain response in the plane of transverse isotropy to a stress acting parallel or normal to it, respectively), and G' (the shear modulus in planes normal to the plane of transverse isotropy). In this notation we have

$$\begin{bmatrix} \sigma_{x'x'} \\ \sigma_{y'y'} \\ \sigma_{z'z'} \\ \tau_{y'z'} \\ \tau_{z'x'} \\ \tau_{x'y'} \end{bmatrix} = \begin{bmatrix} c_1 & c_1 - 2c_4 & c_3 - c_5 & 0 & 0 & 0 \\ c_1 - 2c_4 & c_1 & c_3 - c_5 & 0 & 0 & 0 \\ c_3 - c_5 & c_3 - c_5 & c_2 & 0 & 0 & 0 \\ 0 & 0 & 0 & c_5 & 0 & 0 \\ 0 & 0 & 0 & 0 & c_5 & 0 \\ 0 & 0 & 0 & 0 & 0 & c_4 \end{bmatrix} \begin{bmatrix} \varepsilon_{x'x'} \\ \varepsilon_{y'y'} \\ \varepsilon_{z'z'} \\ \gamma_{y'z'} \\ \gamma_{z'x'} \\ \gamma_{x'y'} \end{bmatrix} \tag{2}$$

If a new coordinate system x, y, z is obtained from the original system x', y', z' by rotation through an angle ϕ about an axis parallel to the strike direction, then $x = x'$. (See again Figure 1.) The direction cosines l_{ij} ($i, j = 1, 2, 3$) of the transformation are given by

$$\begin{bmatrix} l_{11} & l_{12} & l_{13} \\ l_{21} & l_{22} & l_{23} \\ l_{31} & l_{32} & l_{33} \end{bmatrix} = \begin{bmatrix} 1 & 0 & 0 \\ 0 & \cos \phi & \sin \phi \\ 0 & -\sin \phi & \cos \phi \end{bmatrix}, \tag{3}$$

and in the new coordinate system the matrix of elastic moduli is

$$[q_{ij}]^T [C_{ij}] [q_{ij}] =: [a_{ij}] = \begin{bmatrix} a_{11} & a_{12} & a_{13} & a_{14} & a_{15} & a_{16} \\ a_{21} & a_{22} & a_{23} & a_{24} & a_{25} & a_{26} \\ a_{31} & a_{32} & a_{33} & a_{34} & a_{35} & a_{36} \\ a_{41} & a_{42} & a_{43} & a_{44} & a_{45} & a_{46} \\ a_{51} & a_{52} & a_{53} & a_{54} & a_{55} & a_{56} \\ a_{61} & a_{62} & a_{63} & a_{64} & a_{65} & a_{66} \end{bmatrix}, \tag{4}$$

where

$$[q_{ij}] = \begin{bmatrix} l_{11}^2 & l_{12}^2 & l_{13}^2 & l_{12}l_{13} & l_{13}l_{11} & l_{12}l_{11} \\ l_{21}^2 & l_{22}^2 & l_{23}^2 & l_{23}l_{22} & l_{23}l_{21} & l_{22}l_{21} \\ l_{31}^2 & l_{32}^2 & l_{33}^2 & l_{33}l_{32} & l_{33}l_{31} & l_{32}l_{31} \\ 2l_{31}l_{21} & 2l_{32}l_{22} & 2l_{33}l_{23} & l_{33}l_{22}+l_{32}l_{23} & l_{33}l_{21}+l_{31}l_{23} & l_{31}l_{22}+l_{32}l_{21} \\ 2l_{31}l_{11} & 2l_{32}l_{12} & 2l_{33}l_{13} & l_{33}l_{12}+l_{32}l_{13} & l_{33}l_{11}+l_{31}l_{13} & l_{31}l_{12}+l_{32}l_{11} \\ 2l_{21}l_{11} & 2l_{22}l_{12} & 2l_{23}l_{13} & l_{13}l_{22}+l_{12}l_{23} & l_{13}l_{21}+l_{11}l_{23} & l_{11}l_{22}+l_{12}l_{21} \end{bmatrix}, \tag{5}$$

T denotes transposition, and the elastic constants a_{ij} have the following explicit expressions (those not listed vanish):

$$\begin{aligned} a_{11} &= c_1, \\ a_{12} &= a_{21} = (c_1 - 2c_4) \cos^2 \phi + (c_3 - c_5) \sin^2 \phi, \\ a_{13} &= a_{31} = (c_3 - c_5) \cos^2 \phi + (c_1 - 2c_4) \sin^2 \phi, \\ a_{14} &= a_{41} = (c_1 - c_3 - 2c_4 + c_5) \cos \phi \sin \phi, \\ a_{22} &= c_1 \cos^4 \phi + 2c_3 + 2c_5 \cos^2 \phi \sin^2 \phi + c_2 \sin^4 \phi, \\ a_{23} &= a_{32} = \frac{1}{8}(c_1 + c_2 + 6c_3 - 10c_5 - (c_1 + c_2 - 2c_3 - 2c_5) \cos 4\phi), \\ a_{24} &= a_{42} = \frac{1}{4}(c_1 - c_2 + (c_1 + c_2 - 2c_3 - 2c_5) \cos 2\phi) \sin 2\phi, \\ a_{33} &= c_2 \cos^4 \phi + 2c_3 + 2c_5 \cos^2 \phi \sin^2 \phi + c_1 \sin^4 \phi, \\ a_{34} &= a_{43} = -\frac{1}{4}(-c_1 + c_2 + (c_1 + c_2 - 2c_3 - 2c_5) \cos 2\phi) \sin 2\phi, \\ a_{44} &= \frac{1}{8}(c_1 + c_2 - 2c_3 + 6c_5 - (c_1 + c_2 - 2c_3 - 2c_5) \cos 4\phi), \\ a_{55} &= c_5 \cos^2 \phi + c_4 \sin^2 \phi, \\ a_{56} &= a_{65} = (c_4 - c_5) \cos \phi \sin \phi, \\ a_{66} &= c_4 \cos^2 \phi + c_5 \sin^2 \phi. \end{aligned}$$

Next we use the strain-displacement relation under the small strain condition in Cartesian coordinates:

$$[\varepsilon_{ij}] = \begin{bmatrix} \varepsilon_{xx} \\ \varepsilon_{yy} \\ \varepsilon_{zz} \\ \gamma_{yz} \\ \gamma_{zx} \\ \gamma_{xy} \end{bmatrix} = \begin{bmatrix} -\partial u_x / \partial x \\ -\partial u_y / \partial y \\ -\partial u_z / \partial z \\ -\partial u_y / \partial z - \partial u_z / \partial y \\ -\partial u_x / \partial z - \partial u_z / \partial x \\ -\partial u_y / \partial x - \partial u_x / \partial y \end{bmatrix}, \quad (6)$$

where u_x , u_y , and u_z are the components of the displacement.

Finally, the equilibrium equation is

$$\begin{bmatrix} \sigma_{xx} & \tau_{xy} & \tau_{zx} \\ \tau_{xy} & \sigma_{yy} & \tau_{yz} \\ \tau_{zx} & \tau_{yz} & \sigma_{zz} \end{bmatrix} \begin{bmatrix} \partial / \partial x \\ \partial / \partial y \\ \partial / \partial z \end{bmatrix} = \begin{bmatrix} F_x \\ F_y \\ F_z \end{bmatrix}, \quad (7)$$

where (F_x, F_y, F_z) are the three-dimensional point loads. Hence, the generalized Hooke's law expressed in the xyz -coordinates,

$$\begin{bmatrix} \sigma_{xx} \\ \sigma_{yy} \\ \sigma_{zz} \\ \tau_{yz} \\ \tau_{zx} \\ \tau_{xy} \end{bmatrix} = \begin{bmatrix} a_{11} & a_{12} & a_{13} & a_{14} & a_{15} & a_{16} \\ a_{21} & a_{22} & a_{23} & a_{24} & a_{25} & a_{26} \\ a_{31} & a_{32} & a_{33} & a_{34} & a_{35} & a_{36} \\ a_{41} & a_{42} & a_{43} & a_{44} & a_{45} & a_{46} \\ a_{51} & a_{52} & a_{53} & a_{54} & a_{55} & a_{56} \\ a_{61} & a_{62} & a_{63} & a_{64} & a_{65} & a_{66} \end{bmatrix} \begin{bmatrix} \varepsilon_{xx} \\ \varepsilon_{yy} \\ \varepsilon_{zz} \\ \gamma_{yz} \\ \gamma_{zx} \\ \gamma_{xy} \end{bmatrix}, \quad (8)$$

gives rise to the system of equations

$$\sigma_{xx} = a_{11}\varepsilon_{xx} + a_{12}\varepsilon_{yy} + a_{13}\varepsilon_{zz} + a_{14}\gamma_{yz} = -a_{11}\frac{\partial u_x}{\partial x} - a_{12}\frac{\partial u_y}{\partial y} - a_{13}\frac{\partial u_z}{\partial z} - a_{14}\left(\frac{\partial u_y}{\partial z} + \frac{\partial u_z}{\partial y}\right), \quad (9a)$$

$$\sigma_{yy} = a_{12}\varepsilon_{xx} + a_{22}\varepsilon_{yy} + a_{23}\varepsilon_{zz} + a_{24}\gamma_{yz} = -a_{12}\frac{\partial u_x}{\partial x} - a_{22}\frac{\partial u_y}{\partial y} - a_{23}\frac{\partial u_z}{\partial z} - a_{24}\left(\frac{\partial u_y}{\partial z} + \frac{\partial u_z}{\partial y}\right), \quad (9b)$$

$$\sigma_{zz} = a_{13}\varepsilon_{xx} + a_{23}\varepsilon_{yy} + a_{33}\varepsilon_{zz} + a_{34}\gamma_{yz} = -a_{13}\frac{\partial u_x}{\partial x} - a_{23}\frac{\partial u_y}{\partial y} - a_{33}\frac{\partial u_z}{\partial z} - a_{34}\left(\frac{\partial u_y}{\partial z} + \frac{\partial u_z}{\partial y}\right), \quad (9c)$$

$$\tau_{yz} = a_{14}\varepsilon_{xx} + a_{24}\varepsilon_{yy} + a_{34}\varepsilon_{zz} + a_{44}\gamma_{yz} = -a_{14}\frac{\partial u_x}{\partial x} - a_{24}\frac{\partial u_y}{\partial y} - a_{34}\frac{\partial u_z}{\partial z} - a_{44}\left(\frac{\partial u_y}{\partial z} + \frac{\partial u_z}{\partial y}\right), \quad (9d)$$

$$\tau_{zx} = a_{55}\gamma_{zx} + a_{56}\gamma_{xy} = -a_{55}\left(\frac{\partial u_x}{\partial z} + \frac{\partial u_z}{\partial x}\right) - a_{56}\left(\frac{\partial u_x}{\partial y} + \frac{\partial u_y}{\partial x}\right), \quad (9e)$$

$$\tau_{xy} = a_{56}\gamma_{zx} + a_{66}\gamma_{xy} = -a_{56}\left(\frac{\partial u_x}{\partial z} + \frac{\partial u_z}{\partial x}\right) - a_{66}\left(\frac{\partial u_x}{\partial y} + \frac{\partial u_y}{\partial x}\right). \quad (9f)$$

Substituting σ_{xx} , σ_{yy} , σ_{zz} , τ_{yz} , τ_{zx} , τ_{xy} from (9) into (7) enables the equations to be regrouped as Navier–Cauchy equations for a transversely isotropic material as

$$\begin{aligned}
 a_{11} \frac{\partial^2 u_x}{\partial x^2} + a_{66} \frac{\partial^2 u_x}{\partial y^2} + a_{55} \frac{\partial^2 u_x}{\partial z^2} + 2a_{56} \frac{\partial^2 u_x}{\partial y \partial z} + (a_{12} + a_{66}) \frac{\partial^2 u_y}{\partial x \partial y} + (a_{14} + a_{56}) \frac{\partial^2 u_y}{\partial x \partial z} \\
 + (a_{14} + a_{56}) \frac{\partial^2 u_z}{\partial x \partial y} + (a_{13} + a_{55}) \frac{\partial^2 u_z}{\partial x \partial z} + F_x = 0, \quad (10a)
 \end{aligned}$$

$$\begin{aligned}
 (a_{12} + a_{66}) \frac{\partial^2 u_x}{\partial x \partial y} + (a_{14} + a_{56}) \frac{\partial^2 u_x}{\partial x \partial z} + a_{66} \frac{\partial^2 u_y}{\partial x^2} + a_{22} \frac{\partial^2 u_y}{\partial y^2} + a_{44} \frac{\partial^2 u_y}{\partial z^2} + 2a_{24} \frac{\partial^2 u_y}{\partial y \partial z} \\
 + a_{56} \frac{\partial^2 u_z}{\partial x^2} + a_{24} \frac{\partial^2 u_z}{\partial y^2} + a_{34} \frac{\partial^2 u_z}{\partial z^2} + (a_{23} + a_{44}) \frac{\partial^2 u_z}{\partial y \partial z} + F_y = 0, \quad (10b)
 \end{aligned}$$

$$\begin{aligned}
 (a_{14} + a_{56}) \frac{\partial^2 u_x}{\partial x \partial y} + (a_{13} + a_{55}) \frac{\partial^2 u_x}{\partial x \partial z} + a_{56} \frac{\partial^2 u_y}{\partial x^2} + a_{24} \frac{\partial^2 u_y}{\partial y^2} + a_{34} \frac{\partial^2 u_y}{\partial z^2} + (a_{23} + a_{44}) \frac{\partial^2 u_y}{\partial y \partial z} \\
 + a_{55} \frac{\partial^2 u_z}{\partial x^2} + a_{44} \frac{\partial^2 u_z}{\partial y^2} + a_{33} \frac{\partial^2 u_z}{\partial z^2} + 2a_{34} \frac{\partial^2 u_z}{\partial y \partial z} + F_z = 0. \quad (10c)
 \end{aligned}$$

The point loads (F_x, F_y, F_z) applied at the origin of the coordinate system of a full space can be described in terms of body forces (P_x, P_y, P_z) as

$$F_x = P_x \delta(x) \delta(y) \delta(z), \quad F_y = P_y \delta(x) \delta(y) \delta(z), \quad F_z = P_z \delta(x) \delta(y) \delta(z), \quad (11)$$

where δ is the Dirac delta function.

We will now use the double Fourier transform of the displacement components to solve the governing equations (10a)–(10c). We introduce the transform variables α, β corresponding to x, y , respectively, and consider the double Fourier transform of u_i ($i = x, y, z$),

$$\frac{1}{2\pi} \int_{-\infty}^{\infty} \int_{-\infty}^{\infty} u_i(x, y, z) e^{-i(\alpha x + \beta y)} dx dy = \bar{u}_i(\alpha, \beta, z).$$

As is well-known, we have

$$\begin{aligned}
 \frac{1}{2\pi} \int_{-\infty}^{\infty} \int_{-\infty}^{\infty} \frac{\partial u_i(x, y, z)}{\partial x} e^{-i(\alpha x + \beta y)} dx dy &= i\alpha \bar{u}_i(\alpha, \beta, z), \\
 \frac{1}{2\pi} \int_{-\infty}^{\infty} \int_{-\infty}^{\infty} \frac{\partial u_i(x, y, z)}{\partial y} e^{-i(\alpha x + \beta y)} dx dy &= i\beta \bar{u}_i(\alpha, \beta, z), \\
 \frac{1}{2\pi} \int_{-\infty}^{\infty} \int_{-\infty}^{\infty} \frac{\partial^2 u_i(x, y, z)}{\partial x^2} e^{-i(\alpha x + \beta y)} dx dy &= -\alpha^2 \bar{u}_i(\alpha, \beta, z), \quad \dots
 \end{aligned}$$

Since $\int_{-\infty}^{\infty} \int_{-\infty}^{\infty} \delta(x) \delta(y) dx dy = 1$, the double Fourier transforms of (11) reduce to

$$\bar{F}_x = \frac{1}{2\pi} \int_{-\infty}^{\infty} \int_{-\infty}^{\infty} P_x \delta(x) \delta(y) \delta(z) e^{-i(\alpha x + \beta y)} dx dy = \frac{P_x}{2\pi} \delta(z), \quad (12a)$$

$$\bar{F}_y = \frac{1}{2\pi} \int_{-\infty}^{\infty} \int_{-\infty}^{\infty} P_y \delta(x) \delta(y) \delta(z) e^{-i(\alpha x + \beta y)} dx dy = \frac{P_y}{2\pi} \delta(z), \quad (12b)$$

$$\bar{F}_z = \frac{1}{2\pi} \int_{-\infty}^{\infty} \int_{-\infty}^{\infty} P_z \delta(x) \delta(y) \delta(z) e^{-i(\alpha x + \beta y)} dx dy = \frac{P_z}{2\pi} \delta(z). \quad (12c)$$

When $z \neq 0$, this allows us to rewrite the Navier–Cauchy equations (10a)–(10c) as a system of linear ordinary differential equations:

$$\begin{bmatrix} d_{11} & d_{12} & d_{13} \\ d_{21} & d_{22} & d_{23} \\ d_{31} & d_{32} & d_{33} \end{bmatrix} \begin{bmatrix} \bar{u}_x \\ \bar{u}_y \\ \bar{u}_z \end{bmatrix} = \begin{bmatrix} 0 \\ 0 \\ 0 \end{bmatrix}, \quad (13)$$

where

$$d_{11} = a_{11}\alpha^2 + a_{66}\beta^2 - a_{55} \frac{d^2}{dz^2} - 2ia_{56}\beta \frac{d}{dz}, \quad (14a)$$

$$d_{12} = d_{21} = (a_{12} + a_{66})\alpha\beta - i(a_{14} + a_{56})\alpha \frac{d}{dz}, \quad (14b)$$

$$d_{13} = d_{31} = (a_{14} + a_{56})\alpha\beta - i(a_{13} + a_{55})\alpha \frac{d}{dz}, \quad (14c)$$

$$d_{22} = a_{66}\alpha^2 + a_{22}\beta^2 - a_{44} \frac{d^2}{dz^2} - 2ia_{24}\beta \frac{d}{dz}, \quad (14d)$$

$$d_{23} = d_{32} = a_{56}\alpha^2 + a_{24}\beta^2 - a_{34} \frac{d^2}{dz^2} - i(a_{23} + a_{44})\beta \frac{d}{dz}, \quad (14e)$$

$$d_{33} = a_{55}\alpha^2 + a_{44}\beta^2 - a_{33} \frac{d^2}{dz^2} - 2ia_{34}\beta \frac{d}{dz}. \quad (14f)$$

From the elementary theory of linear ordinary differential equations we know that we need to solve the characteristic equation

$$\det [d_{ij}(\alpha, \beta, u)] = 0, \quad (15)$$

where the entries $d_{ij}(\alpha, \beta, u)$ are obtained from (14) by substituting the unknown u (representing the eigenvalue) for d/dz :

$$d_{11}(\alpha, \beta, u) = a_{11}\alpha^2 + a_{66}\beta^2 + a_{55}(iu)^2 - 2a_{56}\beta(iu), \quad (16a)$$

$$d_{12}(\alpha, \beta, u) = d_{21}(\alpha, \beta, u) = (a_{12} + a_{66})\alpha\beta - (a_{14} + a_{56})\alpha(iu), \quad (16b)$$

$$d_{13}(\alpha, \beta, u) = d_{31}(\alpha, \beta, u) = (a_{14} + a_{56})\alpha\beta - (a_{13} + a_{55})\alpha(iu), \quad (16c)$$

$$d_{22}(\alpha, \beta, u) = a_{66}\alpha^2 + a_{22}\beta^2 + a_{44}(iu)^2 - 2a_{24}\beta(iu), \quad (16d)$$

$$d_{23}(\alpha, \beta, u) = d_{32}(\alpha, \beta, u) = a_{56}\alpha^2 + a_{24}\beta^2 + a_{34}(iu)^2 - (a_{23} + a_{44})\beta(iu), \quad (16e)$$

$$d_{33}(\alpha, \beta, u) = a_{55}\alpha^2 + a_{44}\beta^2 + a_{33}(iu)^2 - 2a_{34}\beta(iu). \quad (16f)$$

An algebraic manipulation (details and the physical basis of which are given in the [Appendix](#)) shows that, if we set

$$A_1 = \frac{c_4}{c_5}, \quad A_2 = \frac{1}{2} \left[\frac{c_5^2 + c_1c_2 - c_3^2}{c_2c_5} + \left\{ \left(\frac{c_5^2 + c_1c_2 - c_3^2}{c_2c_5} \right)^2 - 4 \frac{c_1}{c_2} \right\}^{1/2} \right], \quad (17)$$

$$A_3 = \frac{1}{2} \left[\frac{c_5^2 + c_1c_2 - c_3^2}{c_2c_5} - \left\{ \left(\frac{c_5^2 + c_1c_2 - c_3^2}{c_2c_5} \right)^2 - 4 \frac{c_1}{c_2} \right\}^{1/2} \right],$$

the characteristic equation takes on the form

$$c_2 c_5^2 \prod_{j=1}^3 \left(A_j (-u^2 + \alpha^2 + \beta^2 - (iu \cos \phi + \beta \sin \phi)^2) + (iu \cos \phi + \beta \sin \phi)^2 \right) = 0, \quad (18)$$

and its six eigenroots u_1, \dots, u_6 can be expressed as

$$\left. \begin{aligned} u_j &= \frac{-i\beta \sin \phi \cos \phi (-1 + A_j) - \sqrt{A_j(\beta^2 + \alpha^2(\cos^2 \phi + A_j \sin^2 \phi))}}{\cos^2 \phi + A_j \sin^2 \phi} \\ u_{3+j} &= \frac{-i\beta \sin \phi \cos \phi (-1 + A_j) + \sqrt{A_j(\beta^2 + \alpha^2(\cos^2 \phi + A_j \sin^2 \phi))}}{\cos^2 \phi + A_j \sin^2 \phi} \end{aligned} \right\} \quad (i = 1, 2, 3). \quad (19)$$

(In particular, the real parts of u_1, u_2, u_3 are negative and those of u_4, u_5, u_6 are positive.)

Equations (19) represent the first instance in which exact closed-form eigenroots for the inclined transversely isotropic media are proposed. To derive explicitly the solutions to (10a)–(10c), define three displacement functions as follows:

for $z > 0$ (region 1 in Figure 1),

$$\bar{u}_{x1}(\alpha, \beta, z) = A_{x1}^1 e^{u_1 z} + A_{x1}^2 e^{u_2 z} + A_{x1}^3 e^{u_3 z} + A_{x1}^4 e^{u_4 z} + A_{x1}^5 e^{u_5 z} + A_{x1}^6 e^{u_6 z}, \quad (20a)$$

$$\bar{u}_{y1}(\alpha, \beta, z) = A_{y1}^1 e^{u_1 z} + A_{y1}^2 e^{u_2 z} + A_{y1}^3 e^{u_3 z} + A_{y1}^4 e^{u_4 z} + A_{y1}^5 e^{u_5 z} + A_{y1}^6 e^{u_6 z}, \quad (20b)$$

$$\bar{u}_{z1}(\alpha, \beta, z) = A_{z1}^1 e^{u_1 z} + A_{z1}^2 e^{u_2 z} + A_{z1}^3 e^{u_3 z} + A_{z1}^4 e^{u_4 z} + A_{z1}^5 e^{u_5 z} + A_{z1}^6 e^{u_6 z}, \quad (20c)$$

and for $z < 0$ (region 2 in Figure 1),

$$\bar{u}_{x2}(\alpha, \beta, z) = A_{x2}^1 e^{u_1 z} + A_{x2}^2 e^{u_2 z} + A_{x2}^3 e^{u_3 z} + A_{x2}^4 e^{u_4 z} + A_{x2}^5 e^{u_5 z} + A_{x2}^6 e^{u_6 z}, \quad (21a)$$

$$\bar{u}_{y2}(\alpha, \beta, z) = A_{y2}^1 e^{u_1 z} + A_{y2}^2 e^{u_2 z} + A_{y2}^3 e^{u_3 z} + A_{y2}^4 e^{u_4 z} + A_{y2}^5 e^{u_5 z} + A_{y2}^6 e^{u_6 z}, \quad (21b)$$

$$\bar{u}_{z2}(\alpha, \beta, z) = A_{z2}^1 e^{u_1 z} + A_{z2}^2 e^{u_2 z} + A_{z2}^3 e^{u_3 z} + A_{z2}^4 e^{u_4 z} + A_{z2}^5 e^{u_5 z} + A_{z2}^6 e^{u_6 z}. \quad (21c)$$

In (20), the undetermined coefficients $A_{x1}^j, A_{y1}^j,$ and A_{z1}^j ($j = 1, \dots, 6$) can be obtained by assuming the displacements in region 1, $u_{x1}, u_{y1},$ and u_{z1} must be finite when z approaches ∞ . Hence, $A_{x1}^4 = A_{x1}^5 = A_{x1}^6 = 0, A_{y1}^4 = A_{y1}^5 = A_{y1}^6 = 0,$ and $A_{z1}^4 = A_{z1}^5 = A_{z1}^6 = 0$. Similarly, in region 2, $u_{x2}, u_{y2},$ and u_{z2} also must be finite when z approaches $-\infty$. Therefore, $A_{x2}^1 = A_{x2}^2 = A_{x2}^3 = 0, A_{y2}^1 = A_{y2}^2 = A_{y2}^3 = 0,$ and $A_{z2}^1 = A_{z2}^2 = A_{z2}^3 = 0$.

Now, let

$$\begin{aligned} \frac{A_{x1}^j}{D_{11}(\alpha, \beta, u_j)} &= \frac{A_{y1}^j}{D_{21}(\alpha, \beta, u_j)} = \frac{A_{z1}^j}{D_{31}(\alpha, \beta, u_j)} = C_d^j \quad (j = 1, 2, 3), \\ \frac{A_{x2}^j}{D_{11}(\alpha, \beta, u_j)} &= \frac{A_{y2}^j}{D_{21}(\alpha, \beta, u_j)} = \frac{A_{z2}^j}{D_{31}(\alpha, \beta, u_j)} = C_u^j \quad (j = 4, 5, 6), \end{aligned} \quad (22)$$

where D_{11} , D_{21} , and D_{31} are second-order determinants¹ involving the functions d_{ij} ($i, j = 1, 2, 3$) of (16):

$$D_{11}(\alpha, \beta, u_j) = \det \begin{bmatrix} d_{22}(\alpha, \beta, u_j) & d_{23}(\alpha, \beta, u_j) \\ d_{32}(\alpha, \beta, u_j) & d_{33}(\alpha, \beta, u_j) \end{bmatrix}, \quad (23a)$$

$$D_{21}(\alpha, \beta, u_j) = -\det \begin{bmatrix} d_{12}(\alpha, \beta, u_j) & d_{13}(\alpha, \beta, u_j) \\ d_{32}(\alpha, \beta, u_j) & d_{33}(\alpha, \beta, u_j) \end{bmatrix}, \quad (23b)$$

$$D_{31}(\alpha, \beta, u_j) = \det \begin{bmatrix} d_{12}(\alpha, \beta, u_j) & d_{13}(\alpha, \beta, u_j) \\ d_{22}(\alpha, \beta, u_j) & d_{23}(\alpha, \beta, u_j) \end{bmatrix}. \quad (23c)$$

The stress components of (9) are transformed by the double Fourier transform as

$$\bar{\sigma}_{xx} = -i\alpha a_{11}\bar{u}_x - i\beta a_{12}\bar{u}_y - a_{13}\frac{\partial\bar{u}_z}{\partial z} - a_{14}\left(\frac{\partial\bar{u}_y}{\partial z} + i\beta\bar{u}_z\right), \quad (24a)$$

$$\bar{\sigma}_{yy} = -i\alpha a_{12}\bar{u}_x - i\beta a_{22}\bar{u}_y - a_{23}\frac{\partial\bar{u}_z}{\partial z} - a_{24}\left(\frac{\partial\bar{u}_y}{\partial z} + i\beta\bar{u}_z\right), \quad (24b)$$

$$\bar{\sigma}_{zz} = -i\alpha a_{13}\bar{u}_x - i\beta a_{23}\bar{u}_y - a_{33}\frac{\partial\bar{u}_z}{\partial z} - a_{34}\left(\frac{\partial\bar{u}_y}{\partial z} + i\beta\bar{u}_z\right), \quad (24c)$$

$$\bar{\tau}_{yz} = -i\alpha a_{14}\bar{u}_x - i\beta a_{24}\bar{u}_y - a_{34}\frac{\partial\bar{u}_z}{\partial z} - a_{44}\left(\frac{\partial\bar{u}_y}{\partial z} + i\beta\bar{u}_z\right), \quad (24d)$$

$$\bar{\tau}_{zx} = -a_{55}\left(\frac{\partial\bar{u}_x}{\partial z} + i\alpha\bar{u}_z\right) - ia_{56}(\beta\bar{u}_x + \alpha\bar{u}_y), \quad (24e)$$

$$\bar{\tau}_{xy} = -a_{56}\left(\frac{\partial\bar{u}_x}{\partial z} + i\alpha\bar{u}_z\right) - ia_{66}(\beta\bar{u}_x + \alpha\bar{u}_y). \quad (24f)$$

We next consider the plane $z = 0$ separating regions 1 and 2 of Figure 1, and write the pertinent continuity and discontinuity conditions along this plane:

$$\tau_{zx1}(x, y, 0) - \tau_{zx2}(x, y, 0) = P_x\delta(x)\delta(y), \quad u_{x1}(x, y, 0) = u_{x2}(x, y, 0), \quad (25a)$$

$$\tau_{zy1}(x, y, 0) - \tau_{zy2}(x, y, 0) = P_y\delta(x)\delta(y), \quad u_{y1}(x, y, 0) = u_{y2}(x, y, 0), \quad (25b)$$

$$\sigma_{zz1}(x, y, 0) - \sigma_{zz2}(x, y, 0) = P_z\delta(x)\delta(y), \quad u_{z1}(x, y, 0) = u_{z2}(x, y, 0), \quad (25c)$$

where $-\infty < x < \infty$, $-\infty < y < \infty$. The subscripts 1 and 2 denote the limits as $z \rightarrow 0^+$ and $z \rightarrow 0^-$.

Taking the double Fourier transform of (25), we obtain

$$\bar{\tau}_{zx1}(\alpha, \beta, 0) - \bar{\tau}_{zx2}(\alpha, \beta, 0) = P_x/2\pi, \quad \bar{u}_{x1}(\alpha, \beta, 0) = \bar{u}_{x2}(\alpha, \beta, 0), \quad (26a)$$

$$\bar{\tau}_{zy1}(\alpha, \beta, 0) - \bar{\tau}_{zy2}(\alpha, \beta, 0) = P_y/2\pi, \quad \bar{u}_{y1}(\alpha, \beta, 0) = \bar{u}_{y2}(\alpha, \beta, 0), \quad (26b)$$

$$\bar{\sigma}_{zz1}(\alpha, \beta, 0) - \bar{\sigma}_{zz2}(\alpha, \beta, 0) = P_z/2\pi, \quad \bar{u}_{z1}(\alpha, \beta, 0) = \bar{u}_{z2}(\alpha, \beta, 0). \quad (26c)$$

We further introduce the convention

$$D_{i1}^j := D_{i1}(\alpha, \beta, u_j). \quad (27)$$

¹There are similar determinants D_{ij} for all $i, j = 1, 2, 3$, but we don't need the other ones here.

Then we can rewrite the linear system (26) in terms of unknowns $C_d^1, C_d^2, C_d^3, C_u^4, C_u^5, C_u^6$:

$$[f_{ij}] \begin{bmatrix} C_d^1 \\ C_d^2 \\ C_d^3 \\ C_u^4 \\ C_u^5 \\ C_u^6 \end{bmatrix} = \frac{1}{2\pi} \begin{bmatrix} P_x \\ P_y \\ P_z \\ 0 \\ 0 \\ 0 \end{bmatrix}, \tag{28}$$

where

$$\begin{aligned} f_{1j} &= -i(a_{56}(\beta D_{11}^j + \alpha D_{21}^j) + a_{55}(\alpha D_{31}^j - i D_{11}^j u_j)) & (j = 1, 2, 3), \\ f_{1j} &= i(a_{56}(\beta D_{11}^j + \alpha D_{21}^j) + a_{55}(\alpha D_{31}^j - i D_{11}^j u_j)) & (j = 4, 5, 6), \\ f_{2j} &= -i(\alpha a_{14} D_{11}^j + \beta a_{24} D_{21}^j + \beta a_{44} D_{31}^j) - (a_{44} D_{21}^j + a_{34} D_{31}^j) u_j & (j = 1, 2, 3), \\ f_{2j} &= i(\alpha a_{14} D_{11}^j + \beta a_{24} D_{21}^j + \beta a_{44} D_{31}^j) + (a_{44} D_{21}^j + a_{34} D_{31}^j) u_j & (j = 4, 5, 6), \\ f_{3j} &= -i(\alpha a_{13} D_{11}^j + \beta a_{23} D_{21}^j + \beta a_{34} D_{31}^j) - (a_{34} D_{21}^j + a_{33} D_{31}^j) u_j & (j = 1, 2, 3), \\ f_{3j} &= i(\alpha a_{13} D_{11}^j + \beta a_{23} D_{21}^j + \beta a_{34} D_{31}^j) + (a_{34} D_{21}^j + a_{33} D_{31}^j) u_j & (j = 4, 5, 6), \\ f_{4j} &= D_{11}^j, \quad f_{5j} = D_{21}^j, \quad f_{6j} = D_{31}^j & (j = 1, 2, 3), \\ f_{4j} &= -D_{11}^j, \quad f_{5j} = -D_{21}^j, \quad f_{6j} = -D_{31}^j & (j = 4, 5, 6). \end{aligned}$$

Now $u_x, u_y,$ and u_z can be obtained by taking the double inverse Fourier transform of (20) and (21):

For $z > 0$ (region 1),

$$u_{x1}(x, y, z) = \frac{1}{2\pi} \int_{-\infty}^{\infty} \int_{-\infty}^{\infty} \sum_{j=1}^3 C_d^j D_{11}(\alpha, \beta, u_j) e^{i(\alpha x + \beta y) + u_j z} d\alpha d\beta, \tag{29a}$$

$$u_{y1}(x, y, z) = \frac{1}{2\pi} \int_{-\infty}^{\infty} \int_{-\infty}^{\infty} \sum_{j=1}^3 C_d^j D_{21}(\alpha, \beta, u_j) e^{i(\alpha x + \beta y) + u_j z} d\alpha d\beta, \tag{29b}$$

$$u_{z1}(x, y, z) = \frac{1}{2\pi} \int_{-\infty}^{\infty} \int_{-\infty}^{\infty} \sum_{j=1}^3 C_d^j D_{31}(\alpha, \beta, u_j) e^{i(\alpha x + \beta y) + u_j z} d\alpha d\beta. \tag{29c}$$

For $z < 0$ (region 2),

$$u_{x2}(x, y, z) = \frac{1}{2\pi} \int_{-\infty}^{\infty} \int_{-\infty}^{\infty} \sum_{j=4}^6 C_u^j D_{11}(\alpha, \beta, u_j) e^{i(\alpha x + \beta y) + u_j z} d\alpha d\beta, \tag{30a}$$

$$u_{y2}(x, y, z) = \frac{1}{2\pi} \int_{-\infty}^{\infty} \int_{-\infty}^{\infty} \sum_{j=4}^6 C_u^j D_{21}(\alpha, \beta, u_j) e^{i(\alpha x + \beta y) + u_j z} d\alpha d\beta, \tag{30b}$$

$$u_{z2}(x, y, z) = \frac{1}{2\pi} \int_{-\infty}^{\infty} \int_{-\infty}^{\infty} \sum_{j=4}^6 C_u^j D_{31}(\alpha, \beta, u_j) e^{i(\alpha x + \beta y) + u_j z} d\alpha d\beta. \tag{30c}$$

The desired $\sigma_{xx}, \sigma_{yy}, \sigma_{zz}, \tau_{yz}, \tau_{zx},$ and τ_{xy} can also be obtain by the double inverse Fourier transform:

for $z > 0$ (region 1),

$$\sigma_{xx1}(x, y, z) = \frac{1}{2\pi} \int_{-\infty}^{\infty} \int_{-\infty}^{\infty} \sum_{j=1}^3 C_d^j \bar{\sigma}_{xx}^j e^{i(ax+\beta y)+u_j z} d\alpha d\beta, \quad (31a)$$

$$\sigma_{yy1}(x, y, z) = \frac{1}{2\pi} \int_{-\infty}^{\infty} \int_{-\infty}^{\infty} \sum_{j=1}^3 C_d^j \bar{\sigma}_{yy}^j e^{i(ax+\beta y)+u_j z} d\alpha d\beta, \quad (31b)$$

$$\sigma_{zz1}(x, y, z) = \frac{1}{2\pi} \int_{-\infty}^{\infty} \int_{-\infty}^{\infty} \sum_{j=1}^3 C_d^j \bar{\sigma}_{zz}^j e^{i(ax+\beta y)+u_j z} d\alpha d\beta, \quad (31c)$$

$$\tau_{yz1}(x, y, z) = \frac{1}{2\pi} \int_{-\infty}^{\infty} \int_{-\infty}^{\infty} \sum_{j=1}^3 C_d^j \bar{\tau}_{yz}^j e^{i(ax+\beta y)+u_j z} d\alpha d\beta, \quad (31d)$$

$$\tau_{zx1}(x, y, z) = \frac{1}{2\pi} \int_{-\infty}^{\infty} \int_{-\infty}^{\infty} \sum_{j=1}^3 C_d^j \bar{\tau}_{zx}^j e^{i(ax+\beta y)+u_j z} d\alpha d\beta, \quad (31e)$$

$$\tau_{xy1}(x, y, z) = \frac{1}{2\pi} \int_{-\infty}^{\infty} \int_{-\infty}^{\infty} \sum_{j=1}^3 C_d^j \bar{\tau}_{xy}^j e^{i(ax+\beta y)+u_j z} d\alpha d\beta, \quad (31f)$$

for $z < 0$ (region 2),

$$\sigma_{xx2}(x, y, z) = \frac{1}{2\pi} \int_{-\infty}^{\infty} \int_{-\infty}^{\infty} \sum_{j=4}^6 C_u^j \bar{\sigma}_{xx}^j e^{i(ax+\beta y)+u_j z} d\alpha d\beta, \quad (32a)$$

$$\sigma_{yy2}(x, y, z) = \frac{1}{2\pi} \int_{-\infty}^{\infty} \int_{-\infty}^{\infty} \sum_{j=4}^6 C_u^j \bar{\sigma}_{yy}^j e^{i(ax+\beta y)+u_j z} d\alpha d\beta, \quad (32b)$$

$$\sigma_{zz2}(x, y, z) = \frac{1}{2\pi} \int_{-\infty}^{\infty} \int_{-\infty}^{\infty} \sum_{j=4}^6 C_u^j \bar{\sigma}_{zz}^j e^{i(ax+\beta y)+u_j z} d\alpha d\beta, \quad (32c)$$

$$\tau_{yz2}(x, y, z) = \frac{1}{2\pi} \int_{-\infty}^{\infty} \int_{-\infty}^{\infty} \sum_{j=4}^6 C_u^j \bar{\tau}_{yz}^j e^{i(ax+\beta y)+u_j z} d\alpha d\beta, \quad (32d)$$

$$\tau_{zx2}(x, y, z) = \frac{1}{2\pi} \int_{-\infty}^{\infty} \int_{-\infty}^{\infty} \sum_{j=4}^6 C_u^j \bar{\tau}_{zx}^j e^{i(ax+\beta y)+u_j z} d\alpha d\beta, \quad (32e)$$

$$\tau_{xy2}(x, y, z) = \frac{1}{2\pi} \int_{-\infty}^{\infty} \int_{-\infty}^{\infty} \sum_{j=4}^6 C_u^j \bar{\tau}_{xy}^j e^{i(ax+\beta y)+u_j z} d\alpha d\beta, \quad (32f)$$

where

$$\bar{\sigma}_{xx}^j = -i(\alpha a_{11} D_{11}^j + \beta a_{12} D_{21}^j + \beta a_{14} D_{31}^j - i(a_{14} D_{21}^j + a_{13} D_{31}^j)u_j), \tag{33a}$$

$$\bar{\sigma}_{yy}^j = -i(\alpha a_{12} D_{11}^j + \beta a_{22} D_{21}^j + \beta a_{24} D_{31}^j - i(a_{24} D_{21}^j + a_{23} D_{31}^j)u_j), \tag{33b}$$

$$\bar{\sigma}_{zz}^j = -i(\alpha a_{13} D_{11}^j + \beta a_{23} D_{21}^j + \beta a_{34} D_{31}^j - i(a_{34} D_{21}^j + a_{33} D_{31}^j)u_j), \tag{33c}$$

$$\bar{\tau}_{yz}^j = -i(\alpha a_{14} D_{11}^j + \beta a_{24} D_{21}^j + \beta a_{44} D_{31}^j - i(a_{44} D_{21}^j + a_{34} D_{31}^j)u_j), \tag{33d}$$

$$\bar{\tau}_{zx}^j = -i(a_{56}(\beta D_{11}^j + \alpha D_{21}^j) + a_{55}(\alpha D_{31}^j - i D_{11}^j u_j)), \tag{33e}$$

$$\bar{\tau}_{xy}^j = -i(a_{66}(\beta D_{11}^j + \alpha D_{21}^j) + a_{56}(\alpha D_{31}^j - i D_{11}^j u_j)). \tag{33f}$$

In (33), $j = 1, 2, 3$ for $z > 0$ (region 1), and $j = 4, 5, 6$ for $z < 0$ (region 2).

Now introduce polar coordinates (k, θ_x) in the $\alpha\beta$ -plane, so

$$\alpha = k \cos \theta_x \quad \text{and} \quad \beta = k \sin \theta_x.$$

Substituting into (19), we obtain for $j = 1, 2, 3$

$$u_j = k \frac{-i \sin \theta_x \sin \phi \cos \phi (-1 + A_j) - \sqrt{A_j (\sin^2 \theta_x + \cos^2 \theta_x (\cos^2 \phi + A_j \sin^2 \phi))}}{\cos^2 \phi + A_j \sin^2 \phi}, \tag{34}$$

$$u_{j+3} = k \frac{-i \sin \theta_x \sin \phi \cos \phi (-1 + A_j) + \sqrt{A_j (\sin^2 \theta_x + \cos^2 \theta_x (\cos^2 \phi + A_j \sin^2 \phi))}}{\cos^2 \phi + A_j \sin^2 \phi},$$

where $0 < k < \infty$ and $0 < \theta_x < 2\pi$.

We can then rewrite (27) and (22) in terms of k and θ_x :

$$D_{11}^j(k, \theta_x) = k^4 D_{11}^j(\theta_x), \tag{35a}$$

$$D_{21}^j(k, \theta_x) = k^4 D_{21}^j(\theta_x), \tag{35b}$$

$$D_{31}^j(k, \theta_x) = k^4 D_{31}^j(\theta_x), \tag{35c}$$

$$C_d^j(k, \theta_x) = k^{-5} C_d^j(\theta_x), \tag{35d}$$

$$C_u^j(k, \theta_x) = k^{-5} C_u^j(\theta_x). \tag{35e}$$

Equations (33) can also be rewritten as

$$\bar{\sigma}_{xx}^j(k, \theta_x) = k^5 \bar{\sigma}_{xx}^j(\theta_x), \tag{36a}$$

$$\bar{\sigma}_{yy}^j(k, \theta_x) = k^5 \bar{\sigma}_{yy}^j(\theta_x), \tag{36b}$$

$$\bar{\sigma}_{zz}^j(k, \theta_x) = k^5 \bar{\sigma}_{zz}^j(\theta_x), \tag{36c}$$

$$\bar{\tau}_{yz}^j(k, \theta_x) = k^5 \bar{\tau}_{yz}^j(\theta_x), \tag{36d}$$

$$\bar{\tau}_{zx}^j(k, \theta_x) = k^5 \bar{\tau}_{zx}^j(\theta_x), \tag{36e}$$

$$\bar{\tau}_{xy}^j(k, \theta_x) = k^5 \bar{\tau}_{xy}^j(\theta_x). \tag{36f}$$

The exponential terms in (29)–(32) become

$$i(\alpha x + \beta y) + u_j z = k \psi_j(\theta_x), \quad (37)$$

while the element $d\alpha d\beta$ equals

$$d\alpha d\beta = k dk d\theta_x. \quad (38)$$

Using (34), (35) and Equation (37), we can rewrite (29) and (30) as follows:

For $z > 0$ (region 1),

$$u_{x1}(x, y, z) = -\frac{1}{2\pi} \int_0^{2\pi} \sum_{j=1}^3 \frac{C_d^j(\theta_x) D_{11}^j(\theta_x)}{\psi_j(\theta_x)} d\theta_x, \quad (39a)$$

$$u_{y1}(x, y, z) = -\frac{1}{2\pi} \int_0^{2\pi} \sum_{j=1}^3 \frac{C_d^j(\theta_x) D_{21}^j(\theta_x)}{\psi_j(\theta_x)} d\theta_x, \quad (39b)$$

$$u_{z1}(x, y, z) = -\frac{1}{2\pi} \int_0^{2\pi} \sum_{j=1}^3 \frac{C_d^j(\theta_x) D_{31}^j(\theta_x)}{\psi_j(\theta_x)} d\theta_x. \quad (39c)$$

For $z < 0$ (region 2),

$$u_{x2}(x, y, z) = -\frac{1}{2\pi} \int_0^{2\pi} \sum_{j=4}^6 \frac{C_u^j(\theta_x) D_{11}^j(\theta_x)}{\psi_j(\theta_x)} d\theta_x, \quad (40a)$$

$$u_{y2}(x, y, z) = -\frac{1}{2\pi} \int_0^{2\pi} \sum_{j=4}^6 \frac{C_u^j(\theta_x) D_{21}^j(\theta_x)}{\psi_j(\theta_x)} d\theta_x, \quad (40b)$$

$$u_{z2}(x, y, z) = -\frac{1}{2\pi} \int_0^{2\pi} \sum_{j=4}^6 \frac{C_u^j(\theta_x) D_{31}^j(\theta_x)}{\psi_j(\theta_x)} d\theta_x. \quad (40c)$$

Likewise, using (34)–(37), we rewrite (32) for $z > 0$ as

$$\sigma_{xx1}(x, y, z) = \frac{1}{2\pi} \int_0^{2\pi} \sum_{j=1}^3 \frac{C_d^j(\theta_x) \bar{\sigma}_{xx}^j(\theta_x)}{(\psi_j(\theta_x))^2} d\theta_x, \quad (41a)$$

$$\sigma_{yy1}(x, y, z) = \frac{1}{2\pi} \int_0^{2\pi} \sum_{j=1}^3 \frac{C_d^j(\theta_x) \bar{\sigma}_{yy}^j(\theta_x)}{(\psi_j(\theta_x))^2} d\theta_x, \quad (41b)$$

$$\sigma_{zz1}(x, y, z) = \frac{1}{2\pi} \int_0^{2\pi} \sum_{j=1}^3 \frac{C_d^j(\theta_x) \bar{\sigma}_{zz}^j(\theta_x)}{(\psi_j(\theta_x))^2} d\theta_x, \quad (41c)$$

$$\tau_{yz1}(x, y, z) = \frac{1}{2\pi} \int_0^{2\pi} \sum_{j=1}^3 \frac{C_d^j(\theta_x) \bar{\tau}_{yz}^j(\theta_x)}{(\psi_j(\theta_x))^2} d\theta_x, \quad (41d)$$

$$\tau_{zx1}(x, y, z) = \frac{1}{2\pi} \int_0^{2\pi} \sum_{j=1}^3 \frac{C_d^j(\theta_x) \bar{\tau}_{zx}^j(\theta_x)}{(\psi_j(\theta_x))^2} d\theta_x, \quad (41e)$$

$$\tau_{yz1}(x, y, z) = \frac{1}{2\pi} \int_0^{2\pi} \sum_{j=1}^3 \frac{C_d^j(\theta_x) \bar{\tau}_{yz}^j(\theta_x)}{(\psi_j(\theta_x))^2} d\theta_x, \tag{41f}$$

and similarly for $z < 0$, with 1 replaced by 2 in the subscripts on the left-hand side and the sum ranging from 4 to 6.

We now introduce $\omega = e^{i\theta_x}$ (whence in particular $d\omega = i\omega d\theta_x$), and

$$\psi_7(\omega) = \psi_1(\omega)\psi_4(\omega) = \frac{1}{4\omega^2}(\eta_1^1\omega^4 + \eta_2^1\omega^2 + \eta_3^1) = \frac{\eta_1^1}{4\omega^2}(\omega^2 - \alpha_1^2)(\omega^2 - \beta_1^2), \tag{42a}$$

$$\psi_8(\omega) = \psi_2(\omega)\psi_5(\omega) = \frac{1}{4\omega^2}(\eta_1^2\omega^4 + \eta_2^2\omega^2 + \eta_3^2) = \frac{\eta_1^2}{4\omega^2}(\omega^2 - \alpha_2^2)(\omega^2 - \beta_2^2), \tag{42b}$$

$$\psi_9(\omega) = \psi_3(\omega)\psi_6(\omega) = \frac{1}{4\omega^2}(\eta_1^3\omega^4 + \eta_2^3\omega^2 + \eta_3^3) = \frac{\eta_1^3}{4\omega^2}(\omega^2 - \alpha_3^2)(\omega^2 - \beta_3^2), \tag{42c}$$

where, for $j = 1, 2, 3$,

$$\eta_1^j = \frac{((ix + y) \cos \phi + z \sin \phi)^2 - A_j \sin \phi (2(ix + y)z \cos \phi + ((x - iy)^2 + z^2) \sin \phi)}{\cos^2 \phi + A_j \sin^2 \phi}, \tag{43a}$$

$$\eta_2^j = -2 \left(x^2 + y^2 - z^2 - \frac{z(y \sin 2\phi(-1 + A_j) - z(1 + 2A_j))}{\cos^2 \phi + A_j \sin^2 \phi} \right), \tag{43b}$$

$$\eta_3^j = \frac{((-ix + y) \cos \phi + z \sin \phi)^2 - A_j \sin \phi (2(-ix + y)z \cos \phi + ((x + iy)^2 + z^2) \sin \phi)}{\cos^2 \phi + A_j \sin^2 \phi}, \tag{43c}$$

$$\alpha_j^2 = \frac{-\eta_2^j + \sqrt{\eta_2^j - 4\eta_1^j \eta_3^j}}{2\eta_1^j}, \quad \beta_j^2 = \frac{-\eta_2^j - \sqrt{\eta_2^j - 4\eta_1^j \eta_3^j}}{2\eta_1^j}. \tag{43d}$$

In this notation, Equations (39), valid for $z > 0$, become

$$u_{x1}(x, y, z) = -\frac{1}{2\pi} \oint_C \frac{1}{i\omega} \sum_{j=1}^3 C_d^j(\omega) D_{11}^j(\omega) \frac{\psi_{j+3}(\omega)}{\psi_{j+6}(\omega)} d\omega, \tag{44a}$$

$$u_{y1}(x, y, z) = -\frac{1}{2\pi} \oint_C \frac{1}{i\omega} \sum_{j=1}^3 C_d^j(\omega) D_{21}^j(\omega) \frac{\psi_{j+3}(\omega)}{\psi_{j+6}(\omega)} d\omega, \tag{44b}$$

$$u_{z1}(x, y, z) = -\frac{1}{2\pi} \oint_C \frac{1}{i\omega} \sum_{j=1}^3 C_d^j(\omega) D_{31}^j(\omega) \frac{\psi_{j+3}(\omega)}{\psi_{j+6}(\omega)} d\omega, \tag{44c}$$

while (40), valid for $z < 0$, takes on an analogous form, with 1 replaced by 2 on the left-hand sides and the roles of j and $j + 3$ on the right-hand sides reversed.

Next, Equations (41), valid for $z > 0$, become

$$\sigma_{xx1}(x, y, z) = \frac{1}{2\pi} \oint_C \frac{1}{i\omega} \sum_{j=1}^3 C_d^j(\omega) \bar{\sigma}_{xx}^j(\omega) \left(\frac{\psi_{j+3}(\omega)}{\psi_{j+6}(\omega)} \right)^2 d\omega, \quad (45a)$$

$$\sigma_{yy1}(x, y, z) = \frac{1}{2\pi} \oint_C \frac{1}{i\omega} \sum_{j=1}^3 C_d^j(\omega) \bar{\sigma}_{yy}^j(\omega) \left(\frac{\psi_{j+3}(\omega)}{\psi_{j+6}(\omega)} \right)^2 d\omega, \quad (45b)$$

$$\sigma_{zz1}(x, y, z) = \frac{1}{2\pi} \oint_C \frac{1}{i\omega} \sum_{j=1}^3 C_d^j(\omega) \bar{\sigma}_{zz}^j(\omega) \left(\frac{\psi_{j+3}(\omega)}{\psi_{j+6}(\omega)} \right)^2 d\omega, \quad (45c)$$

$$\tau_{yz1}(x, y, z) = \frac{1}{2\pi} \oint_C \frac{1}{i\omega} \sum_{j=1}^3 C_d^j(\omega) \bar{\tau}_{yz}^j(\omega) \left(\frac{\psi_{j+3}(\omega)}{\psi_{j+6}(\omega)} \right)^2 d\omega, \quad (45d)$$

$$\tau_{zx1}(x, y, z) = \frac{1}{2\pi} \oint_C \frac{1}{i\omega} \sum_{j=1}^3 C_d^j(\omega) \bar{\tau}_{zx}^j(\omega) \left(\frac{\psi_{j+3}(\omega)}{\psi_{j+6}(\omega)} \right)^2 d\omega, \quad (45e)$$

$$\tau_{xy1}(x, y, z) = \frac{1}{2\pi} \oint_C \frac{1}{i\omega} \sum_{j=1}^3 C_d^j(\omega) \bar{\tau}_{xy}^j(\omega) \left(\frac{\psi_{j+3}(\omega)}{\psi_{j+6}(\omega)} \right)^2 d\omega. \quad (45f)$$

The counterparts for $z < 0$ are, as before, obtained by replacing 1 with 2 on the left-hand sides and interchanging j and $j + 3$ on the right-hand sides.

In (42), Cauchy's theory of residues can be used to integrate the contours. If we set

$$\psi_j = \frac{\Phi_j}{\omega} \quad (j = 1, 2, 3), \quad (46)$$

and substitute (42) into (44), the result is a new expression for u_x , u_y , and u_z valid for $z > 0$ (region 1):

$$u_{x1}(x, y, z) = -4 \sum_{j=1}^3 \left(C_d^j(\alpha_j) D_{11}^j(\alpha_j) \frac{\Phi_{j+3}(\alpha_j)}{\eta_1^j(2\alpha_j)(\alpha_j^2 - \beta_j^2)} + C_d^j(-\alpha_j) D_{11}^j(-\alpha_j) \frac{\Phi_{j+3}(-\alpha_j)}{\eta_1^j(-2\alpha_j)(\alpha_j^2 - \beta_j^2)} \right), \quad (47a)$$

$$u_{y1}(x, y, z) = -4 \sum_{j=1}^3 \left(C_d^j(\alpha_j) D_{21}^j(\alpha_j) \frac{\Phi_{j+3}(\alpha_j)}{\eta_1^j(2\alpha_j)(\alpha_j^2 - \beta_j^2)} + C_d^j(-\alpha_j) D_{21}^j(-\alpha_j) \frac{\Phi_{j+3}(-\alpha_j)}{\eta_1^j(-2\alpha_j)(\alpha_j^2 - \beta_j^2)} \right), \quad (47b)$$

$$u_{z1}(x, y, z) = -4 \sum_{j=1}^3 \left(C_d^j(\alpha_j) D_{31}^j(\alpha_j) \frac{\Phi_{j+3}(\alpha_j)}{\eta_1^j(2\alpha_j)(\alpha_j^2 - \beta_j^2)} + C_d^j(-\alpha_j) D_{31}^j(-\alpha_j) \frac{\Phi_{j+3}(-\alpha_j)}{\eta_1^j(-2\alpha_j)(\alpha_j^2 - \beta_j^2)} \right), \quad (47c)$$

Since $\Phi_4(-\alpha_1) = \Phi_5(-\alpha_2) = \Phi_6(-\alpha_3) = 0$, this reduces to (still for $z > 0$)

$$u_{x1}(x, y, z) = -4 \sum_{j=1}^3 C_d^j(\alpha_j) D_{11}^j(\alpha_j) \frac{\Phi_{j+3}(\alpha_j)}{\eta_1^j(2\alpha_j)(\alpha_j^2 - \beta_j^2)}, \tag{48a}$$

$$u_{y1}(x, y, z) = -4 \sum_{j=1}^3 C_d^j(\alpha_j) D_{21}^j(\alpha_j) \frac{\Phi_{j+3}(\alpha_j)}{\eta_1^j(2\alpha_j)(\alpha_j^2 - \beta_j^2)}, \tag{48b}$$

$$u_{z1}(x, y, z) = -4 \sum_{j=1}^3 C_d^j(\alpha_j) D_{31}^j(\alpha_j) \frac{\Phi_{j+3}(\alpha_j)}{\eta_1^j(2\alpha_j)(\alpha_j^2 - \beta_j^2)}, \tag{48c}$$

The analogous formulas for $z < 0$, taking into account that in this case $\Phi_1(\alpha_1) = \Phi_2(\alpha_2) = \Phi_3(\alpha_3) = 0$, read as follows:

$$u_{x2}(x, y, z) = -4 \sum_{j=1}^3 C_u^{j+3}(-\alpha_j) D_{11}^{j+3}(-\alpha_j) \frac{\Phi_j(-\alpha_j)}{\eta_1^j(-2\alpha_j)(\alpha_j^2 - \beta_j^2)}, \tag{49a}$$

$$u_{y2}(x, y, z) = -4 \sum_{j=1}^3 C_u^{j+3}(-\alpha_j) D_{21}^{j+3}(-\alpha_j) \frac{\Phi_j(-\alpha_j)}{\eta_1^j(-2\alpha_j)(\alpha_j^2 - \beta_j^2)}, \tag{49b}$$

$$u_{z2}(x, y, z) = -4 \sum_{j=1}^3 C_u^{j+3}(-\alpha_j) D_{31}^{j+3}(-\alpha_j) \frac{\Phi_j(-\alpha_j)}{\eta_1^j(-2\alpha_j)(\alpha_j^2 - \beta_j^2)}, \tag{49c}$$

Using the same approach, with the substitution of (42) into (45), one obtains for $z > 0$

$$\sigma_{xx1}(x, y, z) = \sum_{j=1}^3 \frac{d}{d\omega} \left\{ \omega C_d^j(\omega) \bar{\sigma}_{xx}^j(\omega) \left(\frac{\Phi_{j+3}(\omega)}{\eta_1^j(\omega + \alpha_j)(\omega^2 - \beta_j^2)} \right)^2 \right\}_{\omega \rightarrow \alpha_j}, \tag{50a}$$

$$\sigma_{yy1}(x, y, z) = \sum_{j=1}^3 \frac{d}{d\omega} \left\{ \omega C_d^j(\omega) \bar{\sigma}_{yy}^j(\omega) \left(\frac{\Phi_{j+3}(\omega)}{\eta_1^j(\omega + \alpha_j)(\omega^2 - \beta_j^2)} \right)^2 \right\}_{\omega \rightarrow \alpha_j}, \tag{50b}$$

$$\sigma_{zz1}(x, y, z) = \sum_{j=1}^3 \frac{d}{d\omega} \left\{ \omega C_d^j(\omega) \bar{\sigma}_{zz}^j(\omega) \left(\frac{\Phi_{j+3}(\omega)}{\eta_1^j(\omega + \alpha_j)(\omega^2 - \beta_j^2)} \right)^2 \right\}_{\omega \rightarrow \alpha_j}, \tag{50c}$$

$$\tau_{yz1}(x, y, z) = \sum_{j=1}^3 \frac{d}{d\omega} \left\{ \omega C_d^j(\omega) \bar{\tau}_{yz}^j(\omega) \left(\frac{\Phi_{j+3}(\omega)}{\eta_1^j(\omega + \alpha_j)(\omega^2 - \beta_j^2)} \right)^2 \right\}_{\omega \rightarrow \alpha_j}, \tag{50d}$$

$$\tau_{zx1}(x, y, z) = \sum_{j=1}^3 \frac{d}{d\omega} \left\{ \omega C_d^j(\omega) \bar{\tau}_{zx}^j(\omega) \left(\frac{\Phi_{j+3}(\omega)}{\eta_1^j(\omega + \alpha_j)(\omega^2 - \beta_j^2)} \right)^2 \right\}_{\omega \rightarrow \alpha_j}, \tag{50e}$$

$$\tau_{xy1}(x, y, z) = \sum_{j=1}^3 \frac{d}{d\omega} \left\{ \omega C_d^j(\omega) \bar{\tau}_{xy}^j(\omega) \left(\frac{\Phi_{j+3}(\omega)}{\eta_1^j(\omega + \alpha_j)(\omega^2 - \beta_j^2)} \right)^2 \right\}_{\omega \rightarrow \alpha_j}, \tag{50f}$$

and similarly for $z < 0$

$$\sigma_{xx2}(x, y, z) = \sum_{j=1}^3 \frac{d}{d\omega} \left\{ \omega C_u^{j+3}(\omega) \bar{\sigma}_{xx}^{j+3}(\omega) \left(\frac{\Phi_j(\omega)}{\eta_1^j(\omega - \alpha_j)(\omega^2 - \beta_j^2)} \right)^2 \right\}_{\omega \rightarrow \alpha_j}, \quad (51a)$$

$$\sigma_{yy2}(x, y, z) = \sum_{j=1}^3 \frac{d}{d\omega} \left\{ \omega C_u^{j+3}(\omega) \bar{\sigma}_{yy}^{j+3}(\omega) \left(\frac{\Phi_j(\omega)}{\eta_1^j(\omega - \alpha_j)(\omega^2 - \beta_j^2)} \right)^2 \right\}_{\omega \rightarrow \alpha_j}, \quad (51b)$$

$$\sigma_{zz2}(x, y, z) = \sum_{j=1}^3 \frac{d}{d\omega} \left\{ \omega C_u^{j+3}(\omega) \bar{\sigma}_{zz}^{j+3}(\omega) \left(\frac{\Phi_j(\omega)}{\eta_1^j(\omega - \alpha_j)(\omega^2 - \beta_j^2)} \right)^2 \right\}_{\omega \rightarrow \alpha_j}, \quad (51c)$$

$$\tau_{yz2}(x, y, z) = \sum_{j=1}^3 \frac{d}{d\omega} \left\{ \omega C_u^{j+3}(\omega) \bar{\tau}_{yz}^{j+3}(\omega) \left(\frac{\Phi_j(\omega)}{\eta_1^j(\omega - \alpha_j)(\omega^2 - \beta_j^2)} \right)^2 \right\}_{\omega \rightarrow \alpha_j}, \quad (51d)$$

$$\tau_{zx2}(x, y, z) = \sum_{j=1}^3 \frac{d}{d\omega} \left\{ \omega C_u^{j+3}(\omega) \bar{\tau}_{zx}^{j+3}(\omega) \left(\frac{\Phi_j(\omega)}{\eta_1^j(\omega - \alpha_j)(\omega^2 - \beta_j^2)} \right)^2 \right\}_{\omega \rightarrow \alpha_j}, \quad (51e)$$

$$\tau_{xy2}(x, y, z) = \sum_{j=1}^3 \frac{d}{d\omega} \left\{ \omega C_u^{j+3}(\omega) \bar{\tau}_{xy}^{j+3}(\omega) \left(\frac{\Phi_j(\omega)}{\eta_1^j(\omega - \alpha_j)(\omega^2 - \beta_j^2)} \right)^2 \right\}_{\omega \rightarrow \alpha_j}, \quad (51f)$$

2. Illustrative examples

The closed-form solutions given above demonstrate that several factors can affect the displacements and stresses in an inclined transversely isotropic material. They include: (1) the rotation of the transversely isotropic planes (ϕ), (2) the type and degree of material anisotropy (E/E' , ν/ν' , G/G'), (3) the geometric position (r , ϕ , ξ), as seen in [Figure 2](#), and (4) the type of three-dimensional loading (P_x , P_y , P_z). Based on Equations (48) and (49) for region 1 ($z > 0$) and their counterparts for region 2, a Mathematica program was written to clarify the effect of these factors on the induced displacements and stresses. In this program, the displacements and stresses at any point in the full space can be calculated.

A parametric study is conducted to illustrate the generated analytical solutions and investigate the influence of the rotation of transversely isotropic planes, the geometric position, and the degree and type of rock anisotropy on the displacements and stresses. Two examples will be discussed: the first example presents the effect of ϕ on the displacements and stresses of a material subjected to a vertical point load P_z at $x = y = z = 1$ (as shown in [Figure 3](#) for displacements, and [Figure 4](#) for stresses); the second

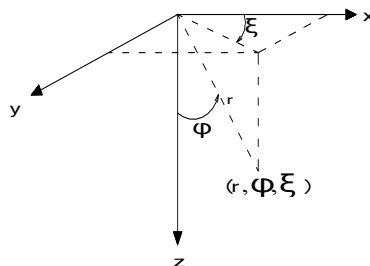


Figure 2. Spherical coordinate system (r , ϕ , ξ).

	E/E'	ν/ν'	G/G'
Rock 1. Isotropic	1.0	1.0	1.0
Rock 2. Transversely isotropic	2.0	1.0	1.0
Rock 3. Transversely isotropic	3.0	1.0	1.0
Rock 4. Transversely isotropic	1.0	0.75	1.0
Rock 5. Transversely isotropic	1.0	1.5	1.0
Rock 6. Transversely isotropic	1.0	1.0	2.0
Rock 7. Transversely isotropic	1.0	1.0	3.0

Table 1. Elastic properties of the hypothetical rocks used in the examples. In each case, $E = 50$ GPa and $\nu = 0.25$.

example exhibits the effect of ϕ on the stresses due to P_z at $\phi = 90^\circ$ and $\zeta = 45^\circ$ (as depicted in Figure 5). Seven types of isotropic and transversely isotropic rocks are considered in our model of the foundation materials. For typical ranges of transversely isotropic rocks, Gerrard [1977] and Amadei et al. [1987] suggested that the ratios E/E' and G/G' range from 1.0 to 3.0, and that ν/ν' vary between 0.75 and 1.5. Hence, the degree of rock anisotropy, specified by the ratios E/E' , ν/ν' , and G/G' is accounted for in the investigation of the anisotropy effect on displacements and stresses. Table 1 lists the rock type and elastic properties for the hypothetical rocks. The values chosen for E and ν are 50 GPa and 0.3.

Figure 3 shows the normalized displacements $u_x r/P_z$, $u_y r/P_z$ and $u_z r/P_z$ versus rotation of the transversely isotropic planes (ϕ), due to a vertical point load (P_z), at $x = y = z = 1$, for the constituted isotropic/transversely isotropic rocks (rock 1/rocks 2–7, Table 1). Figure 3(a) depicts the normalized displacement u_x of the rocks, induced by P_z . It is observed that any value in each curve is symmetric with respect to the origin of the coordinates, and the ratios E/E' (rocks 2 and 3), ν/ν' (rocks 4 and 5), and G/G' (rocks 6 and 7) all strongly influence this displacement. This figure also shows that the magnitude of the normalized induced displacement ($0.00026 \text{ m}^2/\text{GN}$) for rock 1 is independent of the change in ϕ . However, for rocks 2 and 3, the displacement is maximal at about $\phi = 0^\circ\text{--}180^\circ$, and is minimal at approximately $\phi = 60^\circ\text{--}240^\circ$. As for rocks 6 and 7, the displacement is maximal at around $\phi = 50^\circ\text{--}230^\circ$, and is minimal at about $\phi = 100^\circ\text{--}280^\circ$. Figure 3(b) presents the normalized displacement u_y of the rocks, due to P_z . This figure clearly reveals that the displacement induced in transversely isotropic rocks is deeply affected by the ratios E/E' (rocks 2 and 3) and G/G' (rocks 6 and 7), but is only slightly influenced by ν/ν' (rocks 4 and 5). Notably, the normalized displacement ($0.00026 \text{ m}^2/\text{GN}$) of the isotropic rock (rock 1) is also independent of ϕ . Nevertheless, it is found that the values of induced displacement for rocks 2 and 3 would be partially within the range of -0.0004 to 0, meaning there could be an opposite-direction displacement occurring in these media. Figure 3(c) displays the normalized displacement u_z of the rocks, subjected to P_z . Clearly, the ratios E/E' (rocks 2 and 3) and G/G' (rocks 6 and 7) profoundly impact the induced displacement, but the effect of ν/ν' (rocks 4 and 5) is small. The magnitude of the normalized induced displacement for rock 1 is always $0.00179 \text{ m}^2/\text{GN}$; however, for rocks 2, 3, 6, and 7, the values of u_z are nearly greater than those of rock 1. The calculated results for the displacement fields are all in good agreement with Wang and Liao's solutions [Wang and Liao 1999] if the full space is homogeneous, linearly elastic, and the planes of transverse isotropy are parallel to the horizontal axes.

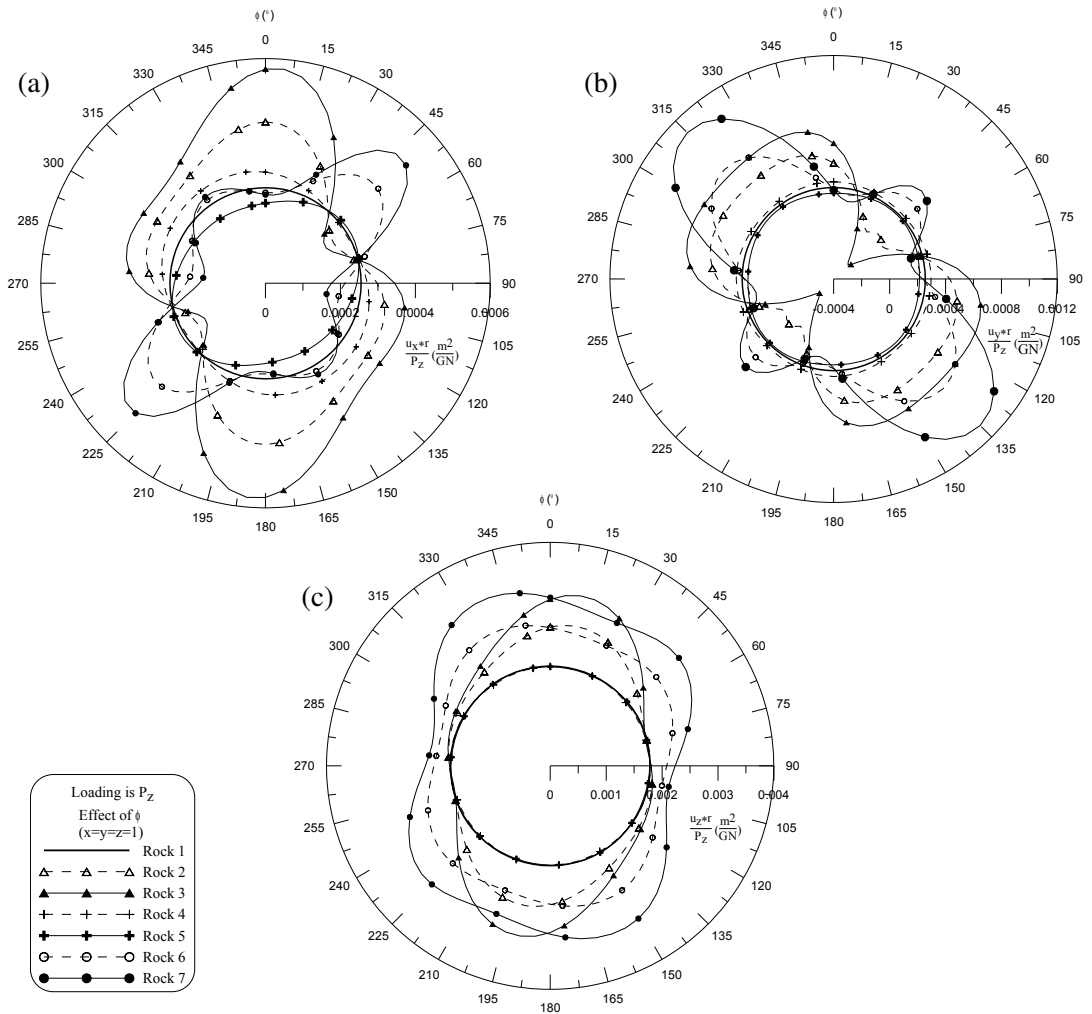


Figure 3. At the position $x = y = z = 1$, the effect of ϕ on the normalized displacement (a) $u_x r/P_z$, (b) $u_y r/P_z$, (c) $u_z r/P_z$.

Figure 4 plots the nondimensional normal stresses $\sigma_{xx}r^2/P_z$, $\sigma_{yy}r^2/P_z$, $\sigma_{zz}r^2/P_z$ and the nondimensional shear stresses $\tau_{yz}r^2/P_z$, $\tau_{zx}r^2/P_z$, $\tau_{xy}r^2/P_z$, versus the rotation of the transversely isotropic planes (ϕ), subjected to a vertical point load (P_z), at $x = y = z = 1$, for the isotropic (rock 1) and transversely isotropic rocks (rocks 2–7). Figure 4(a) illustrates the effect of ϕ on $\sigma_{xx}r^2/P_z$, for rocks 1–7. This figure shows that the induced stress for the isotropic rock (rock 1) has the same value (0.005105) that is again independent of ϕ . However, it is found that the values of induced stress for rocks 1–7 vary between -0.004 and 0.02 , namely, that there is an obvious tensile stress occurring in rock 7. In addition, any value in each curve is symmetric with respect to the origin of the coordinates. Hence, from this figure, it is apparently revealed that the induced stress is greatly influenced by the rotation of the transversely isotropic planes (ϕ), and the type and degree of rock anisotropy (E/E' , ν/ν' , G/G'). Figure 4(b) presents

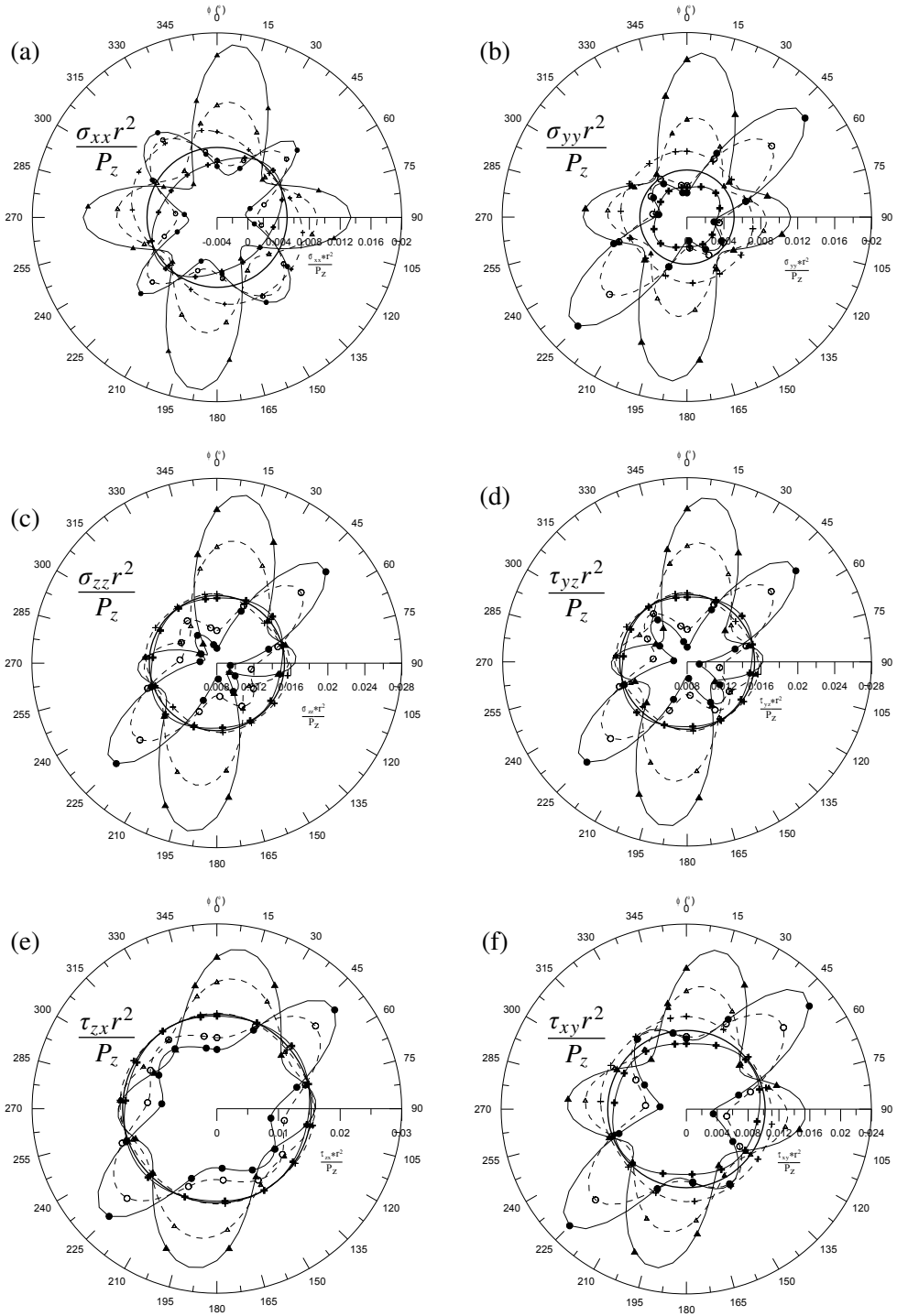


Figure 4. At the position $x = y = z = 1$, the effect of ϕ on the nondimensional normal and shear stresses. For the code indicating the type of rock, see [Figure 3](#).

the effect of ϕ on $\sigma_{yy}r^2/P_z$, for rocks 1–7. Notably, the value in the curves is also symmetric with respect to the origin of the coordinates, and the ratios E/E' (rocks 2 and 3), ν/ν' (rocks 4 and 5), and G/G' (rocks 6 and 7) do also have a considerable influence on the stress. This graph shows that the magnitude of the nondimensional normal stress ($\sigma_{yy}r^2/P_z$) for rock 1 (0.005105) is also independent of ϕ , and the value of the nondimensional stress is within 0.06. In particular, the computed results for rocks 4 and 5 are, respectively, greater than or less than those of rock 1. Figure 4(c) depicts the effect of ϕ on $\sigma_{zz}r^2/P_z$, for rocks 1–7. This stress depends heavily on the ratios E/E' (rocks 2 and 3) and G/G' (rocks 6 and 7). Nevertheless, the effect of the ratios ν/ν' (rocks 4 and 5) on the stress is slight. The maximum value of the nondimensional stress approaches 0.026. Figure 4(d) plots the effect of ϕ on $\tau_{yz}r^2/P_z$, for rocks 1–7. Evidently, the ratios E/E' (rocks 2 and 3) and G/G' (rocks 6 and 7) could intensely affect the induced stress. However, the effect of the ratios ν/ν' (rocks 4 and 5) on the induced stress is still small. The trend of these stress curves in this figure is similar to that in Figure 4(c). Figure 4(e) displays the effect of ϕ on $\tau_{zx}r^2/P_z$, for rocks 1–7. The maximum value of the nondimensional stress is about 0.026. Figure 4(f) shows the effect of ϕ on $\tau_{xy}r^2/P_z$, for rocks 1–7. The effect of the ratios ν/ν' for rocks 4 and 5 in this figure is more explicit than the effect on other shear stresses (Figures 4(d) and 4(e)). Especially, the calculated results of rocks 4 and 5 are, respectively, greater than or less than those of rock 1. The maximum value of the nondimensional stress is within the range of 0.024. The computed results for the stress fields are identical to those estimated from Wang and Liao's solutions [1999], in which the planes of transverse isotropic full space are parallel to the horizontal loading surface.

Figure 5 plots the nondimensional normal stresses ($\sigma_{xx}r^2/P_z$, $\sigma_{yy}r^2/P_z$, $\sigma_{zz}r^2/P_z$) and the nondimensional shear stresses ($\tau_{yz}r^2/P_z$, $\tau_{zx}r^2/P_z$, $\tau_{xy}r^2/P_z$) versus the geometric position ϕ (from 0° to 360°), due to a vertical point load (P_z), at the rotation of the transversely isotropic planes $\phi = 90^\circ$ and the geometric position $\zeta = 45^\circ$, for the constituted isotropic/transversely isotropic rocks (rock 1/rocks 2–7). Figure 5(a) clarifies the effect of ϕ on $\sigma_{xx}r^2/P_z$, for rocks 1–7. It is observed that the magnitudes of the estimated stresses are symmetric with respect to $\phi = 180^\circ$. The upper/lower part of this figure denotes the compressive/tensile stress occurring in the rock media. The maximum values of tensile/compressive stress appeared at $\phi = 0^\circ/180^\circ$ in rock 7. In addition, the induced stresses are found to be influenced by the ratios E/E' (rocks 2 and 3), ν/ν' (rocks 4 and 5), G/G' (rocks 6 and 7), and they are all zero at $\phi = 90^\circ$ and 270° . Figure 5(b) demonstrates the effect of ϕ on $\sigma_{yy}r^2/P_z$, for rocks 1–7. Results reveal that the magnitudes of the computed stresses are also symmetric with respect to $\phi = 180^\circ$, and the tensile and compressive stresses would be expected to occur in all media. However, the maximum values of tensile/compressive stress appeared at approximately $\phi = 125^\circ$ and $235^\circ/55^\circ$ and 305° in rock 4. This means that at a given position ($\phi = 90^\circ$ and $\zeta = 45^\circ$), the decrease in the ratio ν/ν' from 1.0 (rock 1) to 0.75 (rock 4) could remarkably affect the stress (σ_{yy}). Figure 5(c) shows the induced nondimensional normal stress $\sigma_{zz}r^2/P_z$ for rocks 1–7. The distributions and magnitudes of the calculated stresses are quite different from those of Figures 5(a) and 5(b). The tensile/compressive stress can be found within $\phi = 0^\circ\text{--}90^\circ$ and $270^\circ\text{--}360^\circ/90^\circ\text{--}270^\circ$. Moreover, the stress (σ_{zz}) is apparently impacted by the ratios G/G' (rocks 6 and 7). Nevertheless, the stress is affected to only a small degree by the ratios E/E' (rocks 2 and 3) and ν/ν' (rocks 4 and 5). The induced nondimensional shear stress $\tau_{yz}r^2/P_z$ for rocks 1–7 is depicted in Figure 5(d). It is noted that the positive/negative values of τ_{yz} are symmetric with respect to $\phi = 180^\circ$. Additionally, the computed stresses are all zero at $\phi = 0^\circ$, 180° , and 360° . The results of rocks 2, 4, 6, 7 are rather distinct from those of rocks 1, 3, 5. Similarly, the trends can be discovered in

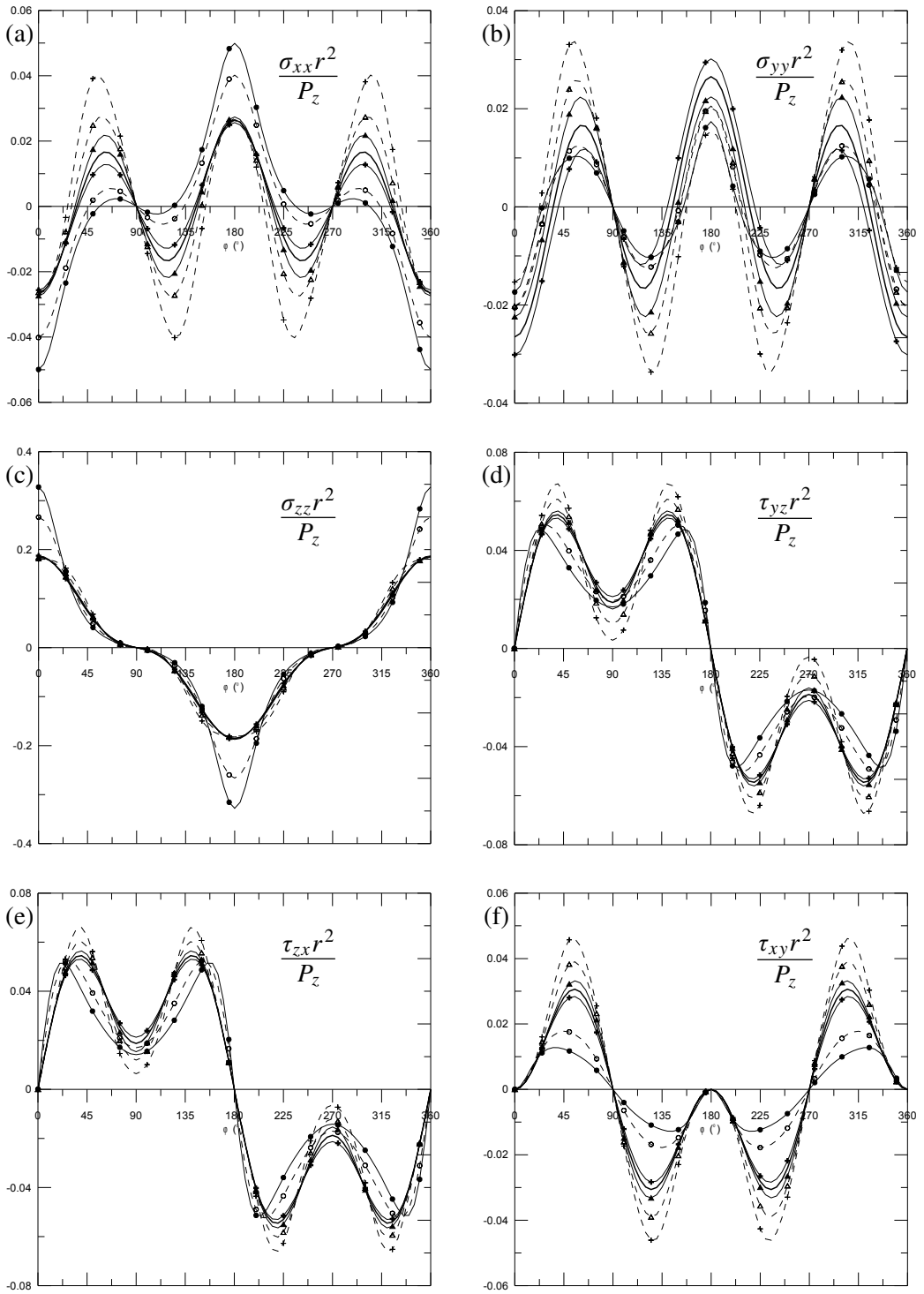


Figure 5. At the position $\phi = 90^\circ$, $\zeta = 45^\circ$, the effect of φ on the nondimensional normal and shear stresses. For the code indicating the type of rock, see Figure 3.

Figure 5(e) for $\tau_{zx}r^2/P_z$. Eventually, the induced nondimensional shear stress $\tau_{xy}r^2/P_z$ for rocks 1–7 is displayed in Figure 5(f). The calculated positive/negative values of τ_{xy} are symmetric with $\phi = 90^\circ$ and 270° . The zero values for τ_{xy} are found at $\phi = 0^\circ, 90^\circ, 180^\circ, 270^\circ$, and 360° . Furthermore, the influences of the type and degree of rock anisotropy in this figure are more explicit than those in Figure 5(d,e). That means again that at $\phi = 90^\circ$ and $\zeta = 45^\circ$, the normal and shear stresses due to a vertical point load are strongly impacted by the geometric position (ϕ) and rock anisotropy ($E/E', \nu/\nu', G/G'$).

The examples are presented to illustrate the derived solutions and demonstrate how the rotation of transversely isotropic planes (ϕ), the geometric position (r, ϕ, ζ), and the degree and type of material anisotropy ($E/E', \nu/\nu', G/G'$) would influence the normalized displacements and nondimensional normal and shear stresses. Results reveal that the displacements and stresses in the inclined isotropic or transversely isotropic rocks (rock 1/rocks 2–7) due to a vertical point load are quite different from the displacements and stresses calculated by assuming the transversely isotropic planes are parallel to the horizontal surface. Hence, it is imperative to consider the dip at an angle of inclination when calculating the induced displacements and stresses in a transversely isotropic material by applied loads.

Conclusions

Analytical solutions are presented for displacements and stresses in a transversely isotropic material (in which the transversely isotropic planes are oriented with respect to the horizontal axes) subjected to three-dimensional point loads. It is known that the stress components due to three-dimensional point loads in an inclined infinite space can be obtained by employing the coordinate transformation formulae with respect to the applied loads. Nevertheless, the displacement components cannot be solved by the same approach. Hence, an efficient method that employs the double Fourier transform in a Cartesian coordinate system is proposed to yield the fundamental solutions for displacements and stresses. First, the characteristic roots for this special material anisotropy are addressed in this article. Next, the double inverse Fourier transform and residue calculus are applied to integrate the contours. The generated solutions for displacements are the same as those of [Hu et al. 2007], which were arrived at by using the triple Fourier transform for an inclined transversely isotropic full space. In addition, they are identical with those of [Wang and Liao 1999] if the planes of transverse isotropy are parallel to the horizontal loading surface. The proposed solutions clarify that the displacements and stresses are governed by

- (1) the rotation of the transversely isotropic planes (ϕ),
- (2) the type and degree of material anisotropy ($E/E', \nu/\nu', G/G'$),
- (3) the geometric position (r, ϕ, ζ), and
- (4) the type of three-dimensional loading (P_x, P_y, P_z).

The present elastic fundamental solutions could not only realistically imitate the actual stratum of loading circumstances in many fields of practical engineering, but also provide the foundations of the boundary integral equation method (BIEM) or the boundary element method (BEM) for solving numerous boundary value problems. Moreover, the addressed solutions can be extended to generate the displacements and stresses due to three-dimensional point loads in the inclined transversely isotropic half-spaces/bimaterials/layered materials. These solutions could be very valuable to solid mechanics, and they will be presented in the near future.

Appendix

In this appendix we give a parallel, more leisurely derivation of the characteristic equation (18). Recall that the x' and y' axes are in the plane of transversely isotropy, and that the generalized Hooke's law for a transversely isotropic material is expressed by Equation (2).

Let $u_{x'}, u_{y'}, u_{z'}$ be the displacements of a point on the axes of a Cartesian coordinate system. The strain-displacement relationship for the small strain condition is given by (6), with x, y, z replaced by x', y', z' .

The equation of force equilibrium is

$$\begin{bmatrix} \sigma_{x'x'} & \tau_{x'y'} & \tau_{x'z'} \\ \tau_{x'y'} & \sigma_{y'y'} & \tau_{y'z'} \\ \tau_{x'z'} & \tau_{y'z'} & \sigma_{z'z'} \end{bmatrix} \begin{bmatrix} \partial/\partial x' \\ \partial/\partial y' \\ \partial/\partial z' \end{bmatrix} - \begin{bmatrix} F_{x'} \\ F_{y'} \\ F_{z'} \end{bmatrix} = \rho \begin{bmatrix} \partial^2 u_{x'}/\partial t^2 \\ \partial^2 u_{y'}/\partial t^2 \\ \partial^2 u_{z'}/\partial t^2 \end{bmatrix}.$$

If we set $(F_{x'}, F_{y'}, F_{z'}) = (0, 0, 0)$, this becomes

$$\rho \frac{\partial^2 u_{x'}}{\partial t^2} = c_1 \frac{\partial^2 u_{x'}}{\partial x'^2} + c_4 \frac{\partial^2 u_{x'}}{\partial y'^2} + c_5 \frac{\partial^2 u_{x'}}{\partial z'^2} + (c_1 - c_4) \frac{\partial^2 u_{y'}}{\partial x' \partial y'} + c_3 \frac{\partial^2 u_{z'}}{\partial x' \partial z'}, \tag{52a}$$

$$\rho \frac{\partial^2 u_{y'}}{\partial t^2} = (c_1 - c_4) \frac{\partial^2 u_{x'}}{\partial x' \partial y'} + c_4 \frac{\partial^2 u_{y'}}{\partial x'^2} + c_1 \frac{\partial^2 u_{y'}}{\partial y'^2} + c_5 \frac{\partial^2 u_{y'}}{\partial z'^2} + c_3 \frac{\partial^2 u_{z'}}{\partial y' \partial z'}, \tag{52b}$$

$$\rho \frac{\partial^2 u_{z'}}{\partial t^2} = c_3 \frac{\partial^2 u_{x'}}{\partial x' \partial z'} + c_3 \frac{\partial^2 u_{y'}}{\partial y' \partial z'} + c_5 \frac{\partial^2 u_{z'}}{\partial x'^2} + c_5 \frac{\partial^2 u_{z'}}{\partial y'^2} + c_2 \frac{\partial^2 u_{z'}}{\partial z'^2}. \tag{52c}$$

For the elastic dynamic problem, an arbitrary time-harmonic body force in the x', y' , and z' directions with angular frequency ω can be written as

$$u_{x'}(x', y', z', t) = u_{x'}^*(x', y', z') \exp(-i\omega t), \tag{53a}$$

$$u_{y'}(x', y', z', t) = u_{y'}^*(x', y', z') \exp(-i\omega t), \tag{53b}$$

$$u_{z'}(x', y', z', t) = u_{z'}^*(x', y', z') \exp(-i\omega t), \tag{53c}$$

where $u_{x'}^*, u_{y'}^*$, and $u_{z'}^*$ represent the complex amplitude of the body force.

Taking the triple Fourier transform of (53) we obtain

$$\bar{u}_{x'}(\alpha, \beta, \gamma) = \frac{1}{(2\pi)^{3/2}} \int_{-\infty}^{\infty} \int_{-\infty}^{\infty} \int_{-\infty}^{\infty} u_{x'}(x', y', z') e^{-i(\alpha x' + \beta y' + \gamma z')} dx' dy' dz',$$

$$\bar{u}_{y'}(\alpha, \beta, \gamma) = \frac{1}{(2\pi)^{3/2}} \int_{-\infty}^{\infty} \int_{-\infty}^{\infty} \int_{-\infty}^{\infty} u_{y'}(x', y', z') e^{-i(\alpha x' + \beta y' + \gamma z')} dx' dy' dz',$$

$$\bar{u}_{z'}(\alpha, \beta, \gamma) = \frac{1}{(2\pi)^{3/2}} \int_{-\infty}^{\infty} \int_{-\infty}^{\infty} \int_{-\infty}^{\infty} u_{z'}(x', y', z') e^{-i(\alpha x' + \beta y' + \gamma z')} dx' dy' dz'.$$

Substituting this and (53) into (52), we have the triple Fourier-type integrals

$$\begin{aligned}\rho\omega^2\bar{u}_{x'}^* &= c_1\alpha^2\bar{u}_{x'}^* + c_4\beta^2\bar{u}_{x'}^* + c_5\gamma^2\bar{u}_{x'}^* + (c_1 - c_4)\alpha\beta\bar{u}_{y'}^* + c_3\alpha\gamma\bar{u}_{z'}^*, \\ \rho\omega^2\bar{u}_{y'}^* &= (c_1 - c_4)\alpha\beta\bar{u}_{x'}^* + c_4\alpha^2\bar{u}_{y'}^* + c_1\beta^2\bar{u}_{y'}^* + c_5\gamma^2\bar{u}_{y'}^* + c_3\beta\gamma\bar{u}_{z'}^*, \\ \rho\omega^2\bar{u}_{z'}^* &= c_3\alpha\gamma\bar{u}_{x'}^* + c_3\beta\gamma\bar{u}_{y'}^* + c_5\alpha^2\bar{u}_{z'}^* + c_5\beta^2\bar{u}_{z'}^* + c_2\gamma^2\bar{u}_{z'}^*.\end{aligned}$$

Rearranging, we obtain

$$\begin{bmatrix} d_{11} - \rho\omega^2 & d_{12} & d_{13} \\ d_{21} & d_{22} - \rho\omega^2 & d_{23} \\ d_{31} & d_{32} & d_{33} - \rho\omega^2 \end{bmatrix} \begin{bmatrix} \bar{u}_{x'}^* \\ \bar{u}_{y'}^* \\ \bar{u}_{z'}^* \end{bmatrix} = \begin{bmatrix} 0 \\ 0 \\ 0 \end{bmatrix}, \quad (54)$$

where

$$[d_{ij}] = \begin{bmatrix} c_1\alpha^2 + c_4\beta^2 + c_5\gamma^2 & (c_1 - c_4)\alpha\beta & c_3\alpha\gamma \\ (c_1 - c_4)\alpha\beta & c_4\alpha^2 + c_1\beta^2 + c_5\gamma^2 & c_3\beta\gamma \\ c_3\alpha\gamma & c_3\beta\gamma & c_5\alpha^2 + c_5\beta^2 + c_2\gamma^2 \end{bmatrix}$$

Expanding the determinant of the matrix in (54) and substituting the expressions of the d_{ij} shows that the eigenvalues of the matrix $[d_{ij}]$ are

$$\rho\omega^2 = \begin{cases} c_5\gamma^2 + c_4(\alpha^2 + \beta^2), \\ \frac{1}{2}(c_1(\alpha^2 + \beta^2) + c_2\gamma^2 + c_5(\alpha^2 + \beta^2 + \gamma^2) + \Delta), \\ \frac{1}{2}(c_1(\alpha^2 + \beta^2) + c_2\gamma^2 + c_5(\alpha^2 + \beta^2 + \gamma^2) - \Delta), \end{cases}$$

where

$$\Delta = \sqrt{((c_1 - c_5)(\alpha^2 + \beta^2) - (c_2 - c_5)\gamma^2)^2 + 4c_3^2(\alpha^2 + \beta^2)\gamma^2}.$$

If we introduce spherical coordinates $(k, \theta_{x'}, \theta_{z'})$ in $\alpha\beta\gamma$ -space (so $\alpha = k \sin \theta_{z'} \cos \theta_{x'}$, $\beta = k \sin \theta_{z'} \sin \theta_{x'}$, $\gamma = k \cos \theta_{z'}$), we see that Δ can be expressed as

$$\Delta = \sqrt{((c_1 - c_5) \sin^2 \theta_{z'} - (c_2 - c_5) \cos^2 \theta_{z'})^2 + 4c_3^2 \sin^2 \theta_{z'} \cos^2 \theta_{z'}}.$$

Introducing the quantity $V^2 = \omega^2/k^2$, the square of the body-wave velocity, leads to a familiar appearance for the eigenvalues:

$$\begin{aligned}V_{\text{SH},\theta,z'} &= \sqrt{\frac{c_5 \cos^2 \theta_{z'} + c_4 \sin^2 \theta_{z'}}{\rho}}, \\ V_{\text{P},\theta,z'} &= \sqrt{\frac{c_1 \sin^2 \theta_{z'} + c_2 \cos^2 \theta_{z'} + c_5 + \Delta}{2\rho}}, \\ V_{\text{SV},\theta,z'} &= \sqrt{\frac{c_1 \sin^2 \theta_{z'} + c_2 \cos^2 \theta_{z'} + c_5 - \Delta}{2\rho}}.\end{aligned}$$

Note that $\theta_{z'}$ can be interpreted as the angle between the direction of wave travel and the z' -axis. The determinant of $[d_{ij}]$ is written as

$$\begin{aligned}
 D &= \det [d_{ij}] = \rho^3 k^6 (V_{SH,\theta,z'} V_{P,\theta,z'} V_{SV,\theta,z'})^2 \\
 &= (c_5 \gamma^2 + c_4 (\alpha^2 + \beta^2)) [(c_1 (\alpha^2 + \beta^2) + c_5 \gamma^2) (c_5 (\alpha^2 + \beta^2) + c_2 \gamma^2) - c_3^2 (\alpha^2 + \beta^2) \gamma^2] \\
 &= c_2 c_5^2 \prod_{i=1}^3 (A_i (\alpha^2 + \beta^2) + \gamma^2) = c_2 c_5^2 k^6 \prod_{i=1}^3 (A_i \sin^2 \theta_{z'} + \cos^2 \theta_{z'}),
 \end{aligned} \tag{55}$$

where A_1, A_2, A_3 are defined in (17).

As depicted in Figure 1, a new coordinate system x, y, z is obtained from the original system x', y', z' by rotating through an angle ϕ about the $x = x'$ axis. Then the value of D in (55) becomes

$$D = \rho^3 k^6 (V_{SH,\theta,t} V_{P,\theta,t} V_{SV,\theta,t})^2 = c_2 c_5^2 k^6 \prod_{i=1}^3 (A_i \sin^2 \theta_t + \cos^2 \theta_t), \tag{56}$$

where θ_t is the angle between the vector (α, β, γ) and the z' axis, which can be expressed in terms of α, β, γ , and ϕ as

$$\cos \theta_t = \frac{\gamma \cos \phi - \beta \sin \phi}{\sqrt{\alpha^2 + \beta^2 + \gamma^2}}, \tag{57}$$

that is,

$$\sin^2 \theta_t = \frac{\alpha^2 + \beta^2 + \gamma^2 - (\gamma \cos \phi - \beta \sin \phi)^2}{\alpha^2 + \beta^2 + \gamma^2}.$$

Hence, (56) can be rearranged as

$$\begin{aligned}
 D &= c_2 c_5^2 k^6 \prod_{i=1}^3 (A_i \sin^2 \theta_t + \cos^2 \theta_t) \\
 &= \frac{c_2 c_5^2 k^6}{(\alpha^2 + \beta^2 + \gamma^2)^3} \prod_{i=1}^3 \left(A_i (\alpha^2 + \beta^2 + \gamma^2 - (\gamma \cos \phi - \beta \sin \phi)^2) + (\gamma \cos \phi - \beta \sin \phi)^2 \right) \\
 &= c_2 c_5^2 \prod_{i=1}^3 \left(A_i (\alpha^2 + \beta^2 + \gamma^2 - (\gamma \cos \phi - \beta \sin \phi)^2) + (\gamma \cos \phi - \beta \sin \phi)^2 \right).
 \end{aligned}$$

If we further set $i\gamma = u$, this becomes

$$\begin{aligned}
 D &= \det [d_{ij}] \\
 &= c_2 c_5^2 \prod_{i=1}^3 \left(A_i (-u^2 + \alpha^2 + \beta^2 - (iu \cos \phi + \beta \sin \phi)^2) + (iu \cos \phi + \beta \sin \phi)^2 \right).
 \end{aligned}$$

The six eigenroots can be generated by setting $D = 0$ in this equation. They are given in (19).

References

[Amadei et al. 1987] B. Amadei, W. Z. Savage, and H. S. Swolfs, “Gravitational stresses in anisotropic rock masses”, *Int. J. Rock Mech. Min.* **24**:1 (1987), 5–14.

[Ding et al. 1997] H. J. Ding, J. Liang, and B. Chen, “The united point force solution for both isotropic and transversely isotropic media”, *Commun. Numer. Methods Eng.* **13**:2 (1997), 95–102.

- [Ding et al. 2006] H. J. Ding, W. Chen, and L. Zhang, *Elasticity of transversely isotropic materials*, Solid Mechanics and its Applications **126**, Springer, Dordrecht, 2006.
- [Fabrikant 2004] V. I. Fabrikant, “A new form of the Green function for a transversely isotropic body”, *Acta Mech.* **167**:1–2 (2004), 101–111.
- [Gerrard 1977] C. M. Gerrard, “Background to mathematical modeling in geomechanics: the roles of fabric and stress history”, pp. 33–120 in *Finite elements in geomechanics*, edited by G. Gudehus, Wiley, London, 1977.
- [Hanson 1999] M. T. Hanson, “Elastic fields for point and partial line loading in transversely isotropic linear elasticity”, *J. Elasticity* **55**:2 (1999), 143–162.
- [Hu et al. 2007] T.-B. Hu, C.-D. Wang, and J.-J. Liao, “Elastic solutions of displacements for a transversely isotropic full space with inclined planes of symmetry subjected to a point load”, *Int. J. Numer. Anal. Methods Geomech.* **31**:12 (2007), 1401–1442.
- [Liao and Wang 1998] J. J. Liao and C. D. Wang, “Elastic solutions for a transversely isotropic half-space subjected to a point load”, *Int. J. Numer. Anal. Methods Geomech.* **22**:6 (1998), 425–447.
- [Liew et al. 2001] K. M. Liew, J. Liang, H. J. Ding, and C. Lu, “Elastic fields in two-joined half-spaces subject to point force and uniform ring loads”, *Comput. Methods Appl. Mech. Eng.* **190**:29–30 (2001), 3749–3769.
- [Pan 2002] E. Pan, “Mindlin’s problem for an anisotropic piezoelectric half-space with general boundary conditions”, *Proc. R. Soc. Lond. A* **458**:2017 (2002), 181–208.
- [Pan and Tonon 2000] E. Pan and F. Tonon, “Three-dimensional Green’s functions in anisotropic piezoelectric solids”, *Int. J. Solids Struct.* **37**:6 (2000), 943–958.
- [Pan and Yuan 2000a] E. Pan and F. G. Yuan, “Three-dimensional Green’s functions in anisotropic bimetals”, *Int. J. Solids Struct.* **37**:38 (2000), 5329–5351.
- [Pan and Yuan 2000b] E. Pan and F. G. Yuan, “Three-dimensional Green’s functions in anisotropic piezoelectric bimetals”, *Int. J. Eng. Sci.* **38**:17 (2000), 1939–1960.
- [Tarn and Wang 1987] J. Q. Tarn and Y. M. Wang, “A fundamental solution for a transversely isotropic elastic space”, *J. Chin. Inst. Eng.* **10**:1 (1987), 13–21.
- [Tonon et al. 2001] F. Tonon, E. Pan, and B. Amadei, “Green’s functions and boundary element method formulation for 3D anisotropic media”, *Comput. Struct.* **79**:5 (2001), 469–482.
- [Wang and Liao 1999] C. D. Wang and J. J. Liao, “Elastic solutions for a transversely isotropic half-space subjected to buried asymmetric-loads”, *Int. J. Numer. Anal. Methods Geomech.* **23**:2 (1999), 115–139.

Received 23 Feb 2008. Accepted 1 Oct 2008.

JYH-JONG LIAO: jjliao@mail.nctu.edu.tw

Department of Civil Engineering, National Chiao Tung University, Hsin-Chu, Taiwan 30010, Taiwan

TIN-BIN HU: tbh.cv89g@nctu.edu.tw

Department of Civil Engineering, National Chiao Tung University, Hsin-Chu, Taiwan 30010, Taiwan

CHENG-DER WANG: cdwang@nuu.edu.tw

Department of Civil and Disaster Prevention Engineering, National United University, No. 1, Lien Da, Kung-Ching Li, Miao-Li, Taiwan 360, Taiwan

AN ANISOTROPIC HETEROGENEOUS BEAM WITH OVERSPECIFIED BOUNDARY CONDITIONS

C. KEVIN LYONS

In this paper a heterogeneous anisotropic cylindrical beam with a rigidly fixed base is considered as an alternative to the relaxed Saint-Venant's problem. The rigidly fixed base results in a problem with overspecified boundary conditions for which a proof of existence is given. The results of this paper indicate that the relaxed Saint-Venant's problem, for loads independent of the axial coordinate, ignores the dependence of the stress field on the axial coordinate. Dependence of the stress field on the axial coordinate could result in warping of transverse cross sections and nonzero in-plane stresses, which is significant for understanding the behavior of natural structures such as wood and mammalian bone.

1. Introduction

Two examples of natural structures that can be represented as heterogeneous anisotropic cylinders are the bole of a tree and long mammalian bones. [Bodig and Jayne \[1993\]](#) describe a cylindrical section of a tree as being an orthotropic material with cylindrical anisotropy, where the axes of symmetry are in the radial direction (\mathbf{e}_R), the tangential direction (\mathbf{e}_T), and the long direction (\mathbf{e}_L) which is directed up the tree. The same paper reports that the compressive strength of wood is weaker in the \mathbf{e}_R and \mathbf{e}_T directions than it is in the \mathbf{e}_L direction. [Barrett et al. \[1981\]](#) notes the fracture toughness of wood is an order of magnitude lower where normal stresses in the \mathbf{e}_R and \mathbf{e}_T directions can open the crack. [Kennedy and Carter \[1985\]](#) note that various material models have been used for long mammalian bones and these include isotropic, transversely isotropic, and cylindrically orthotropic. [Taylor et al. \[2002\]](#) used an orthotropic model to compare elastic constants for the human femur measured by ultrasound to those predicted through a finite element model. [Peterlik et al. \[2006\]](#) found the fracture toughness of bone is greater in the \mathbf{e}_R and \mathbf{e}_T directions than the \mathbf{e}_L direction. [Norman et al. \[1996\]](#) found in the \mathbf{e}_L direction that bone was an order of magnitude stronger in Mode 2 fracture as opposed to Mode 1 fracture, where tension in the \mathbf{e}_R and \mathbf{e}_T directions can open the crack.

[Iesan \[1987\]](#) describes Saint-Venant's problem as determining an equilibrium displacement field for a cylinder loaded by surface forces distributed over its plane ends, and the relaxed Saint-Venant's problem as replacing the distributed surface forces on one end with equivalent resultant loads. To consider a cantilever beam as a relaxed Saint-Venant's problem, the prescribed displacements on the base of the beam are replaced with a stress field that maintains equilibrium; however, this changes the problem from a mixed problem to a traction problem. In solving the relaxed Saint-Venant's problem various constants of integration are developed if the equilibrium displacement field is desired. [Sokolnikoff \[1956\]](#) and [Lyons et al. \[2002\]](#) found these constants of integration could be determined by reintroducing certain

Keywords: Anisotropic, heterogeneous, dynamic, cantilever beam.

This research was supported by the NSERC Discovery Grant 261644-03.

elements of the fixed boundary condition; however, these elements are on specific points or lines and in general the equilibrium displacement field is not able to satisfy the fixed boundary conditions over the complete base of the cylinder. When considering an anisotropic cylindrical cantilever beam as a relaxed Saint-Venant's problem, authors such as Lekhnitskii [1981], Iesan [1987], and Lyons [2002] found that the stresses are zero in the plane defined by \mathbf{e}_R and \mathbf{e}_T . An important question is whether this result is a function of posing the problem as a relaxed Saint-Venant's problem or whether it is a general result.

The fixed boundary conditions considered by Sokolnikoff [1956] and Lyons et al. [2002] include both prescribed displacements and prescribed first derivatives of the displacements at points on the base of the cylinder. Gao and Mura [1991] consider these types of boundary conditions to be overspecified and there is the risk that if they are selected arbitrarily then they could be inconsistent. There are additional conditions imposed on the displacement vector when considering elastodynamic problems and these can be used to better understand the implications of using overspecified boundary conditions.

This paper considers a cylinder that is rigidly fixed at the base and subject to a time dependent forcing function on the free end. The cylinder is composed of a material that is heterogeneous and anisotropic, with elastic coefficients that are independent of the axial coordinate. In this paper the objective of Section 3 is to confirm that the stresses and strains are identically equal to zero on the base of the cylinder when the base is rigidly fixed, the objective of Sections 4 and 5 is to prove the existence of a solution which will indicate the overspecified boundary conditions are consistent, and the objective of Section 6 is to compare specific attributes of the stress field found in this paper to the stress field found when posing the cylinder as a relaxed Saint-Venant's problem.

2. Problem statement

Consider a cylindrical cantilever beam with constant cross sections (Figure 1), where the displacement of the free end combined with the length of the beam is such that geometric nonlinear effects are not significant. Let the region B refer to the interior of the cylinder, ∂B is the boundary, and $\bar{B} = \partial B \cup B$. Let Σ_1 be the open cross section at $x_3 = 0$, let Σ_2 be the open cross section at $x_3 = h$. The lateral surface of the cylinder is Π . In the following Greek indices range from 1 to 2, while Latin indices range from 1

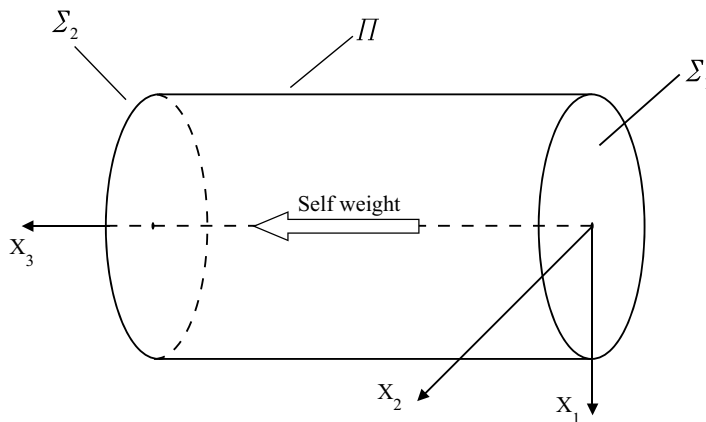


Figure 1. Cylindrical beam in Cartesian coordinates.

to 3. Summation notation is used for repeated indices and a comma followed by a subscript will indicate a partial derivative with respect to the subscript. In addition, the Kronecker delta function (δ_{ij}) will be used.

The beam considered in this paper will be rigidly fixed on Σ_2 . Eringen and Suhubi [1974] give the necessary condition for a body to be locally rigid $d_{ij}(\mathbf{x}, t) = \frac{1}{2}(v_i(\mathbf{x}, t)_{,j} + v_j(\mathbf{x}, t)_{,i}) = 0$. Here, d_{ij} is the rate of deformation tensor, and v_i is the velocity vector.

The boundary conditions for the problem considered in this paper are

$$\begin{aligned} \mathbf{u}(\Sigma_2, t) &= 0 && \text{on } \Sigma_2, \\ d_{ij}(\Sigma_2, t) &= 0 && \text{on } \Sigma_2, \\ \mathbf{s}(\Pi, t) &= 0 && \text{on } \Pi, \\ \mathbf{s}(\Sigma_1, t) &= \mathbf{k}(\Sigma_1)\Phi(t) && \text{on } \Sigma_1. \end{aligned} \tag{1}$$

Here $\mathbf{u}(\Sigma_2, t)$ is the prescribed displacement vector on Σ_2 , $s_i(\mathbf{x}, t) = S_{ij}(\mathbf{x}, t)n_j$, where n_j is the unit vector normal to the surface of interest and $S_{ij}(\mathbf{x}, t)$ is Cauchy’s stress tensor, $\mathbf{k}(\Sigma_1)$ is a vector that is a function of the coordinates on Σ_1 , and $\Phi(t)$ is a scalar function of time.

At $t = 0$ the beam is subject to body loads due to gravity alone. Therefore, the initial conditions are

$$\mathbf{u}(\mathbf{x}, 0) = -\mathbf{q}(\mathbf{x}) \text{ on } \bar{B} \quad \text{and} \quad \mathbf{u}(\mathbf{x}, 0)_{,t} = \zeta(\mathbf{x}) \text{ on } \bar{B}. \tag{2}$$

Here $-\mathbf{q}(\mathbf{x})$ is the displacement vector due to gravity alone, and $\zeta(\mathbf{x})$ is the initial velocity vector.

The constitutive equation is

$$S_{ij} = C_{ijkl}(x_\alpha)E_{kl}. \tag{3}$$

Here S_{ij} is Cauchy’s stress tensor, E_{ij} is the infinitesimal strain tensor, and C_{ijkl} is the elasticity tensor which is independent of the axial coordinate x_3 , symmetric, and positive definite.

The problem considered in this paper is one of linear elasticity, where nonlinear terms in the strain tensor, velocity vector, and acceleration vector are discarded as terms of higher order. In addition, when considering a spatial description of acceleration, the convective components are discarded as terms of higher order. Achenbach [1973] notes that once the problem is completely linearized the distinction between the material and spatial descriptions of motion vanish; therefore, either the notation for the material description or the spatial description can be used. Material coordinates are typically used in solid mechanics; however, in the problem considered by this paper the velocities are prescribed on Σ_2 and thus a spatial description can be useful. This paper uses a material description except for the derivation involving the continuity equation, and Equations (7)–(10); however, given the observations by Achenbach [1973] a new coordinate system is not introduced.

3. Considering stress and strain as x_3 approaches h

Theorem 3.1. Let $\mathbf{u}(\mathbf{x}, t) \in C^{1,2}(\bar{B}) \cap C^{2,2}(B)$. Given Equation (2) and the first two equations of (1), then, $\lim_{x_3 \rightarrow h} u_i(\mathbf{x}, t)_{,j} = 0$.

Proof. The boundary values of the field equations are defined as follows. Let \mathbf{x}_0 be some point on ∂B and let $\mathbf{u}(\mathbf{x}, t)$ tend to a definite limit as the point \mathbf{x} approaches \mathbf{x}_0 from B . Recall Greek indices range

from 1 to 2, while Latin indices range from 1 to 3. Given the first equation of (1), and that x_i and t are independent, then

$$\lim_{x_3 \rightarrow h} \mathbf{u}(\mathbf{x}, t),_{,\alpha} = 0, \tag{4}$$

$$\lim_{x_3 \rightarrow h} \mathbf{v}(\mathbf{x}, t) = 0, \tag{5}$$

$$\lim_{x_3 \rightarrow h} \mathbf{v}(\mathbf{x}, t),_{,\alpha} = 0. \tag{6}$$

Consider the density of the material in \bar{B} to be a function of position and time

$$\rho = \rho(\mathbf{x}, t). \tag{7}$$

The equation of continuity is

$$\frac{D\rho(\mathbf{x}, t)}{Dt} + \rho(\mathbf{x}, t)v_j(\mathbf{x}, t),_j = 0. \tag{8}$$

Expand the material derivative in (8), take the limit as x_3 approaches h , and take into account Equation (5), then

$$\lim_{x_3 \rightarrow h} \frac{D\rho(\mathbf{x}, t)}{Dt} = \lim_{x_3 \rightarrow h} \rho(\mathbf{x}, t),_t. \tag{9}$$

Take the limit of (8) as x_3 approaches h , take into account Equation (9) and the second equation of (1) with $i = j$, then

$$\lim_{x_3 \rightarrow h} \rho(\mathbf{x}, t),_t = 0. \tag{10}$$

Integrating (10) with respect to time it can be seen that the density of the material in B is independent of time as x_3 approaches h .

$$\lim_{x_3 \rightarrow h} \rho(\mathbf{x}, t) = \lim_{x_3 \rightarrow h} \rho(\mathbf{x}). \tag{11}$$

The density at time t is related to the reference density by

$$\rho(\mathbf{x}, t) = \frac{1}{J(\mathbf{x}, t)} \rho(\mathbf{x}, 0).$$

Here, $J(\mathbf{x}, t)$ is the Jacobian determinant, which represents the dilation of an infinitesimal volume at the material point \mathbf{x} . However, given (11)

$$\lim_{x_3 \rightarrow h} \rho(\mathbf{x}) = \lim_{x_3 \rightarrow h} \frac{1}{J(\mathbf{x}, t)} \rho(\mathbf{x}). \tag{12}$$

Recall for infinitesimal strains that

$$J(\mathbf{x}, t) = 1 + \text{div } \mathbf{u}(\mathbf{x}, t). \tag{13}$$

Substitute (13) into (12), then it can be seen that

$$\lim_{x_3 \rightarrow h} \text{div } \mathbf{u}(\mathbf{x}, t) = \lim_{x_3 \rightarrow h} u_j(\mathbf{x}, t),_j = 0. \tag{14}$$

Substitute (4) into (14) and take the derivative of this with time, then

$$\lim_{x_3 \rightarrow h} u_3(\mathbf{x}, t),_3 = 0 \quad \text{and} \quad \lim_{x_3 \rightarrow h} v_3(\mathbf{x}, t),_3 = 0. \tag{15}$$

Set $i = \alpha$ and $j = 3$ in the second equation of (1) and take into account Equation (6), then

$$\lim_{x_3 \rightarrow h} v_\alpha(\mathbf{x}, t)_{,3} = 0. \tag{16}$$

Integrate (16) with respect to time and take into account the first equation of Equation (2), then

$$\lim_{x_3 \rightarrow h} u_\alpha(\mathbf{x}, t)_{,3} = - \lim_{x_3 \rightarrow h} q_\alpha(\mathbf{x})_{,3}. \tag{17}$$

Equation (17) indicates the shear strains are independent of time as x_3 approaches h . This is an unlikely result given the time dependent forcing function being applied to Σ_1 . Therefore, as will be demonstrated in Section 4, the only nontrivial solution is to let $\lim_{x_3 \rightarrow h} q_\alpha(\mathbf{x})_{,3} = 0$, then

$$\lim_{x_3 \rightarrow h} u_\alpha(\mathbf{x}, t)_{,3} = 0. \tag{18}$$

Given equations (4)–(6), (15), (16), and (18) the velocities and the derivatives of the displacements and velocities with respect to the coordinates as x_3 approaches h can be summarized as follows

$$\lim_{x_3 \rightarrow h} u_i(\mathbf{x}, t)_{,j} = 0, \quad \lim_{x_3 \rightarrow h} v_i(\mathbf{x}, t) = 0, \quad \text{and} \quad \lim_{x_3 \rightarrow h} v_i(\mathbf{x}, t)_{,j} = 0. \tag{19}$$

Equation (19) completes the proof of Theorem 3.1. □

Consider the constitutive Equation (3), note the material coefficients are independent of x_3 , and take the limit as x_3 approaches h .

$$\lim_{x_3 \rightarrow h} S_{ij}(\mathbf{u}) = \frac{C_{ijkl}}{2} \left(\lim_{x_3 \rightarrow h} u_{k,l} + \lim_{x_3 \rightarrow h} u_{l,k} \right). \tag{20}$$

Substitute the first equation of (19) into (20), then

$$\lim_{x_3 \rightarrow h} S_{ij}(\mathbf{u}) = 0. \tag{21}$$

Note the results, Equation (19) and (21), follow from assuming infinitesimal strains; in general these results do not hold if finite strains are allowed.

4. Displacement functions

Theorem 4.1. Let $\Phi(t) = at$, for $0 \leq t < t_L$ where a is a constant and t_L is the time when the strains are no longer infinitesimal; given equations (1), (2), and (19), then $u_i(\mathbf{x}, t) = t\zeta_i(\mathbf{x}) - q_i(\mathbf{x})$ and $u_i(\mathbf{x}, t)_{,tt} = 0$.

Proof. The equation of motion in material description is

$$\rho_o(\mathbf{x})v_i(\mathbf{x}, t)_{,t} = S_{ij}(\mathbf{x}, t)_{,j} + \delta_{i3}\rho_o(\mathbf{x})g. \tag{22}$$

Let $\mathbf{U}(\mathbf{x}, t) \in C^{1,2}(\bar{B}) \cap C^{2,2}(B)$ and

$$\begin{aligned} U_i(\mathbf{x}, t) &= u_i(\mathbf{x}, t) + q_i(\mathbf{x}), \\ S_{ij}(\mathbf{q}(\mathbf{x}))_{,j} &= \delta_{i3}\rho_o g. \end{aligned} \tag{23}$$

Rearrange (23)

$$u_i(\mathbf{x}, t) = U_i(\mathbf{x}, t) - q_i(\mathbf{x}). \tag{24}$$

Substitute Equation (24) into the equations of motion, (22), then

$$\rho_o U_i(\mathbf{x}, t)_{,tt} = S_{ij}(\mathbf{x}, t)_{,j}. \tag{25}$$

Substitute (24) into the initial conditions, (2), then

$$U_i(\mathbf{x}, 0) = 0 \quad \text{and} \quad U_i(\mathbf{x}, 0)_{,t} = \zeta_i(\mathbf{x}) \tag{26}$$

Substitute (24) into the first equation of (1), the first equation of (19), and the third and fourth equations of (1).

$$U_i(\Sigma_2, t) = q_i(\Sigma_2), \tag{27}$$

$$U_i(\Sigma_2, t)_{,j} = q_i(\Sigma_2)_{,j}, \tag{28}$$

$$S_{ij}(\mathbf{U}(\Sigma_1, t))n_j^{(\Sigma_1)} = k_i(\Sigma_1)\Phi(t) + S_{ij}(\mathbf{q}(\Sigma_1))n_j^{(\Sigma_1)}, \tag{29}$$

$$S_{ij}(\mathbf{U}(\Pi, t))n_j^{(\Pi)} = S_{ij}(\mathbf{q}(\Pi))n_j^{(\Pi)}. \tag{30}$$

Let

$$U_i(\mathbf{x}, t) = X_i(\mathbf{x})T(t). \tag{31}$$

Here, $X_i(\mathbf{x})$ is a vector function of \mathbf{x} alone, and $T(t)$ is a scalar function of t alone.

Substitute Equation (31) into (25), then

$$\rho_o X_i(\mathbf{x})T(t)_{,tt} = S_{ij}(\mathbf{X}(\mathbf{x}))_{,j}T(t). \tag{32}$$

Separate the variables in (32), then

$$\frac{T(t)_{,tt}}{T(t)} = \frac{S_{ij}(\mathbf{X}(\mathbf{x}))_{,j}}{\rho_o X_i(\mathbf{x})} = b_i.$$

Here b_i are constant; however, $T(t)$ is independent of $X_i(\mathbf{x})$. Therefore, $b_1 = b_2 = b_3 = b$ and

$$T(t)_{,tt} - bT(t) = 0, \tag{33}$$

$$S_{ij}(\mathbf{X}(\mathbf{x}))_{,j} - b\rho_o X_i(\mathbf{x}) = 0. \tag{34}$$

Substitute (31) into the first equation of (26), then

$$X_i(\mathbf{x})T(0) = 0. \tag{35}$$

The only nontrivial solution to (35) is when

$$T(0) = 0. \tag{36}$$

Substitute Equation (31) into the second equation of (26), then

$$X_i(\mathbf{x})T(0)_{,t} = \zeta_i(\mathbf{x}). \tag{37}$$

The only nontrivial solution to (37) is when

$$T(0)_{,t} = c \quad \text{and} \quad X_i(\mathbf{x}) = c^{-1}\zeta_i(\mathbf{x}). \tag{38}$$

Here c is a constant.

Substitute (31) into (27), then

$$X_i(\Sigma_2)T(t) = q_i(\Sigma_2) \tag{39}$$

The only nontrivial solution to (39) is when

$$X_i(\Sigma_2) = q_i(\Sigma_2) = 0. \tag{40}$$

Substitute (31) into (28), then

$$X_i(\Sigma_2),_j T(t) = q_i(\Sigma_2),_j. \tag{41}$$

The only nontrivial solution to (41) is when

$$X_i(\Sigma_2),_j = q_i(\Sigma_2),_j = 0. \tag{42}$$

Substitute Equation (31) into (29), then

$$S_{ij}(\mathbf{X}(\Sigma_1))n_j^{(\Sigma_1)}T(t) = k_i(\Sigma_1)\Phi(t) + S_{ij}(\mathbf{q}(\Sigma_1))n_j^{(\Sigma_1)}. \tag{43}$$

Given (36) and (38) we have $T(t) = ct$; therefore, let $S_{ij}(\mathbf{q}(\Sigma_1))n_j^{(\Sigma_1)} = 0$ in (43) and isolate $T(t)$.

$$T(t) = \frac{k_i(\Sigma_1)\Phi(t)}{S_{ij}(\mathbf{X}(\Sigma_1))n_j^{(\Sigma_1)}}, \quad \text{no sum over } i. \tag{44}$$

By definition $T(t)$ is a scalar function, while the right hand side of (44) is vector valued; therefore, let

$$k_i(\Sigma_1) = S_{ij}(\mathbf{X}(\Sigma_1))n_j^{(\Sigma_1)}. \tag{45}$$

Note, from the definition in 4.1 we have $\Phi(t) = at$; therefore, given (44) and (45)

$$T(t) = at. \tag{46}$$

Substitute (31) into (30), then

$$S_{ij}(\mathbf{X}(\Pi))n_j^{(\Pi)}T(t) = S_{ij}(\mathbf{q}(\Pi))n_j^{(\Pi)}. \tag{47}$$

The only nontrivial solution to (47) is

$$S_{ij}(\mathbf{X}(\Pi))n_j^{(\Pi)} = S_{ij}(\mathbf{q}(\Pi))n_j^{(\Pi)} = 0. \tag{48}$$

Equations (33), (36), and (38) form an initial value problem that can be solved for three cases of b .

CASE 1. Let $b = 0$, then (33) becomes

$$T(t),_{tt} = 0. \tag{49}$$

Integrating (49) twice with respect to time, and taking into account Equation (36) and (38), it can be seen that

$$T(t) = ct. \tag{50}$$

Taking Equation (46) into account, (50) becomes $T(t) = at$. **CASE 2.** Let $b > 0$, and let $b = \lambda^2$, where $\lambda > 0$. Then (33) becomes

$$T(t),_{tt} - \lambda^2 T(t) = 0. \tag{51}$$

Let $T(t) = e^{rt}$, then (51) becomes

$$r^2 - \lambda^2 = 0. \tag{52}$$

Factoring (52) it can be seen that $r = \pm\lambda$, therefore, there are two solutions for $T(t)$.

$$T(t) = c_1 e^{\lambda t} + c_2 e^{-\lambda t}. \tag{53}$$

Considering (36) and (38) it can be seen that $c_1 = -c_2$ and $c_1 = c/2\lambda$; therefore, (53) becomes

$$T(t) = \frac{c}{\lambda} \sinh(\lambda t). \tag{54}$$

Considering (54) and (46) it can be seen for $a \neq 0$ and $t > 0$ there are no solutions for $T(t)$ when $b > 0$.

CASE 3. Let $b < 0$, and let $b = -\lambda^2$, where $\lambda > 0$. Then (33) becomes

$$T(t)_{,tt} + \lambda^2 T(t) = 0. \tag{55}$$

Let $T(t) = e^{rt}$, then (55) becomes

$$r^2 + \lambda^2 = 0. \tag{56}$$

Factoring (56) it can be seen that $r = \pm i\lambda$; therefore, there are two solutions for $T(t)$

$$T(t) = c_1 \cos(\lambda t) + c_2 \sin(\lambda t). \tag{57}$$

Considering (36) and (38), it can be seen that $c_1 = 0$ and $c_2 = c/\lambda$; therefore, (57) becomes

$$T(t) = \frac{c}{\lambda} \sin(\lambda t). \tag{58}$$

Considering (58) and (46) it can be seen for $a \neq 0$ and $t > 0$ there are no solutions for $T(t)$ when $b < 0$.

Combining the solutions for $T(t)$ from the three cases of b results in

$$T(t) = at. \tag{59}$$

Equations (34), (40), (42), (45), and (48) form a boundary value problem defining $\mathbf{X}(\mathbf{x})$ that can be solved for three cases of b . From the analysis of $T(t)$ it was found that $b = 0$; therefore, the equilibrium problem that defines $\mathbf{X}(\mathbf{x})$ is

$$\begin{aligned} S_{ij}(\mathbf{X}(\mathbf{x}))_{,j} &= 0, \\ X_i(\Sigma_2) &= 0, \\ X_i(\Sigma_2)_{,j} &= 0, \\ S_{ij}(\mathbf{X}(\Sigma_1))n_j^{(\Sigma_1)} &= k_i(\Sigma_1), \\ S_{ij}(\mathbf{X}(\Pi))n_j^{(\Pi)} &= 0. \end{aligned} \tag{60}$$

Substitute Equation (59) into the first equation of (38), then from the second equation of (38)

$$X_i(\mathbf{x}) = a^{-1}\zeta_i(\mathbf{x}). \tag{61}$$

Substitute (61) and (59) into (31), and the resulting function into (24), then

$$u_i(\mathbf{x}, t) = t\zeta_i(\mathbf{x}) - q_i(\mathbf{x}) \quad \text{and} \quad u_i(\mathbf{x}, t)_{,tt} = 0 \tag{62}$$

Equation (62) completes the proof of Theorem 4.1. □

5. Nonexistence

Ericksen [1963] gives the main result of nonexistence theorems as nonuniqueness implies nonexistence. Ericksen [1965] notes that it is tacitly hoped in elastostatics that problems are well posed when uniqueness is obtained; however, this is a weak result since it leaves open the possibility of problems where existence fails even though uniqueness is proven. Therefore, nonuniqueness is used in this section as one possible test to determine if solutions to the problem defined by Equation (60) are nonexistent.

Gurtin [1972] presents a nonexistence theorem for the mixed problem of elastostatics where the elasticity tensor is symmetric. The difference between the elastostatics problem defined by (60) and the one considered by Gurtin [1972] is that the third equation of (60) prescribes the strains on Σ_2 and this could affect the method used to form the null data problem. Let $[\mathbf{w}, \mathbf{E}, \mathbf{S}]$ be the difference between two solutions to (60) that are not equal modulo a rigid displacement, where \mathbf{w} is the difference between displacements, \mathbf{E} is the difference between strains, and \mathbf{S} is the difference between stresses. Note, since $\mathbf{E} \neq \mathbf{0}$ in B then $w_i(x)_{,j} \neq 0$ in B . Recall from the proof of Theorem 3.1 that $\lim_{x_3 \rightarrow h} u_i(\mathbf{x}, t)_{,j} = 0$ is solely dependent on the Σ_2 boundary conditions, and this result produced the third equation of (60). Therefore, even though $w_i(x)_{,j} \neq 0$ in B it must still vanish as interior points approach Σ_2 . Thus,

$$w_i(\mathbf{x}) = w_i(\mathbf{x})_{,j} = 0 \text{ on } \Sigma_2, \quad \text{and} \quad s_i(\mathbf{x}) = S_{ij}(\mathbf{w}(\mathbf{x}))n_j = 0 \text{ on } \Sigma_1 \cup \Pi. \tag{63}$$

Equation (63) corresponds to a nontrivial solution of (60) with null data. Thus, Gurtin’s [1972] nonexistence theorem for mixed problems applies to the problem defined by (60), and the task at hand is to determine if (60) has a unique solution in which case nonexistence of a solution is not proven.

The following proof of uniqueness follows Gurtin’s [1981] theorem for elastostatics. Consider the problem defined by (60) and note that \mathbf{C} is positive definite. Let $[\mathbf{X}_1, \mathbf{E}_1, \mathbf{S}_1]$ and $[\mathbf{X}_2, \mathbf{E}_2, \mathbf{S}_2]$ be two solutions to (60), where

$$\mathbf{w}(\mathbf{x}) = \mathbf{X}_1(\mathbf{x}) - \mathbf{X}_2(\mathbf{x}) \quad \text{and} \quad \mathbf{E}(\mathbf{x}) = \mathbf{E}_1(\mathbf{X}_1(\mathbf{x})) - \mathbf{E}_2(\mathbf{X}_2(\mathbf{x})) \tag{64}$$

Here $[\mathbf{w}, \mathbf{E}, \mathbf{S}]$ is an elastic state that satisfies the boundary conditions $\mathbf{w}(\mathbf{x}) = 0$ on Σ_2 and $\mathbf{S}(\mathbf{x})\mathbf{n} = 0$ on $\Sigma_1 \cup \Pi$; therefore,

$$\mathbf{S}(\mathbf{x})\mathbf{n} \cdot \mathbf{w}(\mathbf{x}) = 0 \quad \text{on } \partial B. \tag{65}$$

Substituting (65) into the Theorem of Work and Energy as presented by Gurtin [1981] and noting that the body forces are zero in (60) results in

$$\int_B \mathbf{E} \cdot \mathbf{C}[\mathbf{E}] dV = 0. \tag{66}$$

Since \mathbf{C} is positive definite, (66) can only be true if $\mathbf{E}(\mathbf{x}) = 0$, which results in $\mathbf{S}(\mathbf{x}) = 0$. Therefore, given (64) the solution to (60) is unique up to a rigid displacement.

Let $\mathbf{w}(\mathbf{x}) = \alpha + \eta \times \mathbf{x}$. Here α and η are constant vectors. Given (63) α and η must be identically equal to zero; therefore, the solution to (60) is unique. Thus, the Nonexistence Theorem proposed by Gurtin [1972] is unable to detect the nonexistence of a solution to Equation (60).

6. Remarks on the relaxed Saint-Venant's problem

Iesan [1987] found the following stress function that satisfies the equilibrium problem for Extension, Bending, and Torsion posed as a relaxed Saint-Venant's problem for a material defined by Equation (3).

$$S_{ij}(\Lambda) = C_{ij33}(a_\rho x_\rho + a_3) - a_4 C_{ij\alpha 3} e_{\alpha\beta} x_\beta + T_{ij}(x_\alpha). \quad (67)$$

Here Λ is an infinitesimal equilibrium displacement field, a_q are constants with q ranging from 1 to 4, T_{ij} are the generalized plane stresses that are independent of x_3 , and $e_{\alpha\beta}$ is the two-dimensional alternator symbol. When considering the problem corresponding to (67), Chiriță [1979] and Lyons [2002] found for certain forms of the elasticity tensor that $S_{\alpha\beta}(\Lambda) = 0$ throughout \bar{B} .

Given the third equation of (60) and (3)

$$\lim_{x_3 \rightarrow h} S_{ij}(\mathbf{X}) = 0. \quad (68)$$

Iesan [1987] notes the justification for the relaxed Saint-Venant's problem is based on Saint-Venant's principle, which assumes the effects of posing the problem as a relaxed Saint-Venant's problem are negligible except possibly near the ends of the cylinder. Note in Equation (67) that S_{ij} are independent of x_3 throughout \bar{B} ; however, for Equation (68) to hold and for the stresses to be nonzero in some region of \bar{B} there must be a x_3 dependence. Dependence of the field equations on x_3 indicates warping of the transverse cross sections with the possible result that $S_{\alpha\beta} \neq 0$ throughout \bar{B} . This is an important consideration for anisotropic materials such as trees and bone that are significantly weaker in the x_α directions.

References

- [Achenbach 1973] J. D. Achenbach, *Wave propagation in elastic solids*, Applied Mathematics and Mechanics **16**, North-Holland, Amsterdam, 1973.
- [Barrett et al. 1981] J. D. Barrett, I. P. Haigh, and J. M. Lovegrove, "Fracture mechanics and the design of wood structures", *Philos. Tr. R. Soc. S. A* **299**:1446 (1981), 217–226.
- [Bodig and Jayne 1993] J. Bodig and B. A. Jayne, *Mechanics of wood and wood composites*, Krieger, Malabar, FL, 1993.
- [Chiriță 1979] S. Chiriță, "Saint-Venant's problem for anisotropic circular cylinders", *Acta Mech.* **34**:3–4 (1979), 243–250.
- [Ericksen 1963] J. L. Ericksen, "Non-existence theorems in linear elasticity theory", *Arch. Ration. Mech. An.* **14**:1 (1963), 180–183.
- [Ericksen 1965] J. L. Ericksen, "Nonexistence theorems in linearized elastostatics", *J. Differential Equations* **1**:4 (1965), 446–451.
- [Eringen and Suhubi 1974] A. C. Eringen and E. S. Suhubi, *Elastodynamics, I: Finite motions*, Academic Press, New York, 1974.
- [Gao and Mura 1991] Z. Gao and T. Mura, "Elasticity problems with partially overspecified boundary conditions", *Int. J. Eng. Sci.* **29**:6 (1991), 685–692.
- [Gurtin 1972] M. E. Gurtin, "The linear theory of elasticity", pp. 1–295 in *Mechanics of solids*, edited by C. A. Truesdell, *Handbuch der Physik* **VIa/2**, Springer, Berlin, 1972.
- [Gurtin 1981] M. E. Gurtin, *An introduction to continuum mechanics*, vol. 158, Mathematics in Science and Engineering, Academic Press, New York, 1981.
- [Iesan 1987] D. Iesan, *Saint-Venant's problem*, vol. 1279, Lecture Notes in Mathematics, Springer, New York, 1987.
- [Kennedy and Carter 1985] J. G. Kennedy and D. R. Carter, "Long bone torsion, I: Effects of heterogeneity, anisotropy and geometry", *J. Biomech. Eng. (ASME)* **107** (1985), 183–191.

- [Lekhnitskii 1981] S. G. Lekhnitskii, *Theory of elasticity of an anisotropic body*, Mir, Moscow, 1981.
- [Lyons 2002] C. K. Lyons, “[Stress functions for a heterogeneous section of a tree](#)”, *Int. J. Solids Struct.* **39**:18 (2002), 4615–4625.
- [Lyons et al. 2002] C. K. Lyons, R. B. Guenther, and M. R. Pyles, “[Elastic equations for a cylindrical section of a tree](#)”, *Int. J. Solids Struct.* **39**:18 (2002), 4773–4786.
- [Norman et al. 1996] T. L. Norman, S. V. Nivargikar, and D. B. Burr, “[Resistance to crack growth in human cortical bone is greater in shear than in tension](#)”, *J. Biomech.* **29**:8 (1996), 1023–1031.
- [Peterlik et al. 2006] H. Peterlik, P. Roschger, K. Klaushofer, and P. Fratzl, “[Orientation dependent fracture toughness of lamellar bone](#)”, *Int. J. Fract.* **139**:3–4 (2006), 395–405.
- [Sokolnikoff 1956] I. S. Sokolnikoff, *Mathematical theory of elasticity*, McGraw-Hill, New York, 1956.
- [Taylor et al. 2002] W. R. Taylor, E. Roland, H. Ploeg, D. Hertig, R. Klabunde, M. D. Warner, M. C. Hobatho, L. Rakotomanana, and S. E. Clift, “[Determination of orthotropic bone elastic constants using FEA and modal analysis](#)”, *J. Biomech.* **35**:6 (2002), 767–773.

Received 5 Mar 2008. Revised 2 Aug 2008. Accepted 11 Aug 2008.

C. KEVIN LYONS: kevlyons@interchange.ubc.ca

Faculty of Forestry, University of British Columbia, Department of Forest Resources Management, Forest Sciences Centre, Vancouver B.C. V6T 1Z4, Canada

THERMOELASTIC STABILITY ANALYSIS OF IMPERFECT FUNCTIONALLY GRADED CYLINDRICAL SHELLS

BABAK MIRZAVAND AND M. REZA ESLAMI

Elastic buckling analysis of imperfect FGM cylindrical shells under axial compression in thermal environments is carried out, using two different models for geometrical imperfections. The material properties of the functionally graded shell are assumed to vary continuously through the thickness of the shell according to a power law distribution of the volume fraction of the constituent materials, also temperature dependency of the material properties is considered. Derivation of equations is based on classical shell theory using the Sanders nonlinear kinematic relations. The stability and compatibility equations for the imperfect FGM cylindrical shell are obtained, and the buckling analysis of shell is carried out using Galerkin's method. The novelty of the present work is to obtain closed form solutions for critical buckling loads of the imperfect FGM cylindrical shells, which may be easily used in engineering design applications. The effects of shell geometry, volume fraction exponent, magnitude of initial imperfections, and environment temperature on the buckling load are investigated. The results reveal that initial geometrical imperfections and temperature dependency of the material properties play major roles in dictating the bifurcation point of the functionally graded cylindrical shells under the action of axial compressive loads. Also results show that for a particular value of environment temperature, critical buckling load is almost independent of volume fraction exponent.

1. Introduction

An early attempt to establish occasional discrepancies between the theoretical and experimental buckling loads of cylindrical shells was reported in [Donnell 1934]. Later it was determined that the initial imperfections and the boundary conditions are the principal cause of disagreement. A well known buckling analysis of initially imperfect cylindrical shells is presented in [Donnell and Wan 1950; Donnell 1956]. The analysis is based on the equilibrium path of an imperfect cylindrical shell. Donnell's theory was later extended and applied to buckling problems by other researchers.

Recent studies on new performance materials have addressed new materials known as the functionally graded materials (FGMs). These are high-performance heat resistant materials able to withstand ultra high temperatures and minimize thermal stresses. The stabilization of a functionally graded cylindrical shell under axial harmonic loading is investigated in [Ng et al. 2001]. Shen [2002; 2003] (see also [Shen and Noda 2005]) presented the mechanical postbuckling of FGM cylindrical shells with temperature dependent properties in thermal environments under compressive axial loads and external pressure using a singular perturbation technique. The results reveal that the characteristics of postbuckling are significantly influenced by temperature rise and initial geometric imperfections. Shen [2004] also studied the thermal postbuckling of imperfect functionally graded cylindrical shells. Dynamic buckling of

Keywords: buckling, geometrical imperfection, FGM, cylindrical shell.

functionally graded cylindrical thin shells under non-periodic impulsive loading is studied by [Sofiyev 2003]. [Shahsiah and Eslami 2003a; Shahsiah and Eslami 2003b] investigated the thermal buckling of functionally graded cylindrical shells under several types of loadings based on the Donnell and improved Donnell equations. [Woo et al. 2003; Woo et al. 2005] presented thermomechanical postbuckling analysis of functionally graded plates and shallow cylindrical shells based on the classical and higher order shell theories. [Mirzavand et al. 2005; Mirzavand and Eslami 2006] studied the thermal buckling of imperfect FGM cylindrical shells, under several types of loadings based on the Koiter and Wan–Donnell geometrical imperfection models. Also buckling and free vibration analysis of functionally graded cylindrical shells subjected to a temperature-specified boundary condition is investigated by [Kadoli and Ganesan 2006].

The present article develops the buckling analysis of imperfect functionally graded cylindrical shells under axial compression in thermal environments, using two different models for the geometrical imperfections; namely, the Koiter and Wan–Donnell Models. The cylindrical shell is graded according to a power law form through the thickness direction. The boundary conditions are assumed to be simply supported. The stability and compatibility equations for the imperfect FGM cylindrical shell are obtained, and the buckling analysis of the shell is carried out, using the Galerkin method, leading to the closed form solutions.

2. Fundamental equations

Consider a thin circular cylindrical shell of mean radius R and thickness h with length L made of functionally graded material. The shell is simply supported at its ends and subjected to a uniformly distributed axial compressive load P combined with thermal loading in the form of uniform temperature rise. The normal and shear strains at distance z from the shell middle surface are

$$\bar{\varepsilon}_x = \varepsilon_x + z\kappa_x, \quad \bar{\varepsilon}_\theta = \varepsilon_\theta + z\kappa_\theta, \quad \bar{\gamma}_{x\theta} = \gamma_{x\theta} + 2z\kappa_{x\theta}. \quad (1)$$

The middle-surface kinematic relations are

$$\varepsilon_x = u_{,x} + \frac{1}{2}\beta_x^2, \quad \varepsilon_\theta = \frac{w + v_{,\theta}}{R} + \frac{1}{2}\beta_\theta^2, \quad \gamma_{x\theta} = \frac{u_{,\theta}}{R} + v_{,x} + \beta_x\beta_\theta, \quad (2)$$

where u , v , w are the displacement components at points on the shell middle surface, and ε_x , ε_θ and $\gamma_{x\theta}$ are the middle surface normal and shear strains, respectively. The indices x and θ refer to the axial and circumferential directions, respectively. The rotations are

$$\beta_x = -w_{,x}, \quad \beta_\theta = -\frac{w_{,\theta}}{R} \quad (3)$$

and the curvature components are

$$\kappa_x = \beta_{x,x}, \quad \kappa_\theta = \frac{\beta_{\theta,\theta}}{R}, \quad \kappa_{x\theta} = \frac{1}{2}\left(\frac{\beta_{x,\theta}}{R} + \beta_{\theta,x}\right). \quad (4)$$

The variation of Young's modulus and of the coefficient of thermal expansion of the functionally graded material are given by

$$E(z) = E_m + (E_c - E_m)\left(\frac{2z+h}{2h}\right)^\zeta, \quad \alpha(z) = \alpha_m + (\alpha_c - \alpha_m)\left(\frac{2z+h}{2h}\right)^\zeta, \quad (5)$$

(see [Praveen and Reddy 1998]) where the subscripts m and c refer to the metal and ceramic constituents, and ζ is the volume fraction exponent which takes values greater than or equal to zero. The Poisson's ratio ν is considered to be constant across the thickness.

The force and moment resultants are [Mirzavand and Eslami 2006]

$$\begin{aligned} N_x &= C(\varepsilon_x + \nu\varepsilon_\theta) + B(k_x + \nu k_\theta) - T_0, & N_\theta &= C(\varepsilon_\theta + \nu\varepsilon_x) + B(k_\theta + \nu k_x) - T_0, \\ M_x &= B(\varepsilon_x + \nu\varepsilon_\theta) + D(k_x + \nu k_\theta) - T_1, & M_\theta &= B(\varepsilon_\theta + \nu\varepsilon_x) + D(k_\theta + \nu k_x) - T_1, \end{aligned} \tag{6}$$

$$\begin{aligned} N_{x\theta} &= \frac{1}{2}C(1 - \nu)\gamma_{x\theta} + B(1 - \nu)k_{x\theta}, \\ M_{x\theta} &= \frac{1}{2}B(1 - \nu)\gamma_{x\theta} + D(1 - \nu)k_{x\theta}, \end{aligned} \tag{7}$$

where

$$\begin{aligned} C &= \frac{h}{1 - \nu^2} \left(E_m + \frac{E_{cm}}{\zeta + 1} \right), & B &= \frac{h^2 E_{cm}}{2(1 - \nu^2)} \left(\frac{\zeta}{\zeta^2 + 3\zeta + 2} \right), & D &= \frac{h^3}{4(1 - \nu^2)} \left(\frac{E_m}{3} + \frac{E_{cm}(\zeta^2 + \zeta + 2)}{\zeta^3 + 6\zeta^2 + 11\zeta + 6} \right), \\ T_0 &= \frac{\Delta T h}{1 - \nu} \left(E_m \alpha_m + \frac{E_m \alpha_{cm} + E_{cm} \alpha_m}{\zeta + 1} + \frac{E_{cm} \alpha_{cm}}{2\zeta + 1} \right), & T_1 &= \frac{1}{1 - \nu} \int_{-h/2}^{+h/2} E \alpha \Delta T z \, dz. \end{aligned} \tag{8}$$

Here ΔT is temperature rise from some reference temperature at which there are no thermal stresses.

The equilibrium equations of a perfect FGM cylindrical shell may be derived on the basis of the stationary potential energy criterion, and are given by [Mirzavand and Eslami 2006]

$$\begin{aligned} RN_{x,x} + N_{x\theta,\theta} &= 0, & N_{\theta,\theta} + RN_{x\theta,x} &= 0, \\ \left(D - \frac{B^2}{C} \right) \nabla^4 w + \frac{1}{R} N_\theta - \left(N_x w_{,xx} + \frac{2}{R} N_{x\theta} w_{,x\theta} + \frac{1}{R^2} N_\theta w_{,\theta\theta} \right) &= 0 \end{aligned} \tag{9}$$

3. Analysis

Here the buckling analysis is presented for two common types of axisymmetric imperfections. According to the Koiter model, the axisymmetric geometrical imperfection of cylindrical shell is expressed as [Brush and Almroth 1975]

$$w^* = -\mu h \cos\left(\frac{m\pi x}{L}\right), \quad -\frac{L}{2} \geq x \geq +\frac{L}{2}, \tag{10}$$

where m is the number of half wave in x -direction, and μh represents the amplitude of imperfection of the middle surface of the shell ($0 \leq \mu \leq 1$).

Donnell divides the initial imperfections into two combined components. Based on the experience with buckling problems, only that component which has the same shape as the deflection of the shell under load, which is w , can be taken into consideration [Donnell and Wan 1950; Donnell 1956]. Accordingly, the Wan–Donnell model for the axisymmetric radial imperfection is

$$w^* = \left(\frac{k - 1}{2} \right) w, \tag{11}$$

where the coefficient k is the imperfection parameter, which is a constant number equal or greater than 1. The magnitude of k depends on the material properties and manufacturing process of the cylindrical shell. The value of $k = 1$ represents a perfect shell.

The unloaded shell in the imperfection form, including w^* , is assumed to be stress free. The small angle of rotation $w_{,x}$ in the equations for an initially perfect cylinder is replaced by $(w + w^*)_{,x}$. The form of the equations can be simplified substantially by introducing a circumferential coordinate $y = R\theta$. Using Equations (2) and (3) and by introducing the coordinate y , the net strains for the imperfect cylindrical shell now become

$$\varepsilon_x = u_{,x} + \frac{1}{2}w_{,x}^2 + w_{,x}^*w_{,x}, \quad \varepsilon_y = v_{,y} + \frac{w}{R} + \frac{1}{2}w_{,y}^2, \quad \gamma_{xy} = u_{,y} + v_{,x} + (w + w^*)_{,x}w_{,y}. \quad (12)$$

Similarly, Equations (9) for an initially imperfect cylindrical shell are replaced by

$$N_{x,x} + N_{xy,y} = 0, \quad N_{xy,x} + N_{y,y} = 0, \quad \left(D - \frac{B^2}{C}\right)\nabla^4 w + \frac{1}{R}N_y - (N_x(w + w^*)_{,xx} + 2N_{xy}w_{,xy} + N_yw_{,yy}) = 0. \quad (13)$$

The stability equations of FGM cylindrical shell may be obtained by the application of the minimum potential energy criterion, and are [Mirzavand and Eslami 2006]

$$N_{x1,x} + N_{xy1,y} = 0, \quad N_{xy1,x} + N_{y1,y} = 0, \quad \left(D - \frac{B^2}{C}\right)\nabla^4 w_1 + \frac{N_{y1}}{R} - \left(N_{x1}(w_0 + w^*)_{,xx} + 2N_{xy1}w_{0,xy} + N_{y1}w_{0,yy} + N_{x0}w_{1,xx} + N_{y0}w_{1,yy} + 2N_{xy0}w_{1,xy}\right) = 0, \quad (14)$$

where u_0, v_0, w_0 are related to the equilibrium configuration, and u_1, v_1, w_1 are arbitrary small neighboring increments, and N_{ij1} represent the force resultants related to the neighboring state. Introducing the Airy stress function Φ as

$$N_{x1} = \Phi_{,yy}, \quad N_{y1} = \Phi_{,xx}, \quad N_{xy1} = -\Phi_{,xy} \quad (15)$$

the first and second stability equations are automatically satisfied and the third stability equation reduces to

$$\left(D - \frac{B^2}{C}\right)\nabla^4 w_1 + \frac{\Phi_{,xx}}{R} - \left(\Phi_{,yy}(w_0 + w^*)_{,xx} - 2\Phi_{,xy}w_{0,xy} + \Phi_{,xx}w_{0,yy} + N_{x0}w_{1,xx} + N_{y0}w_{1,yy} + 2N_{xy0}w_{1,xy}\right) = 0. \quad (16)$$

The compatibility equation in terms of the Airy stress function and the lateral displacement component w_1 is [Mirzavand and Eslami 2006]

$$\nabla^4 \Phi - C(1 - \nu^2)\left(\frac{w_{1,xx}}{R} - (w_0 + w^*)_{,xx}w_{1,yy} + 2w_{0,xy}w_{1,xy} - w_{1,xx}w_{0,y}\right) = 0. \quad (17)$$

3.1. Koitr imperfection model. Equations (16) and (17) are a set of linear equations in terms of the variable prebuckling coefficients N_{ij0}, w_0 , and the radial geometric imperfection w^* . The prebuckling coefficients must be known to be able to obtain the buckling load. Consider an imperfect cylindrical shell made of functionally graded material with simply supported edge conditions and subjected to axial compression load P . For the axisymmetric configuration on the primary path, $u_0 = u_0(x), v_0 \equiv 0, w_0 = w_0(x)$ [Brush and Almroth 1975]. For the axisymmetric loading, $N_{xy0} = 0$ and from the first equilibrium equation, however, N_{xx0} is seen to be independent of x . Considering the boundary conditions at the cylinder

ends, where the axial load P is uniformly distributed around the circumference, the axial prebuckling force resultant is

$$N_{x0} = -\frac{P}{2\pi R} - T_0 = -\sigma h - T_0. \tag{18}$$

Using Equation (18) and the equilibrium equations, the other prebuckling coefficients are found to be

$$N_{y0} = C(1 - \nu^2)\frac{w_0}{R} - \nu\sigma h - T_0, \tag{19}$$

$$w_0 = \frac{\nu R(\sigma h + T_0)}{C(1 - \nu^2)} + q \cos \frac{m\pi x}{L}, \tag{20}$$

where

$$q = -\mu h \frac{(\sigma h + T_0)\left(\frac{m\pi}{L}\right)^2}{\left(D - \frac{B^2}{C}\right)\left(\frac{m\pi}{L}\right)^4 - \sigma h\left(\frac{m\pi}{L}\right)^2 + \frac{C(1-\nu^2)}{R^2}}. \tag{21}$$

Introducing the prebuckling coefficients from the above equations into (16) and (17), we obtain the coupled linear equations of stability and compatibility as

$$\begin{aligned} \left(D - \frac{B^2}{C}\right)\nabla^4 w_1 + \frac{\Phi_{,xx}}{R} + \left((\sigma h + T_0)w_{1,xx} - \frac{C(1 - \nu^2)q}{R} \cos \frac{m\pi x}{L} w_{1,yy} - \Phi_{,yy}(\mu h - q)\left(\frac{m\pi}{L}\right)^2 \cos \frac{m\pi x}{L}\right) &= 0, \\ \nabla^4 \Phi - C(1 - \nu^2)\left(\frac{w_{1,xx}}{R} - w_{1,yy}(\mu h - q)\left(\frac{m\pi}{L}\right)^2 \cos \frac{m\pi x}{L}\right) &= 0. \end{aligned} \tag{22}$$

To solve this system of equations, with the consideration of the simply supported boundary conditions, the approximate solutions may be considered as

$$\begin{aligned} w_1 = \alpha_{mn} \cos \frac{m\pi x}{L} \cos \frac{ny}{R}, \quad \Phi = \beta_{mn} \cos \frac{m\pi x}{L} \cos \frac{ny}{R}, \\ + \frac{L}{2} \geq x \geq -\frac{L}{2}, \quad 2\pi R \geq y \geq 0, \quad m, n = 1, 2, \dots, \end{aligned} \tag{23}$$

where m and n are the number of half waves in x and y -directions, respectively, and α_{mn} and β_{mn} are constant coefficients that depend on m and n . Substituting the approximate solutions (23) into Equations (22) gives the residues R_1 and R_2 . Following Galerkin’s method, R_1 and R_2 are made orthogonal with respect to the approximate solutions (23), and then the determinant of the obtained system of equations for the coefficients α_{mn} and β_{mn} is set to zero. For even values of m the determinant of coefficients has no result, but for $m = 4k \pm 1$ (odd values of m) yields

$$s_1(\sigma h + T_0)^3 + s_2(\sigma h + T_0)^2 + s_3(\sigma h + T_0) + s_4 = 0, \tag{24}$$

where we have set

$$\begin{aligned} s_1 = -f_1 f_2, \quad s_2 = f_3 f_4 f_5^2 + f_5(f_3 f_6 + f_4 f_7 - f_1 f_8) - 2f_1 f_2 f_9 + f_6 f_7 - f_1 f_{10}, \\ s_3 = f_5 f_9(f_3 f_6 + f_4 f_7 - f_1 f_8) - f_1 f_2 f_9^2 + 2f_9(f_6 f_7 - f_1 f_{10}), \quad s_4 = f_9^2(f_6 f_7 - f_1 f_{10}), \end{aligned}$$

with

$$\begin{aligned}
 f_1 &= \frac{\pi RL}{2} \left(\left(\frac{m\pi}{L} \right)^4 + 2 \left(\frac{m\pi}{L} \right)^2 \left(\frac{n}{R} \right)^2 + \left(\frac{n}{R} \right)^4 \right), \\
 f_2 &= -\frac{\pi RL}{2} \left(\frac{m\pi}{L} \right)^2, \\
 f_3 &= \frac{\pm 4RLC(1-\nu^2)}{3m} \left(\frac{m\pi}{L} \right)^2 \left(\frac{n}{R} \right)^2, \\
 f_4 &= \mp \frac{4RL}{3m} \left(\frac{m\pi}{L} \right)^2 \left(\frac{n}{R} \right)^2, \\
 f_5 &= \mu h, \\
 f_6 &= \frac{-\pi RL}{2R} \left(\frac{m\pi}{L} \right)^2 \pm \frac{4RL\mu h}{3m} \left(\frac{m\pi}{L} \right)^2 \left(\frac{n}{R} \right)^2, \\
 f_7 &= \frac{\pi RLC(1-\nu^2)}{2R} \left(\frac{m\pi}{L} \right)^2 \mp \frac{4RL\mu h}{3m} C(1-\nu^2) \left(\frac{m\pi}{L} \right)^2 \left(\frac{n}{R} \right)^2, \\
 f_8 &= \frac{\pm 4RLC(1-\nu^2)}{3mR} \left(\frac{n}{R} \right)^2, \\
 f_9 &= -\left(D - \frac{B^2}{C} \right) \left(\frac{m\pi}{L} \right)^2 - \frac{C(1-\nu^2)}{R^2} \left(\frac{m\pi}{L} \right)^{-2}, \\
 f_{10} &= \frac{\pi RL}{2} \left(D - \frac{B^2}{C} \right) \left(\left(\frac{m\pi}{L} \right)^4 + 2 \left(\frac{m\pi}{L} \right)^2 \left(\frac{n}{R} \right)^2 + \left(\frac{n}{R} \right)^4 \right).
 \end{aligned}$$

Solving (24) yields $\sigma h + T_0$ versus the material properties, the shell geometry parameters, the imperfection amplitude, and m and n . The critical axial compression load, in which buckling occurs, can be written as

$$P_{cr} = 2\pi R(\sigma h)_{\min}, \quad (25)$$

where P_{cr} is the critical axial compression load, and $(\sigma h)_{\min}$ is obtained by minimizing the solutions of (24) with respect to m and n .

3.2. Wan–Donnell imperfection model. Similarly, for an FGM cylindrical shell with the Wan–Donnell imperfection model, the prebuckling force resultants and prebuckling deflection may be found to be

$$N_{x0} = -\frac{P}{2\pi R} - T_0 = -\sigma h - T_0, \quad N_{y0} = C(1-\nu^2)\frac{w_0}{R} - \nu\sigma h - T_0, \quad N_{xy0} = 0 \quad (26)$$

and

$$w_0 = \eta \sin \frac{m\pi x}{L}, \quad (27)$$

where

$$\eta = \frac{4(\nu\sigma h + T_0)/m\pi R}{\left(D - \frac{B^2}{C} \right) \left(\frac{m\pi}{L} \right)^4 - (\sigma h + T_0) \left(\frac{k+1}{2} \right) \left(\frac{m\pi}{L} \right)^2 + \frac{C(1-\nu^2)}{R^2}}. \quad (28)$$

Introducing the prebuckling coefficients from the above equations into Equations (16) and (17), result in the coupled linear equations of stability and compatibility as

$$\begin{aligned} \left(D - \frac{B^2}{C}\right)w_{1,xxxx} + \frac{\Phi_{,xx}}{R} - \Phi_{,yy} \left(\frac{k+1}{2}\right) \left(\frac{m\pi}{L}\right)^2 \eta \sin\left(\frac{m\pi x}{L}\right) + (\sigma h + T_0)w_{1,xx} &= 0, \\ \nabla^4 \Phi - C(1 - \nu^2) \frac{w_{1,xx}}{R} &= 0. \end{aligned} \tag{29}$$

To solve the system (29), with the consideration of the simply supported boundary conditions, the approximate solutions may be considered as

$$\begin{aligned} w_1 &= \alpha_m \sin \frac{m\pi x}{L}, & \Phi &= \beta_{mn} \sin \frac{m\pi x}{L} \cos \frac{ny}{R}, \\ L \geq x \geq 0, \quad 2\pi R \geq y \geq 0, & & m, n &= 1, 2, \dots, \end{aligned} \tag{30}$$

where m and n are the number of half waves in x and y -directions, respectively, and α_m and β_{mn} are constant coefficients that depend on m and n . Substituting the approximate solutions (30) into (29) gives the residues R_1 and R_2 . Following Galerkin’s method, R_1 and R_2 are made orthogonal with respect to the approximate solutions given by (30), and then the determinant of the resulting system of equations for the coefficients α_m and β_{mn} is set to zero, which for the odd values of m yields

$$\eta = \frac{-\pi}{\left(\frac{n}{R}\right)^2 \left(\frac{k+1}{2}\right) \left(\frac{8R}{3m}\right)}. \tag{31}$$

Considering (28) and (31), we obtain

$$\frac{P}{2\pi R} = \frac{\frac{C\pi(1-\nu^2)}{R^2} + \pi \left(D - \frac{B^2}{C}\right) \left(\frac{m\pi}{L}\right)^4 - T_0 \left(\frac{k+1}{2}\right) \left(-\left(\frac{n}{R}\right)^2 \left(\frac{32}{3m^2\pi}\right) + \pi \left(\frac{m\pi}{L}\right)^2\right)}{\left(\frac{k+1}{2}\right) \left(-\left(\frac{n}{R}\right)^2 \left(\frac{32\nu}{3m^2\pi}\right) + \pi \left(\frac{m\pi}{L}\right)^2\right)}. \tag{32}$$

The critical axial compression load P_{cr} is obtained by minimizing this with respect to m and n .

4. Numerical results and discussion

The functionally graded materials chosen are zirconium oxide, ZrO_2 , and the titanium alloy Ti-6Al-4V. Their material properties P are given in [Touloukian 1967] as functions of temperature T , of the form

$$P = P_0(1 + P_1T + P_2T^2 + P_3T^3) \tag{33}$$

in which $T = T_0 + \Delta T$ and $T_0 = 300$ K (room temperature), and $P_0, P_1, P_2,$ and P_3 are temperature dependent coefficients that are unique to the constituent materials. Typical values for Young’s modulus E , Poisson’s ratio ν , and the coefficient of thermal expansion α of zirconium oxide and titanium alloy are listed in Table 1. (A term in T^{-1} in Touloukian’s version of (33) has coefficient zero in this case and is omitted.)

Here three comparison cases are presented for the validation of the results. The first comparison is based on the buckling under axial compression in the absence of thermal loading. Let us assume $\mu = 0$ and $k = 1$, in the Koiter and Wan–Donnell models, respectively, which corresponds to the equations for

	ZrO ₂				Ti-6Al-4V			
	P_0	P_1	P_2	P_3	P_0	P_1	P_2	P_3
E (Pa)	$244.27 \cdot 10^9$	$-1.371 \cdot 10^{-3}$	$1.214 \cdot 10^{-6}$	$-3.681 \cdot 10^{-10}$	$122.56 \cdot 10^9$	$-4.586 \cdot 10^{-4}$	0	0
α (Pa)	$12.766 \cdot 10^{-6}$	$-1.491 \cdot 10^{-3}$	$1.006 \cdot 10^{-5}$	$-6.778 \cdot 10^{-11}$	$7.5788 \cdot 10^{-6}$	$6.638 \cdot 10^{-4}$	$-3.147 \cdot 10^{-6}$	0
ν	0.28	0	0	0	0.28	0	0	0

Table 1. Temperature-dependent thermoelastic coefficients for zirconium oxide ZrO₂ and titanium alloy Ti-6Al-4V. From [Touloukian 1967].

thickness ratio, h/R	0.003	0.004	0.005	0.006
this article (Koiter model)	2.40	4.26	6.65	9.58
this article (Wan–Donnell model)	2.52	4.26	6.77	9.66
[Brush and Almroth 1975]	2.40	4.26	6.65	9.58

Table 2. Buckling loads P_{cr} (in MN) for perfect homogeneous shells, in the absence of thermal load ($E = 70$ GPa, $\alpha = 23 \times 10^{-6}$ /K, $\nu = 0.3$, $L/R = 1$).

volume fraction exponent ξ	0.0	0.2	0.5	1.0	2.0	3.0	5.0
this article (Koiter model)	85.90	95.65	106.49	118.74	133.12	141.62	151.59
this article (Wan–Donnell model)	87.89	97.68	108.91	121.81	137.05	145.98	156.27
[Shen 2004]	86.65	96.03	106.54	118.45	132.44	140.69	150.28

Table 3. Buckling temperature difference ΔT_{cr} for perfect FGM cylindrical shells, in the absence of axial compression ($h/r = 0.025$, $L/R = 0.866$).

a perfect cylindrical shell. If, in addition, we take $E_c = E_m$ and $\alpha_c = \alpha_m$ (pure homogeneous metallic shell), the solutions may be validated with the closed form solution obtained in [Brush and Almroth 1975] when $\Delta T = 0$. Table 2 shows the results obtained for a cylindrical shell made of pure aluminum ($L/R = 1$) with the Koiter and Wan–Donnell imperfection models discussed in this article, together with the values given by the closed form solution of Brush and Almroth. The comparison for the two imperfection models, when imperfections are eliminated, is well justified.

Other comparisons are based on the buckling under thermal loading in the absence of axial compression. Assume $\mu = 0$ and $k = 1$, in the Koiter and Wan–Donnell models, respectively (perfect cylindrical shell). For uniform temperature rise loading, in the absence of axial compression, the solution may be validated with the results obtained in [Shen 2004] for FGM shells made from Si₃N₄/SUS304 as shown in Table 3. If, in addition, we take $E_c = E_m$ and $\alpha_c = \alpha_m$ (homogenous shell), the solution may be validated with the closed form solution obtained in [Eslami et al. 1996] for an isotropic cylindrical shell, as shown in Table 4. As seen, in all cases the comparisons are well justified.

Figure 1 plots the variation of the ratio of critical load for the imperfect FGM cylindrical shell P_{cr} to the critical load of the corresponding perfect shell P_{ps} , subjected to axial compression and under

h/r	Si ₃ N ₄			SUS 304		
	0.003	0.005	0.010	0.003	0.005	0.010
this article (Koiter model)	216.42	361.01	721.29	103.07	171.84	343.52
this article (Wan–Donnell model)	216.55	360.84	721.55	103.14	171.86	343.64
[Eslami et al. 1996]	216.61	360.79	722.03	103.16	171.94	343.87

Table 4. Buckling temperature difference ΔT_{cr} for perfect homogenous cylindrical shells, in the absence of axial compression. ($L/R = 0.866$)

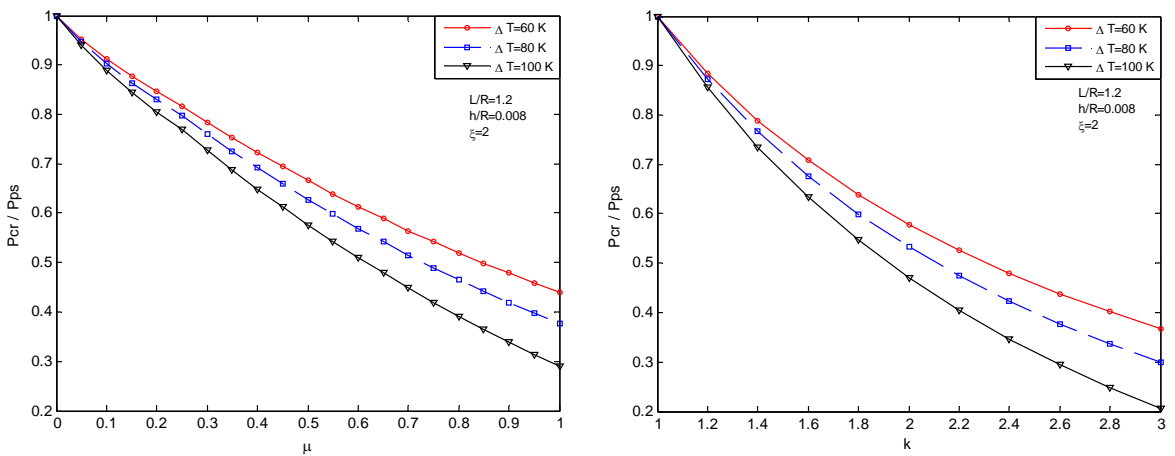


Figure 1. Influence of imperfection magnitude. Left: Koiter imperfection model; right Wan–Donnell imperfection model.

different uniform temperature rise and based on the Koiter imperfection parameter μ and Wan–Donnell imperfection parameter k for $L/R = 1.2$, $h/R = 0.008$, and $\zeta = 2$. As the magnitude of imperfection increases, the buckling ratio decreases. This effect is stronger as the uniform temperature rise increases.

The influence of cylindrical shell geometry on critical axial compression load P_{cr} under a uniform temperature rise $\Delta T = 30$ K for various values of the volume fraction exponent $\zeta = 0.5, 1, 2$ (as well as pure metal and pure ceramic) are illustrated in Figures 2 and 3. Figure 2 shows the buckling loads versus h/R for two imperfection models when the Koiter imperfection amplitude and Wan–Donnell imperfection parameter are 0.5 and 1.2, respectively, and $L/R = 1$. As the ratio h/R increases, the buckling load increases. Figure 3 represents the variation of buckling load versus L/R for two imperfection models when the Wan–Donnell imperfection parameter and the Koiter imperfection amplitude are 2 and 0.5, respectively, and $h/R = 0.005$. The critical buckling load increases as the ratio L/R increases.

The variation of P_{cr} versus volume fraction exponent are plotted for different values of environment temperature in Figure 4 for the two imperfection models. Here, the Koiter imperfection amplitude and Wan–Donnell imperfection parameter are 0.5 and 1.2, respectively, $L/R = 1.2$, and $h/R = 0.008$. As seen in this figures, for a particular value of environment temperature (here, $T = 350$ K for the Koiter model and $T = 360$ K for the Donnell model) the critical buckling load is almost constant for different

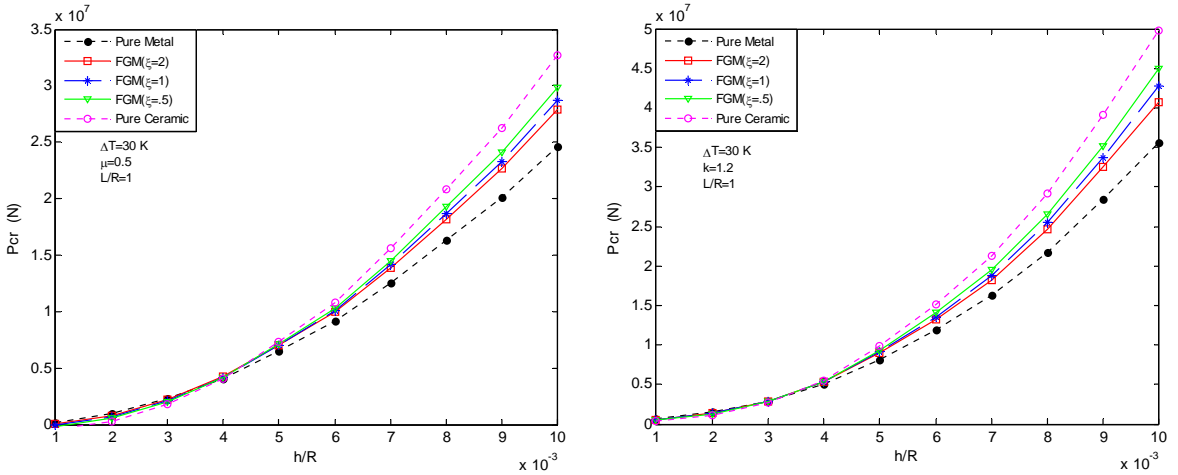


Figure 2. Variation of critical buckling load with h/R according to volume fraction exponent. Left: Koiter imperfection model; right Wan–Donnell imperfection model.

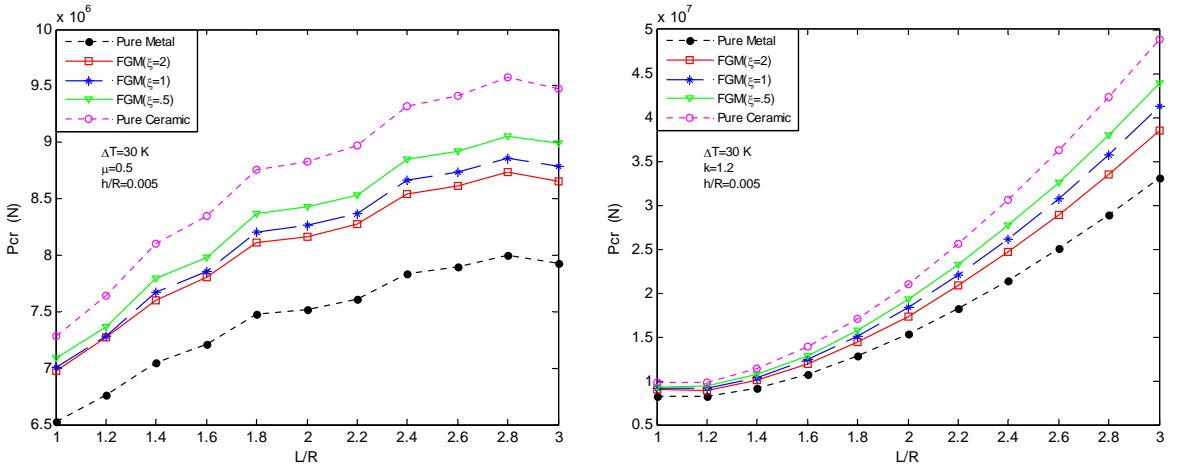


Figure 3. Variation of buckling load with L/R according to volume fraction exponent. Left: Koiter imperfection model; right Wan–Donnell imperfection model.

values of ζ , provided that the other parameters are kept constant. For temperatures less than this particular temperature, critical buckling load decreases as the volume fraction exponent ζ increases, and for temperatures greater than this particular temperature, critical buckling load increases as the volume fraction exponent ζ increases. This particular temperature, extremely depends on the shell parameters such as material properties, geometrical parameters, and magnitude of the initial imperfection. Note that negative values of P_{cr} in Figure 4, left for $T = 420\text{ K} (\Delta T = 120\text{ K})$ display situations that FGM cylindrical shell will buckle before applying any axial compression load, through existing thermal load (thermal buckling).

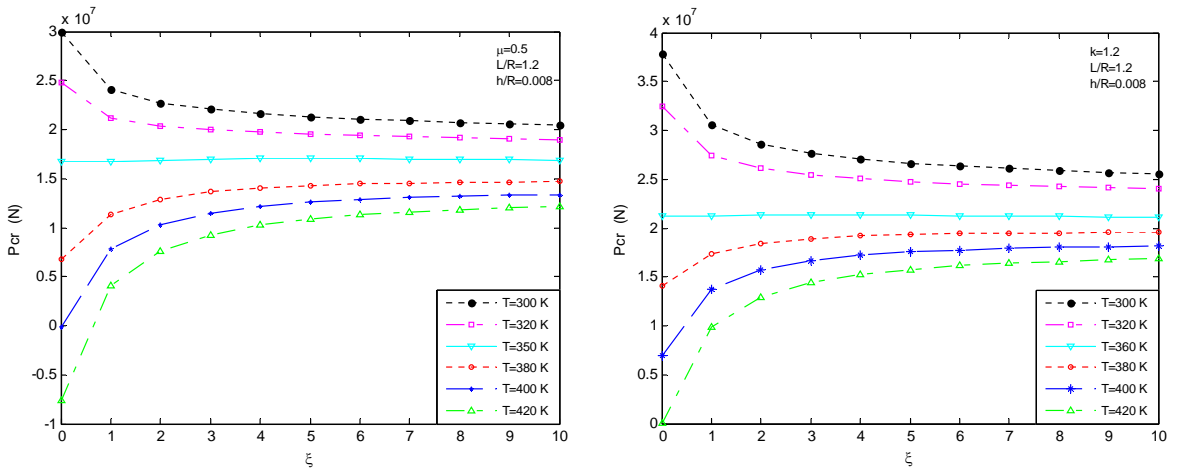


Figure 4. Critical buckling load of shell versus volume fraction exponent ζ and temperature T . Left: Koiter imperfection model; right Wan–Donnell imperfection model.

5. Conclusion

The equilibrium, stability, and compatibility equations for a simply supported imperfect functionally graded cylindrical shell are derived. The buckling analysis of imperfect FGM cylindrical shell under axial compressive load in thermal environments is investigated for two models of initial geometric imperfections, leading to the closed form solutions for the buckling load. The results reveal that effect of initial imperfections on decreasing the buckling load is stronger for larger magnitudes of the thermal loading. It is also shown that the buckling load of an imperfect functionally graded cylindrical shell subjected to thermomechanical loads increases with increasing the shell thickness and/or increasing shell length. Also results show that for a particular value of environment temperature, critical buckling load is almost independent of volume fraction exponent. Beyond this temperature, critical buckling load increases with increasing the volume fraction exponent and below that, critical buckling load decreases with increasing the volume fraction exponent.

References

[Brush and Almroth 1975] D. O. Brush and B. O. Almroth, *Buckling of bars, plates, and shells*, McGraw-Hill, New York, 1975.

[Donnell 1934] L. H. Donnell, “A new theory for the buckling of thin cylinders under axial compression and bending”, *J. Appl. Mech. (ASME)* **56** (1934), 795–806.

[Donnell 1956] L. H. Donnell, “Effect of imperfections on buckling of thin cylinders under external pressure”, *J. Appl. Mech. (ASME)* **23** (1956), 569–575.

[Donnell and Wan 1950] L. H. Donnell and C. C. Wan, “Effect of imperfections on buckling of thin cylinders and columns under axial compression”, *J. Appl. Mech. (ASME)* **17** (1950), 73–83.

[Eslami et al. 1996] M. R. Eslami, A. R. Ziaii, and A. Ghorbanpour, “Thermoelastic buckling of thin cylindrical shells based on improved stability equations”, *J. Therm. Stresses* **19**:4 (1996), 299–315.

[Kadoli and Ganesan 2006] R. Kadoli and N. Ganesan, “Buckling and free vibration analysis of functionally graded cylindrical shells subjected to a temperature-specified boundary condition”, *J. Sound Vib.* **289**:3 (2006), 450–480.

- [Mirzavand and Eslami 2006] B. Mirzavand and M. R. Eslami, “Thermal buckling of imperfect functionally graded cylindrical shells based on the Wan–Donnell model”, *J. Therm. Stresses* **29**:1 (2006), 37–55.
- [Mirzavand et al. 2005] B. Mirzavand, M. R. Eslami, and R. Shahsiah, “Effect of imperfections on thermal buckling of functionally graded cylindrical shells”, *AIAA J.* **43**:9 (2005), 2073–2076.
- [Ng et al. 2001] T. Y. Ng, Y. K. Lam, K. M. Liew, and J. N. Reddy, “Dynamic stability analysis of functionally graded cylindrical shells under periodic axial loading”, *Int. J. Solids Struct.* **38**:8 (2001), 1295–1309.
- [Praveen and Reddy 1998] G. N. Praveen and J. N. Reddy, “Nonlinear transient thermoelastic analysis of functionally graded ceramic-metal plates”, *Int. J. Solids Struct.* **35**:33 (1998), 4457–4476.
- [Shahsiah and Eslami 2003a] R. Shahsiah and M. R. Eslami, “Functionally graded cylindrical shell thermal instability based on improved Donnell equations”, *AIAA J.* **41**:9 (2003), 1819–1826.
- [Shahsiah and Eslami 2003b] R. Shahsiah and M. R. Eslami, “Thermal buckling of functionally graded cylindrical shell”, *J. Therm. Stresses* **26**:3 (2003), 277–294.
- [Shen 2002] H.-S. Shen, “Postbuckling analysis of axially-loaded functionally graded cylindrical shells in thermal environments”, *Compos. Sci. Technol.* **62**:7–8 (2002), 977–987.
- [Shen 2003] H.-S. Shen, “Postbuckling analysis of pressure-loaded functionally graded cylindrical shells in thermal environments”, *Eng. Struct.* **25**:4 (2003), 487–497.
- [Shen 2004] H.-S. Shen, “Thermal postbuckling behavior of functionally graded cylindrical shells with temperature-dependent properties”, *Int. J. Solids Struct.* **41**:7 (2004), 1961–1974.
- [Shen and Noda 2005] H.-S. Shen and N. Noda, “Postbuckling of FGM cylindrical shells under combined axial and radial mechanical loads in thermal environments”, *Int. J. Solids Struct.* **42**:16–17 (2005), 4641–4662.
- [Sofiyev 2003] A. H. Sofiyev, “Dynamic buckling of functionally graded cylindrical thin shells under non-periodic impulsive loading”, *Acta Mech.* **165**:3–4 (2003), 151–163.
- [Touloukian 1967] Y. S. Touloukian, *Thermophysical properties of high temperature solid materials*, MacMillan, New York, 1967.
- [Woo et al. 2003] J. Woo, S. A. Meguid, and K. M. Liew, “Thermomechanical postbuckling analysis of functionally graded plates and shallow cylindrical shells”, *Acta Mech.* **165**:1–2 (2003), 99–115.
- [Woo et al. 2005] J. Woo, S. A. Meguid, J. C. Stranart, and K. M. Liew, “Thermomechanical postbuckling analysis of moderately thick functionally graded plates and shallow shells”, *Int. J. Mech. Sci.* **47**:8 (2005), 1147–1171.

Received 24 Dec 2007. Revised 1 Sep 2008. Accepted 8 Sep 2008.

BABAK MIRZAVAND: bmirzavand@aut.ac.ir

Mechanical Engineering Department, Amirkabir University of Technology, Tehran 15914, Iran

M. REZA ESLAMI: eslami@aut.ac.ir

Mechanical Engineering Department, Amirkabir University of Technology, Tehran 15914, Iran

<http://me.aut.ac.ir/M.Eslami.htm>

NONLINEAR VIBRATION OF AN EDGE-CRACKED BEAM WITH A COHESIVE ZONE, I: NONLINEAR BENDING LOAD-DISPLACEMENT RELATIONS FOR A LINEAR SOFTENING COHESIVE LAW

PRASAD S. MOKASHI AND DANIEL A. MENDELSON

Part I of this paper describes the computations of the quasistatic nonlinear moment-slope relation for an edge-cracked beam element with a strictly linear softening cohesive zone ahead of the crack tip. A static plane stress linear elastic boundary element analysis is used in which the cohesive nonlinearity appears in the crack plane boundary conditions only. An iterative solution scheme is used to determine the unknown cohesive zone length, the cohesive displacement jumps, and the bending mode J -integral. Interpreting the moment-slope relation as a generalized load-displacement relation the bending compliance (and slope) at a given applied moment are calculated from computed J -integral values over a grid of applied moment and crack-length values. The dependence of the moment-slope relation on the cohesive law parameters is studied and the various computed moment-slope relations are then used in Part II to model the dynamic effect of the cohesive zone and law on the free-vibration of an edge-cracked simply-supported beam.

1. Introduction

The major kinematic effect of an edge-crack in a beam is the discontinuity the crack allows in both the net rotation and the net transverse deflection across the crack plane, [Figure 1](#). The discontinuities are resisted by the bonded ligament in an elastic manner if the crack is in small-scale yielding. This allows the use of linear massless rotational and/or shear springs to represent the crack plane in thin structures with through cracks. The idea originated with the line-spring model of [Rice and Levy \[1972\]](#) applied to a static analysis of a through crack in a plate in bending. The model relates the jumps in the rotation $\Delta\theta$ and the jump in transverse deflection Δv to the applied bending moment M and the shear force Q at the crack plane, respectively. For cracks in small-scale yielding for which linear elastic fracture mechanics (LEFM) applies, the spring stiffnesses (or their reciprocals, the compliances) may be found from a two-dimensional elastic analysis of a cracked beam shaped geometry as found in many fracture mechanics handbooks [[Tada et al. 1973](#); [Yokoyama and Chen 1998](#)] as a function of crack length, beam depth, and elastic properties. If the crack tip is attended by a cohesive zone, then the extent of the zone and the plastic stretch in the cohesive zone depend on the load which causes the stiffness (compliance) to depend on the load and the load-displacement relation to be nonlinear. The purpose of this paper is to compute the nonlinear bending load-displacement relation (moment-slope relation) for an edge-crack with a linear softening cohesive law and to study how it depends on the cohesive law parameters.

Keywords: cohesive zone, linear softening, compliance, J -integral, nonlinear load-displacement.

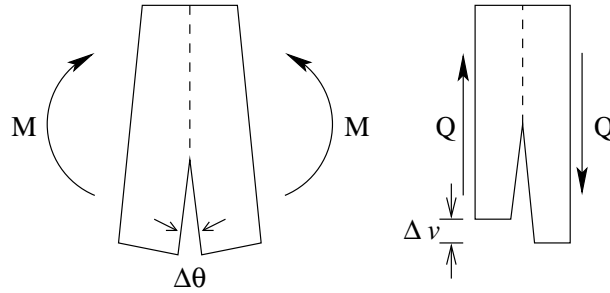


Figure 1. Left: Jump in slope $\Delta\theta$ at the crack plane due to the bending moment M . Right: Jump in deflection Δv at the crack plane due to the shear force Q .

Fracture process zones are typically characterized by nonlinear softening behavior in which the crack plane stress decreases with increasing irreversible deformation of the process zone. The particular relationship between the cohesive traction and the deformation is known as the cohesive or softening law. The softening zone is in general surrounded by a nonlinear plastic hardening region. Four general situations may be delineated. (i) Both the softening and hardening regions are small compared to the K-dominant region surrounding the crack tip, in which case LEFM is appropriate. (ii) The softening zone is small and is surrounded by a large plastic hardening zone, in which case elastic-plastic fracture mechanics is appropriate. (iii) Both the softening zone near the crack plane and the plastic hardening zone are appreciably large, in which case both cohesive zones and a plastic hardening region need to be modeled. (iv) The softening zone is confined to a region near the crack plane and is large compared to a negligible small region of plastic hardening which surrounds the softening zone. This requires a model with only an infinitesimally thin cohesive zone surrounded by elastic material. Typically (i) is referred to as brittle behavior, (ii) and (iii) are ductile behavior, and (iv) is quasibrittle behavior. The present work is concerned with the latter category, which is exhibited by a variety of materials: concrete, rock, ice, certain sands and clays, toughened ceramics, fibrous composites, brittle matrix composites, and a variety of bonded joint geometries and types (adhesive, weld, solder) [Hillerborg et al. 1976; Petersson 1981; González et al. 2004; Cox et al. 1989; Sensmeier and Wright 1989; Bao and Suo 1992; Suo et al. 1993; Botsis and Beldica 1994; Zok and Hom 1990; Bosco and Carpinteri 1995; Bao and McMeeking 1995; Xu et al. 1995; Fett et al. 1995; 1994; Anderson and Stigh 2004; Shetty and Spearing 1997; Yang et al. 1999; Cavalli et al. 2005; Yang et al. 2004; Sorensen 2002; Plaut and Ritchie 2004; Wei and Hutchinson 1998].

Cohesive zones were first introduced into the mathematical analysis of the crack problem nearly simultaneously by Dugdale [1960], Bilby et al. [1963], and Barenblatt [1962], for application to ductile metals. These original analyses assumed that the cohesive stress is constant over the entire cohesive zone. Hillerborg et al. [1976] applied cohesive modeling to quasibrittle materials like concrete and were the first to introduce a softening cohesive law in which after reaching a peak, the cohesive traction reduces as the plastic stretch increases. Many of the studies referenced in the previous paragraph note that all or a significant part of the cohesive law is in a softening mode. Linear and bilinear softening cohesive models have also been used, for example, by Geubelle and Rice [1995], Yang and Ravi-Chandar [1996], and Bažant and Planas [1998] for metals, concrete, and other quasibrittle materials. Exponential and other

nonlinear softening models have been used by Geubelle and Baylor [1998], Bažant and Li [1997], Li and Bažant [1997], Panasyuk and Yarema [2001], and Panasyuk et al. [2003] in the context of quasibrittle materials. Linear softening models have been used in boundary element formulations by Ohtsu and Chahrouh [1995] and Aliabadi [1997] for quasibrittle materials like concrete to study crack propagation. Hanson and Ingrassia [2003] and Hanson et al. [2004] have used linear and bilinear softening cohesive models in numerical crack growth simulations in concrete using the finite element method.

From the work cited above it is clear that cohesive zones occur in many real material systems and that the use of cohesive zone models in computational settings is convenient, useful and prevalent today. Virtually all methods in the literature for determining the form or parameters of a cohesive law for a particular material have been based on destructive testing to failure. This includes all of the work cited above in which this crucial parameter identification is actually carried out. The present work is one of two parts in an effort to develop a nondestructive technique for characterizing the cohesive law of a structural material, or in the case of an interface crack, the cohesive law of the bond or interface material itself. The characterization is based on the nonlinear vibration response of a model of an edge-cracked beam in which the crack plane is replaced by a bending spring and a transverse shear spring and the beam is modeled using Euler–Bernoulli beam theory. Assuming nonlinear behavior in bending only, the spring stiffnesses are calculated in this part of the paper from two-dimensional fracture mechanics solutions for beam like geometries with edge-cracks and mode I cohesive zones. The second part of the paper uses these stiffnesses in a nonlinear beam vibration analysis. In this way the forward problem is posed and solved: that is, for a given cracked beam and cohesive law, the nonlinear beam vibration response at a prescribed static preload is predicted. The eventual goal is to solve the inverse problem of interpreting measured nonlinear vibratory response to ascertain the parameters of a cohesive law for a known crack length and superimposed static preload. The rationale for the assumption of a static preload is given in detail in the second part of the paper.

Specifically the objective of the first part of the paper is to develop a methodology for computing the nonlinear generalized load-displacement (moment-slope) relationship in a two dimensional edge-cracked beam-like geometry with a linear softening cohesive crack ahead of the crack tip subjected to pure bending. The nonlinear spring stiffness for use in the beam vibration analysis is calculated from the nonlinear moment-slope relationship. The analysis begins by solving the crack and cohesive zone boundary value problem using a two-body, iterative, direct boundary element method (BEM). By virtue of the method of solution the results also apply to the situation of two beams bonded together with an edge crack in the plane of the bond. For each softening law studied, the J -integral is obtained from the BEM analysis for a range of crack lengths and applied moments. Then, using the relationship between the J -integral and generalized load and displacement (bending moment and jump in slope across the crack plane) for the cracked geometry, the compliance is derived in terms of the J -integral. Once the compliance is found at a given load the generalized displacement (jump in slope across the crack) may be calculated. This yields the predicted generalized load versus the displacement relationship, which is in turn used in the nonlinear beam vibration analysis presented in the second part of this paper.

The paper starts with a discussion of crack plane compliance and the J -integral and their relationship. This is followed by the BEM formulation and some results on the dependence of the cohesive response on the loading and the cohesive law parameters. Next we describe the numerical analysis for obtaining the generalized load versus displacement relation, and present the curves for a variety of cohesive laws.

2. Crack plane compliance and the J -integral

For an Euler–Bernoulli beam of rectangular cross section and containing a through-surface edge-crack, if axial forces are neglected and only shear and bending loads are considered, then the crack plane is subjected to a net shear force Q and a net bending moment M . The presence of a crack causes a relative jump in displacement and rotation of one flank of the crack relative to the other as shown in [Figure 1](#) for a cracked element in an edge-cracked beam. $\Delta\theta$ represents the jump in slope and Δv represents the jump in the displacement. The increased compliance due to the presence of the crack can be lumped into a continuous spring of zero width that connects the two faces of the crack [[Rice and Levy 1972](#)]. If the beam is now divided at the crack plane into two regions and the crack plane replaced by line(planar)-springs of zero-width, the compliance relations for the line-springs may be written as

$$\Delta\theta = \theta_2 - \theta_1 = \lambda_\theta M, \quad (1)$$

$$\Delta v = v_2 - v_1 = \lambda_v Q, \quad (2)$$

where λ_θ and λ_v are the compliances due to bending moment and shear force respectively. The springs relate the shear force and bending moment to the jump in deflection and rotation, respectively, across the crack plane. Treating each of these as global or generalized load and load-point displacement pairs, basic fracture mechanics principles state that the bending compliance can be written in terms of J_I , the mode I contribution to the J -integral, as [[Kanninen and Popelar 1985](#)]

$$\lambda_\theta(\bar{M}, \bar{a}) = \frac{W}{b} \frac{1}{\bar{M}} \int_0^{\bar{a}} \frac{\partial J_I(\bar{M}, \bar{a})}{\partial \bar{M}} d(\bar{a}). \quad (3)$$

and similarly that the shear compliance may be written in terms of J_{II} , the mode II contribution to the J -integral as

$$\lambda_v(\bar{Q}, \bar{a}) = \frac{W}{b} \frac{1}{\bar{Q}} \int_0^{\bar{a}} \frac{\partial J_{II}(\bar{Q}, \bar{a})}{\partial \bar{Q}} d(\bar{a}). \quad (4)$$

Since in the present two-dimensional setting J_I is actually a function of applied moment per unit thickness and nondimensional crack length to beam depth ratio, we have introduced normalized applied loads and crack length $\bar{M} \equiv M/b$, $\bar{Q} \equiv Q/b$, and $\bar{a} \equiv a/W$. Here b is the (out of plane) beam thickness, a is the crack length, and W is the beam depth; see [Figure 2](#). If the crack tip is elastic or in small-scale yielding (negligible cohesive zone size) then the compliance relations are linear, the compliances are independent of applied loads, and the J -integral components are proportional to their respective applied load. The J -integral components and the compliances may in this case be written directly in terms of the stress-intensity factors, which are well-tabulated for edge-cracked specimens [[Yokoyama and Chen 1998](#); [Tada et al. 1973](#); [Wilson 1970](#); [Tharp 1987](#)]. However, if there is cohesive damage ahead of the crack tip then the J -integral components depend nonlinearly on the applied load and the integrals in (3) or (4) must be used. This requires that the J -integral be evaluated at a fairly fine grid of applied load and crack-length values [[Mendelsohn 2006](#)]. For convenience, the present analysis confines the nonlinearity to the bending spring, and hence the shear compliance can be calculated from the formulas in [[Yokoyama and Chen 1998](#)]. The focus from here on in this paper is then on the nonlinear bending compliance in (3) and the resulting nonlinear \bar{M} – $\Delta\theta$ relation. This requires only the consideration of bending loading leading to mode I loading at the crack tip. The J -integral, which appears in (3), is computed from results

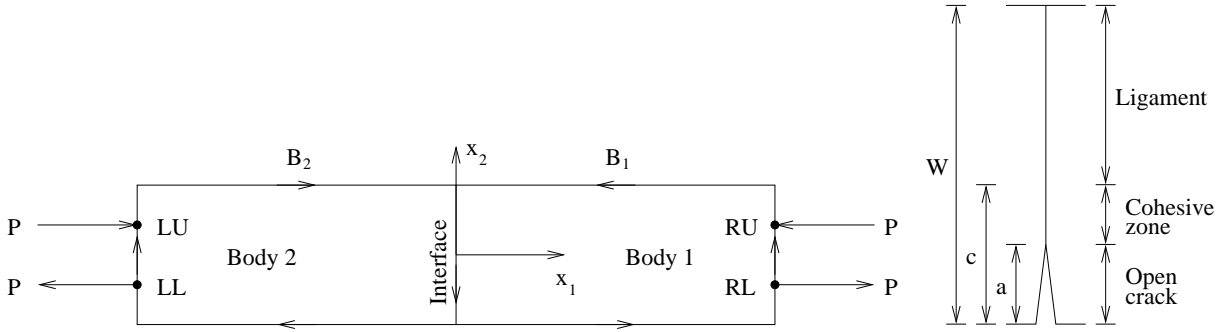


Figure 2. Left: Boundary element geometry showing the crack plane as the interface between two fictitious bodies having boundaries B_1 and B_2 . The couples at the ends load the model in bending (mode I). Right: Interface divided into three regions.

from a two-dimensional elastostatic BEM analysis of an edge-crack with a planar cohesive zone in a beam shaped homogeneous elastic solid subjected to edge-moments as shown in Figure 2, left. The elastic crack tip is a distance a from the bottom of the beam and the end of the cohesive zone is a distance c from the bottom of the beam, Figure 2, right. The cohesive law is the relationship between the normal traction t and the cohesive stretch δ in the cohesive zone which is modeled by a jump in normal displacement across the crack plane:

$$\delta = u_1^{x_1=0^+} - u_1^{x_1=0^-}, \tag{5}$$

where u_1 denotes displacement in the x_1 direction normal to the crack plane. δ_t is the value of δ at $x_2 = -\frac{1}{2}W + a$; see Figure 3, left. A linear softening cohesive law is shown in Figure 3, right, and is written as

$$t(\delta) = t_0 \left[1 - \frac{\delta}{\delta_0} \right], \tag{6}$$

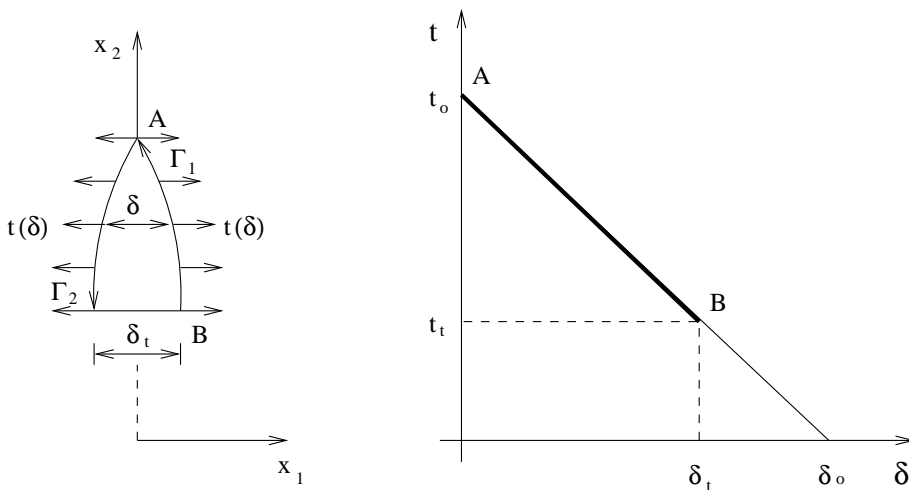


Figure 3. Left: Free body diagram of the cohesive zone. Right: Linear softening cohesive law showing the extent of softening.

where t_0 is the peak cohesive traction and δ_0 is the critical value of cohesive crack opening displacement at which extension of the elastic crack tip or crack growth occurs. The focus is on obtaining the cohesive response to loadings such that the entire cohesive law is exercised, but crack growth does not occur. Following the development in [Kanninen and Popelar 1985] but replacing the Dugdale cohesive law, for which the traction is constant and equal to t_0 over the entire cohesive zone, with the linear softening law in (6) we obtain

$$J_I = \int_0^{\delta_t} t(\delta) d\delta = t_0 \delta_t \left[1 - \frac{1}{2} \frac{\delta_t}{\delta_0} \right], \quad (7)$$

which is the area under the exercised portion of the cohesive law. We restrict δ_t to be less than its value at crack growth δ_0 . As δ_t approaches δ_0 , J_I approaches the critical value for crack growth, $J_{I0} = \frac{1}{2} t_0 \delta_0$, a third parameter in addition to t_0 and δ_0 which can be used to characterize the cohesive law. Crack growth is not modeled in order to keep the envisioned free-vibration experiments as simple as possible. The crack tip opening displacement δ_t is solved for using a two-body, iterative, direct boundary element formulation for an edge crack in a beam shaped solid subjected to pure bending, and the corresponding J -integral from (7).

3. Boundary element formulation and solution scheme

The beam shaped geometry with an edge crack subjected to pure bending is shown in Figure 2, left. The total length L of the beam is taken large enough compared to W to make the crack tip fields independent of any end effects at the load points and for this two-dimensional elasticity model to behave like an Euler–Bernoulli beam. The beam is further divided into two fictitious bodies with the crack plane as the interface between them. The interface is divided into three regions: (i) ligament, (ii) cohesive zone - with a linear softening $t - \delta$ law, and (iii) open crack as shown in Figure 2, right. B_1 and B_2 represent the boundaries of the two bodies that are discretized into elements with constant tractions and displacements. The direct boundary element formulation is applied to each of the two bodies which make up the beam under consideration. Discretizing B_1 and B_2 into N elements each, for each body ($k = 1, 2$) the reciprocal identity gives the two matrix equations

$$[{}_k U_{ij}] [{}_k t_j] + [{}_k T_{ij}] [{}_k u_j] = [0], \quad k = 1, 2. \quad (8)$$

The boundary traction and displacement N -vectors are $[{}_k t_j]$ and $[{}_k u_j]$, where the leading subscript refers to the body and the trailing subscript refers to the direction of traction or displacement. $[{}_k T_{ij}]$ and $[{}_k U_{ij}]$ with $i, j = 1, 2$ are the infinite space Green's matrices for tractions and displacements, respectively in body k . Details of these matrices can be found in [Brebbia and Dominguez 1989] and in the present notation in the doctoral thesis by Young [1994]. The boundary conditions in the crack plane are now described. The bending loading considered leads to a mode I cohesive zone only. A complete formulation with mode I and II cohesive behavior has also been completed and used in the cracked bimaterial beam problem [Mokashi 2007], but is not presented here. Starting with the ligament, normal, and tangential displacements across the fictitious interface are continuous and normal and shear tractions are equal and opposite (stresses are continuous). In the cohesive zone the tangential displacement and the shear traction are continuous across the interface, just as they are in the ligament, while the normal tractions are equal and opposite on either side of the interface and related to the normal displacement jump through the

cohesive law, (6). In the open crack both the normal and shear tractions on either crack surface are zero. The open crack surfaces and the boundaries B_1 and B_2 (except the load points) are traction free. The point loads creating the couples are modeled as constant applied normal traction over the element at whose node they act. These boundary conditions give rise to a $4N \times 4N$ linear system in the remaining unknown tractions and displacements. The matrix equation corresponding to each boundary condition consists of all rows of each of the Green's submatrices and only those columns corresponding to the node at which the boundary condition is applied. The details of the matrices that give rise to the final linear system can be found in the doctoral thesis by Mokashi [2007]. In addition to the $4N$ unknown tractions and displacements, the length of the cohesive zone is also unknown.

An automatic iterative solution scheme is employed to obtain the unknown tractions and displacements and the extent of the cohesive zone. The scheme begins with an initial guess of the number of elements that constitute the extent of the cohesive zone. The evaluated normal traction value in an element of the cohesive zone nearest to the ligament is then compared with t_0 . If it is larger than t_0 , iterations are performed on the number of elements in the cohesive zone until the value of the normal traction in the first element of the ligament, nearest to the cohesive zone, is less than t_0 . The other constraint for the solution is that in the open crack there is no interpenetration of material, that is, the crack exhibits opening displacements only. The solution for displacements is automatically checked for this condition. A representative solution for the normal tractions and displacements at the interface under predominantly mode-I conditions is shown in Figure 4. The interface is composed of 100 elements which provides a sufficient amount of refinement to obtain convergent results. The markers in the rightmost pane of the figure show the traction values in the elements in the cohesive zone, thus indicating the extent to which

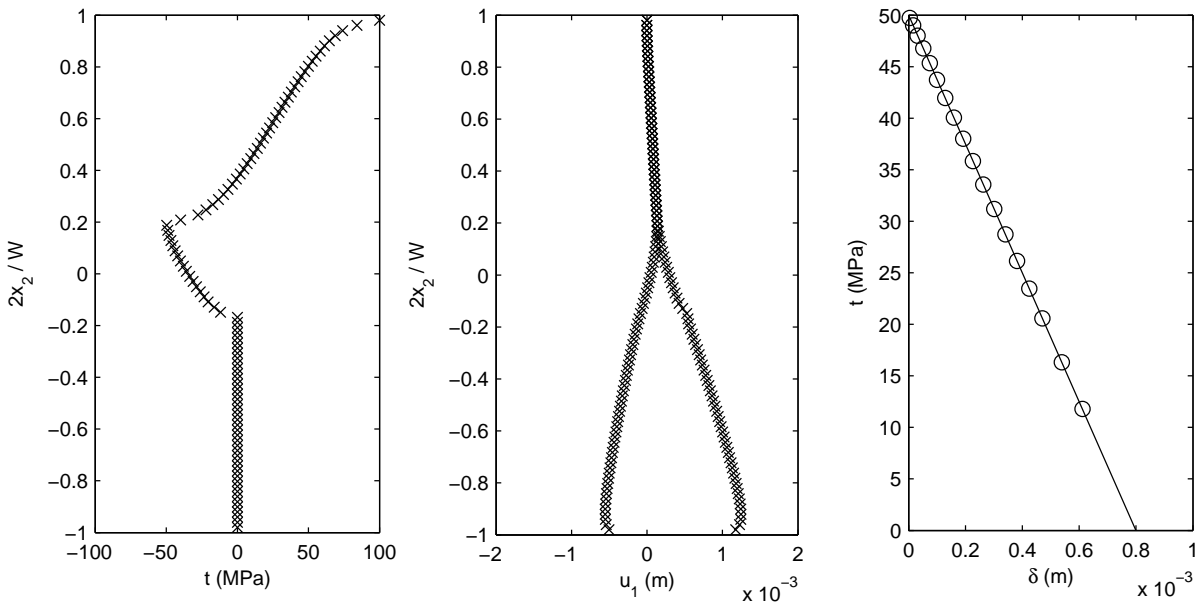


Figure 4. Representative solution for tractions and displacements in the cohesive zone along with the extent of softening ($E = 72800$ MPa, $\nu = 0.3$, $W = 12.5$ mm, $a/W = 0.42$, $\bar{M} = 800.78$ N, $t_0 = 50$ MPa, and $\delta_0 = 0.0008$ m).

the linear cohesive softening law has been exercised (how close δ_t is to δ_0) and the number of elements in the cohesive zone, and hence its length. The element nearest the crack tip has the smallest traction and largest displacement δ_t , while the traction approaches t_0 and the displacement goes to zero at the end of the cohesive zone. In this example the elastic crack is 42 elements long, the cohesive zone is 18 elements long, and δ_t is about 75% of its critical value. The solution shown in [Figure 4](#) is for a material with shear modulus $G = 28,000$ MPa, Poisson's ratio $\nu = 0.3$ and the cohesive law is $t_0 = 50$ MPa and $\delta_0 = 0.0008$ m. In all simulations W is chosen to be 12.5 mm. The total number of elements on the boundaries of both the bodies is 840 making the total size of the linear system 1680×1680 .

4. Extent of cohesive zone and softening

Several linear softening cohesive laws with three basic kinds of parameter variations are considered in this section. For each, the beam is quasistatically loaded such that significantly large cohesive zones are formed ahead of the crack tip. For a given peak cohesive traction and displacement the nonlinear $\bar{M}-\Delta\theta$ relation is obtained over a range of applied moment per unit thickness that exercises the linear softening cohesive law as much as possible, which in turn creates as large as possible cohesive zones, both without crack growth. Before obtaining the load-displacement relations we discuss the dependence of each of these features of the cohesive behavior on the applied moment, peak cohesive traction t_0 , critical opening displacement δ_0 , and the critical J -integral, J_{I0} .

First, as expected, for a given cohesive law and at a given crack length, as the applied moment is increased the cohesive zone length increases as well. When several linear softening cohesive laws having the same value of t_0 and different values of δ_0 are considered, it is observed that for a given crack length and applied moment smaller cohesive zones are formed for the steeper cohesive laws compared to the less steep cohesive laws. As δ_t for the steepest cohesive law approaches its critical value, cohesive zones just begin to form for the less steep cohesive laws. The length of the cohesive zone as it approaches δ_0 is very small for the steepest cohesive law. Now if several cohesive laws with different values of t_0 and the same value of δ_0 are considered then for a given crack length and applied moment the size of the cohesive zone is significantly smaller for the more steep cohesive law compared to the less steep cohesive law. Longer cohesive zones are obtained as δ_t approaches δ_0 for the least steep cohesive law. Similar trends are obtained when several cohesive laws having the same value of J_{I0} , but different values of t_0 and δ_0 , are considered. As the softening curve becomes steeper the size of the cohesive zone becomes markedly smaller, whereas for the less steep cohesive laws very long cohesive zones are obtained. Details of the trends are found in [\[Mokashi 2007\]](#).

A representative variation of the dimensionless J -integral, J/J_{I0} with dimensionless crack length a/W for various values of the applied moment per unit thickness \bar{M} is shown in [Figure 5](#). The cohesive law on which these results are based is $t_0 = 50$ MPa, $\delta_0 = 1.8(10^{-3})$ m, and $J_{I0} = 45(10^3)$ N/m. Similar results for several cohesive laws are also found in [\[Mokashi 2007\]](#).

5. Numerical analysis for obtaining nonlinear load-displacement curves

The nonlinear $\bar{M}-\Delta\theta$ curves for a given crack length are found by first obtaining the bending compliance λ_θ as a function of applied moment by evaluating the integral in (3). Noting that the integral is over crack length, this requires knowledge of $dJ/d\bar{M}$ over a grid of applied moment and crack length values. Next

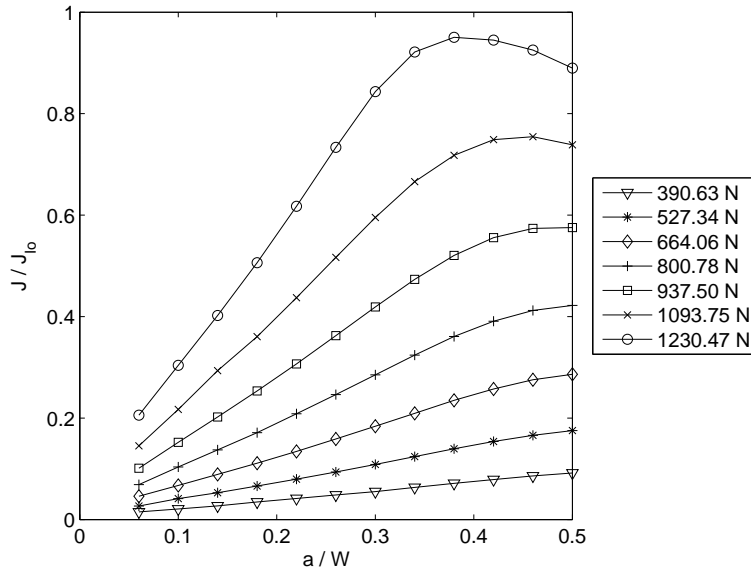


Figure 5. Variation of the dimensionless J -integral (J/J_{I0}) with the dimensionless crack length (a/W) at various values of the normalized moment \bar{M} (as indicated by the markers in the legend). $t_0 = 50$ MPa, $\delta_0 = 0.0018$ m and $J_{I0} = 45(10^3)$ N/m.

$\Delta\theta$ is found from (1) for a range of values of \bar{M} and the calculated λ_θ . At a given crack length a/W the analysis starts by using Newton’s method to obtain the interpolation polynomial $J_{N-1}(\bar{M})$ from the J -integral values obtained from the boundary element calculations at various values of applied moment \bar{M} :

$$J_{N-1}(\bar{M}) = \sum_{i=1}^N J[\bar{M}_1, \dots, \bar{M}_i] \prod_{j=1}^{i-1} (\bar{M} - \bar{M}_j). \tag{9}$$

For N points in the original data, $J_{N-1}(\bar{M})$ is a polynomial of order $(N - 1)$. The coefficients of this interpolating polynomial are obtained using divided differences in the standard way and are denoted by $J[\bar{M}_1, \dots, \bar{M}_i]$ [Atkinson and Han 2004]. Using the original values of applied moment as the skeleton, a denser grid of moment values is created with many points between each of the original values. Using the interpolation polynomial, the values J_n are generated on this finer grid, where the index n ranges over this fine grid of values. The derivative in (3), $dJ/d\bar{M}$, is obtained using central differences. This procedure is repeated to obtain curves of $dJ/d\bar{M}$ at several crack lengths \bar{a} that range between 0.06 and 0.5. At a given moment \bar{M} , an interpolating polynomial of order $(N - 1)$ for $dJ/d\bar{M}$ as a function of \bar{a} , with values of J -integral at N crack lengths \bar{a} , can be written

$$\left(\frac{dJ(\bar{a})}{d\bar{M}}\right)_{N-1} = \sum_{i=1}^N \frac{dJ}{d\bar{M}}[\bar{a}_1, \dots, \bar{a}_i] \prod_{j=1}^{i-1} [\bar{a} - \bar{a}_j]. \tag{10}$$

The coefficients of this interpolating polynomial are again obtained using divided differences and are denoted by $\frac{dJ}{d\bar{M}}[\bar{a}_1, \dots, \bar{a}_i]$. Using the polynomial functions for $\frac{dJ}{d\bar{M}}(\bar{a})$ obtained at several values of \bar{M} , several data points $(dJ/d\bar{M})_n$ are now created at multiple values of crack lengths \bar{a}_n for crack lengths

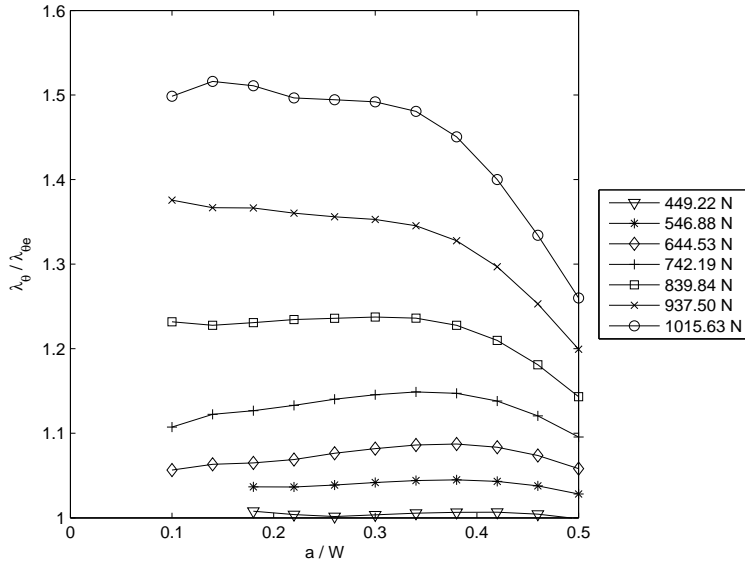


Figure 6. Dimensionless compliance ($\lambda_\theta/\lambda_{\theta e}$) curves with dimensionless crack length a/W . $t_0 = 50$ MPa and $J_{10} = 45(10^3)$ N/m. The values in the legend represent various normalized moments \bar{M} .

ranging from 0 to 0.5. The integral in (3) over crack length is, at a given moment \bar{M} , obtained numerically using the trapezoidal rule. The final expression then for λ_θ can be written as

$$\lambda_\theta = \frac{W}{b} \frac{1}{\bar{M}} \sum_{i=1}^n \frac{1}{2} \left[\left(\frac{dJ(\bar{a})}{d\bar{M}} \right)_i + \left(\frac{dJ(\bar{a})}{d\bar{M}} \right)_{i+1} \right] h_{\bar{a}} \tag{11}$$

where $h_{\bar{a}}$ denotes the increment in crack length \bar{a} . The variation of the dimensionless compliance $\lambda_\theta/\lambda_{\theta e}$ with dimensionless crack length \bar{a} is shown in Figure 6.

The curves are for various values of moment ratio M_R obtained using a set of values of the J -integral corresponding to the cohesive law ($t_0 = 50$ MPa, $J_{10} = 45(10^3)$ N/m) used to generate the curves in Figure 5. The normalization constant $\lambda_{\theta e}$ is the elastic compliance obtained using a set of values of the J -integral for the same beam geometry without considering a cohesive zone ahead of the crack tip. The J -integral for the linear elastic case is obtained in the standard way from the stress intensity factor K_I that is evaluated from the near tip stress fields using a similar boundary element code [Young 1994]. The numerical scheme just discussed is used to obtain the elastic compliance $\lambda_{\theta e}$ from those boundary element results. For reference purposes, the variation of the elastic compliance with crack length is shown in Figure 7.

The normalization is used because both the cohesive and elastic compliances are proportional to (W/b) . Figure 6 shows that at higher crack lengths the increase in compliance due to cohesive deformation ahead of the crack tip is less pronounced than at lower crack lengths. This is due to the almost pure bending like applied stress distribution on the crack plane. For a crack length of half the depth the entire cohesive zone lies in a region of what would be compressive normal stress in the absence of the crack. This effect is more dominant at higher values of applied moment \bar{M} and affects the elastic compliance for the same

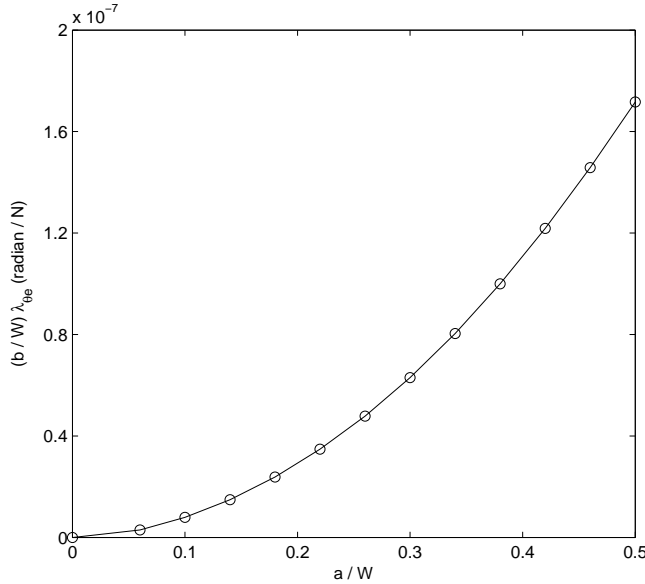


Figure 7. Variation of elastic compliance ($\lambda_{\theta e}$) with dimensionless crack length a/W .

geometry much less as long as the crack tip itself is below the mid-plane. At very low crack lengths and at low load levels the values of compliance are not reliable due to the inaccuracies in the cohesive zone size and in numerically obtaining the derivative $dJ/d\bar{M}$. Only reliable results are reported. Over a middle range of crack lengths the results show consistently that the elastic compliance accounts essentially for the crack length effect and that the additional increase in compliance due to cohesive stretching depends primarily on the applied moment and not on the crack length itself. The dependence of the normalized compliance on the applied moment at a given crack length is itself nonlinear. In order for the compliance to be about 10% larger than the elastic, the load must be 65% more than the elastic moment. But, as the load increases the rate of increase in the inelastic compliances increases and a 50% increase in the inelastic compliance occurs for a shorter crack at 125% more load than the elastic moment.

At a given crack length the jump in rotation $\Delta\theta$ is evaluated by solving (1) at the N discrete calculated values of the compliance, (11), at the chosen values of applied moment. To obtain a smooth $\bar{M}-\Delta\theta$ curve Newton’s method of interpolation is used again to obtain a polynomial $\bar{M}_{N-1}(\Delta\theta)$ of order $(N - 1)$

$$(\bar{M}(\Delta\theta))_{N-1} = \sum_{i=1}^N \bar{M}[\Delta\theta_1, \dots, \Delta\theta_i] \prod_{j=1}^{i-1} (\Delta\theta - \Delta\theta_j). \tag{12}$$

where $\bar{M}[\Delta\theta_1, \dots, \Delta\theta_i]$ are the coefficients of the polynomial obtained by divided differences. Normalized $\bar{M}-\Delta\theta$ curves for the single specific cohesive law ($t_0 = 50$ MPa, $J_{I0} = 45(10^3)$ N/m) at several crack lengths are shown in Figure 8. $\Delta\theta_e$ represents the elastic value of $\Delta\theta$ at $\bar{a} = 0.5$ obtained from the elastic compliance.

To study the effect of the cohesive law parameters, t_0 and δ_0 on the $\bar{M}-\Delta\theta$ relationship, 11 cohesive laws in were considered; see Table 1 on the right. The present study is exploratory and intended to determine the feasibility of the overall nondestructive characterization scheme and is not tied to a particular

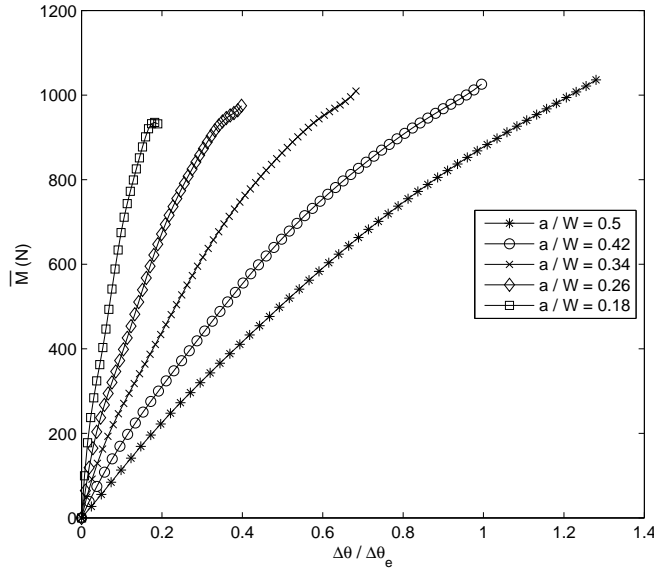


Figure 8. Normalized $\bar{M}-\Delta\theta$ curves at various crack lengths. $t_0 = 50 \text{ MPa}$ and $J_{I0} = 45(10^3) \text{ N/m}$.

material or cohesive process at this point. Therefore the parameter study was performed at only one value of Young’s modulus and Poisson’s ratio and a range of cohesive law parameters and applied moment such that the cohesive laws are well exercised, yet crack growth does not occur, that is, J does not exceed it’s critical value J_{I0} . The critical J -integral values of all of the laws listed below are all less than, or of the order of magnitude of, the value corresponding to the critical stress intensity factor for LEFM crack growth of $60 \text{ MPa}\sqrt{m}$.

Figure 9 shows the $\bar{M}-\Delta\theta$ curves for the various cohesive laws in Table 1. All results are for a beam depth of 1.25 m by appropriate scaling. The curves are clearly grouped by the value of the peak cohesive traction t_0 and show an increase in $\Delta\theta$ for decreasing peak traction at a given moment. Within a group at a particular peak traction t_0 there is a slight dependence on the critical displacement δ_0 (or equivalently the critical J integral J_{I0}). The main feature of that dependence is that the values of the applied moment at which (a) the cohesive law just begins to be exercised, and (b) crack growth occurs both increase with increasing δ_0 (J_{I0}). These values of applied moment are the approximate limits of each of the $\bar{M}-\Delta\theta$ curves shown in Figure 9. These curves provide the properties of the springs used to represent the crack plane in the dynamic beam vibration analysis and are accurate enough to carry out a two-term Taylor series expansion of the data at a given static load level.

t_0	$\delta_0 = 0.8 \text{ mm}$	$\delta_0 = 1.3 \text{ mm}$	$\delta_0 = 1.6 \text{ mm}$	$\delta_0 = 1.8 \text{ mm}$
25 MPa		7 (16.3 N/m)	4 (20 N/m)	1 (22.5 N/m)
50 MPa	11 (20 N/m)	8 (32.5 N/m)	5 (40 N/m)	2 (45 N/m)
75 MPa		9 (48.8 N/m)	6 (60 N/m)	3 (62.5 N/m)

Table 1. Cohesive laws: the first number is the law number; the number in parentheses is J_{I0} for the law.

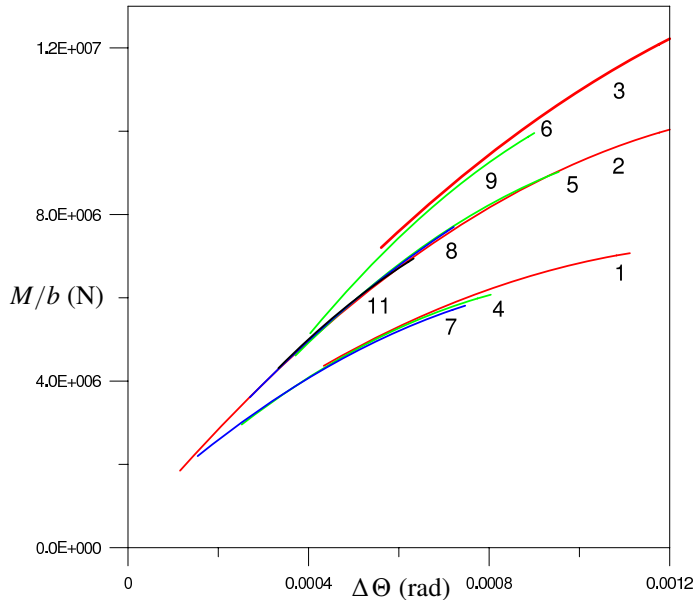


Figure 9. A plot of the $\bar{M}-\Delta\theta$ relationship for the cohesive laws in Table 1 for a dimensionless crack length of $a/W = 0.34$.

6. Conclusion

A BEM formulation for a linear softening cohesive zone problem in an edge cracked beam like geometry which requires an iterative process to determine the length of the cohesive zone to satisfy the nonlinear interfacial boundary conditions has been presented. The behavior of the cohesive zone with respect to the applied load, t_0 , δ_0 and a/W has been examined for nonpropagating cracks. The iterative boundary element solution scheme is robust, as the extent of the cohesive zone along with the solution for tractions and displacements are generally obtained within 3–6 iterations with an arbitrary initial guess.

For a specific linear softening cohesive law applied to the edge cracked beam shaped geometry the variation of the J -integral calculated for various values of applied load and crack lengths a/W are used in an algorithm for generating the nonlinear $\bar{M}-\Delta\theta$ curves. These results have potential application in the characterization of the cohesive behavior ahead of a crack tip in vibration analysis as discussed in the second part of this paper. In particular, a nonlinear free-vibration analysis, using the nonlinear $\bar{M}-\Delta\theta$ curves in Figure 9, is developed for exploring the effect of cohesive law parameters on the magnitude of various nonlinear beam responses.

Finally we note that the results presented here apply equally to a crack in a homogeneous beam and to a crack in a weak interface or bond layer between two beam sections made of the same material. The BEM model for the problem of a cohesive crack in the interface or bond layer between two beam sections of dissimilar materials is the same as for the similar material case, except that even with strictly mode I loading, the material mismatch causes the cohesive behavior to be of a mixed mode nature and a new combined mixed-mode cohesive law has to be used. This is the subject matter of ongoing research.

References

- [Aliabadi 1997] M. H. Aliabadi, “A new generation of boundary element methods in fracture mechanics”, *Int. J. Fract.* **86**:1–2 (1997), 91–125.
- [Anderson and Stigh 2004] T. Anderson and U. Stigh, “The stress-elongation relation for an adhesive layer loaded in peel using equilibrium of energetic forces”, *Int. J. Solids Struct.* **41**:2 (2004), 413–434.
- [Atkinson and Han 2004] K. Atkinson and W. Han, *Elementary numerical analysis*, 3rd ed., Wiley, Hoboken, NJ, 2004.
- [Bao and McMeeking 1995] G. Bao and R. M. McMeeking, “Thermomechanical fatigue cracking in fiber reinforced metal-matrix composites”, *J. Mech. Phys. Solids* **43**:9 (1995), 1433–1460.
- [Bao and Suo 1992] G. Bao and Z. Suo, “Remarks on crack bridging concepts”, *Appl. Mech. Rev.* **45**:8 (1992), 355–366.
- [Barenblatt 1962] G. I. Barenblatt, “The mathematical theory of equilibrium cracks in brittle fracture”, pp. 55–129 in *Advances in Applied Mechanics*, vol. 7, edited by H. L. Dryden and T. von Kármán, Academic Press, New York, 1962.
- [Bažant and Li 1997] Z. P. Bažant and Y. Li, “Cohesive crack with rate-dependent opening and viscoelasticity, I: Mathematical model and scaling”, *Int. J. Fract.* **86**:3 (1997), 247–265.
- [Bažant and Planas 1998] Z. P. Bažant and J. Planas, *Fracture and size effect in concrete and other quasibrittle materials*, CRC Press, Boca Raton, FL, 1998.
- [Bilby et al. 1963] B. A. Bilby, A. H. Cottrell, and K. H. Swinden, “The spread of plastic yield from a notch”, *Proc. R. Soc. A* **272**:1350 (1963), 304–314.
- [Bosco and Carpinteri 1995] C. Bosco and A. Carpinteri, “Discontinuous constitutive response of brittle matrix fibrous composites”, *J. Mech. Phys. Solids* **43**:2 (1995), 261–274.
- [Botsis and Beldica 1994] J. Botsis and C. Beldica, “Strength characteristics and fatigue crack growth in a composite with long aligned fibers”, *Int. J. Fract.* **69**:1 (1994), 27–50.
- [Brebbia and Dominguez 1989] C. A. Brebbia and J. Dominguez, *Boundary elements: an introductory course*, Computational Mechanics, Southampton, 1989.
- [Cavalli et al. 2005] M. N. Cavalli, M. D. Thouless, and Q. D. Yang, “Cohesive-zone modelling of the deformation and fracture of spot-welded joints”, *Fatigue Fract. Eng. Mater. Struct.* **28**:10 (2005), 861–874.
- [Cox et al. 1989] B. N. Cox, M. R. James, D. B. Marshall, W. L. Morris, C. G. Rhodes, and M. Shaw, “Failure mechanisms in titanium aluminide/SiC composites”, pp. 313 in *Proceedings of the 10th International SAMPE Conference* (Birmingham), edited by S. Benson et al., Elsevier, Amsterdam, 1989.
- [Dugdale 1960] D. S. Dugdale, “Yielding of steel sheets containing slits”, *J. Mech. Phys. Solids* **8**:2 (1960), 100–104.
- [Fett et al. 1994] T. Fett, D. Munz, C.-T. Yu, and A. S. Kobayashi, “Determination of bridging stresses in reinforced Al_2O_3 ”, *J. Am. Ceram. Soc.* **77**:12 (1994), 3267–3269.
- [Fett et al. 1995] T. Fett, D. Munz, G. Thun, and H.-A. Bahr, “Evaluation of bridging parameters in aluminas from *R*-curves by use of fracture mechanical weight function”, *J. Am. Ceram. Soc.* **78**:4 (1995), 949–951.
- [Geubelle and Baylor 1998] P. H. Geubelle and J. S. Baylor, “Impact-induced delamination of composites: a 2D simulation”, *Compos. B Eng.* **29**:5 (1998), 589–602.
- [Geubelle and Rice 1995] P. H. Geubelle and J. R. Rice, “A spectral method for three-dimensional elastodynamic fracture problems”, *J. Mech. Phys. Solids* **43**:11 (1995), 1791–1824.
- [González et al. 2004] C. González, J. LLorca, and A. Weck, “Toughness of fiber-reinforced titanium as a function of temperature: Experimental results and micromechanical modeling”, *Acta Mater.* **52**:13 (2004), 3929–3939.
- [Hanson and Ingraffea 2003] J. H. Hanson and A. R. Ingraffea, “Using numerical simulations to compare the fracture toughness values for concrete from the size-effect, two-parameter and fictitious crack models”, *Eng. Fract. Mech.* **70**:7–8 (2003), 1015–1027.
- [Hanson et al. 2004] J. H. Hanson, T. N. Bittencourt, and A. R. Ingraffea, “Three-dimensional influence coefficient method for cohesive crack simulations”, *Eng. Fract. Mech.* **71**:15 (2004), 2109–2124.
- [Hillerborg et al. 1976] A. Hillerborg, M. Modéer, and P.-E. Petersson, “Analysis of crack formation and crack growth in concrete by means of fracture mechanics and finite elements”, *Cement Concrete Res.* **6**:6 (1976), 773–781.

- [Kanninen and Popelar 1985] M. F. Kanninen and C. H. Popelar, *Advanced fracture mechanics*, Oxford University Press, New York, 1985.
- [Li and Bažant 1997] Y. Li and Z. P. Bažant, “Cohesive crack model with rate-dependent opening and viscoelasticity, II: Numerical algorithm, behavior and size effect”, *Int. J. Fract.* **86**:3 (1997), 267–288.
- [Mendelsohn 2006] D. A. Mendelsohn, “Free vibration of an edge-cracked beam with a Dugdale–Barenblatt cohesive zone”, *J. Sound Vib.* **292**:1–2 (2006), 59–81.
- [Mokashi 2007] P. S. Mokashi, *Numerical modeling of homogeneous and bimaterial crack tip and interfacial cohesive zones with various traction-displacement laws*, Ph.D. thesis, The Ohio State University, 2007.
- [Ohtsu and Chahrouh 1995] M. Ohtsu and A. H. Chahrouh, “Fracture analysis of concrete based on the discrete crack model by the boundary element method”, pp. 335–347 in *Fracture of brittle disordered materials: Concrete, rock and ceramics*, edited by G. Baker and B. L. Karihaloo, E & FN Spon, London, 1995.
- [Panasyuk and Yarema 2001] V. V. Panasyuk and S. Y. Yarema, “On the origin of the δ_k -model and the model of plastic strips”, *Mater. Sci. (Russia)* **37**:2 (2001), 346–353.
- [Panasyuk et al. 2003] V. V. Panasyuk, I. I. Luchko, and I. N. Pan’ko, “Deformation model of fracture in concrete”, *Strength Mater.* **35**:2 (2003), 114–121.
- [Pettersson 1981] P. E. Pettersson, “Crack growth and development of fracture zone in plain concrete and similar materials”, Report TVBM-1006, Lund Institute of Technology, Lund, 1981.
- [Plaut and Ritchie 2004] R. H. Plaut and J. L. Ritchie, “Analytical solutions for peeling using beam-on-foundation model and cohesive zone”, *J. Adhesion* **80**:4 (2004), 313–331.
- [Rice and Levy 1972] J. R. Rice and N. Levy, “The part-through surface crack in an elastic plate”, *J. Appl. Mech. (ASME)* **39** (1972), 185–194.
- [Sensmeier and Wright 1989] M. D. Sensmeier and P. K. Wright, “The effect of fiber bridging on fatigue crack growth in titanium matrix composites”, pp. 441 in *Fundamental relationships between microstructure and mechanical properties of metal-matrix composites*, edited by P. K. Liaw and M. M. Gungor, The Minerals, Metals and Materials Society, Indianapolis, 1989.
- [Shetty and Spearing 1997] S. P. Shetty and S. M. Spearing, “Fracture resistance of a fiber-reinforced film adhesive”, *Scr. Mater.* **37**:6 (1997), 787–792.
- [Sorensen 2002] B. F. Sorensen, “Cohesive law and notch sensitivity of adhesive joints”, *Acta Mater.* **50**:5 (2002), 1053–1061.
- [Suo et al. 1993] Z. Suo, S. Ho, and X. Gong, “Notch ductile-to-brittle transition due to localized inelastic band”, *J. Eng. Mater. Technol. (ASME)* **115**:3 (1993), 319–326.
- [Tada et al. 1973] H. Tada, P. C. Paris, and G. R. Irwin, *The stress analysis of cracks handbook*, Del Research Corporation, Hellertown, PA, 1973.
- [Tharp 1987] T. M. Tharp, “A finite element method for edge-cracked beam columns”, *Int. J. Numer. Methods Eng.* **24**:10 (1987), 1941–1950.
- [Wei and Hutchinson 1998] Y. Wei and J. W. Hutchinson, “Interface strength, work of adhesion and plasticity in the peel test”, *Int. J. Fract.* **93**:1–4 (1998), 315–333.
- [Wilson 1970] W. K. Wilson, “Stress intensity factors for deep cracks in bending and compact tension specimens”, *Eng. Fract. Mech.* **2**:2 (1970), 168–171.
- [Xu et al. 1995] H. H. K. Xu, C. P. Ostertag, E. R. Fuller, Jr., L. M. Braun, and I. K. Lloyd, “Fracture resistance of SiC-fiber-reinforced Si_3N_4 composites at ambient and elevated temperatures”, *J. Am. Ceram. Soc.* **78**:3 (1995), 698–704.
- [Yang and Ravi-Chandar 1996] B. Yang and K. J. Ravi-Chandar, “On the role of the process zone in dynamic fracture”, *J. Mech. Phys. Solids* **44**:12 (1996), 1955–1976.
- [Yang et al. 1999] Q. D. Yang, M. D. Thouless, and S. M. Ward, “Numerical simulations of adhesively-bonded beams failing with extensive plastic deformation”, *J. Mech. Phys. Solids* **47**:6 (1999), 1337–1353.
- [Yang et al. 2004] Q. D. Yang, D. J. Shim, and S. M. Spearing, “A cohesive zone model for low cycle fatigue life prediction of solder joints”, *Microelectron. Eng.* **75**:1 (2004), 85–95.

- [Yokoyama and Chen 1998] T. Yokoyama and M.-C. Chen, “[Vibration analysis of edge-cracked beams using a line-spring model](#)”, *Eng. Fract. Mech.* **59**:3 (1998), 403–409.
- [Young 1994] L.-J. Young, *A boundary element analysis of fracture surface and interference for mixed mode loading problems with elastic or plastic crack tips*, Ph.D. thesis, The Ohio State University, 1994.
- [Zok and Hom 1990] F. Zok and C. L. Hom, “[Large scale bridging in brittle matrix composites](#)”, *Acta Metall. Mater.* **38**:10 (1990), 1895–1904.

Received 30 Oct 2007. Revised 10 Jun 2008. Accepted 15 Aug 2008.

PRASAD S. MOKASHI: mokashi.1@osu.edu

Department of Mechanical Engineering, Scott Laboratory, The Ohio State University, 201 W 19th Avenue,, Columbus, Ohio 43210, United States

DANIEL A. MENDELSON: mendelson.1@osu.edu

Department of Mechanical Engineering, Scott Laboratory, The Ohio State University, 201 W 19th Avenue, Columbus, Ohio 43210, United States

NONLINEAR VIBRATION OF AN EDGE-CRACKED BEAM WITH A COHESIVE ZONE, II: PERTURBATION ANALYSIS OF EULER-BERNOULLI BEAM VIBRATION USING A NONLINEAR SPRING FOR DAMAGE REPRESENTATION

DANIEL A. MENDELSON, SRIDHAR VEDACHALAM,
CLAUDIO PECORARI AND PRASAD S. MOKASHI

A nonlinear free-vibration analysis of an Euler–Bernoulli beam with an edge crack and a cohesive zone at the crack tip, represented by bending and shear springs, is presented. Restricting attention to bending nonlinearities, we suppose the beam is loaded statically in bending into the nonlinear region and small amplitude vibrations are then superposed. A two term perturbation expansion is used where the small parameter depends on the ratio of the first and second derivatives of the nonlinear moment-slope relations computed in Part I. The zeroth order term is the linear free-vibration solution (constant spring stiffness equal to the first derivative of the moment-slope relation). Each mode generates a second harmonic (first-order term) whose magnitude depends on the linear spring stiffness and on the small perturbation parameter. Key features of the zeroth and first-order solutions are studied as functions of the moment-slope relations computed in Part I, and the possibility of cohesive property characterization is discussed.

1. Introduction

Material characterization based on vibration characteristics is an important quantitative nondestructive evaluation (QNDE) tool. The presence of cracks in a structure causes an increase in structural and material compliance, reduction in the natural frequencies, and changes in the mode shapes. Natural frequency and mode shape versus crack geometry relationships are of interest, for example, in the assessment of the performance integrity of cracked structures, nondestructive evaluation of the extent and location of cracking, and prediction of the resonant frequency in high-cycle fatigue. The reduction in natural frequencies caused by transverse cracks in linear elastic beams and similar thin structures has been studied extensively both theoretically and experimentally. (See [Gudmundson 1982; Gudmundson 1983; Bamnios and Trochidis 1995a; Bamnios and Trochidis 1995b; Dimarogonas 1996; Chondros and Dimarogonas 1998; Gounaris and Papadopoulos 1997; Chondros et al. 1998; Yokoyama and Chen 1998; Shifrin and Ruotolo 1999; Mahmoud et al. 1999; Li 2001; Chondros 2001]. See also the numerous references in [Kessler et al. 2002], and the extensive review in [Dimarogonas 1996].) A typical beam analysis involves a linear elastic frequency analysis of the vibrating beam, modeled by Euler–Bernoulli or some higher order beam theory on either side of the (infinitesimally thin) crack plane along with one of various models for representing the localized increased compliance of the beam in the neighborhood of the crack plane caused by the presence of the crack. One such model, used in the present analysis and previously by Yokoyama and Chen [1998] and Mendelsohn [2006], is the line-spring model [Rice

Keywords: nonlinear beam vibrations, cracked beam, cohesive zone, material characterization.

and Levy 1972], which replaces the crack plane with shear and bending springs, whose stiffnesses are found from fracture mechanics solutions of edge-cracked geometries under appropriate loading. The analysis of Yokoyama and Chen [1998] assumes elastic behavior at the crack tip(s) which allows the spring constants to be found from well-tabulated elastic fracture mechanics solutions for stress intensity factors. In the absence of material nonlinearity, the spring constants found in this way are independent of load and depend only on crack length and specimen geometry.

The majority of the work cited above in vibration signatures of cracked structures has been linear and elastic and the only nonlinearity that has been studied is that due to intermittent crack face contact during a vibration cycle, known as the breathing crack phenomenon. This results in higher harmonics generated through the coupling of the bending vibrations with longitudinal motions in the direction of the opening and closing crack faces [Dimarogonas 1996; Chondros et al. 2001; Brandon et al. 1999; Sekhar and Balaji Prasad 1998; Ruotolo et al. 1996]. The reductions in natural frequencies compared to the uncracked beam are less than when the crack closure portions of the vibration cycle are prevented from occurring, say due to a static preload.

Turning to material types of nonlinearity, we note, as discussed in detail in the companion paper [Mokashi and Mendelsohn 2008], that many materials exhibit a region of cohesive behavior that is limited to a thin planar zone ahead of the crack tip, often referred to as a cohesive zone. The only beam vibration analysis that considers plastic or cohesive behavior at the crack tip that the authors are aware of is that of [Mendelsohn 2006], who also solves a free-vibration problem for the cracked beam using the line-spring model. However, despite the nonlinear behavior of the $M - \Delta\theta$ relationships found using a Dugdale–Barenblatt cohesive zone, the dynamic response is assumed to be linear and the stiffness constant is taken to be the slope of the nonlinear $M - \Delta\theta$ curve. In other words, at a given static preload M_S , the dynamic response is assumed to take place linearly along the local tangent to the nonlinear $M - \Delta\theta$ curve. Since the crack plane is taken at the midspan, and the applied static preload is in bending only, as will be the case in the present analysis as well, only the symmetric modes activate the bending cohesive behavior and the shear response is always elastic. The shear line-spring stiffness was therefore calculated as in [Yokoyama and Chen 1998] and confirmed by the BEM analysis in the doctoral thesis by Mokashi [2007]. For sufficiently large static preloads, the resulting linear eigenvalue problem results in markedly reduced natural frequencies compared to the elastic cracked case with no cohesive zones.

The present work extends that of Mendelsohn [2006] in two ways. First, it makes use of the nonlinear $M - \Delta\theta$ curves for the linear softening cohesive zone [Mokashi and Mendelsohn 2008], as opposed to those for Dugdale–Barenblatt cohesive zones. This is important for many materials, which exhibit softening behavior before crack growth and ultimate failure. And second, it is the first attempt to address the nonlinearity of the line-spring directly in the dynamic analysis. This is done by employing an asymptotic or perturbation technique used in nonlinear dynamics. The method involves identifying the nonlinear part of the nonlinear bending spring boundary condition, and writing it in such a way that it is multiplied by a parameter, which can be argued to be small. The solution is then expanded in powers of the small parameter, and by collecting terms of like powers of the small parameter, a series of linear boundary conditions are generated. The lowest order boundary conditions are naturally linear, while the nonlinear terms in the original formulation result in nonlinear combinations of lower order results appearing as known loading terms in the higher order linear problems. This method has been widely used for including weak nonlinearities throughout nonlinear dynamics; spatially discrete and

spatially continuous systems, and in the time domain and frequency domain. In problems similar to the present one, Pecorari [2003; 2004] and Pecorari and Poznić [2005] have used a perturbation approach in a frequency domain analysis of wave transmission and reflection at contact interfaces, where the elasto-plastic contact is represented by nonlinear springs. The work presented here is a first step toward evaluating the feasibility of and developing an inverse technique, which would determine the cohesive law parameters from measurements of the nonlinear contributions to the dynamic response of edge-cracked beam specimens.

2. Nonlinear beam vibration formulation

In the following the line-spring model for a cracked beam is introduced, and the relationship between the quasistatic nonlinear bending deformation across the crack-plane and the nonlinear small amplitude dynamic response about a quasistatic preload is discussed. Since the present study is aimed at characterizing only cohesive nonlinearity effects, the well understood nonlinearity due to crack face contact is avoided by assuming a static preload for two reasons. While the contact conditions could be added, and the vibration problem without the static preload could be treated with a slightly modified perturbation method, that would (i) only confuse the issue at hand by mixing the two nonlinear effects, and (ii) require extremely large vibration amplitudes to activate significant cohesive behavior during a test. The latter would be almost impossible to control, so as is commonly done in QNDE, the cohesive zone is activated by the static preload and the superposed vibrations are assumed to be of small amplitude about this preload state.

The resulting nonlinear motions about the static preload are represented as a two-term series in a small parameter which depends on the quasistatic nonlinear bending deformation behavior and on the nondimensional amplitude of the free vibration response. This yields two uncoupled problems; one that is of zeroth order in the small parameter which is the fundamental modified free-vibration eigenvalue problem. The second of these problems (first order in the small parameter) is a forced vibration problem where the source term is the zeroth order contribution to the nonlinear bending spring boundary condition, which is solved for first from the zeroth order problem. For each natural frequency and mode shape from the zeroth order problem, there is a first-order solution with known amplitude and frequency twice that of the natural frequency (that is, the nonlinearity generates a complete set of second harmonics). Consider a simply supported Euler–Bernoulli beam of rectangular cross-section A , containing an edge-crack of length a located a distance c from the left end; see Figure 1. The beam has length L , depth W and thickness b ($A = b \cdot W$), although all measurable results are independent of the thickness b . The presence of the crack allows discontinuities in transverse deflection (Δv) and slope of the deflection ($\Delta \theta$) across the crack-plane [Mokashi and Mendelsohn 2008, Figure 1]. Recalling the line-spring model of the crack-plane presented in [Mokashi and Mendelsohn 2008], we rewrite the bending and shear interactions [Mokashi and Mendelsohn 2008, Equations (1) and (2)] in terms of resistance or stiffness rather than compliance.

$$M = R_N(\Delta \theta) \quad (1a)$$

$$Q = R_T(\Delta v) = K_T \Delta v. \quad (1b)$$

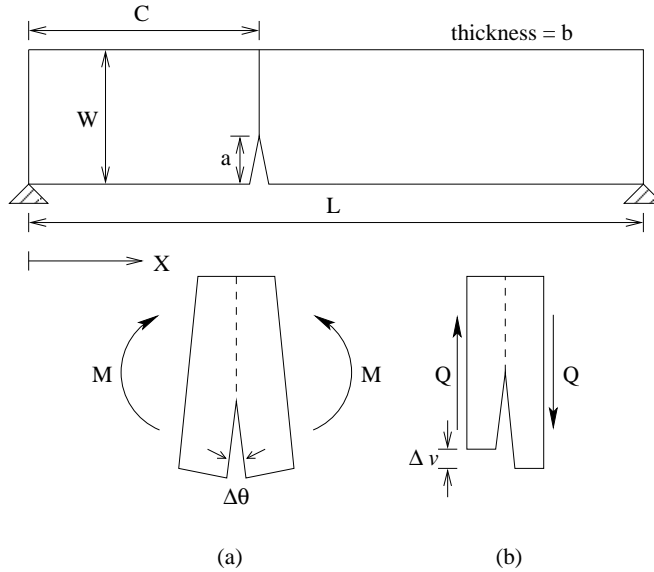


Figure 1. (a) Geometry of an edge-cracked beam. (b) Discontinuity in slope and deflection under mode I and mode II loading, respectively.

Here R represents the resistance to crack-plane deformation. If material behavior is linear for a particular mode, then that R is a linear function of the deformation with slope equal to the stiffness. Since the static preload and resulting cohesive behavior is in bending only, the shear spring is assumed linear throughout, and the second equality in Equation (1b) is used, where K_T is the stiffness obtained from an elastic mode II loading crack solution.

The nonlinearity in the bending spring is now treated. Consider a general nonlinear quasistatic softening relationship for the bending spring (Figure 2) representing any of the predicted relations from [Mokashi and Mendelsohn 2008, Figures 8 and 9]. In order to isolate the bending effects, the crack is placed in the middle of the beam ($c = L/2$) so that the odd modes excite only mode I deformations. Now assume a static mode I preload, represented by the point $[\Delta\theta_s, M_s]$ in Figure 2, and further assume that

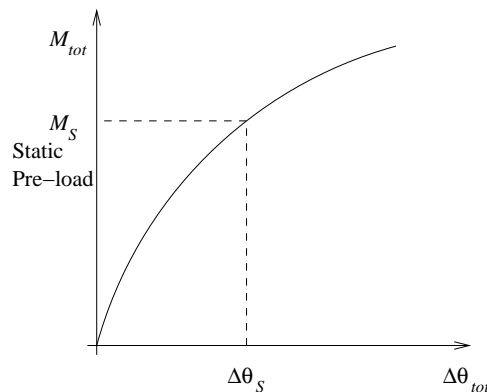


Figure 2. A generic nonlinear quasistatic $M - \Delta\theta$ curve.

small amplitude free vibrations occur about the preload state. Neglecting hysteresis, a first approximation for the dynamic behavior is that the point $[\theta_{\text{tot}}, M_{\text{tot}}]$ lies along the tangent to the curve at $[\Delta\theta_s, M_s]$ [Mendelsohn 2006] where ‘tot’ indicates the total response which is sum of the static and dynamic responses. This is equivalent to taking the total response to be the first two terms of a Taylor series expansion about $[\Delta\theta_s, M_s]$. This approximation is refined here by assuming that the dynamic response is nonlinear as well and that $[\theta_{\text{tot}}, M_{\text{tot}}]$ lies along a parabola at $[\Delta\theta_s, M_s]$, that is, the first three terms in the Taylor series about $[\Delta\theta_s, M_s]$:

$$M_{\text{tot}} = M_s + K_{N0}(\Delta\theta_{\text{tot}} - \Delta\theta_s) + K_{N1}(\Delta\theta_{\text{tot}} - \Delta\theta_s)^2, \tag{2a}$$

$$K_{N0} \equiv [(dM_{\text{tot}}/d\Delta\theta_{\text{tot}})]_{\Delta\theta_{\text{tot}}=\Delta\theta_s}, \tag{2b}$$

$$K_{N1} \equiv (1/2)[(d^2M_{\text{tot}}/d\Delta\theta_{\text{tot}}^2)]_{\Delta\theta_{\text{tot}}=\Delta\theta_s}. \tag{2c}$$

Now, defining the dynamic moment to be the total minus the static moment and similarly for the jump in slope, the nonlinear dynamic representation of the bending spring is obtained as

$$M = K_{N0}\Delta\theta + K_{N1}\Delta\theta^2, \tag{3}$$

where K_{N0} and K_{N1} are defined above and M and $\Delta\theta$ (without subscripts) are the dynamic moment and jump in slope.

2.1. Beam equation of motion and boundary conditions. The equation of motion for an Euler–Bernoulli beam is

$$EI \frac{\partial^4 v}{\partial x^4} + \rho A \frac{\partial^2 v}{\partial t^2} = 0, \tag{4}$$

where EI is the flexural rigidity, ρ is the density, A is the cross-sectional area, $v(x, t)$ is the displacement of the mid-plane, defined positive in the upward direction, and $\theta(x, t) = (\partial v/\partial x)$ is the slope, defined positive in the counter-clockwise direction. The bending moment and shear force are $M(x, t) = EI(\partial^2 v/\partial x^2)$ and $Q(x, t) = EI(\partial^3 v/\partial x^3)$. (See [Mokashi and Mendelsohn 2008, Figure 1] for sign conventions.) The following boundary conditions can be specified for all times $t > 0$. At the simple supports ($x = 0, L$) the displacement and rotational moment are zero. Since the length of the line-spring is always zero, static equilibrium requires that the bending moment and shear force across the crack plane be continuous.

$$\frac{\partial^2 v}{\partial x^2}(c-, t) = \frac{\partial^2 v}{\partial x^2}(c+, t), \tag{5}$$

$$\frac{\partial^3 v}{\partial x^3}(c-, t) = \frac{\partial^3 v}{\partial x^3}(c+, t). \tag{6}$$

where $c-$ and $c+$ indicate limits from the left and right, respectively as x goes to c . The jump in displacement and slope, respectively, across the crack plane are defined as

$$\Delta v(t) \equiv v(c+, t) - v(c-, t), \tag{7}$$

$$\Delta\theta(t) \equiv \frac{\partial v}{\partial x}(c+, t) - \frac{\partial v}{\partial x}(c-, t). \tag{8}$$

The bending moment is related to the change in slope across the crack plane through the nonlinear bending relation (3):

$$M = EI \frac{\partial^2 v}{\partial x^2}(c-, t) = K_{N0} \Delta\theta(t) + K_{N1} (\Delta\theta(t))^2. \tag{9}$$

The shear spring relation is, however, linear:

$$Q = EI(\partial^3 v / \partial x^3) = -K_{T0} \Delta v(t). \tag{10}$$

2.2. Nondimensionalization and perturbed boundary conditions. In the following perturbation analysis, the zeroth order solution will be eigenfunctions of the linear free-vibration problem, involving K_{N0} and K_{T0} only. These eigenfunctions will be determined in terms of a free amplitude constant, say, A_0 , which is assumed to be small compared to the length of the beam. Write the deflection $v(x, t)$ in a variable separable form in the two solution regions: L to the left of crack plane ($0 < \bar{x} < \bar{c}$) and R to the right of the crack plane ($\bar{c} < \bar{x} < \bar{L}$), where $\bar{x} \equiv x/L$. The deflections in the left and right regions are then

$$v(x, t) = v_L(x, t) = A_0 \phi_L(\bar{x}) T(t), \quad 0 < \bar{x} < \bar{c}, \tag{11}$$

$$v(x, t) = v_R(x, t) = A_0 \phi_R(\bar{x}) T(t), \quad \bar{c} < \bar{x} < \bar{L}. \tag{12}$$

A is a free parameter representing the vibration amplitude. Substituting this notation into the linear dimensional boundary conditions (5), (6), (9) and (10) yields

$$\phi_L''(\bar{c}) = \phi_R''(\bar{c}) \tag{13}$$

$$\phi_L'''(\bar{c}) = \phi_R'''(\bar{c}) \tag{14}$$

$$\phi_L''(\bar{c})T(t) = \bar{K}_{N0}[\Delta\phi'T(t) + \epsilon_N(\Delta\phi'^2)T^2(t)], \tag{15}$$

$$\phi_L'''(\bar{c}) = -\bar{K}_{T0}\Delta\phi, \tag{16}$$

where $' \equiv (d/d\bar{x}) = L(\partial/\partial x)$, and

$$\bar{K}_{T0} \equiv (K_{T0} L^3/EI), \tag{17}$$

$$\Delta\phi = \phi_R(\bar{c}) - \phi_L(\bar{c}), \tag{18}$$

$$\bar{K}_{N0} \equiv (K_{N0} L/EI), \tag{19}$$

$$\epsilon_N \equiv (K_{N1}/K_{N0})(A_0/L), \tag{20}$$

$$\Delta\phi' \equiv \phi_R'(\bar{c}) - \phi_L'(\bar{c}). \tag{21}$$

The parameters, \bar{K}_{N0} , \bar{K}_{T0} and ϵ_N are dimensionless and ϵ_N is assumed to be a small quantity, which is easily achieved by keeping the vibration amplitude A_0 several orders of magnitude smaller than the beam length. The deflection of the beam in the left and right regions are now expanded in powers of ϵ_N .

$$\begin{aligned} v(x, t) = v_L(x, t) &= A_0 [\phi_{L0}(\bar{x}) T_0(t) + \epsilon_N \phi_{L1}(\bar{x}) T_1(t) + \dots], \quad 0 < \bar{x} < \bar{c}, \\ v(x, t) = v_R(x, t) &= A_0 [\phi_{R0}(\bar{x}) T_0(t) + \epsilon_N \phi_{R1}(\bar{x}) T_1(t) + \dots], \quad \bar{c} < \bar{x} < \bar{L}. \end{aligned} \tag{22}$$

The solution forms obtained in (22) are substituted in (15) to get the following expression for the nonlinear boundary condition

$$\begin{aligned} \phi_{L0}''(\bar{c}) T_0(t) + \epsilon_N \phi_{L1}''(\bar{c}) T_1(t) \\ = \bar{K}_{N0} [\Delta\phi_0' T_0(t) + \epsilon_N \Delta\phi_1' T_1(t) + \dots \epsilon_N (\Delta\phi_0' T_0(t) + \epsilon_N \Delta\phi_1' T_1(t) + \dots)^2]. \end{aligned} \quad (23)$$

Keeping only the zeroth and first-order terms of ϵ_N , this can be rewritten as

$$\phi_{L0}''(\bar{c}) T_0(t) + \epsilon_N \phi_{L1}''(\bar{c}) T_1(t) = \bar{K}_{N0} [\Delta\phi_0' T_0(t) + \epsilon_N (\Delta\phi_1' T_1(t) + (\Delta\phi_0')^2 T_0^2(t))]. \quad (24)$$

In order that (22) be satisfied for all times t , we must have $T_1(t) = T_0^2(t)$. The solution forms for $v(x, t)$ in (22) are now substituted into the linear nondimensional boundary conditions, (13)–(16). The resulting expressions and (24) are then separated into zeroth order and first-order contributions in ϵ_N , to obtain separate linear nondimensional, time-independent boundary conditions for the zeroth and the first-order problems.

The zeroth order crack plane boundary conditions are written as:

$$\begin{aligned} \phi_{L0}''(\bar{c}) &= \phi_{R0}''(\bar{c}), \\ \phi_{L0}'''(\bar{c}) &= \phi_{R0}'''(\bar{c}), \\ \phi_{L0}''(\bar{c}) - \bar{K}_{N0} \Delta\phi_0' &= 0, \\ \phi_{L0}'''(\bar{c}) + \bar{K}_{T0} \Delta\phi_0 &= 0. \end{aligned} \quad (25)$$

The first-order crack plane boundary conditions are written as:

$$\begin{aligned} \phi_{L1}''(\bar{c}) &= \phi_{R1}''(\bar{c}), \\ \phi_{L1}'''(\bar{c}) &= \phi_{R1}'''(\bar{c}), \\ \phi_{L1}''(\bar{c}) - \bar{K}_{N0} \Delta\phi_1' &= \bar{K}_{N0} (\Delta\phi_0')^2, \\ \phi_{L1}'''(\bar{c}) + \bar{K}_{T0} \Delta\phi_1 &= 0. \end{aligned} \quad (26)$$

Note that the time functions factor out of all of these linear boundary conditions if $T_1(t) = T_0^2(t)$. The zeroth and first-order jumps $\Delta\phi_0$, $\Delta\phi_0'$ and $\Delta\phi_1'$ are defined analogously to the total jumps in (18) and (21) by adding a subscript of 0 or 1.

3. Zeroth order solution

Assuming the time dependence $T_0(t) = \sin(\omega_0 t)$ and substituting the zeroth order contributions to the displacement forms in (22) into the equation of motion, (4), leads to the forms:

$$\begin{aligned} v_{L0}(x, t) &= A_0 \phi_{L0}(\bar{x}) T_0(t) \\ &= A_0 [C_1 \sin(\bar{k}_0 \bar{x}) + C_2 \sin h(\bar{k}_0 \bar{x})] \sin(\omega_0 t), \end{aligned} \quad (27)$$

$$\begin{aligned} v_{R0}(x, t) &= A_0 \phi_{R0}(\bar{x}) T_0(t) \\ &= A_0 [C_3 \sin(\bar{k}_0 \bar{x}) - \tan(\bar{k}_0) \cos(\bar{k}_0 \bar{x})] + C_4 [\sin h(\bar{k}_0 \bar{x}) - \tan h(\bar{k}_0) \cos h(\bar{k}_0 \bar{x})] \sin(\omega_0 t), \end{aligned}$$

where $\bar{k}_0 \equiv k_0 L$ and the wave number k_0 and frequency ω_0 are related by

$$k_0^2 = \omega_0 \sqrt{(\rho A / EI)}. \tag{28}$$

The solution forms in Equation (27) satisfy the simple support boundary conditions of zero displacement and zero moment at $\bar{x} = 0$ and $\bar{x} = 1$. Using a linear system in the unknown constants the boundary conditions (25) can be written as

$$[A] \cdot (\mathbf{x}) = 0 \tag{29}$$

where (\mathbf{x}) is the vector consisting of the four constants C_1, C_2, C_3 and C_4 and $[A]$ is the coefficient matrix, shown below

$$\begin{bmatrix} -\sin(\bar{k}_0 \bar{c}) & \sinh(\bar{k}_0 \bar{c}) & \sin(\bar{k}_0 \bar{c}) - \tan(\bar{k}_0) \cos(\bar{k}_0 \bar{c}) & \tanh(\bar{k}_0) \cosh(\bar{k}_0 \bar{c}) - \sinh(\bar{k}_0 \bar{c}) \\ -\cos(\bar{k}_0 \bar{c}) & \cosh(\bar{k}_0 \bar{c}) & \cos(\bar{k}_0 \bar{c}) + \tan(\bar{k}_0) \sin(\bar{k}_0 \bar{c}) & \tanh(\bar{k}_0) \sinh(\bar{k}_0 \bar{c}) - \cosh(\bar{k}_0 \bar{c}) \\ \tilde{K}_{N0} \cos(\bar{k}_0 \bar{c}) - \sin(\bar{k}_0 \bar{c}) & \tilde{K}_{N0} \cosh(\bar{k}_0 \bar{c}) + \sinh(\bar{k}_0 \bar{c}) & -\tilde{K}_{N0} (\cos(\bar{k}_0 \bar{c}) + \tan(\bar{k}_0) \sin(\bar{k}_0 \bar{c})) & \tilde{K}_{N0} (\tanh(\bar{k}_0) \sinh(\bar{k}_0 \bar{c}) - \cosh(\bar{k}_0 \bar{c})) \\ \tilde{K}_{T0} \sin(\bar{k}_0 \bar{c}) + \cos(\bar{k}_0 \bar{c}) & \tilde{K}_{T0} \sinh(\bar{k}_0 \bar{c}) - \cosh(\bar{k}_0 \bar{c}) & \tilde{K}_{T0} (\tan(\bar{k}_0) \cos(\bar{k}_0 \bar{c}) - \sin(\bar{k}_0 \bar{c})) & \tilde{K}_{T0} (\tanh(\bar{k}_0) \cosh(\bar{k}_0 \bar{c}) - \sinh(\bar{k}_0 \bar{c})) \end{bmatrix}$$

The dimensionless bending and shear stiffnesses in $[A]$ are defined as

$$\tilde{K}_{N0} \equiv \frac{\tilde{K}_{N0}}{\bar{k}_0} = \frac{K_{N0}}{EI k_0} = \frac{12}{EW^3 k_0} \left(\frac{K_{N0}}{b} \right), \tag{30}$$

$$\tilde{K}_{T0} \equiv \frac{\tilde{K}_{T0}}{\bar{k}_0^3} = \frac{K_{T0}}{EI k_0^3} = \frac{12}{EW^3 k_0} \left(\frac{K_{T0}}{b} \right) \tag{31}$$

where W is the depth and b is the thickness of the beam. Setting the determinant of the matrix $[A]$ equal to zero for given crack position, \bar{c} and stiffnesses \tilde{K}_{N0} and \tilde{K}_{T0} yields an infinite number of eigenvalues

$$k_{0n}; \quad n = 1, 2, 3, \dots \tag{32}$$

For a given mode and k_{0n} the mode shapes can be determined by solving any three of the four equations of the linear system, (29), for any three of the constants (C_1, C_2, C_3, C_4) in terms of the fourth and substituting in (27).

4. First-order solution

For each of the infinite zeroth order modes with wavenumber k_{0n} and frequency ω_{0n} ($n = 1, 2, 3, \dots$), there is a first order solution with wavenumber k_{1n} and frequency ω_{1n} . For convenience, the index n is suppressed throughout this section. Since there is already an undetermined amplitude constant A_0 in the zeroth order solution, (27), one of the four constants C_1, C_2, C_3, C_4 may be taken to be unity without loss of generality. Hence from here on, let $C_1 = 1$.

The first-order crack plane boundary conditions can be written time-independently (see Equation (26)) only if $T_1(t) = T_0^2(t)$. For the assumed $T_0(t) = \sin(\omega t)$ above

$$T_1(t) = T_0^2(t) = \sin^2(\omega_0 t) = 1/2 - 1/2 \cos(2\omega_0 t) \cong -1/2 \cos(2\omega_0 t), \tag{33}$$

where the last relation indicates the dynamic contribution to $T_1(t)$. Hence, for the first-order solution, the frequency is $\omega_1 = 2\omega_0$, and $k_1 = \sqrt{2}k_0$, (28). The first order solution for the deflections to the left

and right of the crack planes that satisfy the simple support conditions at $\bar{x} = 0$ and $\bar{x} = 1$ can thus be defined as

$$\begin{aligned}
 v_{L1}(x, t) &= \epsilon_N A_0 \phi_{L1}(\bar{x}) T_1(t) \\
 &= \epsilon_N A_0 [D_1 \sin(\bar{k}_1 \bar{x}) + D_2 \sinh(\bar{k}_1 \bar{x})] (-1/2 \cos(2\omega_0 t)), \\
 v_{R1}(x, t) &= \epsilon_N A_0 \phi_{L1}(\bar{x}) T_1(t) \\
 &= \epsilon_N A_0 [D_3 \sin(\bar{k}_1 \bar{x}) - \tan(\bar{k}_1) \cos(\bar{k}_1 \bar{x}) \\
 &\quad + D_4 [\sinh(\bar{k}_1 \bar{x}) - \tanh(\bar{k}_1) \cosh(\bar{k}_1 \bar{x})] (-1/2 \cos(2\omega_0 t)),
 \end{aligned}
 \tag{34}$$

where $\bar{k}_1 \equiv k_1 L$. The single higher harmonic is at twice the frequency and is phase shifted compared to the fundamental. Similar to the zeroth order, this deflection solution is now substituted in the first-order nondimensional, time-independent boundary conditions, (26), yielding the linear system

$$[B] \cdot (\mathbf{y}) = (Z), \tag{35}$$

where (\mathbf{y}) is the vector consisting of the four constants D_1, D_2, D_3 and D_4 , and the elements of (Z) are $Z_1 = 0, Z_2 = 0, Z_3 = 0$ and $Z_4 = (\tilde{K}_{N0}(\Delta\phi'_0)^2/2\bar{k}_0)$. The term $\Delta\phi'_0$ in the fourth element of (Z) is obtained from the zeroth order mode shape as

$$\Delta\phi'_0 = \phi'_{R0}(\bar{c}) - \phi'_{L0}(\bar{c}). \tag{36}$$

The coefficient matrix $[B]$ is given below

$$\begin{bmatrix}
 -\sin(\bar{k}_1 \bar{c}) & \sinh(\bar{k}_1 \bar{c}) & \sin(\bar{k}_1 \bar{c}) - \tan(\bar{k}_1) \cos(\bar{k}_1 \bar{c}) & \tanh(\bar{k}_1) \cosh(\bar{k}_1 \bar{c}) - \sinh(\bar{k}_1 \bar{c}) \\
 -\cos(\bar{k}_1 \bar{c}) & \cosh(\bar{k}_1 \bar{c}) & \cos(\bar{k}_1 \bar{c}) + \tan(\bar{k}_1) \sin(\bar{k}_1 \bar{c}) & \tanh(\bar{k}_1) \sinh(\bar{k}_1 \bar{c}) - \cosh(\bar{k}_1 \bar{c}) \\
 \frac{\tilde{K}_{T0}}{2\sqrt{2}} \sin(\bar{k}_1 \bar{c}) + \cos(\bar{k}_1 \bar{c}) & \frac{\tilde{K}_{T0}}{2\sqrt{2}} \sinh(\bar{k}_1 \bar{c}) - \cosh(\bar{k}_1 \bar{c}) & \frac{\tilde{K}_{T0}}{2\sqrt{2}} [\tan(\bar{k}_1) \cos(\bar{k}_1 \bar{c}) - \sin(\bar{k}_1 \bar{c})] & \frac{\tilde{K}_{T0}}{2\sqrt{2}} [\tanh(\bar{k}_1) \cosh(\bar{k}_1 \bar{c}) - \sinh(\bar{k}_1 \bar{c})] \\
 \frac{\tilde{K}_{N0}}{\sqrt{2}} \cos(\bar{k}_1 \bar{c}) - \sin(\bar{k}_1 \bar{c}) & \frac{\tilde{K}_{N0}}{\sqrt{2}} \cosh(\bar{k}_1 \bar{c}) + \sinh(\bar{k}_1 \bar{c}) & \frac{\tilde{K}_{N0}}{\sqrt{2}} [-\cos(\bar{k}_1 \bar{c}) - \tan(\bar{k}_1) \sin(\bar{k}_1 \bar{c})] & \frac{\tilde{K}_{N0}}{\sqrt{2}} [\tanh(\bar{k}_1) \sinh(\bar{k}_1 \bar{c}) - \cosh(\bar{k}_1 \bar{c})]
 \end{bmatrix}$$

The nondimensional stiffnesses \tilde{K}_{N0} and \tilde{K}_{T0} are defined in Equation (30), substituting the solutions of (35) for D_1, D_2, D_3 and D_4 into (34) to get the first-order deflection of the beam.

5. Results

The length L and depth of the beam are taken to be 12.5 m and W 1.25 m , respectively. By appropriate scaling, results for any beam with a L/W ratio of 10 may be obtained. The thickness of the beam, b is not a critical parameter since most of the vibration parameters are independent of the thickness. The dimensionless crack ratio \bar{a} is taken to be 0.34 for all results. The material of the beam is chosen as aluminum (Young's modulus $E = 72.8$ GPa, $\nu = 0.3$). Results for other \bar{a} ratios and beam materials do not reveal any new patterns or insights. Since the even modes are antisymmetric about the midspan, the midspan is subjected only to shear and the even mode frequencies do not depend on the nonlinear bending stiffness.

The remaining parameters to prescribe and calculate are $(K_{N0}/b), (K_{N1}/b)$ and (K_{T0}/b) which in turn will determine $\tilde{K}_{N0}, \tilde{K}_{T0}$ and ϵ_N in (30) and (20). For calculation purposes we note that the $\bar{M} - \Delta\theta$ curves from the BEM model [Mokashi and Mendelsohn 2008, Figures 8 and 9] really involve $\bar{M} \equiv M/b$ and are independent of b , the beam thickness. Hence we can approximate (K_{N0}/b) and (K_{N1}/b) ,

Equations (2b)–(2c), from the particular $\bar{M} - \Delta\theta$ curve using central differences. Similarly K_{T0}/b will be independent of b , and is calculated using the elastic analysis presented in [Yokoyama and Chen 1998]:

$$\frac{K_{T0}}{b} = \frac{E}{2(1-\nu^2) \int_0^{\bar{a}} \frac{F_T^2}{1-\bar{a}} d\bar{a}}, \tag{37}$$

where F_T is a function of the dimensionless crack ratio \bar{a}

$$F_T = 1.993 \bar{a} + 4.513 \bar{a}^2 - 9.516 \bar{a}^3 + 4.482 \bar{a}^4. \tag{38}$$

For the crack length $\bar{a} = 0.34$, the shear stiffness per unit thickness is calculated to be $\bar{K}_{T0}/b = 3.3986 \cdot 10^{11} N/m^2$. Finally the perturbation parameter ϵ_N , (20), is easily written in terms of K_{N1}/b and K_{N0}/b by dividing the numerator and denominator by b .

A typical set of results for the eigenvalues and zeroth and first order mode shapes are shown in Figures 3–5. Cohesive law 5 in [Mokashi and Mendelsohn 2008, Table 1] ($t_o = 50$ MPa, $\delta_o = 1.6$ mm) is used and the static preload per unit thickness is taken to be $\bar{M}_s = 7 \cdot 10^6$ N. From the data for the $M - \Delta\theta$ relation shown in [Mokashi and Mendelsohn 2008, Figure 9], the first and second derivatives are calculated using standard central differences as $K_{N0}/b = 8.4 \cdot 10^9$ N and $K_{N1}/b = 5.88 \cdot 10^{12}$ N and the free amplitude constant is taken to be $A_0 = 0.005$ m, which gives a perturbation parameter value of $\epsilon_N = 0.28$. The first four wavenumbers and frequencies from the zeroth order eigenvalue problem are $k_{01} = 0.23883$, $k_{02} = 0.50248$, $k_{03} = 0.72195$, $k_{04} = 1.00389$, $\omega_{01} = 62.881$, $\omega_{02} = 278.337$, $\omega_{03} = 574.577$, $\omega_{04} = 1110.981$. Wave numbers are in m^{-1} and frequencies are in rad/sec. Figure 3 shows the zeroth order mode shapes and slope of the cracked beam with a cohesive zone for the lowest of these modes and compares them to the uncracked case. The presence of the crack causes an increase in maximum deflection and a jump in slope $\Delta\theta_o$ at the crack plane. Figure 4 shows the corresponding lowest mode first-order second harmonic solution for the deflection and slope for the cracked beam with a cohesive zone. The wavenumber and frequency are $k_{11} = 0.33776$ and $\omega_{11} = 125.762$. The magnitude of the first-order response depends on A_0^2 , so it is quite sensitive to A_0 , however the ratio of the first-order magnitudes to the zeroth order magnitudes depend only on A_0 through the perturbation parameter ϵ_N .

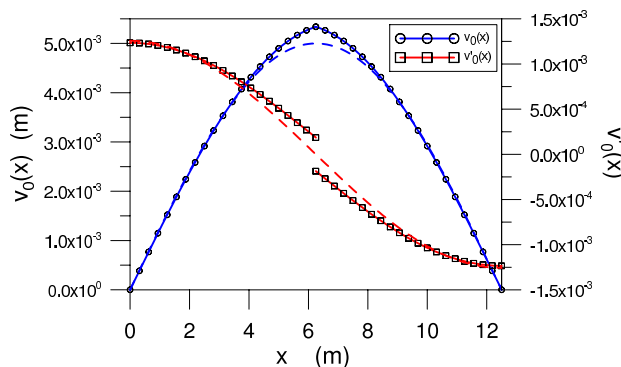


Figure 3. Zeroth-order mode shapes for deflection and slope. The solid curves are the uncracked mode shapes.

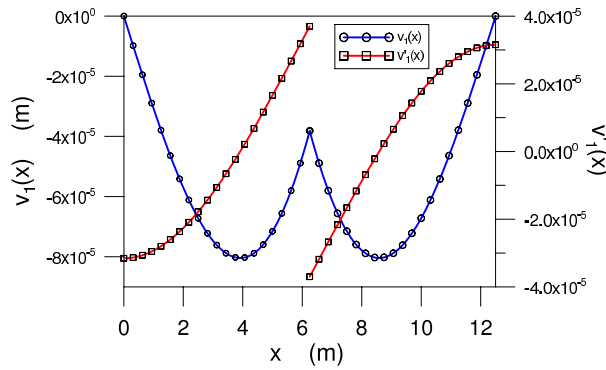


Figure 4. First-order mode shapes for deflection and slope.

The double hump in the first-order deflection appears as K_{N0} is reduced from a very large value representing an intact plane at $x = c$, and the cusp becomes deeper as K_{N0} is further reduced. The shapes of both v_1 and v_1' are independent of K_{N1} and ϵ_N . The jump in slope is distinctly observed and the maximum slopes occur at the crack plane rather than at the supports as in Figure 3. The magnitude of first-order jump in slope is observed to be on the order of 15% of the zeroth order jump in this example. Corresponding results for higher even modes show no effect of the crack or cohesive behavior and higher-order odd modes are similar to the plots shown in Figures 3 and 4, but with increasingly smaller magnitudes and wavelengths.

To study the effect of the cohesive law and its parameters, t_0 and δ_0 on the $\bar{M} - \Delta\theta$ relationship and the dynamic results, 11 cohesive laws were considered [Mokashi and Mendelsohn 2008, Table 1]. The

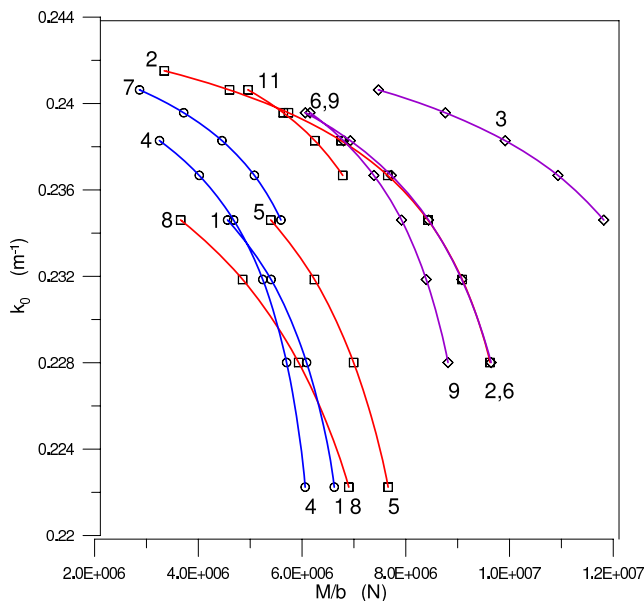


Figure 5. Variation of the first eigenvalue over applied moment.

amplitude of vibration A_0 is 0.001 in these results. All other parameters are as given above. Figure 5 shows the variation of the fundamental eigenvalue over applied static moment, \bar{M}_s for all of the cohesive laws. It can be seen that eigenvalues drop with increasing moments, starting with a maximum eigenvalue of 0.243. This is lower than the first eigenvalue for an uncracked beam ($k_{0\text{uncracked}} \approx 0.25$). The variation in eigenvalues show some dependence on J_0 , that is, with decreasing J_0 , the eigenvalue decreases for a given moment. However, this dependence is not absolute, and some deviations are observed, as seen with cases 7 and 11 of [Mokashi and Mendelsohn 2008, Table 1]. The grouping by peak cohesive traction is only partially evident in these results, but the peak traction still has an influence.

The effect of the cohesive laws on the maximum modal amplitude is seen in Figure 7. When plotted against applied moment, $(v_0)_{\text{max}}$ shows a strong dependence on t_0 . At any given moment, lower stresses lead to higher maximum modal amplitudes. For laws that share a common t_0 , as the slope of the cohesive law becomes steeper J_0 decreases, the cohesive law is exercised at a lower moment, and over the part of the load range the displacement increases with increasing slope of the law. This controls the branching off of, for example, the 6 and 9 curves from the 3 curve. The corresponding plots for $\Delta\theta$ are shown in Figure 8 and they are remarkably similar.

Next the ratios of the first-order responses to the zeroth order responses are plotted against applied moment. Figure 9 shows the maximum modal amplitude ratios (left) and the ratios of the jump in slopes for the first order to the zeroth order against applied moment (right). Both results show a strong dependence on J_0 , that is, with decreasing J_0 , higher ratios are obtained for a given moment. However, deviations to this trend are observed in cases 2, 8 and 11 [Mokashi and Mendelsohn 2008, Table 1].

A sensitivity study was done to understand the dependence of our dynamic model to the key parameters A_0 , \bar{K}_{N0} and \bar{K}_{N1} . Figure 6 (left) shows a plot of k_0 , $(v_0)_{\text{max}}$ and $\Delta\theta_0$ against the zeroth order bending

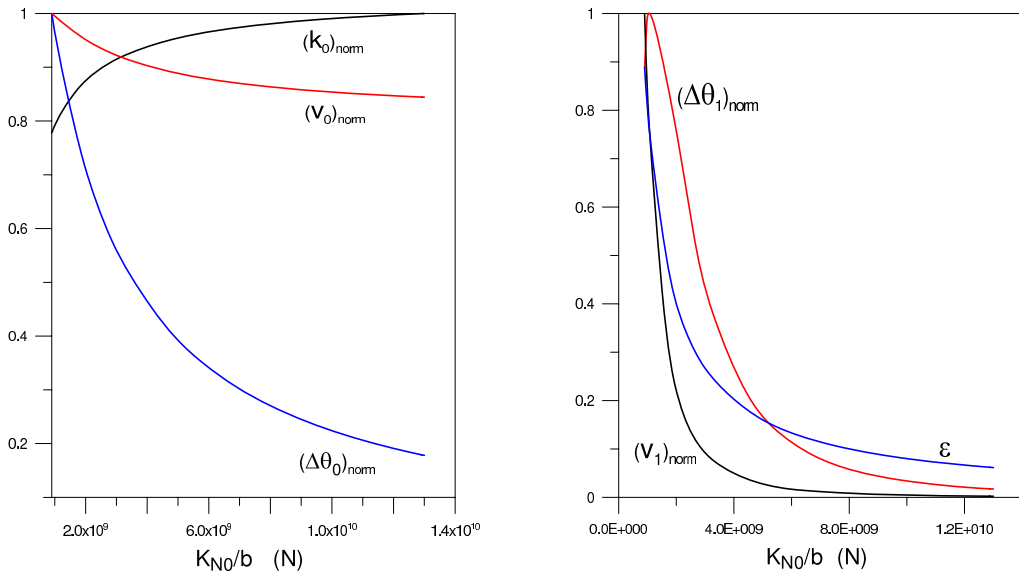


Figure 6. First eigenvalue: variation of k_0 , $(v_0)_{\text{max}}$ and $\Delta\theta_0$ (left); variation of $(v_1)_{\text{max}}$ and $\Delta\theta_1$ and ϵ over bending stiffness (right). $A_0 = 0.01$.

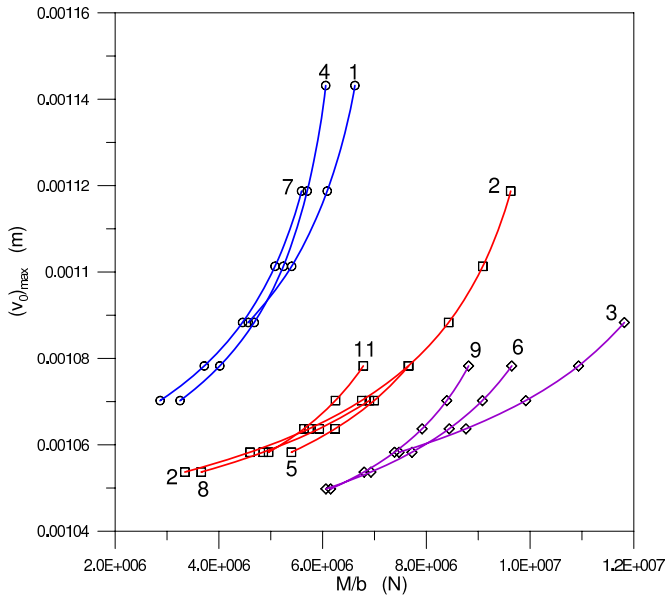


Figure 7. Variation of the maximum modal amplitude for the first eigenvalue over applied moment.

stiffness per unit thickness, \bar{K}_{N0} . The physical range of \bar{K}_{N0} considered spans from very high compliance that approximates a plastic hinge on the lower end to high stiffness approximating an uncracked beam on the higher end. k_0 shows an increase with increasing bending stiffness, asymptotically approaching 0.25, which is the first eigenvalue for the uncracked beam. $(v_0)_{\max}$ and $\Delta\theta_0$, however, decrease with an

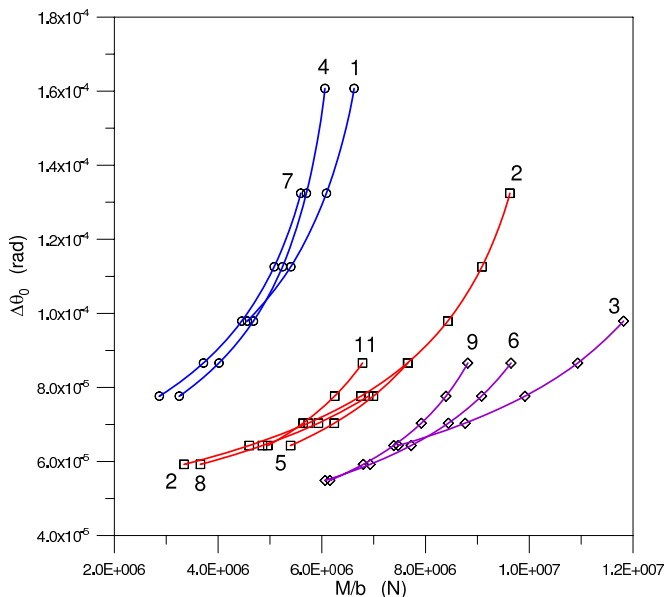


Figure 8. Variation of the jump in slope for the first eigenvalue over applied moment.

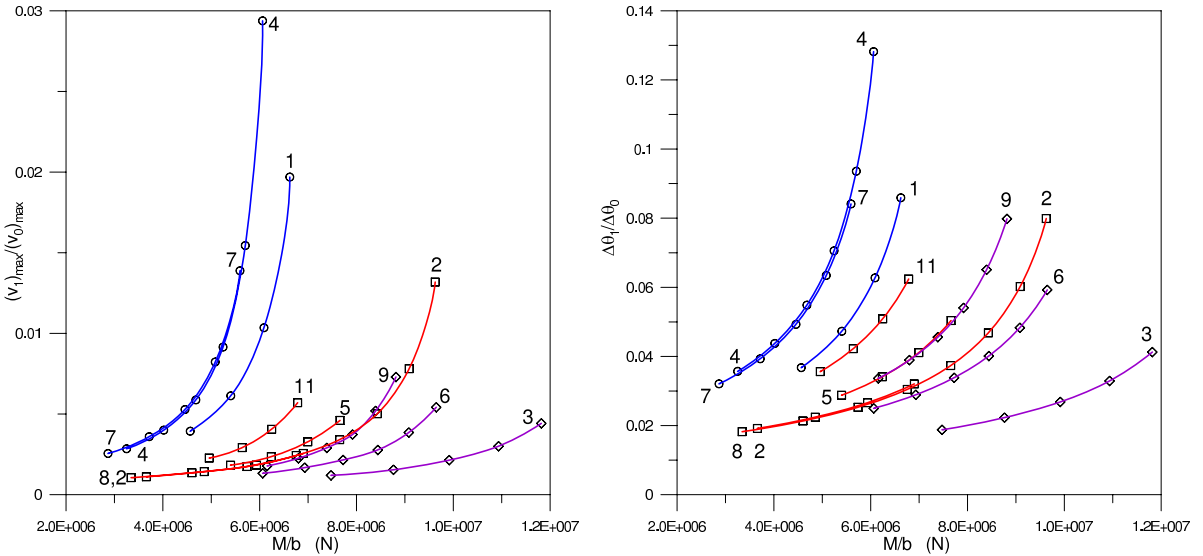


Figure 9. First eigenvalue: ratio of first- to zeroth-order maximum modal amplitude over applied moment (left); ratio of first- to zeroth-order jump in slope over applied moment (right).

increase in \bar{K}_{N0} , asymptotically reaching the uncracked condition. $(v_0)_{\max}$ and $\Delta\theta_0$ scale with A_0 , that is, using different values of A_0 , a family of similar curves can be obtained. A_0 is taken to be 0.01 in Figure 6 (left). Knowing $(v_0)_{\max}$ and $\Delta\theta_0$, it may then be possible to obtain both A_0 and the zeroth order bending stiffness, \bar{K}_{N0} . It is to be noted that k_0 does not depend on either A_0 or \bar{K}_{N1} , and both $(v_0)_{\max}$ and $\Delta\theta_0$ do not depend on \bar{K}_{N1} .

Figure 6 (right) shows a plot of $(v_1)_{\max}$, $\Delta\theta_1$ and ϵ_N against \bar{K}_{N0} . The first-order bending stiffness per unit thickness \bar{K}_{N1} is taken to be $-1 \cdot 10^{12} N$. All the three parameters show a sharp decrease with increasing stiffness. All of these parameters scale with the product $A_0 \cdot \bar{K}_{N1}$, that is, using different values of $A_0 \cdot \bar{K}_{N1}$, a family of similar curves can be obtained. Knowing A_0 and \bar{K}_{N0} from the previous plots and $(v_1)_{\max}$ or $\Delta\theta_1$ from this plot, it may then be possible to obtain the $A_0 \cdot \bar{K}_{N1}$ term. Since A_0 is known, the first-order bending stiffness, \bar{K}_{N1} could then be obtained. Results for the third eigenvalue are in [Vedachalam 2007] and show similar trends.

6. Conclusions

This paper addresses the issue of a linear softening cohesive zone ahead of a crack tip and its effect on the vibrational response of an edge-cracked beam. For a given crack length, presence of the cohesive zone leads to an additional reduction in the fundamental natural frequency, and induces nonlinearity leading to a second harmonic. The dynamic response is controlled by the critical yield stress, t_o or the critical fracture energy J_{I_o} , much more than the crack tip opening displacement δ_o or the slope of the cohesive law. The state of damage affects the $\Delta\theta$ ratios more strongly than the modal amplitude ratios. $\Delta\theta$ ratios can, therefore, be used effectively in cohesive damage characterization. Within physical ranges of the dynamic spring constants, the first-order harmonic is observed to be quite significant when compared to

the fundamental. This model has potential for use in nondestructive cohesive material characterization in beam-like structures. There is potential for determining the dynamic spring constants from the dynamic responses. However, the relationship between the spring constants and the cohesive law parameters is less clear at this point and needs to be explored more in order to move towards an experimental inverse technique based on the present modeling.

References

- [Bamnios and Trochidis 1995a] G. Bamnios and A. Trochidis, “Dynamic behaviour of a cracked cantilever beam”, *Appl. Acoust.* **45**:2 (1995), 97–112.
- [Bamnios and Trochidis 1995b] G. Bamnios and A. Trochidis, “Mechanical impedance of a cracked cantilever beam”, *J. Acoust. Soc. Am.* **97**:6 (1995), 3625–3635.
- [Brandon et al. 1999] J. A. Brandon, A. E. Stephens, E. M. O. Lopes, and A. S. K. Kwan, “Spectral indicators in structural damage identification: a case study”, *Proc. Inst. Mech. Eng. C, J. Mech. Eng. Sci.* **213**:4 (1999), 411–415.
- [Chondros 2001] T. G. Chondros, “The continuous crack flexibility model for crack identification”, *Fatigue Fract. Eng. Mater. Struct.* **24**:10 (2001), 643–650.
- [Chondros and Dimarogonas 1998] T. G. Chondros and A. D. Dimarogonas, “Vibration of a cracked cantilever beam”, *J. Vib. Acoust. (ASME)* **120**:3 (1998), 742–746.
- [Chondros et al. 1998] T. G. Chondros, A. D. Dimarogonas, and J. Yao, “A continuous cracked beam vibration theory”, *J. Sound Vib.* **215**:1 (1998), 17–34.
- [Chondros et al. 2001] T. G. Chondros, A. D. Dimarogonas, and J. Yao, “Vibration of a beam with a breathing crack”, *J. Sound Vib.* **239**:1 (2001), 57–67.
- [Dimarogonas 1996] A. D. Dimarogonas, “Vibrations of cracked structures: a state of the art review”, *Eng. Fract. Mech.* **55**:5 (1996), 831–857.
- [Gounaris and Papadopoulos 1997] G. D. Gounaris and C. A. Papadopoulos, “Analytical and experimental crack identification of beam structures in air or in fluid”, *Comput. Struct.* **65**:5 (1997), 633–639.
- [Gudmundson 1982] P. Gudmundson, “Eigenfrequency changes of structures due to cracks, notches or other geometrical changes”, *J. Mech. Phys. Solids* **30**:5 (1982), 339–353.
- [Gudmundson 1983] P. Gudmundson, “The dynamic behaviour of slender structures with cross-sectional cracks”, *J. Mech. Phys. Solids* **31**:4 (1983), 329–345.
- [Kessler et al. 2002] S. S. Kessler, S. M. Spearing, M. J. Atalla, C. E. S. Cesnik, and C. Soutis, “Damage detection in composite materials using frequency response methods”, *Compos. B Eng.* **33**:1 (2002), 87–95.
- [Li 2001] Q. S. Li, “Dynamic behavior of multistep cracked beams with varying cross section”, *J. Acoust. Soc. Am.* **109**:6 (2001), 3072–3075.
- [Mahmoud et al. 1999] M. A. Mahmoud, M. Abu Zaid, and S. Al Harashani, “Numerical frequency analysis of uniform beams with a transverse crack”, *Commun. Numer. Methods Eng.* **15**:10 (1999), 709–715.
- [Mendelsohn 2006] D. A. Mendelsohn, “Free vibration of an edge-cracked beam with a Dugdale–Barenblatt cohesive zone”, *J. Sound Vib.* **292**:1–2 (2006), 59–81.
- [Mokashi 2007] P. S. Mokashi, *Numerical modeling of homogeneous and bimaterial crack tip and interfacial cohesive zones with various traction-displacement laws*, Ph.D. thesis, The Ohio State University, 2007.
- [Mokashi and Mendelsohn 2008] P. S. Mokashi and D. A. Mendelsohn, “Nonlinear vibration of an edge-cracked beam with a cohesive zone, I: Nonlinear bending load-displacement relations for a linear softening cohesive law”, *J. Mech. Mater. Struct.* **3**:8 (2008), 1573–1588.
- [Pecorari 2003] C. Pecorari, “Nonlinear interaction of plane ultrasonic waves with an interface between rough surfaces in contact”, *J. Acoust. Soc. Am.* **113**:6 (2003), 3065–3072.
- [Pecorari 2004] C. Pecorari, “Adhesion and nonlinear scattering by rough surfaces in contact: beyond the phenomenology of the Preisach–Mayergoyz framework”, *J. Acoust. Soc. Am.* **116**:4 (2004), 1938–1947.

- [Pecorari and Poznić 2005] C. Pecorari and M. Poznić, “Nonlinear acoustic scattering by a partially closed surface-breaking crack”, *J. Acoust. Soc. Am.* **117**:2 (2005), 592–600.
- [Rice and Levy 1972] J. R. Rice and N. Levy, “The part-through surface crack in an elastic plate”, *J. Appl. Mech. (ASME)* **39** (1972), 185–194.
- [Ruotolo et al. 1996] R. Ruotolo, C. Surace, P. Crespo, and D. Storer, “Harmonic analysis of the vibrations of a cantilevered beam with a closing crack”, *Comput. Struct.* **61**:6 (1996), 1057–1074.
- [Sekhar and Balaji Prasad 1998] A. S. Sekhar and P. Balaji Prasad, “Crack identification in a cantilever beam using coupled response measurements”, *J. Eng. Gas Turb. Power (ASME)* **120**:4 (1998), 775–777.
- [Shifrin and Ruotolo 1999] E. I. Shifrin and R. Ruotolo, “Natural frequencies of a beam with an arbitrary number of cracks”, *J. Sound Vib.* **222**:3 (1999), 409–423.
- [Vedachalam 2007] S. Vedachalam, *A perturbation approach to the nonlinear vibration of a cracked and cohesively damaged beam*, Master’s thesis, The Ohio State University, 2007.
- [Yokoyama and Chen 1998] T. Yokoyama and M.-C. Chen, “Vibration analysis of edge-cracked beams using a line-spring model”, *Eng. Fract. Mech.* **59**:3 (1998), 403–409.

Received 30 Oct 2007. Revised 10 Jun 2008. Accepted 15 Aug 2008.

DANIEL A. MENDELSON: mendelsohn.1@osu.edu

Department of Mechanical Engineering, Scott Laboratory, The Ohio State University, 201 W. 19th Avenue, Columbus, OH 43210, United States

SRIDHAR VEDACHALAM: vedachalam.1@osu.edu

Environmental Science Graduate Program, The Ohio State University, 260 Ag. Engineering Building, 590 Woody Hayes Drive, Columbus, OH 43210 United States

CLAUDIO PECORARI: claudio.pecorari@afconsult.com

NDE System Development, AF-KONTROLL AB, Linköping, Sweden, SE-582 22, Sweden

PRASAD S. MOKASHI: mokashi.1@osu.edu

Department of Mechanical Engineering, Scott Laboratory, The Ohio State University, 201 W. 19th Avenue, Columbus, Ohio 43210, United States

SUBMISSION GUIDELINES

ORIGINALITY

Authors may submit manuscripts in PDF format on-line. Submission of a manuscript acknowledges that the manuscript is *original and has neither previously, nor simultaneously, in whole or in part, been submitted elsewhere*. Information regarding the preparation of manuscripts is provided below. Correspondence by email is requested for convenience and speed. For further information, write to:

[Marie-Louise Steele](#)

Division of Mechanics and Computation
Durand Building, Room 262
Stanford University
Stanford CA 94305

LANGUAGE

Manuscripts must be in English. A brief abstract of about 150 words or less must be included. The abstract should be self-contained and not make any reference to the bibliography. Also required are keywords and subject classification for the article, and, for each author, postal address, affiliation (if appropriate), and email address if available. A home-page URL is optional.

FORMAT

Authors are encouraged to use L^AT_EX and the standard article class, but submissions in other varieties of T_EX, and, exceptionally in other formats, are acceptable. Electronic submissions are strongly encouraged in PDF format only; after the refereeing process we will ask you to submit all source material.

REFERENCES

Bibliographical references should be listed alphabetically at the end of the paper and include the title of the article. All references in the bibliography should be cited in the text. The use of B^BT_EX is preferred but not required. Tags will be converted to the house format (see a current issue for examples), however, in the manuscript, the citation should be by first author's last name and year of publication, e.g. "as shown by Kramer, et al. (1994)". Links will be provided to all literature with known web locations and authors are encouraged to provide their own links on top of the ones provided by the editorial process.

FIGURES

Figures prepared electronically should be submitted in Encapsulated PostScript (EPS) or in a form that can be converted to EPS, such as GnuPlot, Maple, or Mathematica. Many drawing tools such as Adobe Illustrator and Aldus FreeHand can produce EPS output. Figures containing bitmaps should be generated at the highest possible resolution. If there is doubt whether a particular figure is in an acceptable format, the authors should check with production by sending an email to:

production@mathscipub.org

Each figure should be captioned and numbered so that it can float. Small figures occupying no more than three lines of vertical space can be kept in the text ("the curve looks like this:"). It is acceptable to submit a manuscript with all figures at the end, if their placement is specified in the text by means of comments such as "Place Figure 1 here". The same considerations apply to tables.

WHITE SPACE

Forced line breaks or page breaks should not be inserted in the document. There is no point in your trying to optimize line and page breaks in the original manuscript. The manuscript will be reformatted to use the journal's preferred fonts and layout.

PROOFS

Page proofs will be made available to authors (or to the designated corresponding author) at a web site in PDF format. Failure to acknowledge the receipt of proofs or to return corrections within the requested deadline may cause publication to be postponed.

Journal of Mechanics of Materials and Structures

Volume 3, N^o 8 October 2008

- A study of penalty formulations used in the numerical approximation of a radially symmetric elasticity problem**
ADAIR R. AGUIAR, ROGER L. FOSDICK AND JESÚS A. G. SÁNCHEZ 1403
- Numerical and experimental studies of deep indentation on single crystals**
YONG X. GAN, XI CHEN AND MANHONG ZHAO 1429
- Prefracture zone modeling for an electrically impermeable interface crack in a piezoelectric bimaterial compound**
VLADIMIR B. GOVORUKHA AND MARC KAMLAH 1447
- A generalized Cosserat point element (CPE) for isotropic nonlinear elastic materials including irregular 3-D brick and thin structures** M. JABAREEN AND M. B. RUBIN 1465
- Axisymmetric indentation of a rigid cylinder on a layered compressible and incompressible halfspace** LUIGI LA RAGIONE, FRANCESCO MUSCEO AND ALFREDO SOLLAZZO 1499
- Elastic solutions for an inclined transversely isotropic material due to three-dimensional point loads**
JYH-JONG LIAO, TIN-BIN HU AND CHENG-DER WANG 1521
- An anisotropic heterogeneous beam with overspecified boundary conditions**
C. KEVIN LYONS 1549
- Thermoelastic stability analysis of imperfect functionally graded cylindrical shells**
BABAK MIRZAVAND AND M. REZA ESLAMI 1561
- nonlinear vibration of an edge-cracked beam with a cohesive zone, I: Nonlinear bending load-displacement relations for a linear softening cohesive law**
PRASAD S. MOKASHI AND DANIEL A. MENDELSON 1573
- Nonlinear vibration of an edge-cracked beam with a cohesive zone, II: Perturbation analysis of Euler-Bernoulli beam vibration using a nonlinear spring for damage representation**
D. A. MENDELSON, S. VEDACHALAM, C. PECORARI AND P. S. MOKASHI 1589